UNIVERSITÀ
DEGLI STUDI
DI PADOVA

Sede Amministrativa: Università degli Studi di Padova

Dipartimento di Ingegneria Civile, Edile e Ambientale (ICEA)

SCUOLA DI DOTTORATO DI RICERCA IN:
SCIENZE DELL'INGEGNERIA CIVILE, AMBIENTALE E DELL'ARCHITETTURA
CURRICOLO: MATERIALI, STRUTTURE, SISTEMI COMPLESSI E ARCHITETTURA
XXXV CICLO

Numerical algorithms and methods for the simulation of flow and deformation processes in energy resources engineering

Direttore della Scuola: Ch.mo Prof. Carmelo Maiorana

Relatore: Prof. Massimiliano Ferronato

Dottorando: Laura Gazzola

UNIVERSITÀ DEGLI STUDI DI PADOVA

Abstract

Department of Civil, Architectural and Environmental Engineering

Doctor of Philosophy

Numerical algorithms and methods for the simulation of flow and deformation processes in energy resources engineering

Laura Gazzola

The accurate and reliable simulation of subsurface processes is fundamental to support engineering activities in energy resources field. Subsurface activities can have significant environmental effects, e.g., earthquakes, land subsidence, fault (re)activation or landslides. These impacts should be predicted and controlled by developing accurate and reliable numerical models.

An accurate modeling activity generally requires large domains with high resolution representations of geological structures and their heterogeneous properties. This is especially true in fractured domains, where the simulation of flow and deformation mechanisms is a tightly coupled process. In addition, the solution of the hydro-mechanical coupling in fractured domains usually requires the solution of a sequence of large-size, non-symmetric and ill-conditioned systems of equations. In this context, to improve the efficiency and robustness of linear solvers, it becomes fundamental the design of ad-hoc preconditioners tailored on the specific problem to solve.

In this thesis, a preconditioning framework is developed and adapted for three models describing the flow and deformation processes in fractured domains. The framework basically consists in: (i) a symbolic permutation of the coefficient matrix blocks in order to avoid singular leading blocks, if any, and to project the Schur complement onto different spaces; (ii) a block-factorization of the coefficient matrix, which allows to isolate the subsystems from the original coupled problem and (iii) an approximation of the single blocks. According to the reordering of the unknowns and the

techniques used for the approximations, different preconditioners can originate. For each analyzed model formulation, two or more alternative preconditioners are developed and tested against a set of numerical cases.

Uncertainties and approximations unavoidably affect any kind of mathematical model of real-world problems. In subsurface applications, uncertainties can be related for instance to the geometry and the mechanical behavior of the porous medium, the variability ranges of the main mechanical parameters, the imposition of the external forces and the boundary conditions. Thus, deterministic model outcomes may induce an excessive confidence in the solution, and stochastic approaches should be preferred.

In this thesis, the focus is on the numerical prediction of land subsidence caused by fluid withdrawal. A methodological approach is proposed to take into account uncertainties into the numerical model, and then train it with the available measurements by the aid of three data assimilation steps. Data assimilation techniques allow to evaluate the model outcomes and update them according to the observations. The expectation is to progressively reduce uncertainties as new measurements become available and the knowledge of the phenomenon increases.

The validation of the methodological approach is performed against a synthetic but realistic test case. Then, it is applied to the development of an Italian off-shore reservoir.

UNIVERSITÀ DEGLI STUDI DI PADOVA

Sommario

Dipartimento di Ingegneria Civile, Edile e Ambientale

Dottorato di Ricerca

Numerical algorithms and methods for the simulation of flow and deformation processes in energy resources engineering

Laura Gazzola

L'accurata e affidabile simulazione dei processi del sottosuolo è fondamentale per supportare le attività di ingegneria nel campo delle risorse energetiche. Le attività del sottosuolo possono avere effetti ambientali significativi, come ad esempio sismi indotti, subsidenza, (ri)attivazione di faglie o smottamenti. Questi impatti dovrebbero essere predetti e controllati attraverso lo sviluppo di modelli numerici accurati e affidabili.

Un'accurata attività di modellazione generalmente richiede grandi domini e la rappresentazione ad alta risoluzione delle strutture geologiche e delle loro proprietà. Questo è particolarmente vero nel caso di domini fratturati, dove la simulazione dei meccanismi di flusso e deformazione è un processo fortemente accoppiato. Inoltre, la soluzione dell'accoppiamento idro-meccanico in domini fratturati solitamente richiede la soluzione di una sequenza di sistemi di equazioni di grande dimensione, non simmetrici e mal condizionati. In questo contesto, per migliorare l'efficienza e la robustezza dei solutori lineari, diventa fondamentale definire precondizionatori ad-hoc su misura per lo specifico problema da risolvere.

In questa tesi, un framework di precondizionamento è stato sviluppato e adattato a tre modelli che descrivono i processi di flusso e deformazione in mezzi fratturati. Il framework consiste fondamentalmente in: (i) una permutazione simbolica dei blocchi della matrice del sistema per evitare blocchi singolari e per proiettare il complemento di Schur in spazi diversi; (ii) una fattorizzazione a blocchi della matrice, che permette di isolare i sottosistemi del sistema a blocchi originale e (iii) una approssimazione

dei singoli blocchi. Diversi precondizionatori possono avere origine a dipendere dal riordinamento delle incognite e dalle tecniche usate per le approssimazioni. Per ognuna delle formulazioni analizzate, due o più alternative di precondizionatori sono state sviluppate e testate su un gruppo di casi test.

Incertezze e approssimazioni affliggono inevitabilmente qualunque tipologia di modello matematico di problemi reali. Nelle applicazioni del sottosuolo, le incertezze possono essere connesse, ad esempio, alla geometria e al comportamente geomeccanico del mezzo poroso, agli intervalli di variabilità dei principali parametri meccanici, all'imposizione delle forzanti esterne e delle condizioni al contorno. Pertanto, risultati del modello deterministici possono portare a un'eccessiva confidenza nella soluzione, mentre approcci stocastici dovrebbero essere prediletti.

In questa tesi, il focus è sulla previsione numerica della subsidenza causata dalla estrazione di fluidi. Viene proposto un approccio metodologico per tenere in considerazione le incertezze del modello numerico, e poi allenarlo con le misure disponibili attraverso tre livelli di data assimilation. Le tecniche di data assimilation permettono di valutare i risultati del modello e aggiornarli in accordo con le osservazioni. L'aspettativa è di ridurre progressivamente le incertezze man mano che nuove misure diventano disponibili e la conoscenza del fenomeno migliora.

L'approccio metodologico è validato in un caso test sintetico, ma realistico, e poi applicato per lo sviluppo di un giacimento italiano off-shore.

Contents

List of Acronyms

AE Average absolute Error

AES Average Ensemble Spread

AMG Algebraic MultiGrid

BiCGStab BiConjugate Gradient Stabilized method

CGPS Continuous Global Positioning System

DA Data Assimilation

DARTS Delft Advanced Research Terra Simulator

DFN Discrete Fracture Network

EnKF Ensemble Kalman Filter

ES Ensemble Smoother

FDM Finite Difference Method

FEM Finite Element Method

FSAI Factorized Sparse Approximate Inverse

FVM Finite Volume Method

GMRES Generalized Minimal Residual Method

gPCE Generalized Polynomial Chaos Expansion

KKT Karush–Kuhn–Tucker

LOO leave-one-out

MC Monte Carlo

MCC modified Cam Clay

MDA Multiple Data Assimilation

PDEs Partial Differential Equations

PDF Probability Density Function

RF Red Flag

SPD symmetric positive definite

SPSD symmetric positive semidefinite

TPFA two-point flux approximation

VEP visco-elasto-plastic

Chapter 1

Introduction

Many engineering activities rely on the accurate and reliable simulation of subsurface processes, especially in the field of energy resources. The underground modeling is used to predict the impacts of human activities and support the decisions of policymakers and stakeholders. An accurate modeling activity is essential especially nowadays, in order to mitigate the climate and energy crisis on a scientific basis.

Subsurface applications are related to, e.g., geothermal energy production [Pan et al., 2019; Wei et al., 2019], groundwater extraction [Galloway and Burbey, 2011; Zhu et al., 2015], CO_2 sequestration [Fan et al., 2019; Liu et al., 2019] and injection [Vasco et al., 2010], hydraulic fracturing [Williams and Sovacool, 2019; Tan et al., 2019], steam injection [Khakim et al., 2012], underground gas extraction [Nagel, 2001; Settari et al., 2008] and storage [Karev, 2019; Firme et al., 2019].

The environmental impacts of these activities are manifold, spanning from induced seismicity [González et al., 2012; Rutqvist et al., 2016] to landslides [Awasthi et al., 2022], possibly causing well damage or breakage. One of the most known and studied effects of the subsurface resources exploitation is land subsidence. The word subsidence denotes the loss of land elevation due to natural or anthropogenic events. According to the literature, anthropogenic drivers are responsible for 76.92% of land subsidence around the world [Bagheri-Gavkosh et al., 2021]. Anthropogenic subsidence operates over hundreds to tens of years and refers to short-term movements [Eid et al., 2022]. It has been recognized on a global scale [Herrera-García et al., 2021], with potential dangerous consequences that are well known within the scientific community, see, e.g., Dinar et al. [2021] and Candela and Koster [2022]. One of the main anthropogenic causes of land subsidence is fluid withdrawal from underground [Gambolati et al.,

2006]. Indeed, the fluid extraction from aquifer systems or hydrocarbon reservoirs, induces pore-pressure to decrease, which may lead to deep compaction processes and consequent shallow subsidence.

Another significant impact of subsurface activities regards the possible (re)activation of preexisting faults and fractures. Fracture deformation can be deliberately induced in some applications, e.g., to enhance permeability through the injection of fluid at high pressure [Rutqvist and Stephansson, 2003; Evans et al., 2005]. On the contrary, the interest can be in avoiding activation of pre-existing faults and fractures, e.g., to prevent induced seismicity of unacceptable magnitude caused by the disposal of waste water [Keranen et al., 2014; Improta et al., 2015; Keranen and Weingarten, 2018].

Thus, it becomes clear that the development of accurate and reliable prediction tools for the modeling of energy-related processes is a fundamental requirement for both the energy companies and the control agencies. In this context, large domains are usually required to achieve the desired accuracy, along with high resolution representations of geological structures and their heterogeneous properties [Ferronato et al., 2010; Castelletto et al., 2013]. This is especially true in the simulation of faults and fracture networks, where flow and deformation mechanisms represent a tightly coupled process. Indeed, fractures are preferred flow pathways with respect to the surrounding matrix, especially when they are in slip or open conditions. In turn, the pressure variation in the fracture networks perturbs the stress state in the surrounding medium and influences the contact mechanics itself.

The coupled simulation of flow and deformation processes in fractured domains requires the solution of a sequence of large-size, often non-symmetric and ill-conditioned systems of equations [Ferronato et al., 2001, 2009]. In a typical simulation, most of the computational burden is committed to solve these systems. Thus, efficient and robust linear solvers are required, meaning that an appropriate design of scalable and robust preconditioning techniques is crucial. Roughly speaking, a preconditioner is an operator that transforms the original system improving its properties and accelerating, or even allowing for, the convergence. Basically, it is an approximate application of the system matrix inverse.

Different preconditioning techniques have been developed in the literature. From

an algebraic point of view, they can be classified into three main categories: (i) incomplete factorizations [Saad, 1994; Lin and Moré, 1999], (ii) approximate inverses [Benzi et al., 1996; Tang, 1999] and (iii) multilevel methods, which include domain decomposition [Toselli and Widlund, 2005; Janna et al., 2013; Dolean et al., 2015] and multigrid-like techniques [McCormick and Ruge, 1982; Stüben, 2001]. In the solution of the coupled hydro-mechanical problem in fractured domains and depending on the specific discretization technique, none of the preconditioners already available in the literature can be straightforwardly applied. Thus, ad-hoc preconditioning frameworks need to be designed tailored on the specific problem to solve, exploiting the block structure and taking advantage from the knowledge of the nature and the structure of the various blocks.

Here, three variants of the coupled model described above have been considered. The first model simulates the mechanics of the 3D medium and the flow through the fracture networks. It uses a blended finite element / finite volume approach to discretize the continuous problem and applies the contact constraints with the aid of Lagrange multipliers. Differently, a unified finite volume method and a penalty approach characterize the second model, where the fluid flow occurs both in the fracture networks and in the surrounding 3D domain. On the contrary, the third model neglects the 3D domain and focuses only on the fracture networks, solving the flow equation stated as an optimization problem. Even if these three models are designed to solve the same physical processes, the arising numerical systems present different properties and characteristics. Thus, the preconditioning framework has to be adapted for each of them.

The underlying frameworks can be summarized in three common steps: (i) a symbolic permutation of the blocks of the coefficient matrix in order to avoid singular leading blocks, if any, and to project the Schur complement onto different spaces; (ii) a block-factorization of the coefficient matrix, which allows to isolate the subsystems from the original coupled problem and (iii) an approximation of the single blocks, and in particular the arising Schur-complements. According to the reordering of the unknowns and the techniques used for the approximations, different preconditioners can originate. For each model two or more alternative preconditioners are developed.

Then, a set of numerical applications are tested to compare the techniques and investigate their efficiency and robustness.

Every model describing real-world phenomena is built over a number of hypotheses and approximations, thus the outcomes should be considered within a confidence interval, despite the level of accuracy the model can reach. Indeed, the reliability of the model predictions depends both on the accuracy of the numerical models and on the correct accounting of the sources of uncertainty.

In this work, the focus is on the simulation of land subsidence caused by the exploitation of hydrocarbon reservoirs. The capability to predict the absolute value of the subsidence and its spatial variability is crucial to identify the areas that are most affected by subsidence and to propose measures to counteract the adverse effects of subsidence [Fokker et al., 2019].

A traditional procedure to study land subsidence consists on the definition of a number of deterministic scenarios as input for a numerical model, whose outcomes are combined to determine confidence intervals. This approach has two main drawbacks: (i) it does not allow to properly account for the uncertainties that unavoidably affect the modeling of real-world phenomena, and (ii) it does not take full advantages from the increasing availability of monitoring data during the life span of the reservoir. Indeed, using all the available measurements takes on a central role in the monitoring phase and for accurate forecasts [Fokker et al., 2019; Bernardi et al., 2021].

Thus, the second goal of this thesis work is to contribute at the development of a comprehensive methodological approach that dynamically accounts for and reduces the uncertainties, training the numerical model with the available measurements. Specifically, the integration of measurements in the numerical model is performed with the aid of Data Assimilation (DA) techniques. In recent years, DA techniques have been successfully used for a number of underground applications, like hydrology and geomechanical engineering. Among the others, Ensemble Smoother (ES) demonstrates to be the preferred choice for geomechanical models [Evensen and Eikrem, 2018].

Recently, another approach combining a geomechanical model and DA has been proposed [Candela et al., 2022]. It considers the ensemble-based approach ESIP [Candela et al., 2017] and a 3D geological subsurface model of the Netherlands, combined

to discriminate the compaction model mainly driving the Dutch subsidence. To the author knowledge, there are no other works providing a sequential DA procedure to improve the prediction of land subsidence.

The methodological approach presented herein has been developed as a tool to support the modeling activities throughout the reservoir life cycle. The numerical model is trained in time according to the availability of new measurements with the expectation of progressively reducing the uncertainties as the knowledge of the specific reservoir improves.

The first step of the workflow consists in the identification of the sources of uncertainties for the specific case study and their propagation from the model input to the output by the generation of a set of ensembles of Monte Carlo (MC) realizations. Then, three successive DA steps are repeatedly performed in time, namely the χ^2-test [Tarantola, 2005], the Red Flag (RF) technique [Nepveu et al., 2010] and ES method [van Leeuwen and Evensen, 1996]. This allows to progressively train the model and improve its overall reliability as the reservoir development proceeds.

The workflow has been first validated against a synthetic, but realistic, test-case and then applied to the Arlua reservoir, which is an off-shore hydrocarbon reservoir buried in the Northern Adriatic basin, Italy. Capabilities and limits of the proposed approach are investigated and discussed.

1.1 Summary

The thesis is organized in Chapters as follows.

- **Chapter 1** introduced the objectives and the relevance of this thesis.
- **Chapter 2** describes the equations that govern the hydro-mechanical behavior of a fractured porous medium and presents the possible strategies for their numerical treatment.
- **Chapter 3** introduces some general concepts about preconditioners, then ad-hoc preconditioning frameworks for the hydro-mechanical coupling in fractured porous media are developed. In particular, analyses are carried out on two formulations

for the full problem and on a model which takes care only of the fracture network, neglecting the 3D domain.

- **Chapter 4** presents a comprehensive methodological approach to reduce uncertainty on land subsidence prediction integrating the available observations through DA techniques.
- **Chapter 5** discusses the numerical results obtained with the DA workflow. The performance of the methodology are investigated on a synthetic application, then a real reservoir is tested to evaluate the robustness and efficiency of the approach in challenging configurations.
- **Chapter 6** concludes the thesis summarizing the most significant outcomes and reporting possible future developments.

Chapter 2

Governing equations and mathematical model

2.1 Introduction

Soil and rocks can be considered as a porous medium [Biot, 1941], made by a solid matrix and an interconnected network of void filled with one or more fluids (gas or liquid). Variations of sources of strength, such as a load or an injection/extraction of fluid, reflect on pore fluid movement and consequently on stress and displacement field of solid skeleton. The distribution of the stresses between the solid matrix (effective stress) and the fluid (pressure) is described by Terzaghi's principle [Terzaghi, 1925; Bishop, 1959; Verruijt, 2013]:

$$\widehat{\boldsymbol{\sigma}} = \boldsymbol{\sigma} - \alpha_B p \mathbf{i} \tag{2.1}$$

where, following the classical Voigt notation [Voigt, 1887], $\widehat{\boldsymbol{\sigma}} = [\hat{\sigma}_x, \hat{\sigma}_y, \hat{\sigma}_z, \hat{\tau}_{xy}, \hat{\tau}_{yz}, \hat{\tau}_{xz}]^T$ and $\boldsymbol{\sigma} = [\sigma_x, \sigma_y, \sigma_z, \tau_{xy}, \tau_{yz}, \tau_{xz}]^T$ are the total and effective stress vector, respectively, α_B is the Biot coefficient [Biot, 1941], p is the average fluid pressure and $\mathbf{i}$ is the vectorial form of the Kronecker delta, i.e., $\mathbf{i} = [1, 1, 1, 0, 0, 0]^T$. The stress vectors have 6 components, instead of 9, because we assume to work with a non-polar continuum [Hadjesfandiari and Dargush, 2011], i.e., the balance of angular momentum yields to a symmetric stress tensor:

$$\hat{\tau}_{xy} = \hat{\tau}_{yx}, \quad \hat{\tau}_{yz} = \hat{\tau}_{zy}, \quad \hat{\tau}_{xz} = \hat{\tau}_{zx},$$
$$\tau_{xy} = \tau_{yx}, \quad \tau_{yz} = \tau_{zy}, \quad \tau_{xz} = \tau_{zx}$$

The Biot coefficient is defined as:

$$\alpha_B = 1 - \frac{C_r}{C_b} \tag{2.2}$$

where C_r and C_b are the grain and bulk compressibility, respectively. The average fluid pressure is computed as a weighted sum over the number of phases n_p:

$$p = \sum_{j=1}^{n_p} S_j p_j \tag{2.3}$$

where S_j and p_j are the saturation and pressure of phase j.

As a result, it is clear that to fully describe the behavior of a porous medium, both a flow and a mechanical model are needed to compute the pressure and stress distributions, respectively.

The presence of natural or induced discontinuities, like faults and fractures, highly influences the fluid pressure distribution and the coupled hydro-mechanical behavior. On the other hand, fluid pressure variations and fluid flux exchange between the discontinuities and the matrix entail a complex behavior of the discontinuity itself, which can open, close, slip or even propagate. Hence, the presence of faults and fractures requires a special treatment in the model.

In the next paragraphs, the governing equations for the hydro-mechanical problem in fractured media are described; the chapter ends with an overview of the methods mostly used for their numerical treatment.

2.2 Flow model

A thermal multiphase multi-component flow in porous media is described through tha mass and energy conservation equations. The mass conservation equations can be written as:

$$\frac{\partial}{\partial t}\left(\phi \sum_{j=1}^{n_p} x_{ij}\rho_j S_j\right) + \nabla \cdot \left(\sum_{j=1}^{n_p} x_{ij}\rho_j \boldsymbol{v}_j\right) + \sum_{j=1}^{n_p} x_{ij}\rho_j q_j = 0, \quad i = 1, ..., n_c \tag{2.4}$$

where i and j refer to the component and the phase, respectively, with n_c and n_p their total number, t is the time, ϕ is the porosity and is a function of the displacement $\boldsymbol{u}$, S_j, x_{ij} and ρ_j are the phase saturation, composition and density, respectively, and q_j is the sink/source term. The phase velocity $\boldsymbol{v}_j$ is described by Darcy's law rearranged by Muskat and Meres [1936]:

$$\boldsymbol{v}_j = -\boldsymbol{K}\frac{k_{rj}}{\mu_j}\left(\nabla p_j - \rho_j \boldsymbol{g}\right) \tag{2.5}$$

where $\boldsymbol{K}$ is the absolute permeability tensor, k_{rj}, μ_j and p_j are the phase relative permeability, viscosity and pressure, respectively, and $\boldsymbol{g}$ is the gravity acceleration vector. In the previous equations, $\nabla\cdot$ is the divergence operator, while ∇ is the gradient operator.

We assume thermal equilibrium between the fluids and the solid skeleton, thus, the overall energy balance can be written as:

$$\frac{\partial}{\partial t}\left(\phi\sum_{j=1}^{n_p} U_j\rho_j S_j + (1-\phi)\,U_r\right) + \nabla\cdot\left(\sum_{j=1}^{n_p} h_j\rho_j\boldsymbol{v}_j\right) - \nabla\cdot(\kappa\nabla T) + \sum_{j=1}^{n_p} h_j\rho_j q_j = 0 \tag{2.6}$$

where U_j and U_r are the phase and rock internal energies, respectively, h_j is the phase enthalpy, κ is the thermal conduction coefficient and T is the temperature.

To close the system, it is generally assumed instantaneous thermodynamic equilibrium of the fluid mixtures by imposing the equality of the fugacities for each component [Chen et al., 2006; Cusini et al., 2018]:

$$f_{ij}\left(p, T, x_{ij}\right) - f_{ik}\left(p, T, x_{ik}\right) = 0, \quad \forall j \neq k = 1, ..., n_p, \quad i = 1, ..., n_c \tag{2.7}$$

where the fugacity f_{ij} of the component i and the phase j can be defined as the product:

$$f_{ij} = x_{ij}\psi_{ij}p_j \tag{2.8}$$

between the mole fractions x_{ij}, the fugacity coefficient ψ_{ij} and the pressure p_j. Moreover, let us assume the impact of the capillary pressure on the phase behavior to be negligible and all components be able to dissolve in all fluid phases. Finally, the system

is supplemented with linear constraints for the phase compositions and saturations:

$$\sum_{i=1}^{n_c} x_{ij} = 1, \quad j = 1, ..., n_p \tag{2.9}$$

$$\sum_{j=1}^{n_p} S_j = 1 \tag{2.10}$$

The problem is well-posed with the imposition of appropriate initial and boundary conditions.

2.3 Geomechanical model

The geomechanical model solves the equilibrium equations, i.e., Cauchy's balance of linear momentum. Inside the continuous domain, the equations read:

$$-\nabla \cdot \widehat{\boldsymbol{\sigma}} = \boldsymbol{F}_V \tag{2.11}$$

where $\boldsymbol{F}_V$ is the vector of the body forces. On the boundary of the continuum, the surface stress equilibrium reads:

$$\hat{\boldsymbol{\sigma}} \cdot \boldsymbol{n} = \boldsymbol{F}_S \tag{2.12}$$

where $\boldsymbol{n}$ is the normal to the boundary and $\boldsymbol{F}_S$ is the vector of the surface forces.

The effective stress tensor $\boldsymbol{\sigma}$ depends on the strain $\boldsymbol{\varepsilon}$ according to the constitutive relationship:

$$\boldsymbol{\sigma} = \hat{\mathbf{D}} : \boldsymbol{\varepsilon} \tag{2.13}$$

where $\hat{\mathbf{D}}$ is the rank-four constitutive tensor. The strain tensor $\boldsymbol{\varepsilon}$ depends on the displacement field $\boldsymbol{u}$ according to the small strain hypothesis:

$$\boldsymbol{\varepsilon} = \nabla^s \boldsymbol{u} \tag{2.14}$$

with ∇^s the symmetric gradient operator.

The operator $\hat{\mathbf{D}}$ is in general non-linear. The simplest case is the isotropic linear-elastic constitutive model, for which $\hat{\mathbf{D}}$ is defined as:

$$\hat{\mathbf{D}} = \frac{E(1-\nu)}{(1+\nu)(1-2\nu)} \begin{bmatrix} 1 & \frac{\nu}{1-\nu} & \frac{\nu}{1-\nu} & 0 & 0 & 0 \\ \frac{\nu}{1-\nu} & 1 & \frac{\nu}{1-\nu} & 0 & 0 & 0 \\ \frac{\nu}{1-\nu} & \frac{\nu}{1-\nu} & 1 & 0 & 0 & 0 \\ 0 & 0 & 0 & \frac{1-2\nu}{2(1-\nu)} & 0 & 0 \\ 0 & 0 & 0 & 0 & \frac{1-2\nu}{2(1-\nu)} & 0 \\ 0 & 0 & 0 & 0 & 0 & \frac{1-2\nu}{2(1-\nu)} \end{bmatrix} \tag{2.15}$$

where E is the Young modulus and ν is the Poisson coefficient.

Two non-linear constitutive laws frequently used to describe the behavior of the subsurface are the modified Cam Clay (MCC) [De Souza Neto et al., 2008] and the visco-elasto-plastic (VEP) [Vermeer and Neher, 1999] models. Both of them are elasto-plastic models, i.e., they allow for both elastic and plastic (non-reversible) deformations. Moreover, both MCC and VEP are comprised within the class of the rate-independent models, meaning that the deformation is independent from the load application rate and/or from the time of the loading process.

2.3.1 Modified Cam-Clay model

The MCC model is largely used to model geomaterials because it is able to describe many of their characteristics, such as the softening with increase of volume, the hardening with compaction and the volumetric-deviatoric coupling. The original Cam Clay formulation has been updated and improved, and its applicability field has been extended [Roscoe and Burland, 1968], obtaining the so called MCC. This constitutive law is accurate in describing the behavior of clay in normal-consolidation or weakly over-consolidation state, with monotonic quasi-static loading condition [Wood, 1991].

MCC considers the existence of an elastic domain, i.e., a range of stresses for which the behavior of the material can be considered purely elastic without permanent deformation, delimited by a yield surface. If the loading conditions overcome the yielding, plastic non-reversible deformations arise and the yield stress develops, i.e., the hardening phenomenon starts. Considering the small strain hypothesis, the increment of

the total deformation can be defined as the sum of the elastic and the plastic components. Dividing this sum for the infinitesimal time dt, the total deformation rate $\dot{\boldsymbol{\varepsilon}}$ can be defined as the sum:

$$\dot{\boldsymbol{\varepsilon}} = \dot{\boldsymbol{\varepsilon}}^e + \dot{\boldsymbol{\varepsilon}}^p \tag{2.16}$$

The elastic component $\dot{\boldsymbol{\varepsilon}}^e$ can be written as:

$$\dot{\boldsymbol{\varepsilon}}^e = \hat{\mathbf{D}}^{-1}\dot{\boldsymbol{\sigma}} \tag{2.17}$$

where $\hat{\mathbf{D}}$ is the elasticity matrix and $\dot{\boldsymbol{\sigma}}$ is the rate of the stress vector. In the context of the MCC law, matrix $\hat{\mathbf{D}}$ is defined by a constant Poisson ratio ν and a stress-dependent Young modulus E, according to:

$$E = -\left(1-2\nu\right)\frac{\sigma_x+\sigma_y+\sigma_z}{k^*} \tag{2.18}$$

where k^* is the modified swelling index. The yielding surface is explicitly defined as:

$$F = \mathrm{p}_c - \mathrm{p}_{c,y} = 0 \tag{2.19}$$

with p_c a representation of the stress state in the plane of the stress invariant (p, q), also denoted as equivalent pressure, and $\mathrm{p}_{c,y}$ the reference stress which describes the behavior in hardening conditions. The term p_c is defined as:

$$\mathrm{p}_c = \mathrm{p} + \frac{c}{\tan\theta} + \frac{q^2}{M^2\left(p+\frac{c}{\tan\theta}\right)} \tag{2.20}$$

where $\mathrm{p} = -\sigma_x+\sigma_y+\sigma_z/3$ is the volumetric stress, c is the cohesion, θ is the friction angle,

$$q = \sqrt{\sigma_x\left(\sigma_x-\sigma_y\right)+\sigma_y\left(\sigma_y-\sigma_z\right)+\sigma_z\left(\sigma_z-\sigma_x\right)+3\left(\tau_{xy}^2+\tau_{yz}^2+\tau_{zx}^2\right)}$$

is the deviatoric stress, M is the slope of the critical state line in the (p, q) plane, i.e.,

$$M = 3\sqrt{\frac{\left(1-K_0^{NC}\right)^2}{\left(1+2K_0^{NC}\right)^2}+\frac{\left(1-K_0^{NC}\right)\left(1-2\nu\right)\left(\lambda^*/k^*-1\right)}{\left(1+2K_0^{NC}\right)\left(1-2\nu\right)\lambda^*/k^*-\left(1-K_0^{NC}\right)\left(1+\nu\right)}}$$

with K_0^{NC} the ratio between the horizontal and vertical stress in normal-consolidation-state and λ^* the modified compression index.

The second term in Eq. (2.19) is defined as:

$$\mathrm{p}_{c,y} = \mathrm{p}_{c,y,0}\, exp\left[-\frac{\varepsilon_x^p + \varepsilon_y^p + \varepsilon_z^p}{\lambda^* - k^*}\right] \tag{2.21}$$

where $\mathrm{p}_{c,y,0}$ is a function of the maximum volumetric stress ever experienced by the material before loading. When the yielding condition (2.19) is satisfied, the plastic deformation rate $\dot{\boldsymbol{\varepsilon}}^p$ is governed by the flow rule:

$$\dot{\boldsymbol{\varepsilon}}^p = \dot{\gamma}\frac{\partial \mathrm{p}_c}{\partial \boldsymbol{\sigma}} \tag{2.22}$$

where $\dot{\gamma}$ is the plastic multiplier rate.

2.3.2 Visco-elasto-plastic model

Differently from MCC, VEP considers also viscous effects, which can explain delayed displacements in response to variations of the strength sources. In the VEP model there is not a classical explicit yield function, and the plastic strain is non-zero at every stress level [Belytschko et al., 2013], being dependent on the stress state and the plastic deformation aged by the material.

As for MCC, the deformation rate can be considered as the sum of the elastic and the plastic components as in Eq. (2.16). The elastic and plastic components can be described as in Eq. (2.17) and Eq. (2.22), respectively. For the VEP case, the plastic multiplier rate is computed as:

$$\dot{\gamma} = \frac{\mu^*}{\tau^* \frac{\partial \mathrm{p}_c}{\partial \mathrm{p}}}\left(\frac{\mathrm{p}_c}{\mathrm{p}_{c,y}}\right)^{\frac{\lambda^* - k^*}{\mu^*}} \tag{2.23}$$

where μ^* is the creep index, τ^* is a reference time related to the normal consolidation state in a standard oedometer test and p_c and $\mathrm{p}_{c,y}$ are defined as in Eq. (2.20) and Eq. (2.21), respectively. According to this model, the stress state lies on an ellipse, which evolves during the loading/unloading path.

2.4 Faults and fractures

Over the fracture surfaces, the traction balance has to be guaranteed:

$$t_N - p = 0 \tag{2.24}$$

where t_N is the normal component (with respect to the fracture-local reference frame) of the traction vector $\boldsymbol{t}$ and p is the pressure.

Moreover, the following contact constraints have to be enforced:

$$t_N = \boldsymbol{t} \cdot \boldsymbol{n}_i \leq 0 \tag{2.25}$$

$$g_N = [\![\boldsymbol{u}]\!] \cdot \boldsymbol{n}_i \geq 0 \tag{2.26}$$

$$t_N g_N = 0 \tag{2.27}$$

where $\boldsymbol{n}_i$ is a unitary vector orthogonal to the fracture plane i, $[\![\boldsymbol{u}]\!]$ is the relative displacement, which is also called jump, and g_N is its normal component. These equations are also referred as the Karush–Kuhn–Tucker (KKT) complementary conditions for normal contact [Karush, 1939; Kuhn and Tucker, 1951; Simo and Hughes, 2006]. Eq. (2.25) means that there can be only compression or null stress on the faults. Eq. (2.26) prevents the compenetration of the fault surfaces and Eq. (2.27) allows a non-zero traction only when the fracture is closed.

Finally, a friction law completes the system. The most used is the Mohr - Coulomb friction law:

$$\|\boldsymbol{t}_T\|_2 - \tau_{\max}(t_N) \leq 0 \tag{2.28}$$

$$\dot{\boldsymbol{g}}_T \cdot \boldsymbol{t}_T - \tau_{\max}(t_N) \|\dot{\boldsymbol{g}}_T\|_2 = 0 \tag{2.29}$$

where $\boldsymbol{t}_T$ is the tangential component (with respect to the fracture-local reference frame) of the traction vector, $\dot{\boldsymbol{g}}_T$ is the tangential velocity and $\tau_{max} = c - t_N tan(\theta)$ is the limit value provided by the static Coulomb criterion, with c and θ the cohesion and friction angle, respectively. Eqs. (2.28) and (2.29) are also referred as the KKT conditions for

frictional contact; the first one defines an upper bound for the magnitude of the tangential traction vector $\boldsymbol{t}_T$ based on the Mohr – Coulomb criterion, while the second one imposes that $\boldsymbol{t}_T$ is collinear to the tangential relative displacement $\boldsymbol{g}_T$, which is possible only when $\|\boldsymbol{t}_T\|_2 = \tau_{\max}$. Since a static Coulomb criterion is employed, in Eq. (2.29) the quantity $\dot{\boldsymbol{g}}_T$ is replaced with the increment $\Delta \boldsymbol{g}_T$ with respect to the previously converged time-step [Wohlmuth, 2011].

The fault surfaces can be subdivided into three regions:

- stick: the fracture is closed and any relative displacements between the two surfaces of the fracture is allowed; a compression acts on the fault, but its components have to be determined;
- slip: the fracture is compressed and closed in the normal direction ($g_N = 0$ and t_N unknown), but the inequality (2.28) becomes an equality ($\|\boldsymbol{t}_T\|_2 = \tau_{\max}$) and a tangential displacement occurs;
- open: the fracture is fully open and free to move, with the relative displacement $[\![\boldsymbol{u}]\!] \neq 0$ and the traction vector $\boldsymbol{t} = 0$.

Even if in general fractures can propagate, in this thesis their trace is considered fixed and well defined in the time domain of interest.

2.5 Problem solution

The flow and the geomechanical models used to describe the subsurface processes are theoretically coupled. Thus, the two models should be solved at the same time using a fully coupled approach. The simultaneous solution of the equations provides accurate results and it must be used when the coupling is non-negligible, such as when dealing with local models or with highly fractured porous media. As a matter of fact, the fractures are preferred flow pathways with respect to the surrounding matrix, especially when they are in slip or open conditions. In turn, the pressure variation perturbs the stress state in the surrounding medium and influences the contact mechanics itself.

However, the algebraic system that arises from the coupled model can be quite difficult to solve, with the number of unknowns easily growing [Ferronato et al., 2001].

From a numerical point of view, the coefficient matrix resulting from the discretization can be severely ill-conditioned [Ferronato et al., 2009], requiring advanced solvers and preconditioners. Thus, whenever coupling is deemed to be less important, e.g., in large scale models in long time simulation periods, it can be adopted a one-way coupled approach, meaning that the flow problem is first solved and the resulting pressure distribution is used as input for the geomechanical model. Consequently, in the geomechanical model only the external strength changes with time according to the time stepping of the flow model. This sequential approach is easier to implement and generally more efficient to apply, and the experience shows that the solution obtained in this way does not differ significantly from the one obtained with a fully coupled model at large time and space scales [Gambolati et al., 2000; Ye et al., 2018]. The one-way coupled approach has proven to provide accurate results with respect to a fully-coupled approach when the changes of the pore volume (i.e. porosity and rock compressibility), due to the stress path within the reservoir, are properly accounted for by the fluid flow simulator in reservoir simulations [Segura et al., 2011].

It is clear that the solution strategy has to be properly chosen each time, according to the characteristics of the specific application. Whatever the approach, a discretization method is needed to numerically solve the model equations. In the context of faulted poroelastic system, the most used techniques are the Finite Difference Method (FDM) [Gaspar et al., 2003, 2006], the Finite Element Method (FEM) [Salimzadeh et al., 2018] and the Finite Volume Method (FVM) [Droniou, 2014; Ucar et al., 2018]. The choice of the most suitable approach for the specific application is not trivial, given that each one can offer specific advantages. FDM is the oldest discretization scheme, and it is still attractive thanks to its simplicity and convenience for structured grids. However, it becomes unsuitable for complex geometries, especially in multiple dimensions [Peiró and Sherwin, 2005]. FEM overcomes these deficiencies, being versatile in handling highly heterogeneous, geometrically intricate domains with irregular boundaries [Stein, 2014] and efficient with material and geometric non-linearities. Differently from FEM, FVM is also locally conservative at the discrete level [Hughes, 2012]. This guarantees that the mass/energy balance is enforced locally and the velocity field is conservative, the latter being a key requirement for accurate transport computations.

Within the continuous domain, faults and fractures behave as internal discontinuities, where the contact constraint equations need ad-hoc methods to be numerically imposed. From a mathematical point of view, two methods are mainly used to handle discontinuities: the penalty and the Lagrangian approach.

The penalty approach [Zienkiewicz et al., 2000; Mergheim et al., 2004; Bathe, 2006] imposes the non-penetration condition introducing stiff springs between the faces of the fractures. When the stress on the faces is such that the failure criterion is exceeded, the springs break and the contact surfaces are free to move. However, the elastic springs deform for any non-zero stress value, thus the method is not mathematically exact. Moreover, this approach may cause severe ill-conditioning of the stiffness matrix because of the introduction of the penalty coefficient [Ferronato et al., 2012]. However, thanks to its ease of implementation, this method is widely used. Some recent applications can be found in Settgast et al. [2017], Camargo et al. [2022] and Shovkun and Tchelepi [2022].

On the other hand, the contact conditions can be prescribed using the Lagrange multipliers [Wriggers and Zavarise, 2004; Simo and Hughes, 2006; Hild and Renard, 2010; Jha and Juanes, 2014], namely in an analytically exact way. The multipliers represent additional unknowns with the physical meaning of the contact stresses. The inconvenience is the additional cost of solving an augmented algebraic system with the so-called saddle-point structure. However, the increase of the computational cost is generally compensated by a more robust non-linear convergence and a more stable numerical behavior. Some recent applications can be found in Franceschini et al. [2016], Köppel et al. [2019] and Berge et al. [2020].

Other methods have been developed in the literature, such as the augmented Lagrangian approach [Simo and Laursen, 1992; Zienkiewicz et al., 2000], Nitsche's method [Hansbo and Hansbo, 2002; Hansbo, 2005] and the mortar method [Farah et al., 2015; Seitz et al., 2016]. These techniques place in between the penalty and the Lagrangian approach.

Chapter 3

Preconditioners for coupled hydro-poromechanics in fractured domains

3.1 Introduction

To numerically solve the hydro-poromechanical problem, the system of Partial Differential Equations (PDEs) presented in Chapter 2 is first discretized using a suitable scheme tailored for the purpose of the simulation, such as the FEM or the FVM. The system of non-linear algebraic equations arising from the discretization is addressed by a Newton-Krylov method, leading to a sequence of linear systems that can be written in compact form as:

$$\mathcal{A}\boldsymbol{x} = \boldsymbol{b} \tag{3.1}$$

where $\mathcal{A}$ is, in general, a sparse non-symmetric matrix, $\boldsymbol{x}$ is the vector of the unknowns and $\boldsymbol{b}$ is the right-hand side, usually representing a residual vector. In real-world applications, the size of system (3.1) can grow up to several millions of unknowns. Thus, the solution of the system simply inverting $\mathcal{A}$, i.e., $\boldsymbol{x} = \mathcal{A}^{-1}\boldsymbol{b}$, is not affordable and the system is numerically solved by a linear solver. Traditionally, linear solvers can be classified as direct and iterative solvers, the latter being in practice mandatory for the size of the system and the features of modern computational architectures, thanks to their much smaller memory footprint and better degree of algorithmic parallelism [Benzi, 2002; Davis, 2006].

Iterative methods based on projections/orthogonalizations onto Krylov subspaces [Saad, 2003], such as the Generalized Minimal Residual Method (GMRES) [Saad and Schultz, 1986] and the BiConjugate Gradient Stabilized method (BiCGStab) [van der Vorst, 1992], are the preferred choices. However, robustness, scalability and computational efficiency of this class of methods are tightly connected with the choice of a proper preconditioning technique. The *robustness* regards the capability of the algorithm to converge to the solution independently of the specific problem at hand. The *scalability* is the ability to solve an increasingly refined problem with an approximately constant number of iterations. The *efficiency* is a measure of the computational burden and memory storage required to solve a system of equations at a given precision. In particular, the algorithmic scalability is a key feature for a modern preconditioning framework, in view of the development of problems of increasing size by exploiting the availability of massively parallel computational platforms.

Generally speaking, a preconditioner $\mathcal{M}^{-1}$ is an operator that transforms a linear system into an equivalent one, which properties are such that the solver convergence is accelerated. The system can be either left-preconditioned:

$$\mathcal{M}^{-1}\mathcal{A}\boldsymbol{x} = \mathcal{M}^{-1}\boldsymbol{b}$$

or right-preconditioned:

$$\mathcal{A}\mathcal{M}^{-1}\boldsymbol{y} = \boldsymbol{b}, \qquad \boldsymbol{x} = \mathcal{M}^{-1}\boldsymbol{y}$$

or split-preconditioned:

$$\mathcal{M}_1^{-1}\mathcal{A}\mathcal{M}_2^{-1}\boldsymbol{y} = \mathcal{M}_1^{-1}\boldsymbol{b}, \qquad \boldsymbol{x} = \mathcal{M}_2^{-1}\boldsymbol{y}$$

if the preconditioner is available in a factorized form $\mathcal{M}^{-1} = \mathcal{M}_1^{-1}\mathcal{M}_2^{-1}$. Right preconditioning is often preferred in residual minimizing algorithms because it preserves the norm of the residual vector $\mathbf{r} = \boldsymbol{b} - \mathcal{A}\mathcal{M}^{-1}\mathcal{M}\boldsymbol{x} = \boldsymbol{b} - \mathcal{A}\boldsymbol{x}$. It has to be noted that the preconditioned matrix is never explicitly computed, since iterative solver algorithms require only the application of the preconditioner to vectors at each iteration.

Generally speaking, the aim of a preconditioner is to improve the spectral properties of the coefficient matrix $\mathcal{A}$ by clustering the eigenspectrum around a non-zero value [Benzi, 2002]. This means that the preconditioner $\mathcal{M}^{-1}$ should approximate in some sense the matrix inverse $\mathcal{A}^{-1}$. In addition, a preconditioner should be as cheap to compute as possible and its application to a vector should be cost-effective. Thus, using the words by Saad [2003], finding a good preconditioner can be viewed rather as *a combination of art and science* than a rigorous mathematical exercise.

Traditionally, preconditioners have been classified into two groups: physically-based and algebraic [Wathen, 2015]. In the former group, the methods are specifically designed for the problem at hand, trying to exploit as much as possible the knowledge of the PDEs and the discretization scheme. In general, physically-based preconditioners exhibit a great efficiency, but they can be barely applied to problems different from the ones they are designed for. On the other side, purely algebraic preconditioners are built upon the coefficient matrix only, with no (or little) knowledge of the underlying physical problem and its properties. These preconditioners are usually more robust and more appropriate for a broad use, even if they can perform poorer than physically-based ones.

The algebraic category includes three main classes: (i) incomplete factorizations [Saad, 1994; Lin and Moré, 1999], (ii) approximate inverses [Benzi et al., 1996; Tang, 1999] and (iii) multilevel methods, which include domain decomposition [Toselli and Widlund, 2005; Janna et al., 2013; Dolean et al., 2015] and multigrid-like techniques [McCormick and Ruge, 1982; Stüben, 2001]. The basic idea behind the incomplete factorization methods is to somehow approximate the factorization $\mathcal{A} = \mathcal{L}\mathcal{U}$ of the coefficient matrix in a cost-effective way. A simple approximation of the triangular factors $\mathcal{L}$ and $\mathcal{U}$ can be obtained by discarding a number of fill-in entries according to some rules, e.g., Saad [1994]. This kind of preconditioners is intrinsically highly sequential in both its computation and application stages. However, some degree of parallelism can be achieved through level-scheduling and other approaches, e.g., Anderson and Saad [1989], Hysom and Pothen [1999] and Gupta [2017]. Incomplete factorizations can be very effective; however their robustness may be jeopardized by issues concerning their

existence and numerical stability. Other methods have been developed inspired by incomplete factorizations, e.g., multilevel ILU preconditioners [Bollhöfer and Saad, 2006] and recursive multilevel approaches, like ARMS [Saad and Suchomel, 2002].

Approximate inverses have been developed to overcome some of the deficiencies of incomplete factorizations. This kind of preconditioners is basically built as an explicit approximation of the matrix inverse with a given sparse pattern. Several techniques are available, e.g., minimizing the Frobenius norm over a set of matrices with a prescribed sparsity pattern [Frederickson, 1975; Grote and Huckle, 1997] or approximating the inverse of the triangular factors, e.g., through the two-sided Gram-Schmidt algorithm as in Benzi et al. [1996]. Even if $\mathcal{A}$ is symmetric positive definite (SPD), there is no guarantee that $\mathcal{M}^{-1}$ is SPD as well. Thus, other methods have been developed, such as the Factorized Sparse Approximate Inverse (FSAI) [Kolotilina and Yeremin, 1993; Janna and Ferronato, 2011] which maintains the symmetry by computing an approximation of the lower Cholesky factor of the inverse.

Both incomplete factorizations and approximate inverses lack on scalability. On the opposite, multilevel methods are optimal with respect to scalability issues, hence they are usually more attractive for parallel computations. Domain decomposition techniques belong to the class of the divide-and-conquer methods. These techniques are based on a spatial decomposition of the problem domain into several subdomains, which can be disjoint or overlapped, thus allowing the exploitation of the parallel computational resources. Two main variants have been developed: the Additive Schwarz algorithm, which updates the solution at the end of the process, and the Multiplicative Schwarz algorithm, which performs the update each time a local solution is obtained, see e.g., Nabben [2003] for a comparison.

Finally, multigrid methods rely on the idea of projecting the error obtained after applying a few iterations of local relaxation methods onto a coarser grid. In this way, part of the low frequency error on a finer grid can be more easily corrected on the coarse grid, since the smooth components turn into oscillatory modes. Moreover, the resulting system has a smaller size. Thus, multigrid-like techniques consist of the complementary use of: (i) a smoother that reduces high frequency errors, (ii) a coarse grid correction that reduces low frequency errors, and (iii) restriction and interpolation operators

to move from one grid to another. Starting from the original work by Brandt [1977], a wide range of multigrid approaches has been developed in the literature, extending the applicability of this method, originally designed for elliptic PDEs. One of the most effective methods for a generic linear system is the Algebraic MultiGrid (AMG), where the restriction and prolongation operators are defined in a purely algebraic way. AMG gathers indirectly information on the grid from the system matrix. Since it does not require the grid topology, AMG can handle complex domain geometries and properties anisotropy. Even if many variants have been developed over the years, e.g., Brezina et al. [2012]; Franceschini et al. [2019b] and Paludetto Magri et al. [2019], robustness and efficiency can be an issue for AMG whenever used as a black-box tool in problems with a non-symmetric block structure. The reader is referred to Xu and Zikatanov [2017] for a review on these methods.

Summarizing, it is clear that, in complex problems, such as the coupled hydro-poromechanics in fractured porous media, ad-hoc preconditioners need to be designed. The coefficient matrix arising from this kind of coupling has, in general, a non-symmetric block structure, which characteristics can significantly change according to the numerical strategy used to discretize the continuous equations. Few studies can be found in the literature, e.g., Franceschini et al. [2019a] and Camargo et al. [2021], about preconditioners for this kind of problems, but none of them can be straightforwardly and effectively applied to the problems described in the following sections. Thus, original ad-hoc preconditioners have to be designed, exploiting the block structure of the problem and taking advantage from the knowledge of the nature and the structure of the various blocks. The underlying preconditioning framework consists of (i) a symbolic permutation of the blocks of the coefficient matrix in order to avoid singular leading blocks, if any, and to project the Schur complement onto different spaces; (ii) a block-factorization of the coefficient matrix, which allows to isolate the subsystems from the original coupled problem and (iii) an approximation of the single blocks, and in particular the arising Schur complement. According to the reordering of the unknowns and the techniques used for the approximations, different preconditioners can originate.

In the following, three models have been investigated. The first two address the hydro-poromechanical coupling in fractured porous media, the main difference being

the discretization technique and the approach used to impose the contact constraints on the fractures. The third model neglects the 3D domain and focuses only on the fracture network, solving the flow equation stated as a PDE-constrained optimization problem. For each model ad-hoc preconditioners are developed and tested.

3.2 DFN stabilized Lagrangian formulation

In this section, the pure mechanic problem originally presented in Franceschini et al. [2020] is extended to the flow in fractures, as described in Franceschini et al. [2022], and a scalable and efficient preconditioning framework is developed.

Section 3.2.1 recalls the strong form of the physical problem, already described in Chapter 2, while Section 3.2.2 introduces the weak formulation, in order to understand the meaning and features of each block of the Jacobian system. Two options for the preconditioning framework are presented in Section 3.2.3 and some numerical results are reported in Section 3.2.4, with the aim of comparing the proposed approaches. Section 3.2.5 discusses the outcomes, while Section 3.2.6 introduces one possible future development.

3.2.1 Problem statement

Let us consider an open elastic domain $\Omega \subset \mathbb{R}^3$, with $\partial\Omega$ its boundary and $\boldsymbol{n}_\Omega$ the outer normal vector to $\partial\Omega$, such that $\overline{\Omega} = \Omega \cup \partial\Omega$. As commonly done in geological simulations, quasi-static conditions and infinitesimal strains within the open time interval $\mathcal{T} = (0, t_{\max}]$ are assumed. The set of internal boundaries $\Gamma = \cup_{i=1}^{n_f} \Gamma_i$ represents a fracture network consisting of n_f surfaces. The external boundary is subdivided into two non-overlapping subsets, $\partial\Omega_u$ and $\partial\Omega_\sigma$, where Dirichlet and Neumann boundary conditions are prescribed, respectively. Each fracture Γ_i consists of two overlapping surfaces, Γ_i^- and Γ_i^+, with the orientation defined by a unitary vector $\boldsymbol{n}_i$ orthogonal to the fracture plane, which is $\boldsymbol{n}_i = \boldsymbol{n}_i^- = -\boldsymbol{n}_i^+$ by convention. The pressure field is defined on the union Γ of the two-dimensional (2D) domains Γ_i, with $\partial\Gamma_i$ a one-dimensional (1D) curve defining the boundary of each fracture and $\overline{\Gamma}_i = \Gamma_i \cup \partial\Gamma_i$. The curve $\partial\Gamma_i$ is subdivided into two non-overlapping subsets, $\partial\Gamma_{i,p}$ and $\partial\Gamma_{i,q}$, where Dirichlet and

Neumann boundary conditions for the pressure field are imposed, respectively. The vector $\boldsymbol{m}_i$ denotes the outer normal direction to $\partial\Gamma_i$. The fluid is assumed to be incompressible, and body forces and buoyancy effects are neglected. The projection of the stress tensor $\boldsymbol{\sigma}$ along $\boldsymbol{n}_i$, $\boldsymbol{t} = \boldsymbol{\sigma}\cdot\boldsymbol{n}_i^- = -\boldsymbol{\sigma}\cdot\boldsymbol{n}_i^+ = (t_N\boldsymbol{n}_i + \boldsymbol{t}_T)$, is the traction vector over Γ_i, with t_N and $\boldsymbol{t}_T$ its normal and tangential component, respectively, with respect to the fracture-local reference frame. The traction $\boldsymbol{t}$ on Γ_i controls the possible slipping and aperture of the fracture according to the Coulomb frictional law. A schematic representation of the considered conceptual framework is shown in the left panel of Fig. 3.1.

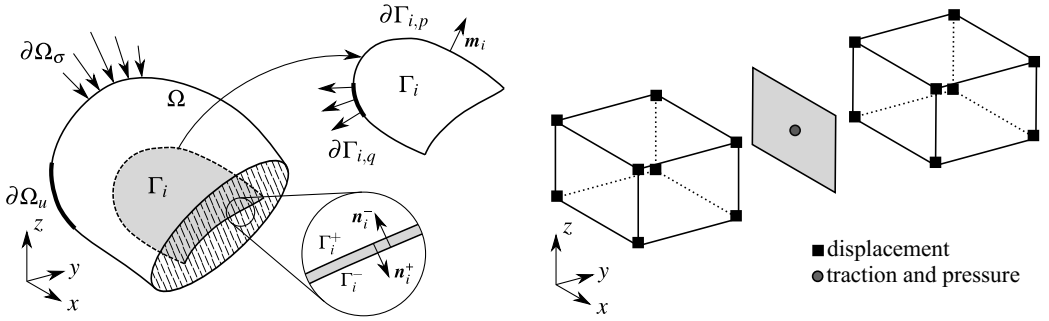

FIGURE 3.1: Conceptual scheme of the elastic domain and embedded fracture network (left) and example of low-order discretization (right).

The strong form of the initial boundary value problem includes the mass balance, Eq. (2.4), on the fractures, the linear momentum balance, Eq. (2.11), on the 3D domain and the traction balance, Eq. (2.24), on the fractures. These equations are here recalled for the sake of clarity, conveniently rearranged considering the aforementioned hypotheses. The system to be solved is:

$$-\nabla\cdot\boldsymbol{\sigma}(\boldsymbol{u}) = \boldsymbol{0} \qquad \text{in } \Omega\times\mathcal{T} \tag{3.2}$$

$$\dot{g}_N(\boldsymbol{u}) + \nabla\cdot\boldsymbol{q}(\boldsymbol{u},p) = q_s \qquad \text{in } \cup_{i=1}^{n_f}\Gamma_i\times\mathcal{T} \tag{3.3}$$

$$t_N - p = 0 \qquad \text{on } \cup_{i=1}^{n_f}\Gamma_i\times\mathcal{T} \tag{3.4}$$

The system is subject to the following boundary conditions:

$$\boldsymbol{u} = \bar{\boldsymbol{u}} \qquad \text{on } \partial\Omega_u \times \mathcal{T} \tag{3.5}$$

$$\boldsymbol{\sigma}(\boldsymbol{u}) \cdot \boldsymbol{n}_\Omega = \bar{\boldsymbol{t}} \qquad \text{on } \partial\Omega_\sigma \times \mathcal{T} \tag{3.6}$$

$$p = \bar{p} \qquad \text{on } \cup_{i=1}^{n_f} \partial\Gamma_{i,p} \times \mathcal{T} \tag{3.7}$$

$$\boldsymbol{q}(\boldsymbol{u}, p) \cdot \boldsymbol{m}_i = \bar{q} \qquad \text{on } \cup_{i=1}^{n_f} \partial\Gamma_{i,q} \times \mathcal{T} \tag{3.8}$$

and initial conditions:

$$\boldsymbol{u}|_{t=0} = \boldsymbol{u}_0 \qquad \text{in } \overline{\Omega} \tag{3.9}$$

$$p|_{t=0} = p_0 \qquad \text{in } \cup_{i=1}^{n_f} \overline{\Gamma}_i \tag{3.10}$$

Finally, the contact constraints, Eqs. (2.25)-(2.29), over each fracture surface Γ_i and for every time in $\mathcal{T}$ are imposed:

$$t_N = \boldsymbol{t} \cdot \boldsymbol{n}_i \leq 0, \qquad g_N = [\![\boldsymbol{u}]\!] \cdot \boldsymbol{n}_i \geq 0, \qquad t_N g_N = 0 \tag{3.11}$$

$$\|\boldsymbol{t}_T\|_2 - \tau_{\max}(t_N) \leq 0, \qquad \dot{\boldsymbol{g}}_T \cdot \boldsymbol{t}_T - \tau_{\max}(t_N) \|\dot{\boldsymbol{g}}_T\|_2 = 0 \tag{3.12}$$

Assuming laminar flow, the fluid volumetric flux in the fracture domain can be computed according to Darcy's law [Witherspoon et al., 1980]:

$$\boldsymbol{q}(\boldsymbol{u}, p) = -\frac{C_f(\boldsymbol{u})}{\mu} \nabla p \tag{3.13}$$

where ∇p is the fluid pressure gradient, μ the fluid viscosity (constant), and C_f the isotropic fracture hydraulic conductivity modeled as in Garipov et al. [2016]:

$$C_f = C_{f,0} + \frac{g_N^3}{12} \tag{3.14}$$

with $C_{f,0}$ the conductivity related to two irregular surfaces that are in contact [Zhang et al., 2013]; $[\![\boldsymbol{u}]\!] = (\boldsymbol{u}|_{\Gamma_i^+} - \boldsymbol{u}|_{\Gamma_i^-}) = (g_N \boldsymbol{n}_i + \boldsymbol{g}_T)$ the relative displacement (jump) across Γ_i, where g_N and $\boldsymbol{g}_T$ are the normal and tangential components, respectively, and $\boldsymbol{u}|_{\Gamma_i^+}$ and $\boldsymbol{u}|_{\Gamma_i^-}$ are the restrictions of $\boldsymbol{u}$ on Γ_i^+ and Γ_i^-. A static Coulomb criterion is

employed, with $\tau_{\max} = c - t_N \tan(\theta)$, thus the tangential velocity $\dot{\boldsymbol{g}}_T$ in Eq. (3.12) is replaced with the tangential displacement increment $\Delta \boldsymbol{g}_T$ with respect to the previously converged time step [Wohlmuth, 2011].

The fracture domain Γ is assumed to be fixed with no propagation. It can be partitioned into three portions: (i) stick; (ii) slip and (iii) open, which properties are described in Section 2.4.

For additional details regarding the governing formulation, the reader is referred to Kikuchi and Oden [1988]; Laursen [2003]; Wriggers [2006] and Franceschini et al. [2020].

3.2.2 Discrete formulation

To numerically solve the problem presented in Section 3.2.1, a blended finite element / finite volume discretization is used, with low-order finite elements for the mechanics and a cell-centered finite volume scheme for the fluid flow, as common in geological and reservoir simulations. The contact constraints are imposed with the aid of Lagrange multipliers [Hild and Renard, 2010; Jha and Juanes, 2014; Franceschini et al., 2016; Berge et al., 2020; Köppel et al., 2019], which represent the contact forces acting on the fracture surfaces. This field is discretized as a cell-centered variable. As a consequence, the traction appears as primary variable, sharing the same representation as the fluid pressure field, thus no interpolation is needed. An example of this discretization is shown in the rightmost panel of Fig. 3.1.

The discrete approximations $\{\boldsymbol{u}^h, \boldsymbol{t}^h, p^h\}$ of the unknowns $\{\boldsymbol{u}, \boldsymbol{t}, p\}$ can be defined as:

$$\boldsymbol{u}^h = \sum_{i=1}^{n_u} \boldsymbol{\eta_i} u_i \in \boldsymbol{\mathcal{V}}^h, \qquad \boldsymbol{t}^h = \sum_{j=1}^{n_t} \boldsymbol{\mu}_j t_j \in \boldsymbol{\mathcal{M}}^h(t_N^h), \qquad p^h = \sum_{k=1}^{n_p} \chi_k p_k \in \mathcal{P}^h, \tag{3.15}$$

where the finite-dimensional subspaces $\boldsymbol{\mathcal{V}}^h$, $\boldsymbol{\mathcal{M}}^h(t_N^h)$ and $\mathcal{P}^h$ are:

$$\boldsymbol{\mathcal{V}}^h \subset \boldsymbol{\mathcal{V}} = \{\boldsymbol{\eta} \in [H^1(\Omega)]^3 : \boldsymbol{\eta} = \overline{\boldsymbol{u}} \text{ on } \partial\Omega_u\} \tag{3.16}$$

$$\begin{aligned}\boldsymbol{\mathcal{M}}^h(t_N^h) \subset \boldsymbol{\mathcal{M}}(t_N) = \{&\boldsymbol{\mu} \in [L^2(\Gamma)]^3 : \mu_N \leq 0, (\boldsymbol{\mu}, \boldsymbol{v})_\Gamma \leq (\tau_{\max}(t_N), ||\boldsymbol{v}_T||_2)_\Gamma, \\ &\boldsymbol{v} \in [H^{1/2}(\Gamma)]^3 \text{ with } v_N \geq 0\}\end{aligned} \tag{3.17}$$

$$\mathcal{P}^h \subset \mathcal{P} = \{\chi \in L^2(\Gamma), \chi_{|\Omega_e} \in \mathbb{P}_0(\Omega_e) \; \forall \, \Omega_e \in \Omega^h\} \tag{3.18}$$

As before, the subscripts N and T denote the normal and tangential components of a vector with respect to a fracture-local reference frame. In Eq. (3.15), n_u, n_t, and n_p denote the number of discrete displacement, traction and pressure unknowns, respectively. In Eq. (3.18), Ω_e refers to a single finite element.

The weak form of the set of equations in Section 3.2.1 reads [Franceschini et al., 2020]: find $\{\boldsymbol{u}^h, \boldsymbol{t}^h, p^h\} \in \boldsymbol{\mathcal{V}}^h \times \boldsymbol{\mathcal{M}}^h(t_N^h) \times \mathcal{P}^h$ such that

$$\mathcal{R}_u = (\nabla^s \boldsymbol{\eta}, \boldsymbol{\sigma})_\Omega + \sum_{i=1}^{n_f} (\llbracket \boldsymbol{\eta} \rrbracket, \boldsymbol{t}^h - p^h \boldsymbol{n}_i)_{\Gamma_i} - (\boldsymbol{\eta}, \bar{\boldsymbol{t}})_{\partial\Omega_\sigma} = 0 \qquad \forall \boldsymbol{\eta} \in \boldsymbol{\mathcal{V}}_0^h, \tag{3.19}$$

$$\mathcal{R}_{t,i} = (t_N^h - \mu_N, g_N)_{\Gamma_i} + (\boldsymbol{t}_T^h - \boldsymbol{\mu}_T, \Delta \boldsymbol{g}_T)_{\Gamma_i} \geq 0 \qquad \forall \boldsymbol{\mu} \in \boldsymbol{\mathcal{M}}^h(t_N^h), \tag{3.20}$$

$$\mathcal{R}_{p,i} = \left(\chi, \frac{\Delta g_N}{\Delta t}\right)_{\Gamma_i} + [\chi, p^h]_{\mathcal{F}_i} - F_{\mathcal{F}_i}(\chi) + G_{\mathcal{F}_i}(\chi) - (\chi, q_s)_{\Gamma_i} = 0 \quad \forall \chi \in \mathcal{P}^h, \tag{3.21}$$

where $\boldsymbol{\mathcal{V}}_0^h$ is $\boldsymbol{\mathcal{V}}^h$ with homogeneous conditions along $\partial\Omega_u$ and Δt is the time step size. Eq. (3.20) and Eq. (3.21) hold for any fracture i. In Eq. (3.21), $[\chi, p^h]_{\mathcal{F}}$ is a weighted inner product representing the classical two-point flux approximation (TPFA) scheme, which is introduced to allow a unified presentation of the coupled finite element / finite volume model [Eymard et al., 2000, 2007; Agélas et al., 2010]. Finally, $F_{\mathcal{F}}$ and $G_{\mathcal{F}}$ collect the boundary conditions to be prescribed on $\partial\Gamma_p$ and $\partial\Gamma_q$, respectively. For further details, the reader is referred to Franceschini et al. [2020].

To solve the problem in Eqs. (3.19)-(3.21), the variational inequality in Eq. (3.20) is transformed into a variational equality by applying an active-set algorithm [Nocedal and Wright, 2006; Antil et al., 2006; Franceschini et al., 2020], which allows to identify the subdivision into stick/slip/open regions for every Γ_i. At a given step of the

active-set algorithm, the stick/slip/open regions of each fracture Γ_i are fixed and the inequality (3.20) becomes:

$$\mathcal{R}_{t,i} = (\boldsymbol{\mu}, \boldsymbol{g})_{\Gamma_i^{\text{stick}}} + (\mu_N, g_N)_{\Gamma_i^{\text{slip}}} + \frac{1}{k}\left(\boldsymbol{\mu}_T, \boldsymbol{t}_T^h - \boldsymbol{t}_T^*\right)_{\Gamma_i^{\text{slip}}} + \frac{1}{k}\left(\boldsymbol{\mu}, \boldsymbol{t}^h\right)_{\Gamma_i^{\text{open}}} = 0 \qquad (3.22)$$

where k is a coefficient that ensures the dimensional consistency of the equation. Introducing in Eqs. (3.19), (3.22) and (3.21) the finite-dimensional bases of $\boldsymbol{\mathcal{V}}_0^h$, $\boldsymbol{\mathcal{M}}^h(t_N^h)$ and $\mathcal{P}^h$ yields the following system of nonlinear discrete residual equations:

$$\mathbf{r}(\boldsymbol{u}^\ell, \boldsymbol{t}^\ell, \boldsymbol{p}^\ell) = \begin{bmatrix} \mathbf{r}_u(\boldsymbol{u}^\ell, \boldsymbol{t}^\ell, \boldsymbol{p}^\ell) \\ \mathbf{r}_t(\boldsymbol{u}^\ell, \boldsymbol{t}^\ell, \boldsymbol{p}^\ell) \\ \mathbf{r}_p(\boldsymbol{u}^\ell, \boldsymbol{t}^\ell, \boldsymbol{p}^\ell) \end{bmatrix} = \mathbf{0}, \qquad (3.23)$$

which is solved by a Newton-Krylov method. In Eq. (3.23), the algebraic vectors $\boldsymbol{u}^\ell \in \mathbb{R}^{n_u}$, $\boldsymbol{t}^\ell \in \mathbb{R}^{n_t}$ and $\boldsymbol{p}^\ell \in \mathbb{R}^{n_p}$ collect the coefficients u_i, t_j and p_k of the discrete displacement, traction and pressure fields of Eq. (3.15) and ℓ is the active-set counter. After convergence of the Newton-Krylov method at the ℓ-th step of the active-set algorithm, a consistency check is carried out in order to verify whether the obtained stick/slip/open region subdivision meets the assumed original configuration. If not, the region subdivision is updated and a new step is performed. The algorithm stops when the consistency check does not require to modify the stick/slip/open region subdivision. At this point, convergence is achieved and the simulation advances to the next time step.

The discretization approach presented herein is intrinsically unstable, as it does not fulfill the inf-sup condition [Wohlmuth, 2011]. Thus, a global algebraic stabilization is needed, which relaxes the zero jump and the impenetrability conditions between the two fracture surfaces in the traction balance equation, and the fluid incompressibility constraint in the mass balance equation [Franceschini et al., 2020].

At a given active-set iteration ℓ, the Newton linearization of system (3.23) generates a sequence of linear systems and vector updates. To advance by one Newton iteration

k, the steps are:

$$\begin{aligned} &\text{solve } \mathcal{J}^{\ell,(k)}\delta\mathbf{x} = -\mathbf{r}^{\ell,(k)} \quad \Rightarrow \quad \begin{bmatrix} \boldsymbol{A} & \boldsymbol{C}_1 & \boldsymbol{Q}_1 \\ \boldsymbol{C}_2 & -\boldsymbol{H} & \mathbf{0} \\ \boldsymbol{Q}_2 & \mathbf{0} & \boldsymbol{T} \end{bmatrix}^{\ell,(k)} \begin{bmatrix} \delta\boldsymbol{u} \\ \delta\boldsymbol{t} \\ \delta\boldsymbol{p} \end{bmatrix} = - \begin{bmatrix} \mathbf{r}_u \\ \mathbf{r}_t \\ \mathbf{r}_p \end{bmatrix}^{\ell,(k)}, \\ &\text{update } \mathbf{x}^{\ell,(k+1)} = \mathbf{x}^{\ell,(k)} + \delta\mathbf{x} \quad \Rightarrow \quad \begin{bmatrix} \boldsymbol{u} \\ \boldsymbol{t} \\ \boldsymbol{p} \end{bmatrix}^{\ell,(k+1)} = \begin{bmatrix} \boldsymbol{u} \\ \boldsymbol{t} \\ \boldsymbol{p} \end{bmatrix}^{\ell,(k)} + \begin{bmatrix} \delta\boldsymbol{u} \\ \delta\boldsymbol{t} \\ \delta\boldsymbol{p} \end{bmatrix}. \end{aligned} \tag{3.24}$$

A detailed definition of the Jacobian sub-blocks can be found in Franceschini et al. [2022]. The global matrix $\mathcal{J}$ is in general large, sparse, and non-symmetric, with properties that change with the evolution of the stick/slip/open regions in the fracture network, as shown in Fig. 3.2. The features that follow are worth summarizing.

1. The first block row of $\mathcal{J}$ includes the contributions arising from the linear momentum balance of the 3D domain Ω. None of the submatrices depends on the fracture state and can be assembled once at the beginning of the whole simulation if an elastic constitutive law is used. In particular, $\boldsymbol{A}$ is the classical SPD elastic stiffness matrix, while $\boldsymbol{C}_1$ and $\boldsymbol{Q}_1$ are tall rectangular blocks collecting a surface measure of the fracture elements and transferring tractions and pressures to the 3D body as applied forces.

2. In the second block row of $\mathcal{J}$, $\boldsymbol{C}_2$ varies as the stick/slip/open fracture regions evolve through the active-set algorithm, in both the entry values and the non-zero pattern (Fig. 3.2). If all the fracture elements are in stick mode, then $\boldsymbol{C}_2 = \boldsymbol{C}_1^T$, otherwise the frictional law derivatives appear and $\boldsymbol{C}_2 \neq \boldsymbol{C}_1^T$.

3. When all fractures belong to the stick region, $\boldsymbol{H}$ is the symmetric positive semidefinite (SPSD) stabilization matrix. In case of sliding, non-symmetric diagonal 2×2 blocks arise, one for each traction component along the local tangential direction to the fracture surface. For an open element, the corresponding row of $\boldsymbol{H}$ has a single non-zero entry in the main diagonal, with no contribution from the stabilization term (Fig. 3.2). In any case, $\boldsymbol{H}$ is singular and cannot be regularly inverted.

4. The third block row of $\mathcal{J}$ includes the contributions arising from the fluid mass balance on the fracture network. The coupling between fluid flow and fracture mechanics is controlled by $\boldsymbol{Q}_2$. In particular, when all fracture elements are in stick mode, $\boldsymbol{Q}_2 = \boldsymbol{0}$ and $\mathcal{J}$ is reducible with a 2×2 symmetric saddle-point matrix as leading block. Otherwise, contributions from the flux derivative with respect to the displacements appear, i.e., $\boldsymbol{Q}_2$ entries depend on the current pressure solution (Fig. 3.2). Differently from $\boldsymbol{C}_1^T$ and $\boldsymbol{C}_2$, there is no simple relationship linking $\boldsymbol{Q}_1^T$ and $\boldsymbol{Q}_2$.

5. $\boldsymbol{T}$ is the sum of the standard transmissibility matrix arising from the TPFA discretization in the 2D domain Γ and the stabilization contribution. As such, it is SPD with the 5-point stencil of a 2D discrete Laplacian. Moreover, $\boldsymbol{T}$ has a block diagonal structure for all non-intersecting fractures. Observe also that traction and pressure fields are always decoupled.

From the considerations above, it is clear that matrix $\mathcal{J}$ changes nature with the evolution of the fracture conditions, moving from a reducible matrix with a symmetric saddle-point leading block to a general non-symmetric and indefinite matrix. These characteristics require the definition of a unique preconditioning framework which ensures robustness, scalability and computational efficiency.

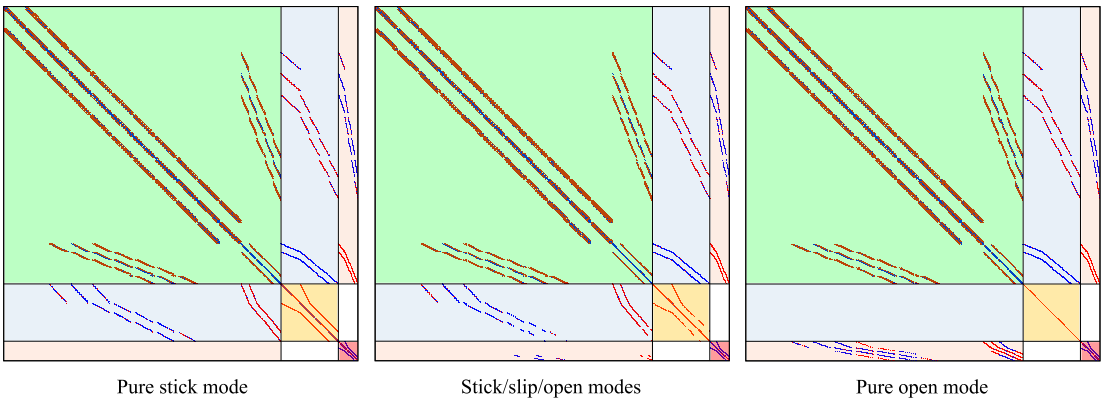

FIGURE 3.2: Non-zero pattern of $\mathcal{J}$ with the evolution of the stick/slip/open fracture regions.

3.2.3 Preconditioning framework

A preconditioner $\mathcal{M}^{-1}$ of $\mathcal{J}$ is an operator which approximates in some sense $\mathcal{J}^{-1}$. The exact application of $\mathcal{J}^{-1}$ to some vector $\mathbf{w} \in \mathbb{R}^{n_u+n_t+n_p}$ provides the vector $\mathbf{v} \in \mathbb{R}^{n_u+n_t+n_p}$ such that:

$$\left\{\begin{array}{rcrcrcl} \boldsymbol{A}\mathbf{v}_u & + & \boldsymbol{C}_1\mathbf{v}_t & + & \boldsymbol{Q}_1\mathbf{v}_p & = & \mathbf{w}_u \\ \boldsymbol{C}_2\mathbf{v}_u & - & \boldsymbol{H}\mathbf{v}_t & & & = & \mathbf{w}_t \\ \boldsymbol{Q}_2\mathbf{v}_u & & & + & T\mathbf{v}_p & = & \mathbf{w}_p \end{array}\right. , \tag{3.25}$$

with $\mathbf{v}_u, \mathbf{w}_u \in \mathbb{R}^{n_u}$, $\mathbf{v}_t, \mathbf{w}_t \in \mathbb{R}^{n_t}$, and $\mathbf{v}_p, \mathbf{w}_p \in \mathbb{R}^{n_p}$ natural subvectors of $\mathbf{v}$ and $\mathbf{w}$, respectively. The aim is to approximate the solution of the multi-physics system (3.25) by exploiting the physics-based variable partitioning. The idea is to first reduce the system to a single-physics problem, and then prolong it back to the full multi-physics space. According to the selected sequence of reductions, different algorithms may arise. Here, two options are presented and compared.

First method: traction-pressure-displacement approach

Traction and pressure variables live on the fractures and are mutually decoupled independently of the stick/slip/open region partitioning. Therefore, it is natural to exploit this condition and perform a simultaneous reduction of both these variable sets, projecting them onto the displacement space. This corresponds to compute $\mathbf{v}_t$ and $\mathbf{v}_p$ from the second and third equation of system (3.25), respectively, and introduce them in the first equation, thus eliminating both physics from the equilibrium equation. Since $\boldsymbol{H}$ is singular, a regular surrogate is needed. Here, a block diagonal approximation $\widetilde{\boldsymbol{H}}$ is used, where each block is the 3×3 local stabilization matrix computed for each fracture element. From the system (3.25), $\mathbf{v}_t$ and $\mathbf{v}_p$ are:

$$\mathbf{v}_t \simeq -\widetilde{\boldsymbol{H}}^{-1} \left(\mathbf{w}_t - \boldsymbol{C}_2\mathbf{v}_u\right) \tag{3.26}$$

$$\mathbf{v}_p = \boldsymbol{T}^{-1} \left(\mathbf{w}_p - \boldsymbol{Q}_2\mathbf{v}_u\right) \tag{3.27}$$

Substituting Eq. (3.26) and Eq. (3.27) into the first equation of system (3.25), it becomes:

$$\left(\boldsymbol{A} + \boldsymbol{C}_1\widetilde{\boldsymbol{H}}^{-1}\boldsymbol{C}_2 - \boldsymbol{Q}_1\boldsymbol{T}^{-1}\boldsymbol{Q}_2\right)\mathbf{v}_u \simeq \mathbf{w}_u + \boldsymbol{C}_1\widetilde{\boldsymbol{H}}^{-1}\mathbf{w}_t - \boldsymbol{Q}_1\boldsymbol{T}^{-1}\mathbf{w}_p, \tag{3.28}$$

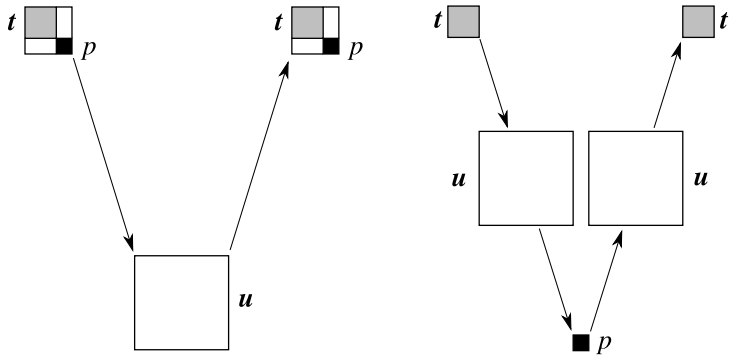

FIGURE 3.3: Schematic representation of the multi-physics reduction preconditioning framework: t-p-u (left) and t-u-p (right) approach.

which represents a single-physics equilibrium equation on the 3D domain where the elimination of fracture tractions and pressures introduces fictitious stiffness contributions. The matrix at the left-hand side of Eq. (3.28) is the Schur complement $\boldsymbol{S}$:

$$\boldsymbol{S} = \boldsymbol{A} + \boldsymbol{C}_1 \widetilde{\boldsymbol{H}}^{-1} \boldsymbol{C}_2 - \boldsymbol{Q}_1 \boldsymbol{T}^{-1} \boldsymbol{Q}_2 \tag{3.29}$$

Solution to Eq. (3.28) provides $\mathbf{v}_u$, which, introduced into Eq. (3.26) and Eq. (3.27), yields the final vector $\mathbf{v}$. The multi-physics reduction order performed in this case is traction-pressure-displacement (t-p-u) and is schematically summarized in the leftmost panel of Fig. 3.3.

The computation and inversion of $\boldsymbol{S}$ in Eq. (3.29) cannot be performed exactly. An explicit approximation $\widetilde{\boldsymbol{S}}$ is computed replacing $\boldsymbol{T}$ in Eq. (3.29) by its diagonal. The inverse $\widetilde{\boldsymbol{S}}^{-1}$ is applied inexactly by means of an AMG operator, which can be efficiently used in mechanical problems preserving a linear complexity with respect to the problem size. This is a key property to guarantee the solver scalability. Recent examples of effective AMG preconditioners can be found, for instance, in Brandt et al. [2015], D'Ambra et al. [2018] and Paludetto Magri et al. [2019]. In particular, here, the application of $\widetilde{\boldsymbol{S}}^{-1}$ is approximated by GAMG [May et al., 2016], which is the state-of-the-art aggregation based multigrid provided by the PETSc package [Balay et al., 2020].

From an algebraic viewpoint, the preconditioning operator $\mathcal{M}_1^{-1}$ arising from the t-p-u approach can be written as an inexact block LDU factorization of $\mathcal{J}$. Using the

permutation matrix $\mathcal{Q}_1$:

$$\mathcal{Q}_1 = \begin{bmatrix} \mathbf{0} & \boldsymbol{I}_t & \mathbf{0} \\ \mathbf{0} & \mathbf{0} & \boldsymbol{I}_p \\ \boldsymbol{I}_u & \mathbf{0} & \mathbf{0} \end{bmatrix}, \tag{3.30}$$

where $\boldsymbol{I}_n$ is the identity matrix in $\mathbb{R}^{n_n \times n_n}$ and $\mathbf{0}$ the zero matrix of proper size, the block LDU factorization reads:

$$\mathcal{Q}_1 \mathcal{J} \mathcal{Q}_1^T \simeq \mathcal{L}_1 \mathcal{D}_1 \mathcal{U}_1, \tag{3.31}$$

with:

$$\mathcal{L}_1 = \begin{bmatrix} \boldsymbol{I}_t & \mathbf{0} & \mathbf{0} \\ \mathbf{0} & \boldsymbol{I}_p & \mathbf{0} \\ -\boldsymbol{C}_1 \widetilde{\boldsymbol{H}}^{-1} & \boldsymbol{Q}_1 \boldsymbol{T}^{-1} & \boldsymbol{I}_u \end{bmatrix}, \mathcal{D}_1 = \begin{bmatrix} -\widetilde{\boldsymbol{H}} & \mathbf{0} & \mathbf{0} \\ \mathbf{0} & \boldsymbol{T} & \mathbf{0} \\ \mathbf{0} & \mathbf{0} & \widetilde{\boldsymbol{S}} \end{bmatrix}, \mathcal{U}_1 = \begin{bmatrix} \boldsymbol{I}_t & \mathbf{0} & -\widetilde{\boldsymbol{H}}^{-1} \boldsymbol{C}_2 \\ \mathbf{0} & \boldsymbol{I}_p & \boldsymbol{T}^{-1} \boldsymbol{Q}_2 \\ \mathbf{0} & \mathbf{0} & \boldsymbol{I}_u \end{bmatrix} \tag{3.32}$$

Hence, the final expression of $\mathcal{M}_1^{-1}$ is:

$$\mathcal{M}_1^{-1} = \begin{bmatrix} \boldsymbol{I}_t & \mathbf{0} & \widetilde{\boldsymbol{H}}^{-1} \boldsymbol{C}_2 \\ \mathbf{0} & \boldsymbol{I}_p & -\boldsymbol{T}^{-1} \boldsymbol{Q}_2 \\ \mathbf{0} & \mathbf{0} & \boldsymbol{I}_u \end{bmatrix} \begin{bmatrix} -\widetilde{\boldsymbol{H}}^{-1} & \mathbf{0} & \mathbf{0} \\ \mathbf{0} & \boldsymbol{T}^{-1} & \mathbf{0} \\ \mathbf{0} & \mathbf{0} & \widetilde{\boldsymbol{S}}^{-1} \end{bmatrix} \begin{bmatrix} \boldsymbol{I}_t & \mathbf{0} & \mathbf{0} \\ \mathbf{0} & \boldsymbol{I}_p & \mathbf{0} \\ \boldsymbol{C}_1 \widetilde{\boldsymbol{H}}^{-1} & -\boldsymbol{Q}_1 \boldsymbol{T}^{-1} & \boldsymbol{I}_u \end{bmatrix} \tag{3.33}$$

The multi-physics reduction approach proposed herein can be equivalently recast in other ways as well. Since a twofold approximation for $\boldsymbol{T}^{-1}$ is used, i.e., exact in $\mathcal{L}_1$, $\mathcal{U}_1$ and inexact in $\widetilde{\boldsymbol{S}}$, $\mathcal{M}_1^{-1}$ can be regarded as a member of the mixed constraint preconditioner class [Bergamaschi et al., 2008; Ferronato et al., 2010]. Similarly, the upper and lower block triangular factors in Eq. (3.33) play the role of decoupling operators for the original multi-physics problem and are the outcome of the general-purpose algebraic procedure defined in Ferronato et al. [2019]. Finally, $\mathcal{M}_1^{-1}$ can be also regarded as an example of application in a 3×3 block non-symmetric context of the multigrid reduction framework [Bui et al., 2018, 2020], where fracture and body variables play the role of fine and coarse nodes, respectively, and $\widetilde{\boldsymbol{H}}$ replaces $\boldsymbol{H}$ in matrix $\mathcal{J}$.

A matrix measure of the quality of the approximations $\widetilde{\boldsymbol{H}}$ and $\widetilde{\boldsymbol{S}}$ introduced in $\mathcal{M}_1^{-1}$ can be defined as:

$$\begin{aligned} E_H &= I_t - \widetilde{H}^{-1} H \\ E_S &= I_u - \widetilde{S}^{-1} S \end{aligned} \tag{3.34}$$

It can be proven [Franceschini et al., 2022] that the eigenvalues $\lambda_1 \in \mathbb{C}$ of the preconditioned matrix with the t-p-u approach are either 1, with multiplicity n_p, or such that:

$$|\lambda_1 - 1| \leq (1 + \zeta) \max\{\varepsilon_H, \varepsilon_S\}, \tag{3.35}$$

with $\varepsilon_H = \|E_H\|$, $\varepsilon_S = \|E_S\|$, $\zeta = \|\mathcal{Z}\|$ and

$$\mathcal{Z} = \begin{bmatrix} \widetilde{\boldsymbol{H}}^{-1}\boldsymbol{C}_2\widetilde{\boldsymbol{S}}^{-1}\boldsymbol{C}_1 & -\widetilde{H}^{-1}\boldsymbol{C}_2 \\ \widetilde{\boldsymbol{S}}^{-1}\boldsymbol{C}_1 & \mathbf{0} \end{bmatrix} \tag{3.36}$$

for any compatible matrix norm.

This shows that the distance of $\widetilde{\boldsymbol{H}}^{-1}\boldsymbol{H}$ from the identity and the approximation quality of $\widetilde{\boldsymbol{S}}^{-1}$ are key factors for the overall performance of $\mathcal{M}_1^{-1}$. While $\widetilde{\boldsymbol{H}}$ is fixed, notice, however, that $\widetilde{\boldsymbol{S}}$ has algebraic properties variable with the fracture state and the evolution of the stick/slip/open regions throughout the active-set algorithm. In stick mode, the contribution $\boldsymbol{C}_1\widetilde{\boldsymbol{H}}^{-1}\boldsymbol{C}_2$ is SPSD and $\boldsymbol{Q}_2 = 0$. Hence, $\widetilde{\boldsymbol{S}}$ is SPD. Also in slip mode the contribution $\boldsymbol{C}_1\widetilde{\boldsymbol{H}}^{-1}\boldsymbol{C}_2$ is positive definite and $\boldsymbol{Q}_2 = 0$, so $\widetilde{\boldsymbol{S}}$ remains positive definite, though mildly non-symmetric. With open elements, however, $\boldsymbol{Q}_2$ depends on the current pressure solution and no theoretical considerations can be made in general. In these conditions, $\widetilde{\boldsymbol{S}}$ is an indefinite non-symmetric matrix, thus it is not suited to be effectively approximated by any AMG.

Second method: traction-displacement-pressure approach

An alternative multi-physics reduction sequence relies on the scheme sketched in the rightmost panel of Fig. 3.3, i.e., following the order traction-displacement-pressure (t-u-p). Introducing the traction variables, Eq. (3.26), into the first equation of system (3.25) yields:

$$\left(\boldsymbol{A} + \boldsymbol{C}_1\widetilde{\boldsymbol{H}}^{-1}\boldsymbol{C}_2\right)\mathbf{v}_u + \boldsymbol{Q}_1\mathbf{v}_p \simeq \mathbf{w}_u + \boldsymbol{C}_1\widetilde{\boldsymbol{H}}^{-1}\mathbf{w}_t, \tag{3.37}$$

where the matrix at the left-hand side is the first-level Schur complement:

$$\boldsymbol{S}_1 = \boldsymbol{A} + \boldsymbol{C}_1\widetilde{\boldsymbol{H}}^{-1}\boldsymbol{C}_2 \tag{3.38}$$

From a physical viewpoint, $\boldsymbol{S}_1$ is an elasticity matrix with fictitious stiffness contributions arising from the traction elimination along the fractures. Then, a second reduction is performed by computing $\mathbf{v}_u$ from Eq. (3.37) and introducing it in the third equation of the system (3.25):

$$\left(\boldsymbol{T} - \boldsymbol{Q}_2 \boldsymbol{S}_1^{-1} \boldsymbol{Q}_1\right) \mathbf{v}_p \simeq \mathbf{w}_p - \boldsymbol{Q}_2 \boldsymbol{S}_1^{-1} \left(\mathbf{w}_u + \boldsymbol{C}_1 \widetilde{\boldsymbol{H}}^{-1} \mathbf{w}_t\right). \tag{3.39}$$

The matrix at the left-hand side of Eq. (3.39) is the second-level Schur complement:

$$\boldsymbol{S}_2 = \boldsymbol{T} - \boldsymbol{Q}_2 \boldsymbol{S}_1^{-1} \boldsymbol{Q}_1, \tag{3.40}$$

which, from a physical standpoint, represents a modified transmissibility matrix including the effect of the stiffness of the 3D medium surrounding the fractures.

The computation of $\boldsymbol{S}_1$ can be performed exactly, but its inverse has to be approximated. Since its nature is the same as that of $\boldsymbol{S}$ of Eq. (3.29), an AMG operator can be effectively used, such as GAMG. In the following, $\widetilde{\boldsymbol{S}}_1^{-1}$ refers to the operator that approximately applies $\boldsymbol{S}_1^{-1}$. By distinction, $\boldsymbol{S}_2$ cannot be computed exactly. Recalling the physical interpretation of $\boldsymbol{T}$ and $\boldsymbol{S}_1$, the contribution $\boldsymbol{Q}_2 \boldsymbol{S}_1^{-1} \boldsymbol{Q}_1$ can be approximated by the diagonal fixed-stress matrix introduced as a preconditioner in White et al. [2016] and Castelletto et al. [2016]. Denoting by $\boldsymbol{S}_K$ such a matrix, $\boldsymbol{S}_2$ is approximated as:

$$\boldsymbol{S}_2 \simeq \widetilde{\boldsymbol{S}}_2 = \boldsymbol{T} - \boldsymbol{S}_K, \tag{3.41}$$

where the diagonal entries of $\boldsymbol{S}_K$ are:

$$[\boldsymbol{S}_K]_k = \frac{|\Omega_k|}{\overline{K}_k}, \qquad k = 1, \ldots, n_p, \tag{3.42}$$

with $|\Omega_k|$ a measure of the volume of the cells surrounding the k-th fracture element and $\overline{K}_k$ an estimate of the associated bulk modulus.

The computation of $|\Omega_k|$ and $\overline{K}_k$ in Eq. (3.42) can be carried out using the information arising from the discretization grid and the material properties or considering a general algebraic approach, as sketched in Castelletto et al. [2016].

Similarly to the t-p-u approach, the preconditioning operator $\mathcal{M}_2^{-1}$ can be written

as an inexact block LDU factorization of the Jacobian matrix $\mathcal{J}$, after an appropriate permutation with the permutation matrix $\mathcal{Q}_2$:

$$\mathcal{Q}_2 = \begin{bmatrix} \mathbf{0} & \boldsymbol{I}_t & \mathbf{0} \\ \boldsymbol{I}_u & \mathbf{0} & \mathbf{0} \\ \mathbf{0} & \mathbf{0} & \boldsymbol{I}_p \end{bmatrix} \tag{3.43}$$

The block LDU factorization reads:

$$\mathcal{Q}_2 \mathcal{J} \mathcal{Q}_2^T \simeq \mathcal{L}_2 \mathcal{D}_2 \mathcal{U}_2, \tag{3.44}$$

with:

$$\mathcal{L}_2 = \begin{bmatrix} \boldsymbol{I}_t & \mathbf{0} & \mathbf{0} \\ -\boldsymbol{C}_1 \widetilde{\boldsymbol{H}}^{-1} & \boldsymbol{I}_u & \mathbf{0} \\ \mathbf{0} & \boldsymbol{Q}_2 \widetilde{\boldsymbol{S}}_1^{-1} & \boldsymbol{I}_p \end{bmatrix}, \; \mathcal{D}_2 = \begin{bmatrix} -\widetilde{\boldsymbol{H}} & \mathbf{0} & \mathbf{0} \\ \mathbf{0} & \boldsymbol{S}_1 & \mathbf{0} \\ \mathbf{0} & \mathbf{0} & \widetilde{\boldsymbol{S}}_2 \end{bmatrix}, \; \mathcal{U}_2 = \begin{bmatrix} \boldsymbol{I}_t & -\widetilde{\boldsymbol{H}}^{-1} \boldsymbol{C}_2 & \mathbf{0} \\ \mathbf{0} & \boldsymbol{I}_u & \widetilde{\boldsymbol{S}}_1^{-1} \boldsymbol{Q}_1 \\ \mathbf{0} & \mathbf{0} & \boldsymbol{I}_p \end{bmatrix} \tag{3.45}$$

The final expression of $\mathcal{M}_2^{-1}$ is therefore:

$$\begin{aligned} \mathcal{M}_2^{-1} = & \begin{bmatrix} \boldsymbol{I}_t & \widetilde{\boldsymbol{H}}^{-1} \boldsymbol{C}_2 & -\widetilde{\boldsymbol{H}}^{-1} \boldsymbol{C}_2 \widetilde{\boldsymbol{S}}_1^{-1} \boldsymbol{Q}_1 \\ 0 & \boldsymbol{I}_u & -\widetilde{\boldsymbol{S}}_1^{-1} \boldsymbol{Q}_1 \\ 0 & 0 & \boldsymbol{I}_p \end{bmatrix} \begin{bmatrix} -\widetilde{\boldsymbol{H}}^{-1} & 0 & 0 \\ 0 & \widetilde{\boldsymbol{S}}_1^{-1} & 0 \\ 0 & 0 & \widetilde{\boldsymbol{S}}_2^{-1} \end{bmatrix} \cdot \\ & \cdot \begin{bmatrix} \boldsymbol{I}_t & 0 & 0 \\ \boldsymbol{C}_1 \widetilde{\boldsymbol{H}}^{-1} & \boldsymbol{I}_u & 0 \\ -\boldsymbol{Q}_2 \widetilde{\boldsymbol{S}}_1^{-1} \boldsymbol{C}_1 \widetilde{\boldsymbol{H}}^{-1} & -\boldsymbol{Q}_2 \widetilde{\boldsymbol{S}}_1^{-1} & \boldsymbol{I}_p \end{bmatrix} \end{aligned} \tag{3.46}$$

Like the t-p-u approach, also $\mathcal{M}_2^{-1}$ can be equivalently recast in other ways. For instance, it can be viewed as a mixed constraint preconditioner [Bergamaschi et al., 2007; Janna et al., 2012b] or as a double application of the multigrid reduction framework.

Similar to Eq. (3.34), a matrix measure of the quality of the approximations $\widetilde{\boldsymbol{S}}_1$ and $\widetilde{\boldsymbol{S}}_2$ introduced in $\mathcal{M}_2^{-1}$ can be defined as:

$$\begin{aligned} \boldsymbol{E}_{S_1} &= \boldsymbol{I}_u - \widetilde{\boldsymbol{S}}_1^{-1} \boldsymbol{S}_1 \\ \boldsymbol{E}_{S_2} &= \boldsymbol{I}_p - \widetilde{\boldsymbol{S}}_2^{-1} \hat{\boldsymbol{S}}_2 \end{aligned} \tag{3.47}$$

where $\hat{\boldsymbol{S}}_2 = \boldsymbol{T} - \boldsymbol{Q}_2 \widetilde{\boldsymbol{S}}_1^{-1} \boldsymbol{Q}_1$. Notice that the error term $\boldsymbol{E}_{S_2}$ impacting on the quality of $\mathcal{M}_2^{-1}$ does not depend on $\boldsymbol{S}_2$, but on $\hat{\boldsymbol{S}}_2$. Hence, the proposed approximation $\widetilde{\boldsymbol{S}}_2$ of Eq.

(3.41) should better resemble $\hat{\boldsymbol{S}}_2$ than $\boldsymbol{S}_2$. The eigenvalues $\lambda_2 \in \mathbb{C}$ of the preconditioned matrix with the t-u-p approach are such that:

$$|\lambda_2 - 1| \leq (1+\gamma)\max\{\varepsilon_H, \varepsilon_{S_1}, \varepsilon_{S_2}\} \tag{3.48}$$

with $\varepsilon_H = \|\boldsymbol{E}_H\|$, $\varepsilon_{S_1} = \|\boldsymbol{E}_{S_1}\|$, $\varepsilon_{S_2} = \|\boldsymbol{E}_{S_2}\|$, $\gamma = \|\mathcal{G}\|$ and

$$\mathcal{G} = \begin{bmatrix} \boldsymbol{C}_{2H}\hat{\boldsymbol{I}}_Q\boldsymbol{C}_{1S} & -\boldsymbol{C}_{2H}\hat{\boldsymbol{I}}_Q & \boldsymbol{C}_{2H}\boldsymbol{Q}_{1S} \\ \hat{\boldsymbol{I}}_Q\boldsymbol{C}_{1S} & -\boldsymbol{Q}_{1S}\boldsymbol{Q}_{2S} & \boldsymbol{Q}_{1S} \\ -\boldsymbol{Q}_{2S}\boldsymbol{C}_{1S} & \boldsymbol{Q}_{2S} & 0 \end{bmatrix},$$

$$\boldsymbol{C}_{1S} = \widetilde{\boldsymbol{S}}_1^{-1}\boldsymbol{C}_1, \quad \boldsymbol{C}_{2H} = \widetilde{H}^{-1}\boldsymbol{C}_2, \quad \boldsymbol{Q}_{1S} = \widetilde{\boldsymbol{S}}_1^{-1}\boldsymbol{Q}_1, \boldsymbol{Q}_{2S} = \widetilde{\boldsymbol{S}}_2^{-1}\boldsymbol{Q}_2, \quad \hat{\boldsymbol{I}}_Q = \boldsymbol{I}_u + \boldsymbol{Q}_{1S}\boldsymbol{Q}_{2S}$$

for any compatible matrix norm. The complete proof can be found in Franceschini et al. [2022].

Since the eigenvalue bound is similar for the two approaches, they are expected to behave similarly. However, with $\mathcal{M}_2^{-1}$ an additional contribution to the error arises, ε_{S_2}, and there is no guarantee that a cluster of eigenvalues is exactly 1. It has to be noted also that the cost for the $\mathcal{M}_2^{-1}$ application is approximately twice that of $\mathcal{M}_1^{-1}$. The cost of $\mathcal{M}_2^{-1}$ can be possibly decreased by applying an incomplete block factorization, i.e., only $\mathcal{D}_2^{-1}\mathcal{L}_2^{-1}$, but some loss in accuracy might be expected.

As with the t-p-u approach, the Schur complements $\boldsymbol{S}_1$, Eq. (3.38), and $\widetilde{\boldsymbol{S}}_2$, Eq. (3.41), have algebraic properties that change with the fracture state and the evolution of the stick/slip/open partitioning. $\boldsymbol{S}_1$ is symmetric in stick mode and non-symmetric otherwise, but in any case it is positive definite. By distinction, $\widetilde{\boldsymbol{S}}_2$ is symmetric anyway, but can be indefinite with open fracture elements, because $\boldsymbol{Q}_2$ depends on the current pressure solution and no a-priori considerations can be done.

3.2.4 Application

Three sets of numerical experiments are used to investigate the robustness, scalability and computational performance of the proposed preconditioning framework. The first set (Test 1) consists of a small size single-fracture problem and is used to analyze and compare the robustness of the t-p-u and t-u-p approaches. The second set (Test

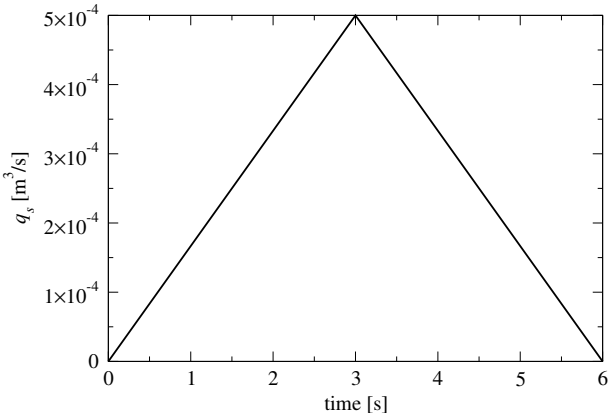

FIGURE 3.4: Flow rate in time for all the test cases.

2) simulates the behavior of a number of uniformly discretized fractures with the aim at investigating the weak scalability and mesh independence. Finally, a realistic application (Test 3), representing a tilted well in a hydraulic fracturing stimulation process, helps in verifying the computational efficiency in a meaningful context. For the sake of simplicity, the test cases considered herein are characterized by distinct discontinuities without crossing fractures. However, the possible presence of networks of crossing fractures does not impact on the preconditioning algorithm. In fact, the only difference relies on the inner block structure of all matrices in $\mathcal{J}$, with the exception of $\boldsymbol{A}$. Such a structure is no longer fracture-based but fracture-network-based, i.e., crossing fractures contribute to the same inner block.

In all test cases, a linearly increasing flow discharge q_s is first injected in the fractures, with a maximum value of $5 \cdot 10^{-4}$ m^{3}s^{-1}, and then extracted, as shown in Fig. 3.4. The overall process lasts for 6 s and is discretized into 12 uniform time steps ($\Delta t = 0.5$ s). The homogeneous rock material has Young's modulus and Poisson's ratio equal to $3 \cdot 10^3$ MPa and 0.25, respectively. The friction coefficient for the fractures is 0.577, i.e., the friction angle θ is $30°$, with the cohesion c set to zero. According to Zhang et al. [2013], the initial conductivity value $C_{f,0}$ of Eq. (3.14) is equal to 10 mD $\cdot$ m $= 9.87 \cdot 10^{-15}$m$^2 \cdot$ m. On the corners of the fracture boundary $\partial\Gamma_i$ embedded in the 3D body Ω, a constant zero pressure ($p_0 = 0$ MPa) is imposed.

For each time step, an outer loop (active-set strategy) is coupled with an inner loop (Newton's method). Starting from the last converged stick/slip/open region partitioning, the exit criterion for Newton's method is that the 2-norm of the non-linear

residual in Eq. (3.23) is reduced by a factor 10^6. At convergence, a consistency check is carried out to verify the active/inactive status of each fracture element. If the initial stick/slip/open region partitioning has to be updated, another inner Newton's loop is performed. At each Newton's iteration, the system (3.24) is solved by a right-preconditioned full GMRES algorithm [Saad and Schultz, 1986], initialized by the zero vector and stopped when the linear residual is reduced by a factor 10^8. Hence, for each entire simulation there are three iteration counters: (i) the outer active-set strategy, N_ℓ; (ii) the inner Newton's loop, N_N, and (iii) the preconditioned GMRES method, N_G. The average GMRES iteration count for a single linear system is denoted by $\overline{N}_G$, with $N_{G,\min}$ and $N_{G,\max}$ the minimum and maximum value, respectively, required during the entire simulation.

Test 1: Robustness

The purpose of this test case is to verify the robustness of the proposed t-p-u and t-u-p approaches and highlight the main differences. The 10 m×10 m×0.15 m domain with a single 2-m long vertical fracture is shown in Fig. 3.5. The top and bottom surfaces are fixed along the z-direction, while the vertical sides approximately parallel to the fracture are compressed by a uniform normal load $\sigma_0 = 100$ MPa. The out-of-plane displacement of the two remaining external surfaces of the 3D body is prevented. The computational grid consists of 2,944 nodes, 2,046 elements and 120 fracture elements, thus the number of unknowns is: $n_u = 8,832$, $n_t = 360$, and $n_p = 120$.

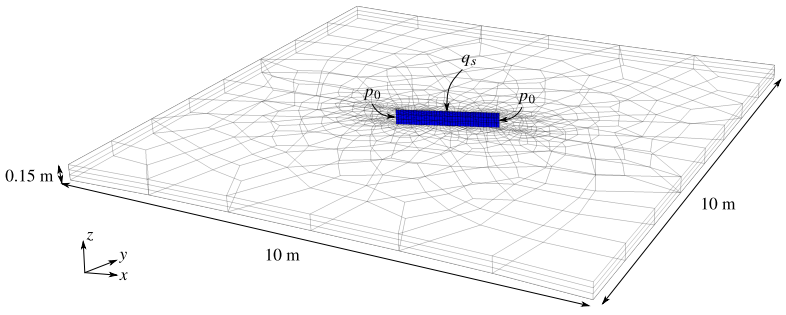

FIGURE 3.5: Test 1: Domain configuration, computational grid and injection location. The vertical exaggeration factor is 2.

Initially, nested direct methods are used to apply $\widetilde{\boldsymbol{S}}^{-1}$ in the t-p-u approach and $\widetilde{\boldsymbol{S}}_1^{-1}$ in the t-u-p approach. The results, which are reported in the upper rows of Table

TABLE 3.1: Test 1: Average number of linear iterations $\overline{N}_G$ for the t-p-u and t-u-p approach with nested direct solvers (upper rows) and AMG algorithms (lower rows) applied to approximate either $\widetilde{\boldsymbol{S}}^{-1}$ or $\widetilde{\boldsymbol{S}}_1^{-1}$ for each time step. The total number of active-set N_ℓ and Newton iterations N_N are reported in the rightmost columns. * means that N_ℓ and N_N refer to the first six steps only.

$\widetilde{\boldsymbol{S}}^{-1}$ or $\widetilde{\boldsymbol{S}}_1^{-1}$		$\overline{N}_G$												N_ℓ	N_N
	t [s]	0.5	1.0	1.5	2.0	2.5	3.0	3.5	4.0	4.5	5.0	5.5	6.0		
direct	t-p-u	2.0	5.0	4.0	4.6	7.8	9.3	5.9	5.4	4.9	4.6	4.5	2.0	58	253
method	t-u-p	2.0	5.0	4.0	4.0	6.5	7.4	7.2	5.0	2.0	2.0	2.0	2.0	33	153
AMG	t-p-u	80.0	72.0	72.0	62.2	57.3	43.0	–	–	–	–	–	–	22*	79*
	t-u-p	80.0	72.0	72.0	61.8	56.1	30.9	16.0	27.7	46.2	67.6	81.0	81.0	43	199

3.1, can be considered as the best potential outcome with regard to the average number of linear iterations $\overline{N}_G$. The two approaches behave quite similarly as far as $\overline{N}_G$ is concerned. The very small average number of GMRES iterations to converge confirms that the approximations introduced in the construction of $\widetilde{\boldsymbol{H}}$, $\widetilde{\boldsymbol{S}}$ and $\widetilde{\boldsymbol{S}}_2$ are pretty much acceptable.

This result can significantly change when AMG strategies are introduced instead of inner direct methods, as it is in practice mandatory for large-size real-world simulations. The values of $\overline{N}_G$ for each time step, N_ℓ and N_N are provided in the lower rows of Table 3.1. As before, the values are almost the same for the two approaches in the first six simulation steps, with a significant increase of $\overline{N}_G$ with respect to the use of nested direct solvers mainly due to the bad elemental aspect ratio $\left(\sim 10^{-2}\right)$ used to create this test case. The main difference between the t-p-u and the t-u-p approach is met at the seventh time step, where GMRES convergence cannot be achieved with the t-p-u framework. Although the t-p-u reduction method is generally more efficient than t-u-p, it appears to be less robust in some configurations of the stick/slip/open fracture regions. Similar behaviors have also been observed with other numerical experiments as well.

The reason for such an outcome stems from the algebraic properties of the (approximate) Schur complement matrices, $\widetilde{\boldsymbol{S}}$ in the t-p-u approach and $\boldsymbol{S}_1$ and $\widetilde{\boldsymbol{S}}_2$ in the t-u-p approach, arising at the seventh time step of the simulation. To this aim, the eigenvalue distributions of such matrices is plotted in Fig. 3.6. With the current stick/slip/open region configuration, $\widetilde{\boldsymbol{S}}$ turns out to be non-symmetric and one eigenvalue with a negative real part arises. Notice also the large ratio between the maximum and minimum

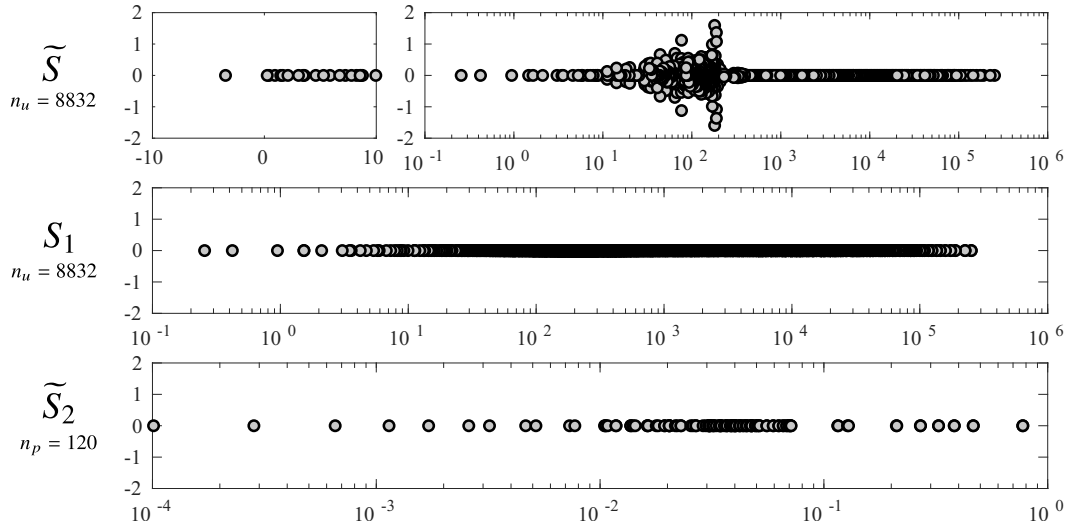

FIGURE 3.6: Test 1: Eigenvalue distribution in the complex plane for $\widetilde{\boldsymbol{S}}$, $\boldsymbol{S}_1$ and $\widetilde{\boldsymbol{S}}_2$ at the seventh time step. For $\widetilde{\boldsymbol{S}}$ a zoom around zero in arithmetic scale is also reported.

eigenvalue modulus (Table 3.2). In this condition, the AMG method used to approximate the application of $\widetilde{\boldsymbol{S}}^{-1}$ loses its theoretical properties and is no longer effective. Replacing AMG with another indefinite inner preconditioner for $\widetilde{\boldsymbol{S}}$, such as an incomplete LU factorization with partial fill-in, can fix this issue, at the cost of losing the method scalability. By distinction, in the t-u-p approach the first-level Schur complement $\boldsymbol{S}_1$ is theoretically guaranteed positive definite independently of the fracture condition. As it can be seen from Fig. 3.6 and Table 3.2, here AMG appears to work quite effectively despite the conditioning of $\boldsymbol{S}_1$ is the same as $\widetilde{\boldsymbol{S}}$. The second-level Schur complement $\widetilde{\boldsymbol{S}}_2$ is symmetric by construction, but can be indefinite. In this case, $\widetilde{\boldsymbol{S}}_2$ turns out to be still positive definite, but in any case its inversion by a nested direct solver would ensure an effective preconditioner behavior.

On summary, the t-p-u approach can be computationally more efficient than t-u-p. However, it may lack of robustness in large problems whenever the stick/slip/open

TABLE 3.2: Test 1: Maximum and minimum eigenvalue modulus for $\widetilde{\boldsymbol{S}}$, $\boldsymbol{S}_1$ and $\widetilde{\boldsymbol{S}}_2$ at the seventh time step.

	$\lvert\lambda_{\max}\rvert$	$\lvert\lambda_{\min}\rvert$	$\lvert\lambda_{\max}\rvert/\lvert\lambda_{\min}\rvert$
$\widetilde{\boldsymbol{S}}$	$2.52 \cdot 10^{5}$	$2.56 \cdot 10^{-1}$	$9.88 \cdot 10^{5}$
$\boldsymbol{S}_1$	$2.52 \cdot 10^{5}$	$2.56 \cdot 10^{-1}$	$9.88 \cdot 10^{5}$
$\widetilde{\boldsymbol{S}}_2$	$7.74 \cdot 10^{-1}$	$1.01 \cdot 10^{-4}$	$7.66 \cdot 10^{3}$

region partitioning in a full simulation gives rise to an indefinite matrix $\widetilde{\boldsymbol{S}}$. Even if more expensive, the t-u-p approach proves to be more robust, because it concentrates the source of possible numerical issues into $\widetilde{\boldsymbol{S}}_2$, which is a symmetric matrix with a 2D graph connection that can be effectively addressed by a nested direct solver. For this reason, the t-u-p approach is preferred in a full simulation, where unpredictable fracture configurations may arise. Therefore, in the following numerical experiments only the t-u-p approach is used.

Test 2: Mesh independence

In this Section, the algorithmic weak scalability, i.e., the mesh independence, of the proposed t-u-p algorithm is investigated. First, the test case shown in Fig. 3.7 (Test 2a) is considered, consisting of a unitary cube with four vertical fractures, where a fluid injection and extraction is prescribed at the center of each fracture, simulating the action of a horizontal well. The external faces parallel to the fractures are subjected to a compressive constant load ($\sigma_0 = 10$ MPa), while displacements on the other boundary faces are prevented. The pressure solution on the fracture surfaces at time $t = 3$ s, which is the moment of maximum fluid injection rate, is shown in the rightmost panel of Fig. 3.7.

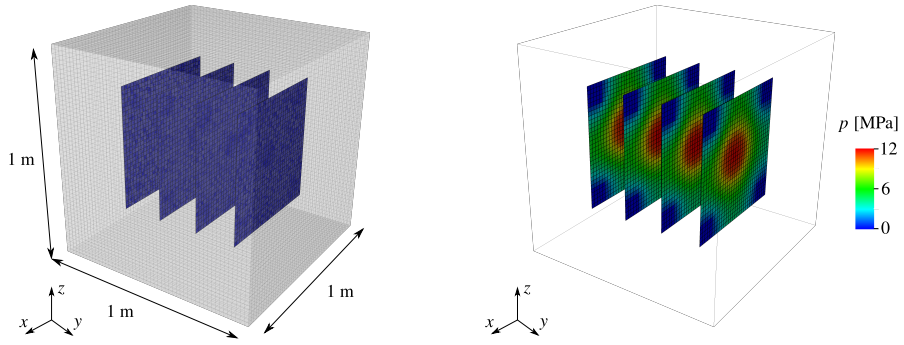

FIGURE 3.7: Test 2a: Domain configuration (left) and pressure solution at time $t = 3$ s (right).

Two uniform grid refinements are considered, with the linear elemental size varying from $h = 0.04$ m to $h = 0.02$ m. The number of unknowns for the coarse and fine discretization is listed in Table 3.3. The overall performance of the non-linear solution algorithm is reported in Table 3.4, where the number of: (i) steps ℓ of the active-set algorithm, and (ii) iterations N_N of the inner Newton's loop, are reported for every

TABLE 3.3: Test 2a: Problem size for the coarse and fine mesh.

	coarse	fine
n_u	55,080	408,045
n_t	2,700	10,800
n_p	900	3,600
total	58,680	422,445

simulation time for both the coarse and fine discretization. The same pieces of information are graphically summarized in the top panel of Fig. 3.8, where red dots refer to the beginning of a new time step and the non-linear residual decreases quadratically during each Newton's loop. If the stick/slip/open configuration obtained at convergence is not consistent with the initial one, the region subdivision is updated. At this occurrence, the non-linear relative residual increases back to 1 and a new Newton's loop is carried out.

TABLE 3.4: Test 2a: Newton's iterations N_N for each simulation time and active-set step ℓ for the coarse (top rows) and the fine mesh (bottom rows). * means that Newton's scheme does not converge and starting from a completely closed configuration is required. Fig. 3.8 reports the corresponding non-linear convergence profiles for each combination of time and active-set iterations.

		time [s]											
	ℓ	0.5	1.0	1.5	2.0	2.5	3.0	3.5	4.0	4.5	5.0	5.5	6.0
coarse	1	2	2	2	2	5	6	6	6	4	2	2	2
	2				5	4	5	5	5	2			
	3					3		5					
fine	1	2	2	2	6	6	5	7*	6*	6	3	2	2
	2			5	5	5	6	7	6	5	2		
	3			4	4	4	5	5	5	5			
	4			4	3		4	5	4	4			
	5							4	4				

The simulation is built so that all the status (stick/slip/open) are experimented along the fracture surfaces. At the beginning, all elements are in stick conditions, then the slip and open regions progressively increase until $t = 3$ s, where almost all fractures are open. Starting from $t = 3.5$ s, the elements start to close again until they return to the initial condition at $t = 6$ s. When a large number of fracture elements belongs to either the slip or the open region, the non-linear problem is more difficult and requires more active-set steps and inner Newton's iterations to converge. Quite intuitively, a larger number of fracture elements should require more non-linear iterations, as it can

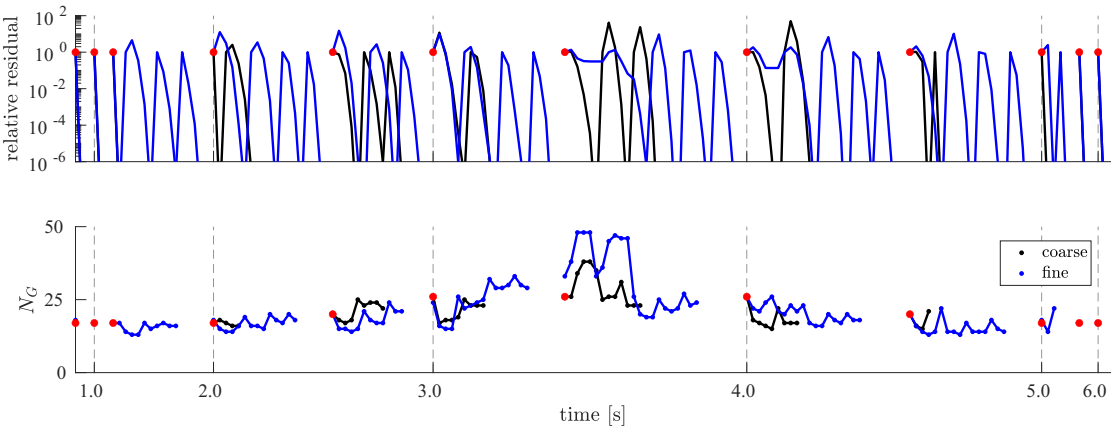

FIGURE 3.8: Test 2a: Non-linear convergence profiles (top panel) and number of linear iterations N_G for each Jacobian system solution (bottom panel). Red dots denote the beginning of the time step.

be appreciated in Table 3.4. The coarse mesh totals $N_\ell = 20$ and $N_N = 75$, while the fine mesh requires $N_\ell = 35$ and $N_N = 154$. By distinction, the linear solver performance is practically unaffected by the mesh refinement, as shown in the bottom panel of Fig. 3.8 where the GMRES iterations number N_G at every Jacobian system solution is plotted and in Table 3.5 where the average value $\overline{N}_G$ for each time step is reported. The linear iteration count tends to increase when the non-linear problem is more difficult, i.e., around $t = 3$ s. This can be motivated by the different dynamics occurring at this point, with a modification in the relative weight of each block in the overall Jacobian matrix. However, the proposed solution method appears to be fully scalable with respect to the grid size.

TABLE 3.5: Test 2a: Average number of linear iterations $\overline{N}_G$ for the coarse and fine mesh.

t [s]	0.5	1.0	1.5	2.0	2.5	3.0	3.5	4.0	4.5	5.0	5.5	6.0
coarse	17.0	17.0	17.0	16.8	21.2	21.3	28.8	18.3	18.0	17.0	17.0	17.0
fine	18.0	17.0	15.5	16.9	18.2	25.1	32.5	20.4	15.4	18.0	17.0	17.0

The investigated problem couples embedded 2D structures, i.e., the fractures, with the variables living in 3D domain. Therefore, a progressive grid refinement changes also the relative size of the blocks appearing in the Jacobian matrix $\mathcal{J}$, thus potentially modifying the overall problem conditioning. To analyze the behavior of the proposed algorithm with different 2D-to-3D ratios, i.e., the value of $(n_t + n_p)$ with respect to n_u, a second test case is introduced (Test 2b) consisting of a unitary cube with 7 vertical

fractures (Fig. 3.9). The model has been regularly refined six times, with the mesh size varying from $h = 0.1$ m to $h = 0.0167$ m. The number of unknowns for each refinement level, along with the percentage of 3D and 2D variables with respect to the total, is listed in Table 3.6. As with Test 2a, fluid injection and extraction are prescribed at the center of each fracture simulating the action of a horizontal well. The external faces parallel to the fractures are subjected to a compressive constant load ($\sigma_0 = 10$ MPa), while displacements on the other boundary faces are prevented. Fig. 3.9 shows the pressure solution at $t = 3$ s.

TABLE 3.6: Test 2b: Mesh size and percentage of 3D (n_u) and 2D ($n_t + n_p$) variables with respect to the total for different refinement levels.

level	1	2	3	4	5	6
cells	$10 \times 10 \times 10$	$20 \times 20 \times 20$	$30 \times 30 \times 30$	$40 \times 40 \times 40$	$50 \times 50 \times 50$	$60 \times 60 \times 60$
n_u	4,668	31,050	97,176	221,046	420,600	714,018
n_t	972	3,888	8,749	15,552	24,300	34,992
n_p	324	1,296	2,916	5,184	8,100	11,664
total	5,964	36,234	108,840	241,782	453,060	760,674
3D	78.3%	85.7%	89.3%	91.4%	92.8%	93.9%
2D	21.7%	14.3%	10.7%	8.6%	7.2%	6.1%

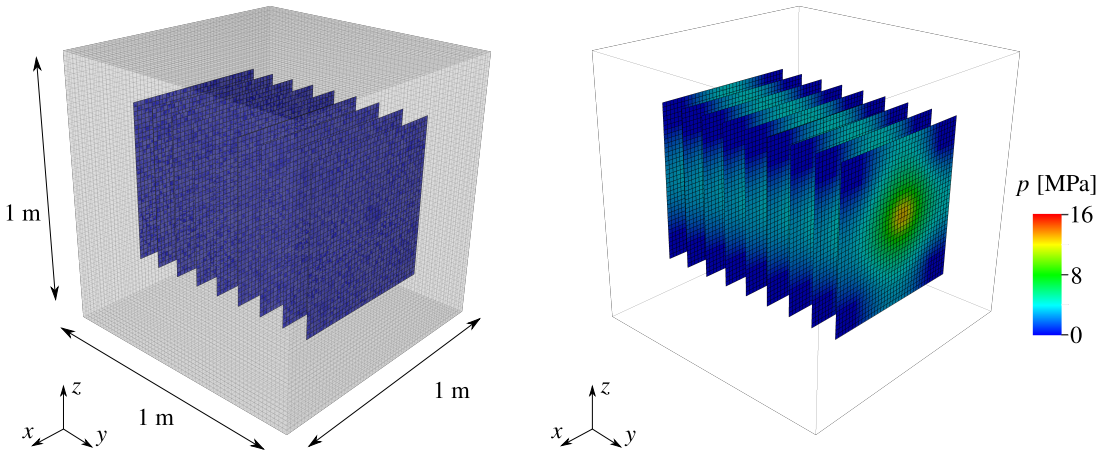

FIGURE 3.9: Test 2b: Domain configuration (left) and pressure solution at time $t = 3$ s (right).

Observe that after six refinements the size of the 2D blocks decreases from 21.7% to only 6.1% of the overall size of $\mathcal{J}$. Moreover, even with the last refinement level, which totals more than 750,000 unknowns, the size of $\widetilde{\boldsymbol{S}}_2$ is around 11,500, thus fully justifying the use of a nested direct solver. As already observed in Test 2a, it is expected that the overall number of non-linear iterations, i.e., N_ℓ and N_N, increases as the grid is progressively refined. This is observed in the left panel of Fig. 3.10, which provides

the variation of N_ℓ and N_N relative to $N_{\ell,0}$ and $N_{N,0}$, respectively, i.e., the total number of active-set steps and Newton iterations obtained with the coarsest grid. The purpose is to show how the non-linear iteration counts vary with increasing refinement level. The right panel of Fig. 3.10 provides the average, maximum and minimum number of GMRES iterations required by the linear solver. The average value is practically constant around 17 iterations and the extreme values vary between 13 and 22. Hence, the t-u-p algorithm shows a very stable behavior also when the relative size of the matrix blocks in $\mathcal{J}$ changes.

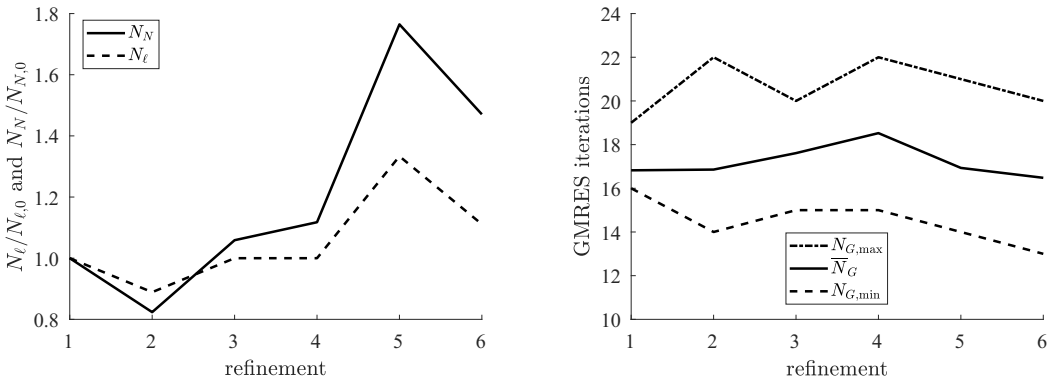

FIGURE 3.10: Test 2b: active-set and Newton's iterations relative to those for the coarsest grid (left) and average, maximum and minimum GMRES iterations (right) for each refinement level.

Test 3: Realistic application

Finally, the performance of the t-u-p preconditioner is verified in a realistic application, which simulates a tilted well intersecting 9 fractures. The domain is comprised within a 5.0 m×1.6 m×2.3 m box. The well inclination is -15° with respect to the horizontal plane. The fractures have the same size, but different relative positions with respect to the well, i.e., the well does not intersect all of them at the same location. The domain undergoes a compressive load parallel to the fractures ($\sigma_0 = 10$ MPa), while displacements are prevented on the other boundary faces. The pressure at the four corners of every fracture is set to 0. The model totals 342,642 nodes and 5,184 fracture elements, corresponding to $n_u = 1,027,926$, $n_t = 15,552$, $n_p = 5,184$, and an overall system size of 1,048,662 unknowns. An example of the pressure solution obtained at $t = 3.5$ s is reported in the leftmost panel of Fig. 3.11.

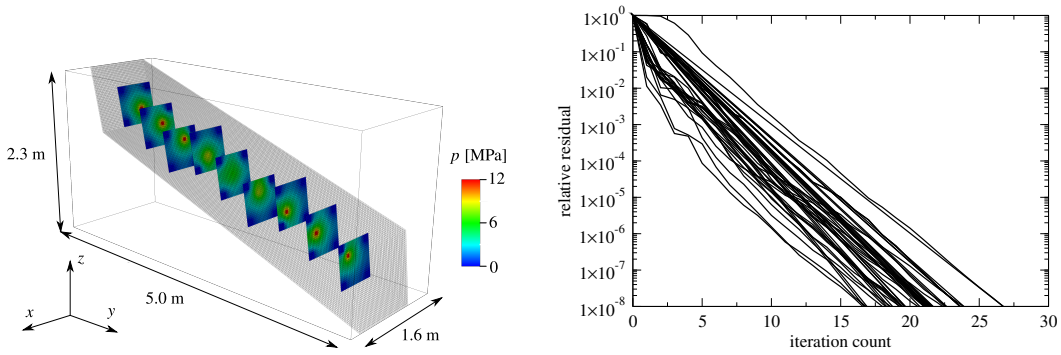

FIGURE 3.11: Test 3: Pressure solution at $t = 3.5$ s (left) and GMRES convergence profiles for all the Newton iterations at the same time (right).

The problem turns out to be particularly challenging because of the grid distortion and the different stick/slip/open region partitioning simultaneously obtained in each fracture. Thus, the overall non-linear simulation requires several active-set steps and restarts for the inner Newton's loop. The performance of the non-linear solution algorithm is summarized in Table 3.7, where the active-set steps and Newton's loop iterations at every simulation time are reported.

TABLE 3.7: Test 3: Newton's iterations for each simulation time and active-set step ℓ. The average number of GMRES iterations $\overline{N}_G$ per time step is also reported.

	time [s]											
ℓ	0.5	1.0	1.5	2.0	2.5	3.0	3.5	4.0	4.5	5.0	5.5	6.0
1	2	2	6	8	8	16	2	5	5	4	3	2
2		5	6	6	6	6	6	6	6	4	2	
3		4	5	5	5	6	5	5	4	2		
4		5	5	5	5	5	5	5	4	3		
5			4	5	5	4	4	4	5			
6								4	4			
$\overline{N}_G$	25.0	22.3	23.3	25.9	29.2	26.8	22.9	21.2	20.5	22.1	21.3	21.0

Despite the challenging configuration, the linear solver proves to be stable and efficient, as pointed out by the average GMRES iterations number reported in Table 3.7. Over the entire simulation, the average number of iterations is $\overline{N}_G = 24.2$, with a minimum $N_{G,\min} = 16$ and a maximum $N_{G,\max} = 185$. The latter corresponds to a Newton step where a large number of fracture elements move from one configuration to another. As an example, Fig. 3.11 shows all the convergence profiles obtained by a right-preconditioned GMRES accelerated by the t-u-p approach for the Newton loop at $t = 3.5$ s, proving the great stability of the solver behavior, even if the fracture state

changes significantly.

3.2.5 Discussion

In this section, the frictional contact mechanics with fluid flow in fracture networks has been numerically solved with the aid of a blended finite element/finite volume formulation. The strongly non-linear problem that arises is addressed by an active-set strategy paired with an inner Newton scheme. From the linearization a non-symmetric indefinite 3×3 block Jacobian matrix is obtained, which algebraic properties change during the simulation according to the evolution of the fractures state. For this problem, standard global approaches cannot be effectively used. Thus, a robust, scalable and efficient preconditioning framework has been proposed, which exploits the physics-based variable partitioning and the use of multigrid techniques for the sake of algorithmic scalability. The basic idea relies on (i) restricting the system to a single-physics problem, (ii) approximately solve it by an inner AMG, and (iii) prolong the solution back to the full multi-physics problem. According to the reduction sequences, two approaches have been developed, denoted as t-p-u (traction-pressure-displacement) and t-u-p (traction-displacement-pressure), and compared in a set of numerical examples.

Theoretical analyses show that the proposed approaches are expected to have a similar convergence rate, with a slight advantage for the t-p-u approach because of a more clustered eigenvalue distribution for the preconditioned matrix and a smaller application cost. Indeed, this is confirmed by the numerical experiments when nested direct solvers are used in the preconditioner application, but t-p-u approach may soon lose robustness when AMG methods are introduced. The reason stems from the possible indefiniteness of the arising Schur complement, which is avoided in the t-u-p approach.

The t-u-p approach proves to be algorithmically scalable with respect to the computational grid size and the relative size of the Discrete Fracture Network (DFN) to the full 3D domain. Although the non-linear problem can become harder to solve, the iteration count for the inner linear solver is independent of the discretization size.

The application in a realistic configuration shows the computational efficiency of the proposed approach. Despite the difficulty met by the non-linear algorithm, due

to the combination of variable stick/slip/open operating modes for the different fractures, the linear solver exhibits a very stable behavior throughout the full simulation and a remarkable efficiency also in a sequential implementation.

Future developments regard the implementation of the proposed preconditioning framework in high performance computing infrastructures, in order to fully exploit the algorithmic scalability and test the actual parallel efficiency. A natural extension of the work presented in this section regards the consideration of the (multi-phase) fluid flow not only through the fracture network, but in the porous medium matrix as well. An overview of the changes in the model formulation to tackle this new physical problem is presented in the following paragraph.

3.2.6 Extension to fluid flow in the 3D porous domain

The natural evolution of the model presented in the previous paragraphs is the extension of the fluid flow in the porous matrix. Thus, the mass balance holds not only in the fracture network, as in Eq. (3.3), but also in the 3D domain:

$$\frac{\partial}{\partial t}\left(\rho\phi\right) + \nabla \cdot \left(\rho \boldsymbol{v}\right) = q_s \tag{3.49}$$

where $\boldsymbol{v}$ is the mass flux described by Darcy's law, Eq. (2.5), and q_s is the source term.

The discretization of Eq. (3.49) follows exactly the procedure reported in Section 3.2.2 for the mass balance, i.e., the FVM is used and the pressure unknown lies now in the center of both fracture and 3D elements. At the end, the system has a 4×4 block structure where the additional block, i.e., the one related to the pressure in the 3D domain, has the same properties as the block $\boldsymbol{T}$ in Eq. (3.24). Thus, the preconditioning strategy can be built similarly to the one in Section 3.2.3.

3.3 DFN penalized formulation

In this section, a different approach for solving the hydro-poromechanical problem is considered, specifically using the FVM in a unified approach to discretize both the mass and the momentum balance equations. This model is described in Novikov et al. [2022] and implemented in the open-source Delft Advanced Research Terra Simulator

(DARTS). DARTS has already been used for hydrocarbon [Khait and Voskov, 2018a; Lyu et al., 2021a], geothermal [Khait and Voskov, 2018b; Wang et al., 2020; de Hoop et al., 2022] and CO_2 sequestration [Kala and Voskov, 2019; Lyu et al., 2021b] applications. Here, an ad-hoc preconditioning framework for the fully hydro-poromechanical coupled problem in fractured domains is developed and tested.

Section 3.3.1 briefly presents the strong form of the physical problem, while in Section 3.3.2 the weak form is derived. A first preconditioning framework is developed and tested in Section 3.3.3. The testing phase draws attention to some limits of the proposed approach, which are deeply analyzed in Section 3.3.4, where a different configuration of the proposed preconditioning approach is described and tested. Finally, Section 3.3.5 gathers the main findings and defines the steps for future developments.

3.3.1 Problem statement

Considering a poroelastic fractured domain, the single-flow is governed by the momentum and fluid mass balance equations, as in Eq. (2.11) and Eq. (3.49), respectively:

$$-\nabla \cdot \hat{\boldsymbol{\sigma}}(\boldsymbol{u}, p) = \boldsymbol{F}_V \tag{3.50}$$

$$\frac{\partial}{\partial t}\left(\rho\, \phi(\boldsymbol{u}, p)\right) + \nabla \cdot \left(\rho\, \boldsymbol{v}(p)\right) = q_s \tag{3.51}$$

The porosity ϕ is, in general, a function of pressure and displacement:

$$\phi = \phi_0 + \frac{\alpha_B/3 - \phi_0}{K_r}(p - p_0) + \alpha_B \nabla^s \left(\boldsymbol{u} - \boldsymbol{u}_0\right) \tag{3.52}$$

where the subscript 0 denotes the reference state of a variable and K_r is the bulk modulus of the solid phase. Darcy's velocity $\boldsymbol{v}(p)$ is computed according to Eq. (2.5). Contact constraints, i.e., Eq. (3.11) and Eq. (3.12), are imposed along the fractures.

3.3.2 Discrete formulation

The main unknowns of this formulation are the displacement $\boldsymbol{u}$ in Ω, the gap $\boldsymbol{g}$ in Γ and the pressure p in $\Omega \cup \Gamma$. Differently from the previous model, here the FVM is used also for the momentum balance. The discrete approximations $\{\boldsymbol{u}^h, \boldsymbol{g}^h, p^h\}$ of the unknowns

$\{\boldsymbol{u}, \boldsymbol{g}, p\}$ can be defined as:

$$\boldsymbol{u}^h = \sum_{i=1}^{n_u} \boldsymbol{\eta_i} u_i \in \boldsymbol{\mathcal{V}}^h, \qquad \boldsymbol{g}^h = \sum_{j=1}^{n_g} \boldsymbol{\mu}_j g_j \in \boldsymbol{\mathcal{M}}^h(t_N^h, \Delta \boldsymbol{g}_T), \qquad p^h = \sum_{k=1}^{n_p} \chi_k p_k \in \mathcal{P}^h, \tag{3.53}$$

where the finite-dimensional subspaces $\boldsymbol{\mathcal{V}}^h$, $\boldsymbol{\mathcal{M}}^h(t_N^h, \Delta \boldsymbol{g}_T)$ and $\mathcal{P}^h$ are:

$$\boldsymbol{\mathcal{V}}^h \subset \boldsymbol{\mathcal{V}} = \{\boldsymbol{\eta} \in [L^2(\Omega)]^3, \boldsymbol{\eta}_{|\Omega_e} \in \mathbb{P}_1(\Omega_e)\ \forall \Omega_e \in \Omega^h : \boldsymbol{\eta} = \overline{\boldsymbol{u}} \text{ on } \partial\Omega_u\} \tag{3.54}$$

$$\begin{aligned} \boldsymbol{\mathcal{M}}^h(t_N^h, \Delta \boldsymbol{g}_T) \subset \boldsymbol{\mathcal{M}}(t_N, \Delta \boldsymbol{g}_T) = \{&\boldsymbol{\mu} \in [L^2(\Gamma)]^3, \boldsymbol{\mu}_{|\Omega_e} \in \mathbb{P}_1(\Omega_e)\ \forall \Omega_e \in \Omega^h : \\ &\mu_N \geq 0, (\boldsymbol{v}, \boldsymbol{\mu})_\Gamma \leq (\tau_{\max}(t_N), ||\boldsymbol{\mu}_T||_2)_\Gamma, \boldsymbol{v} \in [L^2(\Gamma)]^3 \text{ with} \\ &v_N \geq 0, ||\boldsymbol{v}_T||_2 \leq \tau_{max}, ||\boldsymbol{\mu}_T||_2 \leq ||\Delta \boldsymbol{g}_T||_2\} \end{aligned} \tag{3.55}$$

$$\mathcal{P}^h \subset \mathcal{P} = \{\chi \in L^2(\Gamma), \chi_{|\Omega_e} \in \mathbb{P}_1(\Omega_e)\ \forall \Omega_e \in \Omega^h\} \tag{3.56}$$

with the notation already described in Section 3.2.2.

The discrete weak form of the problem may be derived as:
find $\{\boldsymbol{u}^h, \boldsymbol{g}^h, p^h\} \in \boldsymbol{\mathcal{V}}^h \times \boldsymbol{\mathcal{M}}^h(t_N^h, \Delta \boldsymbol{g}_T) \times \mathcal{P}^h$ such that

$$\mathcal{R}_u = \sum_{\delta \in \mathcal{F}(\Omega_e)} |\delta| \left(\boldsymbol{\sigma} - \alpha_B p^h \boldsymbol{i}\right) \Big|_{\boldsymbol{x}_\delta} \boldsymbol{n}_\delta - |V| \boldsymbol{F}_V \Big|_{\boldsymbol{x}_V} = 0 \tag{3.57}$$

$$\mathcal{R}_{g,i} = (t_N, g_N^h - \mu_N)_{\Gamma_i} + (\boldsymbol{t}_T, \Delta \boldsymbol{g}_T^h - \boldsymbol{\mu}_T)_{\Gamma_i} \geq 0 \qquad i = 1, \ldots, n_f \tag{3.58}$$

$$\mathcal{R}_p = |V| \frac{\partial}{\partial t} (\rho \phi) \Big|_{\boldsymbol{x}_V} + \sum_{\delta \in \mathcal{F}(\Omega_e)} |\delta| \rho \boldsymbol{v} \Big|_{\boldsymbol{x}_\delta} \boldsymbol{n}_\delta - |V| q_s \Big|_{\boldsymbol{x}_V} = 0 \tag{3.59}$$

where $\mathcal{F}$ represents the set of faces of a cell Ω_e with $|V|$ and $\boldsymbol{x}_V$ its volume and center, respectively. Considering a single face δ, $|\delta|$ is its area, $\boldsymbol{x}_\delta$ refers to its center and $\boldsymbol{n}_\delta$ to the outward normal unit vector. This formulation introduces an additional complexity, which is the gradient approximation of the displacement $\boldsymbol{u}$ and pressure p, both assumed to be piecewise-linear. This issue is treated with a gradient splitting and a gradient reconstruction, following the work by Terekhov [2020]. The variational inequality in Eq. (3.58) is solved using a penalty regularization [Garipov et al., 2016; Gallyamov et al., 2018], which leads to the following return-mapping algorithm [Novikov et al.,

2022]:

$$g_N^{k+1} - g_N^k = 0 \tag{3.60}$$

$$\widetilde{\boldsymbol{f}}_T^{'} = \boldsymbol{f}_T^{'k} + \varepsilon_T \left(\boldsymbol{g}_T^{k+1} - \boldsymbol{g}_T^k \right) \tag{3.61}$$

$$\boldsymbol{f}_T^{'k+1} - \widetilde{\boldsymbol{f}}_T^{'} + \left\langle \widetilde{\Phi} \right\rangle \frac{\widetilde{\boldsymbol{f}}_T^{'}}{|\widetilde{\boldsymbol{f}}_T^{'}|} = \boldsymbol{0} \qquad \text{with} \qquad \widetilde{\Phi} = |\widetilde{\boldsymbol{f}}_T^{'}| - f_N^{'k+1} tan(\theta) \tag{3.62}$$

where index k refers to the time step, while subscripts N and T refer to the normal and tangential components, respectively. The trial traction $\widetilde{\boldsymbol{f}}_T^{'}$ is the effective tangential traction $\boldsymbol{f}_T^{'}$ conveniently penalized with the penalty coefficient ε_T [Simo and Laursen, 1992]. The result of the Macaulay brackets $\langle \cdot \rangle$ is 0 if the argument is negative, otherwise it is equal to the argument itself.

The final system of nonlinear discrete residual equations reads:

$$\mathbf{r}(\boldsymbol{u}, \boldsymbol{g}, \boldsymbol{p}) = \begin{bmatrix} \mathbf{r}_u(\boldsymbol{u}, \boldsymbol{g}, \boldsymbol{p}) \\ \mathbf{r}_g(\boldsymbol{u}, \boldsymbol{g}, \boldsymbol{p}) \\ \mathbf{r}_p(\boldsymbol{u}, \boldsymbol{g}, \boldsymbol{p}) \end{bmatrix} = \mathbf{0}, \tag{3.63}$$

which is solved by a Newton-Krylov method. In Eq. (3.63), the algebraic vectors $\boldsymbol{u}$, $\boldsymbol{g}$ and $\boldsymbol{p}$ collect the coefficients u_i, g_j and p_k of the discrete displacement, gap and pressure fields of Eq. (3.53). To advance by one Newton iteration k, the steps are:

$$\begin{aligned} &\text{solve } \mathcal{J}^k \delta\mathbf{x} = -\mathbf{r}^k \qquad \Rightarrow \qquad \begin{bmatrix} \boldsymbol{J}_{uu} & \boldsymbol{J}_{up} & \boldsymbol{J}_{ug} \\ \boldsymbol{J}_{pu} & \boldsymbol{J}_{pp} & \boldsymbol{J}_{pg} \\ \boldsymbol{J}_{gu} & \boldsymbol{J}_{gp} & \boldsymbol{J}_{gg} \end{bmatrix}^k \begin{bmatrix} \delta\boldsymbol{u} \\ \delta\boldsymbol{g} \\ \delta\boldsymbol{p} \end{bmatrix} = - \begin{bmatrix} \mathbf{r}_u \\ \mathbf{r}_g \\ \mathbf{r}_p \end{bmatrix}^k, \\ &\text{update } \mathbf{x}^{k+1} = \mathbf{x}^k + \delta\mathbf{x} \quad \Rightarrow \qquad \begin{bmatrix} \boldsymbol{u} \\ \boldsymbol{g} \\ \boldsymbol{p} \end{bmatrix}^{k+1} = \begin{bmatrix} \boldsymbol{u} \\ \boldsymbol{g} \\ \boldsymbol{p} \end{bmatrix}^k + \begin{bmatrix} \delta\boldsymbol{u} \\ \delta\boldsymbol{g} \\ \delta\boldsymbol{p} \end{bmatrix}. \end{aligned} \tag{3.64}$$

For additional details on this formulation, the reader is pointed to Novikov et al. [2022].

3.3.3 3×3 preconditioning framework

To develop the preconditioning framework, the same concepts presented in Section 3.2.3 have been considered. In particular, the aim is to exploit the physics-based variable partitioning by first reducing the problem to a single-physics problem, and then prolonging it back to the full multi-physics space. Different algorithms may arise depending on the sequence of reductions. Here, two options for a 3×3 block preconditioner are presented and then compared through four test cases.

3×3 block Jacobian: pressure - gap - displacement approach

Considering the 3×3 structure of the Jacobian, the following permutation has been considered:

$$\mathcal{Q}\mathcal{J}\mathcal{Q}^T = \begin{bmatrix} \mathbf{0} & \boldsymbol{I}_p & \mathbf{0} \\ \mathbf{0} & \mathbf{0} & \boldsymbol{I}_g \\ \boldsymbol{I}_u & \mathbf{0} & \mathbf{0} \end{bmatrix} \begin{bmatrix} \boldsymbol{J}_{uu} & \boldsymbol{J}_{up} & \boldsymbol{J}_{ug} \\ \boldsymbol{J}_{pu} & \boldsymbol{J}_{pp} & \boldsymbol{J}_{pg} \\ \boldsymbol{J}_{gu} & \boldsymbol{J}_{gp} & \boldsymbol{J}_{gg} \end{bmatrix} \begin{bmatrix} \mathbf{0} & \mathbf{0} & \boldsymbol{I}_u \\ \boldsymbol{I}_p & \mathbf{0} & \mathbf{0} \\ \mathbf{0} & \boldsymbol{I}_g & \mathbf{0} \end{bmatrix} = \begin{bmatrix} \boldsymbol{J}_{pp} & \boldsymbol{J}_{pg} & \boldsymbol{J}_{pu} \\ \boldsymbol{J}_{gp} & \boldsymbol{J}_{gg} & \boldsymbol{J}_{gu} \\ \boldsymbol{J}_{up} & \boldsymbol{J}_{ug} & \boldsymbol{J}_{uu} \end{bmatrix} \tag{3.65}$$

Similarly to the framework presented in Section 3.2.3, the preconditioning operator $\mathcal{M}^{-1}$ can be written from an algebraic point of view as an inexact block LDU factorization of the Jacobian $\mathcal{J}$. The exact LDU factorization of the permuted Jacobian reads:

$$\begin{aligned} \begin{bmatrix} \boldsymbol{J}_{pp} & \boldsymbol{J}_{pg} & \boldsymbol{J}_{pu} \\ \boldsymbol{J}_{gp} & \boldsymbol{J}_{gg} & \boldsymbol{J}_{gu} \\ \boldsymbol{J}_{up} & \boldsymbol{J}_{ug} & \boldsymbol{J}_{uu} \end{bmatrix} = \begin{bmatrix} \boldsymbol{I}_p & \mathbf{0} & \mathbf{0} \\ \boldsymbol{J}_{gp}\boldsymbol{J}_{pp}^{-1} & \boldsymbol{I}_g & \mathbf{0} \\ \boldsymbol{J}_{up}\boldsymbol{J}_{pp}^{-1} & \left(\boldsymbol{J}_{ug} - \boldsymbol{J}_{up}\boldsymbol{J}_{pp}^{-1}\boldsymbol{J}_{pg}\right)\boldsymbol{S}_1^{-1} & \boldsymbol{I}_u \end{bmatrix} \begin{bmatrix} \boldsymbol{J}_{pp} & \mathbf{0} & \mathbf{0} \\ \mathbf{0} & \boldsymbol{S}_1 & \mathbf{0} \\ \mathbf{0} & \mathbf{0} & \boldsymbol{S}_2 \end{bmatrix} \cdot \\ \cdot \begin{bmatrix} \boldsymbol{I}_p & \boldsymbol{J}_{pp}^{-1}\boldsymbol{J}_{pg} & \boldsymbol{J}_{pp}^{-1}\boldsymbol{J}_{pu} \\ \mathbf{0} & \boldsymbol{I}_g & \boldsymbol{S}_1^{-1}\left(\boldsymbol{J}_{gu} - \boldsymbol{J}_{gp}\boldsymbol{J}_{pp}^{-1}\boldsymbol{J}_{pu}\right) \\ \mathbf{0} & \mathbf{0} & \boldsymbol{I}_u \end{bmatrix} \end{aligned} \tag{3.66}$$

where the first- and second-level Schur complements are:

$$\boldsymbol{S}_1 = \boldsymbol{J}_{gg} - \boldsymbol{J}_{gp}\boldsymbol{J}_{pp}^{-1}\boldsymbol{J}_{pg} \tag{3.67}$$

$$\boldsymbol{S}_2 = \boldsymbol{J}_{uu} - \boldsymbol{J}_{up}\boldsymbol{J}_{pp}^{-1}\boldsymbol{J}_{pu} - \left(\boldsymbol{J}_{ug} - \boldsymbol{J}_{up}\boldsymbol{J}_{pp}^{-1}\boldsymbol{J}_{pg}\right)\boldsymbol{S}_1^{-1}\left(\boldsymbol{J}_{gu} - \boldsymbol{J}_{gp}\boldsymbol{J}_{pp}^{-1}\boldsymbol{J}_{pu}\right) \tag{3.68}$$

Assuming that $\boldsymbol{J}_{gp} = \boldsymbol{0}$, Eq. (3.66) becomes:

$$\begin{bmatrix} \boldsymbol{J}_{pp} & \boldsymbol{J}_{pg} & \boldsymbol{J}_{pu} \\ \boldsymbol{0} & \boldsymbol{J}_{gg} & \boldsymbol{J}_{gu} \\ \boldsymbol{J}_{up} & \boldsymbol{J}_{ug} & \boldsymbol{J}_{uu} \end{bmatrix} = \begin{bmatrix} \boldsymbol{I}_p & \boldsymbol{0} & \boldsymbol{0} \\ \boldsymbol{0} & \boldsymbol{I}_g & \boldsymbol{0} \\ \boldsymbol{J}_{up}\boldsymbol{J}_{pp}^{-1} & \left(\boldsymbol{J}_{ug} - \boldsymbol{J}_{up}\boldsymbol{J}_{pp}^{-1}\boldsymbol{J}_{pg}\right)\boldsymbol{J}_{gg}^{-1} & \boldsymbol{I}_u \end{bmatrix} \begin{bmatrix} \boldsymbol{J}_{pp} & \boldsymbol{0} & \boldsymbol{0} \\ \boldsymbol{0} & \boldsymbol{J}_{gg} & \boldsymbol{0} \\ \boldsymbol{0} & \boldsymbol{0} & \boldsymbol{S} \end{bmatrix} \cdot \cdot \begin{bmatrix} \boldsymbol{I}_p & \boldsymbol{J}_{pp}^{-1}\boldsymbol{J}_{pg} & \boldsymbol{J}_{pp}^{-1}\boldsymbol{J}_{pu} \\ \boldsymbol{0} & \boldsymbol{I}_g & \boldsymbol{J}_{gg}^{-1}\boldsymbol{J}_{gu} \\ \boldsymbol{0} & \boldsymbol{0} & \boldsymbol{I}_u \end{bmatrix} \tag{3.69}$$

Now, only one Schur complement arises:

$$\boldsymbol{S} = \boldsymbol{J}_{uu} - \boldsymbol{J}_{up}\boldsymbol{J}_{pp}^{-1}\boldsymbol{J}_{pu} - \left(\boldsymbol{J}_{ug} - \boldsymbol{J}_{up}\boldsymbol{J}_{pp}^{-1}\boldsymbol{J}_{pg}\right)\boldsymbol{J}_{gg}^{-1}\boldsymbol{J}_{gu} \tag{3.70}$$

The final algebraic expression of the preconditioner $\mathcal{M}^{-1}$ is therefore:

$$\mathcal{M}^{-1} = \begin{bmatrix} \boldsymbol{I}_p & -\boldsymbol{J}_{pp}^{-1}\boldsymbol{J}_{pg} & -\boldsymbol{J}_{pp}^{-1}\left(\boldsymbol{J}_{pu} - \boldsymbol{J}_{pg}\boldsymbol{J}_{gg}^{-1}\boldsymbol{J}_{gu}\right) \\ \boldsymbol{0} & \boldsymbol{I}_g & -\boldsymbol{J}_{gg}^{-1}\boldsymbol{J}_{gu} \\ \boldsymbol{0} & \boldsymbol{0} & \boldsymbol{I}_u \end{bmatrix} \begin{bmatrix} \boldsymbol{J}_{pp}^{-1} & \boldsymbol{0} & \boldsymbol{0} \\ \boldsymbol{0} & \boldsymbol{J}_{gg}^{-1} & \boldsymbol{0} \\ \boldsymbol{0} & \boldsymbol{0} & \widetilde{\boldsymbol{S}}^{-1} \end{bmatrix} \cdot \cdot \begin{bmatrix} \boldsymbol{I}_p & \boldsymbol{0} & \boldsymbol{0} \\ \boldsymbol{0} & \boldsymbol{I}_g & \boldsymbol{0} \\ -\boldsymbol{J}_{up}\boldsymbol{J}_{pp}^{-1} & -\left(\boldsymbol{J}_{ug} - \boldsymbol{J}_{up}\boldsymbol{J}_{pp}^{-1}\boldsymbol{J}_{pg}\right)\boldsymbol{J}_{gg}^{-1} & \boldsymbol{I}_u \end{bmatrix} \tag{3.71}$$

where the approximation $\widetilde{\boldsymbol{S}}$ of the Schur complement is computed considering the diagonal of $\boldsymbol{J}_{pp}$ and a 3×3 block-diagonal of $\boldsymbol{J}_{gg}$.

3×3 block Jacobian: gap - pressure - displacement approach

The second preconditioning approach considers again the projection onto the displacement space, but following the order gap - pressure - displacement. The symbolic permutation of the matrix leads to:

$$\mathcal{Q}\mathcal{J}\mathcal{Q}^T = \begin{bmatrix} \boldsymbol{0} & \boldsymbol{0} & \boldsymbol{I}_g \\ \boldsymbol{0} & \boldsymbol{I}_p & \boldsymbol{0} \\ \boldsymbol{I}_u & \boldsymbol{0} & \boldsymbol{0} \end{bmatrix} \begin{bmatrix} \boldsymbol{J}_{uu} & \boldsymbol{J}_{up} & \boldsymbol{J}_{ug} \\ \boldsymbol{J}_{pu} & \boldsymbol{J}_{pp} & \boldsymbol{J}_{pg} \\ \boldsymbol{J}_{gu} & \boldsymbol{J}_{gp} & \boldsymbol{J}_{gg} \end{bmatrix} \begin{bmatrix} \boldsymbol{0} & \boldsymbol{0} & \boldsymbol{I}_u \\ \boldsymbol{0} & \boldsymbol{I}_p & \boldsymbol{0} \\ \boldsymbol{I}_g & \boldsymbol{0} & \boldsymbol{0} \end{bmatrix} = \begin{bmatrix} \boldsymbol{J}_{gg} & \boldsymbol{J}_{gp} & \boldsymbol{J}_{gu} \\ \boldsymbol{J}_{pg} & \boldsymbol{J}_{pp} & \boldsymbol{J}_{pu} \\ \boldsymbol{J}_{ug} & \boldsymbol{J}_{up} & \boldsymbol{J}_{uu} \end{bmatrix} \tag{3.72}$$

which can be factorized as:

$$\begin{bmatrix} \boldsymbol{J}_{gg} & \boldsymbol{J}_{gp} & \boldsymbol{J}_{gu} \\ \boldsymbol{J}_{pg} & \boldsymbol{J}_{pp} & \boldsymbol{J}_{pu} \\ \boldsymbol{J}_{ug} & \boldsymbol{J}_{up} & \boldsymbol{J}_{uu} \end{bmatrix} = \begin{bmatrix} \boldsymbol{I}_g & \boldsymbol{0} & \boldsymbol{0} \\ \boldsymbol{J}_{pg}\boldsymbol{J}_{gg}^{-1} & \boldsymbol{I}_p & \boldsymbol{0} \\ \boldsymbol{J}_{ug}\boldsymbol{J}_{gg}^{-1} & \left(\boldsymbol{J}_{up} - \boldsymbol{J}_{ug}\boldsymbol{J}_{gg}^{-1}\boldsymbol{J}_{gp}\right)\boldsymbol{S}_1^{-1} & \boldsymbol{I}_u \end{bmatrix} \begin{bmatrix} \boldsymbol{J}_{gg} & \boldsymbol{0} & \boldsymbol{0} \\ \boldsymbol{0} & \boldsymbol{S}_1 & \boldsymbol{0} \\ \boldsymbol{0} & \boldsymbol{0} & \boldsymbol{S}_2 \end{bmatrix} \cdot \cdot \begin{bmatrix} \boldsymbol{I}_g & \boldsymbol{J}_{gg}^{-1}\boldsymbol{J}_{gp} & \boldsymbol{J}_{gg}^{-1}\boldsymbol{J}_{gu} \\ \boldsymbol{0} & \boldsymbol{I}_p & \boldsymbol{S}_1^{-1}\left(\boldsymbol{J}_{pu} - \boldsymbol{J}_{pg}\boldsymbol{J}_{gg}^{-1}\boldsymbol{J}_{gu}\right) \\ \boldsymbol{0} & \boldsymbol{0} & \boldsymbol{I}_u \end{bmatrix} \tag{3.73}$$

The first- and second-level Schur complements are defined as:

$$\boldsymbol{S}_1 = \boldsymbol{J}_{pp} - \boldsymbol{J}_{pg}\boldsymbol{J}_{gg}^{-1}\boldsymbol{J}_{gp} \tag{3.74}$$

$$\boldsymbol{S}_2 = \boldsymbol{J}_{uu} - \boldsymbol{J}_{ug}\boldsymbol{J}_{gg}^{-1}\boldsymbol{J}_{gu} - \left(\boldsymbol{J}_{up} - \boldsymbol{J}_{ug}\boldsymbol{J}_{gg}^{-1}\boldsymbol{J}_{gp}\right)\boldsymbol{S}_1^{-1}\left(\boldsymbol{J}_{pu} - \boldsymbol{J}_{pg}\boldsymbol{J}_{gg}^{-1}\boldsymbol{J}_{gu}\right) \tag{3.75}$$

Under the hypothesis $\boldsymbol{J}_{gp} = \boldsymbol{0}$, Eq. (3.73) is simplified as:

$$\begin{bmatrix} \boldsymbol{J}_{gg} & \boldsymbol{0} & \boldsymbol{J}_{gu} \\ \boldsymbol{J}_{pg} & \boldsymbol{J}_{pp} & \boldsymbol{J}_{pu} \\ \boldsymbol{J}_{ug} & \boldsymbol{J}_{up} & \boldsymbol{J}_{uu} \end{bmatrix} = \begin{bmatrix} \boldsymbol{I}_g & \boldsymbol{0} & \boldsymbol{0} \\ \boldsymbol{J}_{pg}\boldsymbol{J}_{gg}^{-1} & \boldsymbol{I}_p & \boldsymbol{0} \\ \boldsymbol{J}_{ug}\boldsymbol{J}_{gg}^{-1} & \boldsymbol{J}_{up}\boldsymbol{J}_{pp}^{-1} & \boldsymbol{I}_u \end{bmatrix} \begin{bmatrix} \boldsymbol{J}_{gg} & \boldsymbol{0} & \boldsymbol{0} \\ \boldsymbol{0} & \boldsymbol{J}_{pp} & \boldsymbol{0} \\ \boldsymbol{0} & \boldsymbol{0} & \boldsymbol{S} \end{bmatrix} \cdot \cdot \begin{bmatrix} \boldsymbol{I}_g & \boldsymbol{0} & \boldsymbol{J}_{gg}^{-1}\boldsymbol{J}_{gu} \\ \boldsymbol{0} & \boldsymbol{I}_p & \boldsymbol{J}_{pp}^{-1}\left(\boldsymbol{J}_{pu} - \boldsymbol{J}_{pg}\boldsymbol{J}_{gg}^{-1}\boldsymbol{J}_{gu}\right) \\ \boldsymbol{0} & \boldsymbol{0} & \boldsymbol{I}_u \end{bmatrix} \tag{3.76}$$

where the Schur complement is defined as:

$$\boldsymbol{S} = \boldsymbol{J}_{uu} - \boldsymbol{J}_{ug}\boldsymbol{J}_{gg}^{-1}\boldsymbol{J}_{gu} - \boldsymbol{J}_{up}\boldsymbol{J}_{pp}^{-1}\left(\boldsymbol{J}_{pu} - \boldsymbol{J}_{pg}\boldsymbol{J}_{gg}^{-1}\boldsymbol{J}_{gu}\right) \tag{3.77}$$

The preconditioner $\mathcal{M}^{-1}$ has the final algebraic expression:

$$\mathcal{M}^{-1} = \begin{bmatrix} \boldsymbol{I}_g & \boldsymbol{0} & -\boldsymbol{J}_{gg}^{-1}\boldsymbol{J}_{gu} \\ \boldsymbol{0} & \boldsymbol{I}_p & -\boldsymbol{J}_{pp}^{-1}\left(\boldsymbol{J}_{pu} - \boldsymbol{J}_{pg}\boldsymbol{J}_{gg}^{-1}\boldsymbol{J}_{gu}\right) \\ \boldsymbol{0} & \boldsymbol{0} & \boldsymbol{I}_u \end{bmatrix} \begin{bmatrix} \boldsymbol{J}_{gg}^{-1} & \boldsymbol{0} & \boldsymbol{0} \\ \boldsymbol{0} & \boldsymbol{J}_{pp}^{-1} & \boldsymbol{0} \\ \boldsymbol{0} & \boldsymbol{0} & \widetilde{\boldsymbol{S}}^{-1} \end{bmatrix} \cdot \cdot \begin{bmatrix} \boldsymbol{I}_g & \boldsymbol{0} & \boldsymbol{0} \\ -\boldsymbol{J}_{pg}\boldsymbol{J}_{gg}^{-1} & \boldsymbol{I}_p & \boldsymbol{0} \\ -\left(\boldsymbol{J}_{ug} - \boldsymbol{J}_{up}\boldsymbol{J}_{pp}^{-1}\boldsymbol{J}_{pg}\right)\boldsymbol{J}_{gg}^{-1} & -\boldsymbol{J}_{up}\boldsymbol{J}_{pp}^{-1} & \boldsymbol{I}_u \end{bmatrix} \tag{3.78}$$

In Eq. (3.78), the approximate Schur complement $\widetilde{\boldsymbol{S}}$ is computed using the diagonal of $\boldsymbol{J}_{pp}$ and a 3×3 block diagonal of $\boldsymbol{J}_{gg}$.

The preconditioning frameworks have been implemented on a prototype MATLAB code [MATLAB, 2021b]. Four test cases have been considered in order to test the effectiveness of the proposed approaches and compare them in terms of number of GMRES iterations required to solve the problems.

Numerical results

The domain of the first two tests is a 1 m×1 m×1 m cube with a single vertical fracture (Fig. 3.12). The bottom and lateral surfaces are fixed, while a constant load $\sigma_0 = 10$ MPa is applied on the top surface. The homogeneous rock material has Young's modulus and Poisson's ratio equal to 10^3 MPa and 0.25, respectively. The simulation lasts for 30 days. The first and second test case differ for the computational mesh, which is hexahedral in the first test case and tetrahedral in the second one. The number of 3D and 2D elements and the sizes of the Jacobian sub-blocks are reported in Table 3.8.

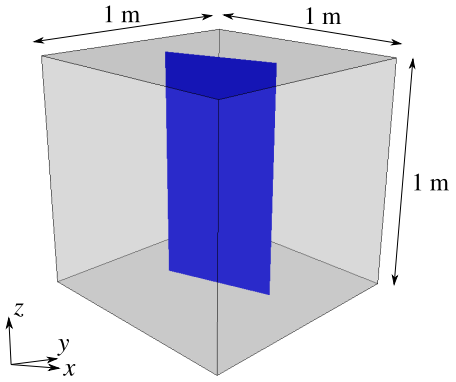

FIGURE 3.12: Domain configuration for test case 1 and 2.

TABLE 3.8: Number of elements and sizes of the Jacobian blocks for each test case.

Test case	**1**	**2**	**3**	**4**
3D elem	1,024	3,050	8,194	1,836
2D elem	16	50	91	25
n_u	3,072	9,150	24,582	5,520
n_p	1,040	3,100	8,285	1,865
n_g	48	150	273	75

The third test case considers a single-fracture problem with a displaced reservoir, as shown in Fig. 3.13. A constant pressure load equal to 35 MPa is prescribed on the

reservoir layer. The material rock is homogeneous with Young's modulus and Poisson's ratio equal to 14,950 MPa and 0.15, respectively. The tetrahedral mesh with an indication of the reservoir and the fracture location is shown in Fig. 3.13, while Table 3.8 reports the size of the problem.

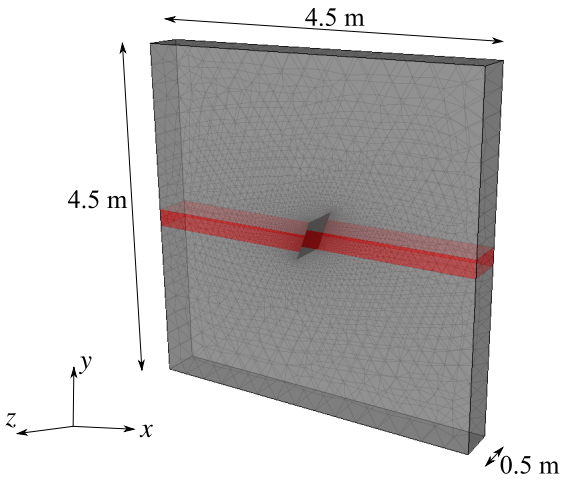

FIGURE 3.13: Test case 3: domain configuration with the reservoir layer in red.

The last test case refers again to a homogeneous domain with a single fracture, but in this case an injection and an extraction sources are located on the two opposite corners (Fig. 3.14). Young's modulus is set equal to 10^3 MPa, while Poisson's ratio is 0.25. The injector and the producer are characterized through their bottom hole pressure, which is set equal to 28 MPa. The size of the problem is reported in Table 3.8.

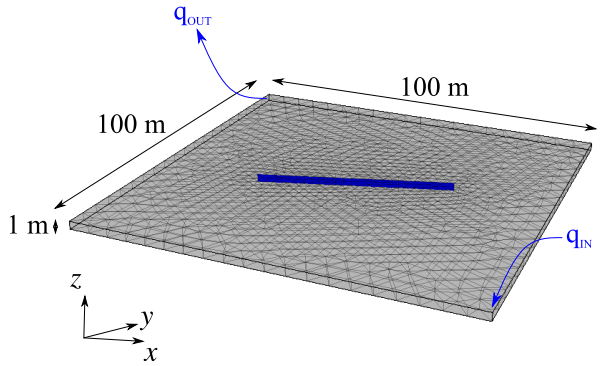

FIGURE 3.14: Domain configuration of the test case 4, with the fracture in blue and the indication of the injection and extraction location. The vertical exaggeration factor is 5.

First, the non-zeros number and the Frobenius norm have been computed for each sub-block of the Jacobian, then the preconditioning approaches have been applied to

the test cases and compared in term of number of GMRES iterations required to solve the system.

The non-zeros number and the Frobenius norm, reported in Table 3.9 and Table 3.10, respectively, give an indication about the relative importance of each Jacobian sub-block. Such values clearly show that the block $\boldsymbol{J}_{gp}$ is basically empty, thus justifying the hypothesis of neglecting it in the definition of the 3×3 block preconditioners.

TABLE 3.9: Number of non-zeros of each Jacobian sub-block. An * indicates that the number changed during the simulation, thus the average is reported.

Test case	**1**	**2**	**3**	**4**
$\boldsymbol{J}_{uu}$	63,694	150,322	412,297	89,600
$\boldsymbol{J}_{up}$	10,708	59,660	164,437	35,704
$\boldsymbol{J}_{ug}$	1,240	3,515	8,270	1,755
$\boldsymbol{J}_{pu}$	11,191*	60,108*	0	35,369*
$\boldsymbol{J}_{pp}$	12,726	30,075	8,285	17,641*
$\boldsymbol{J}_{pg}$	292	1,688	0	832*
$\boldsymbol{J}_{gu}$	640	1,500	2,278*	734*
$\boldsymbol{J}_{gp}$	0	0	170*	0
$\boldsymbol{J}_{gg}$	230	740	1,201*	359*

TABLE 3.10: Average Frobenius norm in time of each Jacobian sub-block. The values related to block $\boldsymbol{J}_{pp}$ are normalized dividing by the time step size. The $\sim$ is used when the value of the norm slightly varies during the simulation time.

Test case	**1**	**2**	**3**	**4**
$\boldsymbol{J}_{uu}$	1.78e+07	3.01e+06	3.79e+10	1.33e+07
$\boldsymbol{J}_{up}$	1.02e+00	1.35e+00	2.73e+06	1.35e+02
$\boldsymbol{J}_{ug}$	8.20e+05	1.74e+05	1.70e+09	1.30e+05
$\boldsymbol{J}_{pu}$	$\sim$8.03e+03	$\sim$1.06e+03	0.00e+00	$\sim$1.08e+05
$\boldsymbol{J}_{pp}$	1.08e+04	2.55e+03	2.81e+08	$\sim$5.97e+07
$\boldsymbol{J}_{pg}$	$\sim$1.00e+03	$\sim$5.70e+01	0.00e+00	$\sim$8.27e+03
$\boldsymbol{J}_{gu}$	2.43e+01	1.24e+01	$\sim$1.45e+03	$\sim$8.85e+00
$\boldsymbol{J}_{gp}$	0.00e+00	0.00e+00	$\sim$2.27e-13	0.00e+00
$\boldsymbol{J}_{gg}$	1.49e+05	1.25e+05	$\sim$1.46e+07	$\sim$7.81e+04

The preconditioners have been applied in the solution of the four test cases in two ways: (i) by using nested direct solvers and (ii) by approximating the block inverses. The aim of the former test is to evaluate the overall effectiveness of the proposed approaches, while with the latter case the influence of the approximations is evaluated.

Indeed, approximations are mandatory in complex real cases where the sizes of the matrices do not allow for the use of nested direct methods. Results of the first and second preconditioning approach are reported in Fig. 3.15 and Fig. 3.16, respectively.

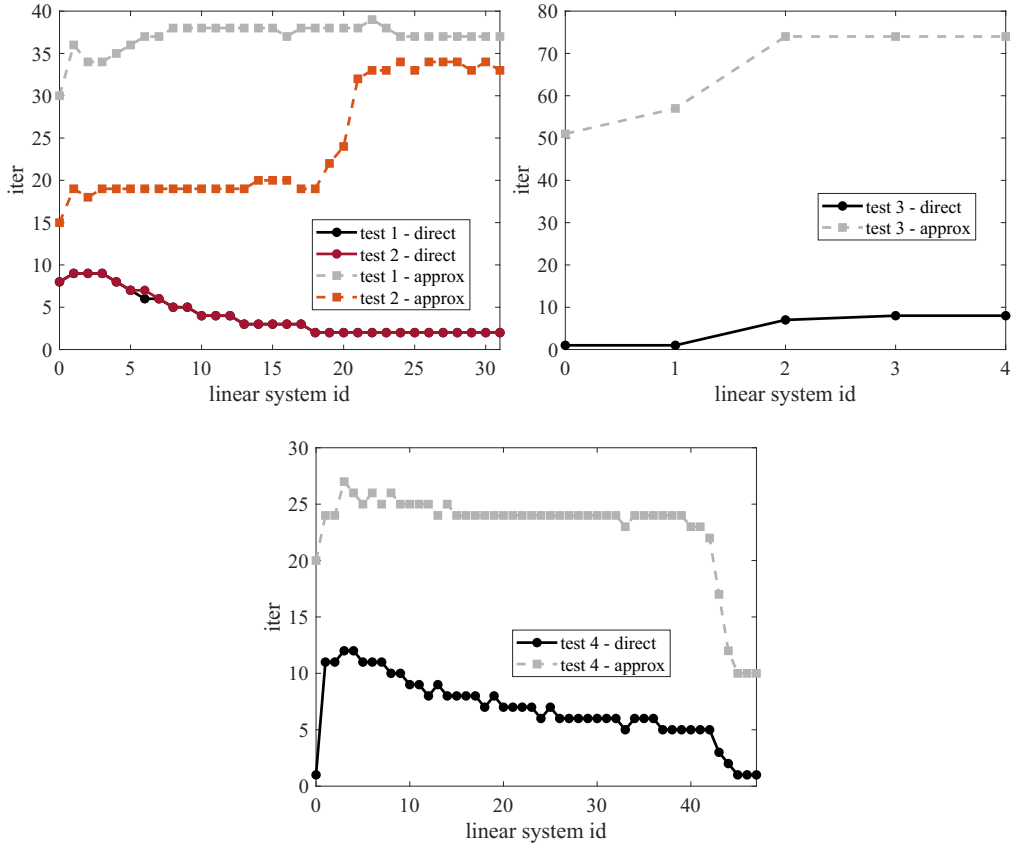

FIGURE 3.15: Linear iterations required to solve the four test cases with the 3×3 preconditioner, that follows the order pressure - gap - displacement.

Results in terms of convergence profiles are promising. The application of the preconditioners with nested direct solvers for the inner block inverses demonstrates the effectiveness of the proposed approaches, with the iterations number required to solve the linear system lower than 10 for all the test cases. However, when the preconditioners make use of inner approximations, the convergence profiles show a non negligible increase in the iterations number. In order to investigate which block approximation has the main impact on the system solution, the mechanical sub-blocks, i.e., the ones referred to the displacement and the gap unknowns, have been joined together and the 2×2 hydro-poromechanical problem has been analyzed.

Two preconditioning frameworks, based on the two possible reordering of the unknowns are presented and compared in Section 3.3.4.

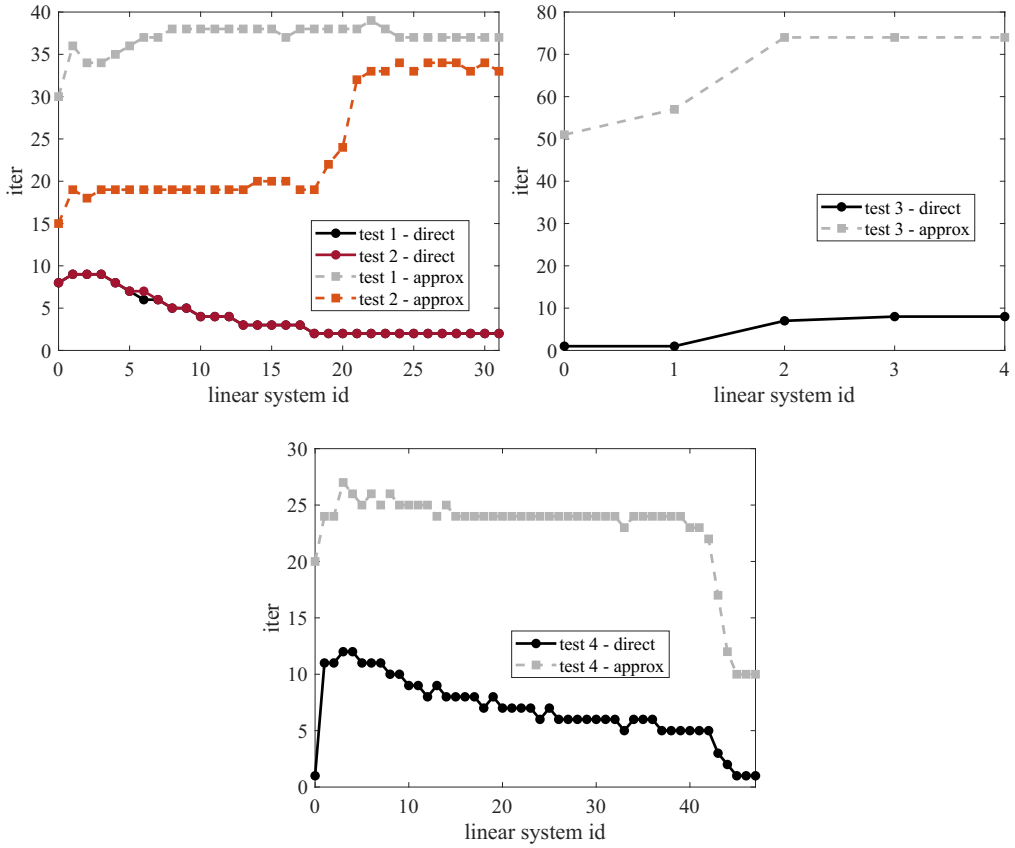

FIGURE 3.16: Linear iterations required to solve the four test cases with the 3×3 preconditioner, that follows the order gap - pressure - displacement.

3.3.4 2×2 preconditioning framework

The analyses consider the hydro-poromechanical coupling without the distinction between the 3D domain and the fractures, i.e., keeping together the displacements $\boldsymbol{u}$ and the gaps $\boldsymbol{g}$, and working with a 2×2 block Jacobian. The aim is to identify which of the two main physics mainly influences the solution of the problem.

2×2 block Jacobian: mechanic - pressure approach

First, the mechanic - flow ordering is considered:

$$\begin{bmatrix} \boldsymbol{J}_{uu} & \boldsymbol{J}_{ug} & \boldsymbol{J}_{up} \\ \boldsymbol{J}_{gu} & \boldsymbol{J}_{gg} & \boldsymbol{J}_{gp} \\ \boldsymbol{J}_{pu} & \boldsymbol{J}_{pg} & \boldsymbol{J}_{pp} \end{bmatrix} \rightarrow \begin{bmatrix} \boldsymbol{J}_{kk} & \boldsymbol{J}_{kp} \\ \boldsymbol{J}_{pk} & \boldsymbol{J}_{pp} \end{bmatrix} \tag{3.79}$$

Similarly to the framework presented in Section 3.3.3, the preconditioning operator $\mathcal{M}_1^{-1}$ can be written as an inexact block LDU factorization of the Jacobian $\mathcal{J}$:

$$\mathcal{Q}_1 \mathcal{J} \mathcal{Q}_1^T \simeq \mathcal{L}_1 \mathcal{D}_1 \mathcal{U}_1, \tag{3.80}$$

where in this case the permutation matrix $\mathcal{Q}_1$ is the block-diagonal identity matrix. The LDU factorization reads:

$$\begin{bmatrix} \boldsymbol{J}_{kk} & \boldsymbol{J}_{kp} \\ \boldsymbol{J}_{pk} & \boldsymbol{J}_{pp} \end{bmatrix} = \begin{bmatrix} \boldsymbol{I}_k & \boldsymbol{0} \\ \boldsymbol{J}_{pk}\boldsymbol{J}_{kk}^{-1} & \boldsymbol{I}_p \end{bmatrix} \begin{bmatrix} \boldsymbol{J}_{kk} & \boldsymbol{0} \\ \boldsymbol{0} & \boldsymbol{S}_p \end{bmatrix} \begin{bmatrix} \boldsymbol{I}_k & \boldsymbol{J}_{kk}^{-1}\boldsymbol{J}_{kp} \\ \boldsymbol{0} & \boldsymbol{I}_p \end{bmatrix} \tag{3.81}$$

where $\boldsymbol{S}_p$ is the Schur complement:

$$\boldsymbol{S}_p = \boldsymbol{J}_{pp} - \boldsymbol{J}_{pk}\boldsymbol{J}_{kk}^{-1}\boldsymbol{J}_{kp} \tag{3.82}$$

The final expression of the preconditioner $\mathcal{M}_1^{-1}$ is therefore:

$$\mathcal{M}_1^{-1} = \begin{bmatrix} \boldsymbol{I}_k & -\boldsymbol{J}_{kk}^{-1}\boldsymbol{J}_{kp} \\ \boldsymbol{0} & \boldsymbol{I}_p \end{bmatrix} \begin{bmatrix} \boldsymbol{J}_{kk}^{-1} & \boldsymbol{0} \\ \boldsymbol{0} & \widetilde{\boldsymbol{S}}_p^{-1} \end{bmatrix} \begin{bmatrix} \boldsymbol{I}_k & \boldsymbol{0} \\ -\boldsymbol{J}_{pk}\boldsymbol{J}_{kk}^{-1} & \boldsymbol{I}_p \end{bmatrix} \tag{3.83}$$

where $\widetilde{\boldsymbol{S}}_p$ is an approximation of the Schur complement computed considering a diagonal approximation of $\boldsymbol{J}_{kk}^{-1}$.

2×2 block Jacobian: pressure - mechanic approach

A similar preconditioner is built considering the alternative multi-physics reduction, thus projecting the problem onto the pressure space:

$$\begin{bmatrix} \boldsymbol{J}_{pp} & \boldsymbol{J}_{pu} & \boldsymbol{J}_{pg} \\ \boldsymbol{J}_{up} & \boldsymbol{J}_{uu} & \boldsymbol{J}_{ug} \\ \boldsymbol{J}_{gp} & \boldsymbol{J}_{gu} & \boldsymbol{J}_{gg} \end{bmatrix} \rightarrow \begin{bmatrix} \boldsymbol{J}_{pp} & \boldsymbol{J}_{pk} \\ \boldsymbol{J}_{kp} & \boldsymbol{J}_{kk} \end{bmatrix} \tag{3.84}$$

In this formulation, the LDU factorization of the system matrix reads:

$$\begin{bmatrix} \boldsymbol{J}_{pp} & \boldsymbol{J}_{pk} \\ \boldsymbol{J}_{kp} & \boldsymbol{J}_{kk} \end{bmatrix} = \begin{bmatrix} \boldsymbol{I}_p & \boldsymbol{0} \\ \boldsymbol{J}_{kp}\boldsymbol{J}_{pp}^{-1} & \boldsymbol{I}_k \end{bmatrix} \begin{bmatrix} \boldsymbol{J}_{pp} & \boldsymbol{0} \\ \boldsymbol{0} & \boldsymbol{S}_k \end{bmatrix} \begin{bmatrix} \boldsymbol{I}_p & \boldsymbol{J}_{pp}^{-1}\boldsymbol{J}_{pk} \\ \boldsymbol{0} & \boldsymbol{I}_k \end{bmatrix} \tag{3.85}$$

where the Schur complement is:

$$\boldsymbol{S}_k = \boldsymbol{J}_{kk} - \boldsymbol{J}_{kp}\boldsymbol{J}_{pp}^{-1}\boldsymbol{J}_{pk} \tag{3.86}$$

The final algebraic expression of the preconditioner $\mathcal{M}_2^{-1}$ reads:

$$\mathcal{M}_2^{-1} = \begin{bmatrix} \boldsymbol{I}_p & -\boldsymbol{J}_{pp}^{-1}\boldsymbol{J}_{pk} \\ \boldsymbol{0} & \boldsymbol{I}_k \end{bmatrix} \begin{bmatrix} \boldsymbol{J}_{pp}^{-1} & \boldsymbol{0} \\ \boldsymbol{0} & \widetilde{\boldsymbol{S}}_k^{-1} \end{bmatrix} \begin{bmatrix} \boldsymbol{I}_p & \boldsymbol{0} \\ -\boldsymbol{J}_{kp}\boldsymbol{J}_{pp}^{-1} & \boldsymbol{I}_k \end{bmatrix} \tag{3.87}$$

where $\widetilde{\boldsymbol{S}}_k^{-1}$ is the approximate Schur complement computed using the diagonal of $\boldsymbol{J}_{pp}$ in Eq. (3.86).

Numerical results

The two preconditioning frameworks presented in the previous paragraphs have been tested on the four test cases described in Section 3.3.3. The preconditioners have been applied with the aid of nested direct solvers, in order to evaluate the framework effectiveness. Then, they have been applied considering the approximation of (i) the Schur complement and (ii) the mechanic/flow block, with the aim to identify which approximation has the main impact on the solution of the coupled problem.

The results in terms of iterations number required to solve the linear systems are reported in Fig. 3.17 and Fig. 3.18 for the preconditioner with ordering mechanics - flow, and in Fig. 3.19 and Fig. 3.20 for the flow - mechanics one.

The application of the preconditioners with nested direct solvers demonstrates the effectiveness of the approaches, with the number of iterations required to solve the systems lower than 10 for all the test cases. This confirms the results already obtained in Section 3.3.3. The approximation of the Schur complement (Fig. 3.17 and Fig. 3.18), i.e., of the pressure block of the Jacobian (Fig. 3.19 and Fig. 3.20), preserves the accuracy of

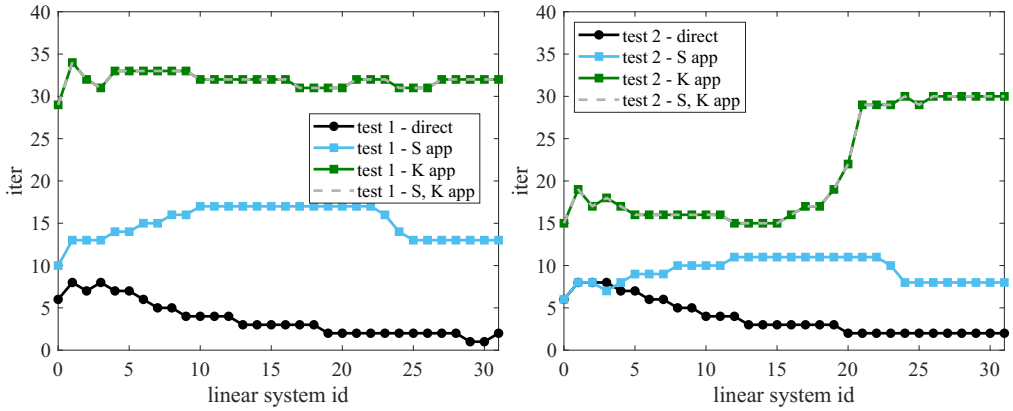

FIGURE 3.17: Linear iterations required to solve the test case 1 (left) and 2 (right) with the 2x2 approach that follows the order mechanic - flow.

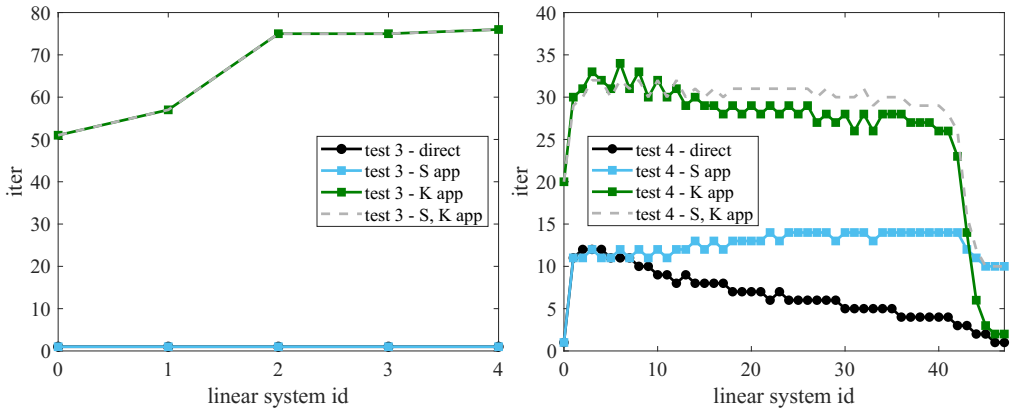

FIGURE 3.18: Linear iterations required to solve the test case 3 (left) and 4 (right) with the 2x2 approach that follows the order mechanic - flow. When the preconditioner is directly applied or if only $\boldsymbol{S}$ is approximated, just 1 iteration is needed for the test case 3.

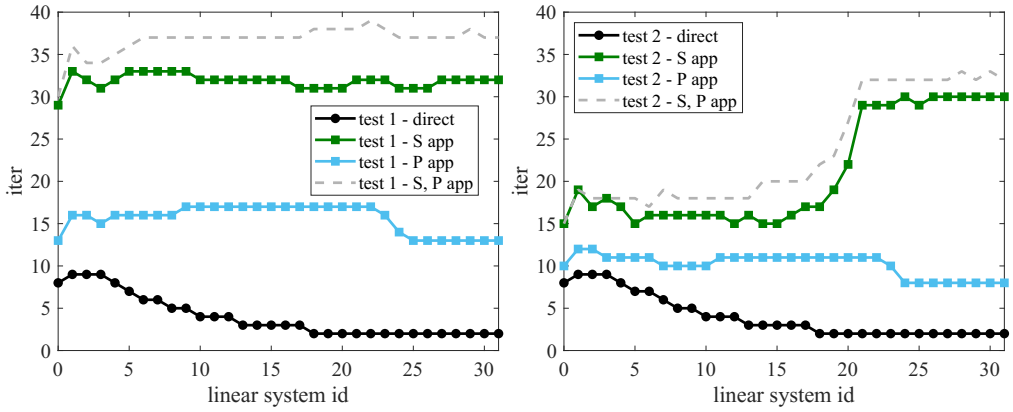

FIGURE 3.19: Linear iterations required to solve the test case 1 (left) and 2 (right) with the 2x2 approach that follows the order flow - mechanic.

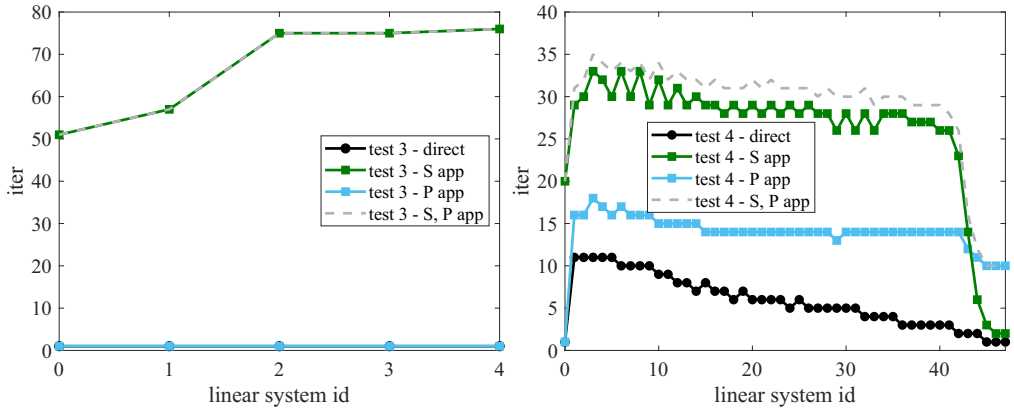

FIGURE 3.20: Linear iterations required to solve the test case 3 (left) and 4 (right) with the 2x2 approach that follows the order flow - mechanic. If the preconditioner is directly applied or if only $\boldsymbol{S}$ is approximated, only 1 iteration is needed for the test case 3.

the preconditioner approaches, with a slight increase in the iterations number. On the contrary, an approximate application of the mechanical block involves a non negligible deterioration of the convergence profiles.

3.3.5 Discussion

In this section, the coupled hydro-mechanical problem in fractured domain, solved with a finite volume formulation and a penalty approach, has been considered. According to the framework developed for the blended FEM - FVM Lagrangian formulation in Section 3.2, different preconditioners have been proposed exploiting the physics-based block partitioning of the problem. First, two preconditioning approaches have been developed considering the 3×3 structure of the Jacobian, and compared through four test cases. The numerical results show the effectiveness of the proposed frameworks, but also point out some limits in the approximation of the mechanical block. This can be easily overcome moving from the MATLAB prototype code to an ad-hoc implementation that allows to take advantage from different kinds of approximate application of the preconditioner sub-blocks, such as multigrid techniques.

Future developments will regard a more advanced implementation of the preconditioning framework and an extensive testing phase, to prove its scalability and robustness.

3.4 DFN as a PDE-constrained optimization

In Section 3.2 and Section 3.3, two formulations for the simulation of the coupled hydro-poromechanical problem in porous media have been presented. These models consider an explicit discrete representation of the fractures in a conforming domain. The conformity requirement can be particularly demanding for intricate fracture networks where there is a multi-scale geometry with many fracture intersections. When the presence of faults and fractures has a dominant impact on the fluid flow dynamics, e.g., when the fracture hydraulic transmissivity is much higher than rock transmissivity, the influence of the porous rock matrix can be neglected with minor impact on the flow prediction. In addition, modeling only the fracture network reduces the computational cost. However, other issues arise, such as the imposition of the interface conditions, especially at the fracture intersections. This problem has been effectively restated as a PDE-constrained optimization problem in Berrone et al. [2013, 2016, 2017]. The main advantage of this formulation is that it allows for the use of independent, and possibly non nonconforming, meshes for each fracture. From an algebraic point of view, a symmetric saddle-point matrix with a rank-deficient leading block arises. The properties of this system have been investigated herein and a proper block preconditioning strategy has been designed and tested.

Section 3.4.1 recalls the problem definition for the flow in fracture networks. The algebraic problem arising from the PDE optimization is described in Section 3.4.2. The preconditioning framework is derived in Section 3.4.3 and the results of the numerical tests are reported in Section 3.4.4. Finally, Section 3.4.5 summarizes the outcomes and suggests possible future perspectives.

3.4.1 Problem statement

In this model, the fractures are explicitly represented as intersecting planar polygons in a 3D structure, neglecting the surrounding underground rock formation. Let Ω be a connected three-dimensional fracture network consisting of the union of n_f intersecting planar polygons $\overline{\omega}_i$, $i = 1, \ldots, n_f$, where $\overline{\omega}_i = \omega_i \cup \Gamma_i$ is the closure of the open planar domain ω_i with its linear boundary Γ_i. The fluid flow through ω_i is assumed

laminar and described by the mass balance coupled with Darcy's law. Dirichlet and Neumann boundary conditions are imposed on Γ_i. The problem is supplemented with the constraint conditions, corresponding to the physical requirement of continuity of the hydraulic head and conservation of hydraulic fluxes across the linear intersections between fractures. These intersections are also called traces. The system to be solved is:

$$-\nabla \cdot (\boldsymbol{K} \nabla h) = q, \qquad \text{in } \omega_i \in \Omega, \tag{3.88}$$

$$h_{|\Gamma_i^D} = h_i^D, \qquad \text{on } \Gamma_i^D, \tag{3.89}$$

$$\boldsymbol{K} \nabla h \cdot \boldsymbol{n}_i = g_i, \qquad \text{on } \Gamma_i^N, \tag{3.90}$$

where $\Gamma_i^D \cup \Gamma_i^N = \Gamma_i$, $\Gamma_i^D \cap \Gamma_i^N = \emptyset$, and $\Gamma_i^D \neq \emptyset$. In the previous equations, h is the hydraulic head, $\boldsymbol{K}$ is the fracture transmissibility tensor, which is assumed to be symmetric and uniformly positive definite, $\boldsymbol{n}_i$ is the outward normal to Γ_i, q is the known discharge within the fracture, and h_i^D and g_i are the given hydraulic head and flux prescribed along the fracture boundary, respectively. Since the fracture network is connected, there is a flux exchange through the linear traces between the intersecting polygons. Let $\sigma_k^{i,j}$ denote the intersection between $\overline{\omega}_i$ and $\overline{\omega}_j$, which is assumed to be a single close segment, with Σ the union of the n_s traces, $\Sigma = \cup_{k=1}^{n_s} \sigma_k^{i,j}$. Indicating by h_i the restriction of h to $\overline{\omega}_i$, the continuity of the hydraulic head and the conservation of fluxes across the traces requires that:

$$h_{i|\sigma_k^{i,j}} - h_{j|\sigma_k^{i,j}} = 0, \qquad \forall\, \sigma_k^{i,j} \in \Sigma, \tag{3.91}$$

$$[\![\boldsymbol{K} \nabla h_i \cdot \boldsymbol{n}_k^i]\!]_{\sigma_k^{i,j}} + [\![\boldsymbol{K} \nabla h_j \cdot \boldsymbol{n}_k^j]\!]_{\sigma_k^{i,j}} = 0, \qquad \forall\, \sigma_k^{i,j} \in \Sigma, \tag{3.92}$$

with $\boldsymbol{n}_k^i$ the outer normal to the trace $\sigma_k^{i,j}$ lying on the fracture $\overline{\omega}_i$ and the symbol $[\![\cdot]\!]_{\sigma_k^{i,j}}$ denoting the jump of the quantity within brackets through $\sigma_k^{i,j}$. The DFN flow model consists of finding the hydraulic head $h : \Omega \to \mathbb{R}$ satisfying the governing PDEs (3.88)-(3.90) under the constraints (3.91)-(3.92).

3.4.2 Discrete formulation

The number of the fractures and their different sizes, which can change of orders of magnitude, entail a complex and multi-scale geometry that is not trivial to address. Traditionally, a numerical solution to the problem presented in Section 3.4.1, Eqs. (3.88)-(3.92), requires some form of (at least partial) conformity in the meshes introduced on the fractures. This issue is circumvented in the approach originally proposed by Berrone et al. [2013], where the solution is obtained by a PDE-constrained optimal control problem. This method allows for the use of nonconforming meshes, i.e., meshes in which elements are free to arbitrarily cross fracture intersections, thus simplifying the mesh generation process. The coupling conditions at traces are enforced through the minimization of a properly designed cost functional. The functional expresses the error in the fulfillment of the interface conditions, and the solution is obtained as the minimum of this functional constrained by the equations describing the flow on each fracture [Berrone et al., 2014, 2017].

Let us introduce an appropriate measurable function space $\mathcal{H}$ for the representation of h, such as:

$$\mathcal{H} = \left\{ \eta \in H^1(\omega_i) : \eta_{|\Gamma_i^D} = h_i^D, \forall i = 1, \dots, n_f \right\}, \tag{3.93}$$

with $\mathcal{H}_0$ the corresponding counterpart with homogeneous conditions along Γ_i. A mixed formulation is used, where the jump $[\![\boldsymbol{K}\nabla h_i \cdot \boldsymbol{n}_k^i]\!]_{\sigma_k^{i,j}}$, living along every trace $\sigma_k^{i,j}$ for all i and j, is described by the unknown function $u_i : \sigma_k^{i,j} \to \mathbb{R}$ belonging to the proper measurable function space $\mathcal{U}_i$, which is defined according to the selection of $\mathcal{H}$. For example, considering $\mathcal{H}$ as in Eq. (3.93), $\mathcal{U}_i$ can be selected as a subspace of $L^2(\sigma_k^{i,j})$, with the global space $\mathcal{U}$ including all $\mathcal{U}_i$. The set of constraints (3.91)-(3.92) can be prescribed by minimizing the functional $\psi(h, u) : \mathcal{H} \times \mathcal{U} \to \mathbb{R}$:

$$\psi(h, u) = \sum_{\sigma_k^{i,j} \in \Sigma} \left(\|h_i - h_j\|_{\mathcal{H}}^2 + \|u_i + u_j + \alpha\,(h_i - h_j)\|_{\mathcal{U}}^2 \right) \tag{3.94}$$

where $\alpha \in \mathbb{R}$ is a regularization parameter. The minimization of $\psi(h, u)$ under the conditions provided by Eqs. (3.88)-(3.90) is enforced by using Lagrange multipliers.

The weak form reads:

$$(\nabla\eta, \boldsymbol{K}\nabla h)_{\omega_i} - (\eta, u)_{\sigma_k^{i,j}} = -(\eta, q)_{\omega_i} + (\eta, g_i)_{\gamma_i^N}\,, \qquad \forall\, \eta \in \mathcal{H}_0,\ i = 1, \dots, n_f \quad (3.95)$$

Denoting by $p \in \mathcal{P}$ the Lagrange multipliers living in the appropriate space $\mathcal{P}$, the DFN flow solution is obtained by finding $(h, u, p) \in \mathcal{H} \times \mathcal{U} \times \mathcal{P}$ that minimizes:

$$\Psi(h, u, p) = \psi(h, u) + p \sum_i \left[a_i(\eta, h) - c_i(\eta, u) - q_i(\eta)\right], \qquad \forall\, \eta \in \mathcal{H}_0 \quad (3.96)$$

with $a_i(\eta, h) = (\nabla\eta, \boldsymbol{K}\nabla h)$, $c_i = (\eta, u)_{\sigma_k^{i,j}}$, and $q_i = -(\eta, q)_{\omega_i} + (\eta, g_i)_{\gamma_i^N}$.

The minimization of $\Psi(h, u, p)$ in Eq. (3.96) is carried out approximately by replacing the function spaces $\mathcal{H}, \mathcal{U}$ and $\mathcal{P}$ with their discrete counterparts $\mathcal{H}^h, \mathcal{U}^h$ and $\mathcal{P}^h$ with finite size n_h, n_u, and n_p, respectively. One of the advantage of this method is that the minimization process requires iteratively solving local and almost independent linear systems, each defined on one fracture of the network, and these fracture-local problems only need to share information at the interfaces. Thus, allowing for a natural parallel implementation with a high scalability potential.

The discrete counterpart, $\Psi(h^h, u^h, p^h)$, with $(h^h, u^h, p^h) \in \mathcal{H}^h, \mathcal{U}^h, \mathcal{P}^h$, is obtained by writing the three variables as linear combinations of the respective basis functions. Denoting with $\boldsymbol{h} = [h_1, ..., h_{n_h}]^T$, $\boldsymbol{u} = [u_1, ..., u_{n_u}]^T$ and $\boldsymbol{p} = [p_1, ..., p_{n_p}]^T$ the vectors collecting the components of these linear combinations, the final expression of the discrete function to be minimized reads:

$$\Psi(\boldsymbol{h}, \boldsymbol{u}, \boldsymbol{p}) = \begin{bmatrix} \boldsymbol{h} & \boldsymbol{u} \end{bmatrix}^T \begin{bmatrix} \boldsymbol{G}^h & -\alpha\boldsymbol{B} \\ -\alpha\boldsymbol{B}^T & \boldsymbol{G}^u \end{bmatrix} \begin{bmatrix} \boldsymbol{h} \\ \boldsymbol{u} \end{bmatrix} + \boldsymbol{p}^T(\boldsymbol{A}\boldsymbol{h} - \boldsymbol{C}\boldsymbol{u} - \boldsymbol{q}) \quad (3.97)$$

The reader is referred to Berrone et al. [2013] for a detailed description of this approach. Here, the focus is on the linearized algebraic problem that derives from such a formulation, which is a large size symmetric saddle-point matrix with a rank-deficient leading block. The algebraic problem resulting from the first order optimality conditions can

be stated as [Berrone et al., 2019]:

$$\begin{aligned} \boldsymbol{G}^h \boldsymbol{h} - \alpha \boldsymbol{B} \boldsymbol{u} + \boldsymbol{A}^T \boldsymbol{p} &= \boldsymbol{0}, \quad \text{(energy minimization)} \\ -\alpha \boldsymbol{B}^T \boldsymbol{h} + \boldsymbol{G}^u \boldsymbol{u} - \boldsymbol{C}^T \boldsymbol{p} &= \boldsymbol{0}, \quad \text{(energy minimization)} \\ \boldsymbol{A}\boldsymbol{h} - \boldsymbol{C}\boldsymbol{u} &= \boldsymbol{q}, \quad \text{(mass balance)} \end{aligned} \tag{3.98}$$

where $\boldsymbol{h} \in \mathbb{R}^{n_h}$ is the hydraulic head on the fractures, $\boldsymbol{u} \in \mathbb{R}^{n_u}$ is the flux on the traces, $\boldsymbol{p} \in \mathbb{R}^{n_p}$ is the Lagrange multiplier and $\boldsymbol{q} \in \mathbb{R}^{n_p}$ derives from the boundary conditions and the forcing terms. Usually, $n_p = n_h$, while according to the problem n_u can be either larger or smaller than n_h. The coefficient $\alpha \in \mathbb{R}$ is a user-specified positive parameter, usually on the order of 1. The matrices $\boldsymbol{G}^h \in \mathbb{R}^{n_h \times n_h}$, $\boldsymbol{A} \in \mathbb{R}^{n_h \times n_h}$ and $\boldsymbol{C} \in \mathbb{R}^{n_h \times n_u}$ are fracture-local, whereas $\boldsymbol{B} \in \mathbb{R}^{n_h \times n_u}$ and $\boldsymbol{G}^u \in \mathbb{R}^{n_u \times n_u}$ operate on degrees of freedom related to different fractures. Their properties can be summarized as follows:

- $\boldsymbol{G}^h$ and $\boldsymbol{G}^u$ are SPSD, usually rank-deficient;
- $\boldsymbol{B}$ and $\boldsymbol{C}$ are rectangular coupling blocks, whose entries are given by inner products between the basis functions of the main unknowns along the fracture traces;
- $\boldsymbol{A}$ is SPD with a block diagonal structure. Each diagonal block arises from the discretization of a $-\nabla \cdot (\hat{\boldsymbol{K}} \nabla)$ operator over a fracture, where $\hat{\boldsymbol{K}}$ is a proper diffusion tensor, hence inherits the usual structure of a 2-D discrete Laplacian. Block size depends on each fracture dimension and can significantly differ one from the other.

The system of Eqs. (3.98) can be written in a compact form as:

$$\begin{bmatrix} \boldsymbol{G}^h & -\alpha \boldsymbol{B} & \boldsymbol{A}^T \\ -\alpha \boldsymbol{B}^T & \boldsymbol{G}^u & -\boldsymbol{C}^T \\ \boldsymbol{A} & -\boldsymbol{C} & \boldsymbol{0} \end{bmatrix} \begin{pmatrix} \boldsymbol{h} \\ \boldsymbol{u} \\ \boldsymbol{p} \end{pmatrix} = \begin{pmatrix} \boldsymbol{0} \\ \boldsymbol{0} \\ \boldsymbol{q} \end{pmatrix} \quad \Rightarrow \quad \mathcal{Z}\boldsymbol{x} = \boldsymbol{f} \tag{3.99}$$

where $\mathcal{Z}$ is a symmetric saddle-point matrix with a rank-deficient leading block. The solution to such problems is required in several applications and is the object of a significant number of works. For a review on methods and ideas, see for instance Benzi

et al. [2005]. With an SPD leading block, as it often arises in Navier-Stokes equations, mixed finite element formulations of flow in porous media, poroelasticity, etc., an optimal preconditioner exists based on the approximation of the Schur complement matrix [Elman et al., 2005]. However, if the leading block is singular the problem is generally more difficult and the only available result is for the case of maximal rank deficiency [Estrin and Greif, 2015]. In the next paragraph, an ad-hoc preconditioner is presented.

3.4.3 Preconditioning framework

Matrix $\mathcal{Z}$ in Eq. (3.99) is a classical example of the discretization of a coupled multiphysics problem. Following the procedure presented in Section 3.2.3, a preconditioner $\mathcal{M}^{-1}$ can be defined from an algebraic viewpoint as an inexact block LDU factorization of the matrix $\mathcal{Z}$ conveniently permuted through the matrices $\mathcal{Q}_r$ and $\mathcal{Q}_c$. The permutation matrices are defined so that the leading blocks of $\mathcal{Z}$ are non singular, thus satisfying Theorem 1 of Ferronato et al. [2019]. The application of a row and column block permutation leads to the equivalent system:

$$\widetilde{\mathcal{Z}}\widetilde{\boldsymbol{x}} = \widetilde{\boldsymbol{f}}, \qquad \text{with} \qquad \widetilde{\mathcal{Z}} = \mathcal{Q}_r \mathcal{Z} \mathcal{Q}_c, \qquad \widetilde{\boldsymbol{x}} = \mathcal{Q}_c^T \boldsymbol{x}, \qquad \widetilde{\boldsymbol{f}} = \mathcal{Q}_r \boldsymbol{f}, \tag{3.100}$$

A possible choice for the permutation matrices is:

$$\mathcal{Q}_r = \begin{bmatrix} \mathbf{0} & \mathbf{0} & \boldsymbol{I}_h \\ \boldsymbol{I}_h & \mathbf{0} & \mathbf{0} \\ \mathbf{0} & \boldsymbol{I}_u & \mathbf{0} \end{bmatrix} \qquad \mathcal{Q}_c = \begin{bmatrix} \boldsymbol{I}_h & \mathbf{0} & \mathbf{0} \\ \mathbf{0} & \mathbf{0} & \boldsymbol{I}_h \\ \mathbf{0} & \boldsymbol{I}_u & \mathbf{0} \end{bmatrix} \tag{3.101}$$

where $\boldsymbol{I}_n$ is the identity matrix in $\mathbb{R}^{n_n \times n_n}$ and $\mathbf{0}$ the zero matrix of proper size, and such that the permuted system reads:

$$\widetilde{\mathcal{Z}} = \begin{bmatrix} \boldsymbol{A} & \mathbf{0} & -\boldsymbol{C} \\ \boldsymbol{G}^h & \boldsymbol{A} & -\alpha \boldsymbol{B} \\ -\alpha \boldsymbol{B}^T & -\boldsymbol{C}^T & \boldsymbol{G}^u \end{bmatrix} \qquad \widetilde{\boldsymbol{x}} = \begin{pmatrix} \boldsymbol{h} \\ \boldsymbol{p} \\ \boldsymbol{u} \end{pmatrix} \qquad \widetilde{\boldsymbol{f}} = \begin{pmatrix} \boldsymbol{q} \\ \mathbf{0} \\ \mathbf{0} \end{pmatrix} \tag{3.102}$$

The block LDU factorization of the matrix $\widetilde{\mathcal{Z}}$ in Eq. (3.100) reads:

$$\widetilde{\mathcal{Z}} = \mathcal{Q}_r \mathcal{Z} \mathcal{Q}_c = \mathcal{L}\mathcal{D}\mathcal{U} \tag{3.103}$$

with:

$$\begin{gathered}\mathcal{L} = \begin{bmatrix} \boldsymbol{I}_h & \boldsymbol{0} & \boldsymbol{0} \\ \boldsymbol{G}^h \boldsymbol{A}^{-1} & \boldsymbol{I}_h & \boldsymbol{0} \\ -\alpha \boldsymbol{B}^T \boldsymbol{A}^{-1} & -\boldsymbol{C}^T \boldsymbol{A}^{-1} & \boldsymbol{I}_u \end{bmatrix}, \quad \mathcal{D} = \begin{bmatrix} \boldsymbol{A} & \boldsymbol{0} & \boldsymbol{0} \\ \boldsymbol{0} & \boldsymbol{A} & \boldsymbol{0} \\ \boldsymbol{0} & \boldsymbol{0} & \boldsymbol{S} \end{bmatrix}, \\ \mathcal{U} = \begin{bmatrix} \boldsymbol{I}_h & \boldsymbol{0} & -\boldsymbol{A}^{-1}\boldsymbol{C} \\ \boldsymbol{0} & \boldsymbol{I}_h & \boldsymbol{A}^{-1}\left(-\alpha \boldsymbol{B} + \boldsymbol{G}^h \boldsymbol{A}^{-1} \boldsymbol{C}\right) \\ \boldsymbol{0} & \boldsymbol{0} & \boldsymbol{I}_u \end{bmatrix}\end{gathered} \tag{3.104}$$

The matrix $\boldsymbol{S}$ is the Schur complement of $\widetilde{\mathcal{Z}}$ computed with respect to the third block row:

$$\boldsymbol{S} = \boldsymbol{G}^u - \alpha \boldsymbol{B}^T \boldsymbol{A}^{-1} \boldsymbol{C} - \boldsymbol{C}^T \boldsymbol{A}^{-1} \left(\alpha \boldsymbol{B} - \boldsymbol{G}^h \boldsymbol{A}^{-1} \boldsymbol{C}\right) \tag{3.105}$$

Introducing the matrices $\boldsymbol{E} = \boldsymbol{B} - \boldsymbol{C}$ and $\boldsymbol{F} = \boldsymbol{A}^{-1}\boldsymbol{C}$, the Schur complement in Eq. (3.105) can be rewritten as:

$$\boldsymbol{S} = \boldsymbol{G}^u + \boldsymbol{F}^T \left(\boldsymbol{G}^h - 2\alpha \boldsymbol{A}\right) \boldsymbol{F} - \alpha \left(\boldsymbol{E}^T \boldsymbol{F} + \boldsymbol{F}^T \boldsymbol{E}\right) \tag{3.106}$$

The preconditioner $\mathcal{M}^{-1}$ can be expressed as:

$$\begin{aligned}\mathcal{M}^{-1} = &\begin{bmatrix} \boldsymbol{I}_h & \boldsymbol{0} & \boldsymbol{A}^{-1}\boldsymbol{C} \\ \boldsymbol{0} & \boldsymbol{I}_h & -\boldsymbol{A}^{-1}\left(-\alpha \boldsymbol{B} + \boldsymbol{G}^h \boldsymbol{A}^{-1} \boldsymbol{C}\right) \\ \boldsymbol{0} & \boldsymbol{0} & \boldsymbol{I}_u \end{bmatrix} \begin{bmatrix} \boldsymbol{A}^{-1} & \boldsymbol{0} & \boldsymbol{0} \\ \boldsymbol{0} & \boldsymbol{A}^{-1} & \boldsymbol{0} \\ \boldsymbol{0} & \boldsymbol{0} & \widetilde{\boldsymbol{S}}^{-1} \end{bmatrix} \cdot \\ &\cdot \begin{bmatrix} \boldsymbol{I}_h & \boldsymbol{0} & \boldsymbol{0} \\ -\boldsymbol{G}^h \boldsymbol{A}^{-1} & \boldsymbol{I}_h & \boldsymbol{0} \\ \left(\alpha \boldsymbol{B}^T - \boldsymbol{C}^T \boldsymbol{A}^{-1} \boldsymbol{G}^h\right) \boldsymbol{A}^{-1} & \boldsymbol{C}^T \boldsymbol{A}^{-1} & \boldsymbol{I}_u \end{bmatrix}\end{aligned} \tag{3.107}$$

where $\widetilde{\boldsymbol{S}}^{-1}$ is a proper approximation of the inverse of the Schur complement. Indeed, as already stated before, the preconditioner cannot be computed explicitly in large-size applications. Thus, the LDU factorization is used to build an inexact application of the preconditioner. In this case, since $\boldsymbol{A}$ is an SPD matrix with the classic Laplacian structure, it is possible to efficiently apply its inverse. The crucial point for an efficient and robust preconditioner is the approximation of the Schur complement $\widetilde{\boldsymbol{S}}$.

In order to evaluate the effectiveness of the Schur complement approximation, system (3.102) has been projected onto the flux space:

$$\boldsymbol{S}\boldsymbol{u} = \boldsymbol{b} \quad \text{with} \quad \boldsymbol{b} = \left(\alpha \boldsymbol{B}^T - \boldsymbol{F}^T \boldsymbol{G}^h\right) \boldsymbol{A}^{-1} \boldsymbol{q} \tag{3.108}$$

Applications of increasing size are tested in the next paragraph to investigate different Schur complement approximations.

3.4.4 Numerical results

Four problems of increasing size and complexity have been analyzed (Table 3.11). The smallest problem, $\mathrm{P_A}$, is a simple domain with 4 fractures, whereas the biggest case, $\mathrm{P_D}$, includes almost 400 fractures of different sizes. Fig. 3.21 shows the mesh domain for the case $\mathrm{P_C}$.

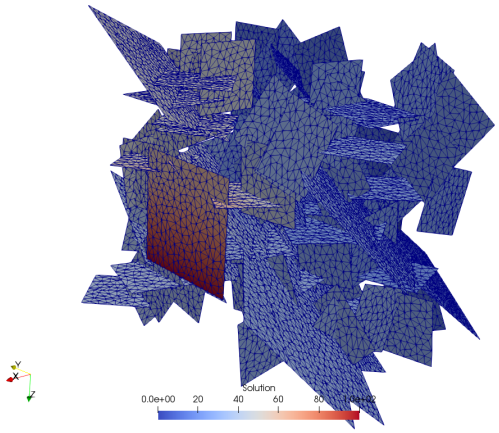

FIGURE 3.21: 3D mesh domain for the case $\mathrm{P_C}$.

TABLE 3.11: Problem size.

	$\mathrm{P_A}$	$\mathrm{P_B}$	$\mathrm{P_C}$	$\mathrm{P_D}$
n_h	787	13,732	39,288	93,768
n_u	206	5,085	8,219	18,276
N	1,780	32,549	86,795	205,812

The non-zero pattern of the matrices of the smallest problem is shown in Fig. 3.22. Matrices $\boldsymbol{A}$, $\boldsymbol{C}$ and $\boldsymbol{G}^h$ are block diagonal. Being each block related to a fracture, these matrices are fracture-local. Instead, matrices $\boldsymbol{B}$ and $\boldsymbol{G}^u$ connect degrees of freedom related to different fractures. In particular, matrix $\boldsymbol{B}$ is made by the same diagonal blocks as $\boldsymbol{C}$ with additional extra-diagonal terms corresponding to intersections between fractures. Thus, the matrix $\boldsymbol{E} = \boldsymbol{B} - \boldsymbol{C}$ is zero on the diagonal blocks and contains the same terms as $\boldsymbol{B}$ outside. Matrix $\boldsymbol{F}$, being defined as $\boldsymbol{A}^{-1}\boldsymbol{C}$, is also block diagonal, with the same size and structure of $\boldsymbol{C}$.

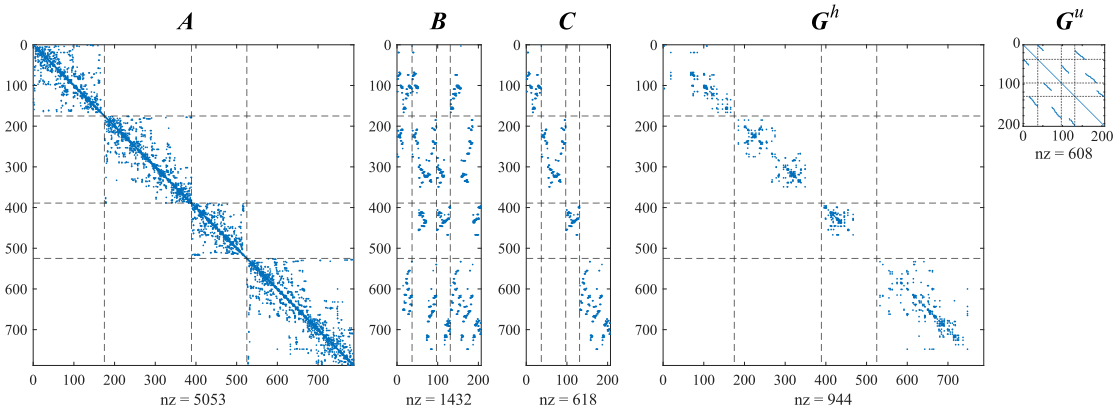

FIGURE 3.22: Structure and number of non-zeros (nz) of the sub-block matrices for case P_A.

On the basis of these considerations, the Schur complement in Eq. (3.106) can be written as:

$$\boldsymbol{S} = \boldsymbol{S}_D - \boldsymbol{S}_E \tag{3.109}$$

where $\boldsymbol{S}_D = \boldsymbol{G}^u + \boldsymbol{F}^T \left(\boldsymbol{G}^h - 2\alpha \boldsymbol{A}\right) \boldsymbol{F}$ and $\boldsymbol{S}_E = \alpha \left(\boldsymbol{E}^T \boldsymbol{F} + \boldsymbol{F}^T \boldsymbol{E}\right)$. Matrix $\boldsymbol{S}_D$ contains the diagonal blocks of $\boldsymbol{S}$ and $\boldsymbol{S}_E$ the off-diagonal part. Therefore, $\boldsymbol{S}_D$ is SPD, whereas $\boldsymbol{S}_E$ is indefinite.

A key property for $\boldsymbol{S}$ is being SPD. It is therefore natural to consider $\hat{\boldsymbol{S}} = \boldsymbol{S}_D$, that is the block diagonal and positive definite part. The results in terms of number of iterations (iter), ratio between the non-zeros of the approximate Schur complement and the exact one (μ) and the conditioning number (κ) are reported in Table 3.12. Despite the preconditioning, the number of iterations required to solve the system is still high and the conditioning number of the preconditioned matrix is not very different from the original one.

TABLE 3.12: Results considering the approximation $\hat{\boldsymbol{S}} = \boldsymbol{S}_D$. The $*$ indicates that the problem does not converge, with the residual stagnating around 10^{-5}.

Case	iter	μ	$\kappa\left(\hat{S}_3^{-1} S_3\right)$	$\kappa\left(S_3\right)$
P_A	125	0.3921	3.10e+04	1.67e+04
P_B	300	0.3958	2.08e+06	4.90e+05
P_C	$*$	0.3619	1.40e+08	1.72e+09
P_D	957	0.3594	7.39e+06	1.15e+09

Approximating $\boldsymbol{S}$ with its diagonal blocks appears to be not enough for an efficient solution of the system. Thus, from here on also the off-diagonal part is taken into

account. Aiming at understanding the importance of the single blocks of $\boldsymbol{S}$ as a preconditioner, the two contributions $\boldsymbol{S}_D$ and $\boldsymbol{S}_E$ are filtered separately, naming $\hat{\boldsymbol{S}}_D$ and $\hat{\boldsymbol{S}}_E$ their approximation. First, only the extra-diagonal part of $\boldsymbol{S}$ is approximated:

$$\hat{\boldsymbol{S}} = \boldsymbol{S}_D - \hat{\boldsymbol{S}}_E \tag{3.110}$$

where $\hat{\boldsymbol{S}}_E$ is obtained by filtering each column j of the product $\boldsymbol{E}^T\boldsymbol{F}$ neglecting the entries such that:

$$\left|\left(\boldsymbol{E}^T\boldsymbol{F}\right)_{ij}\right| < \tau \left\|\left(\boldsymbol{E}^T\boldsymbol{F}\right)_j\right\|_2 \tag{3.111}$$

Results for different values of τ are reported in Table 3.13.

TABLE 3.13: Results computing $\boldsymbol{S}$ with the sparsified $\boldsymbol{S}_E$. The * indicates the case when $\hat{\boldsymbol{S}}$ becomes indefinite.

τ	case P_A			case P_B		
	iter	μ	$\kappa\left(\hat{S}_3^{-1}S_3\right)$	iter	μ	$\kappa\left(\hat{S}_3^{-1}S_3\right)$
5×10^{-2}	*	0.8306	5.47e+03	*	0.4747	6.41e+08
10^{-2}	8	0.9398	1.79e+02	26	0.6171	5.07e+06
	case P_C			case P_D		
10^{-2}	*	0.9577	3.26e+09	*	0.8056	4.68e+07
10^{-3}	7	0.9950	2.28e+04	*	0.9742	3.44e+10

Finally, we consider the preconditioner $\hat{\boldsymbol{S}}$:

$$\hat{\boldsymbol{S}} = \hat{\boldsymbol{S}}_D - \boldsymbol{S}_E \tag{3.112}$$

where the extra-diagonal blocks are computed exactly, while the diagonal ones are approximated neglecting the entries s_{ij} of the product $\boldsymbol{F}^T\left(\boldsymbol{G}^h - 2\alpha\boldsymbol{A}\right)\boldsymbol{F}$ such that:

$$|s_{ij}| < \tau\sqrt{|s_{ii}\ s_{jj}|} \tag{3.113}$$

Results for the four matrices are reported in Table 3.14.

In both cases, i.e., when approximating only $\boldsymbol{S}_E$ or $\boldsymbol{S}_D$, the level of fill-in of $\hat{\boldsymbol{S}}$ required to reach convergence is close to one, i.e., $\hat{\boldsymbol{S}}$ tends to be the exact Schur complement ($\mu = 1$). This is because $\hat{\boldsymbol{S}}$ can easily become indefinite after the filtering. As an example, in Fig. 3.23, the ten smallest eigenvalues of the exact and the approximated

TABLE 3.14: Results computing $\boldsymbol{S}$ after the sparsification of $\boldsymbol{S}_D$. The * indicates the case when $\hat{\boldsymbol{S}}$ becomes indefinite.

τ	case P_A			case P_B		
	iter	μ	$\kappa\left(\hat{S}_3^{-1}S_3\right)$	iter	μ	$\kappa\left(\hat{S}_3^{-1}S_3\right)$
5×10^{-1}	*	0.6604	1.47e+04	*	0.6114	3.51e+08
10^{-1}	10	0.9217	1.99e+03	*	0.6351	4.62e+07
10^{-2}	3	0.9910	2.99e+00	*	0.8902	1.84e+05
10^{-3}	2	0.9987	1.06e+00	*	0.9925	2.33e+04
	case P_C			case P_D		
10^{-2}	*	0.9928	2.34e+04	*	0.9851	4.39e+05
10^{-3}	2	0.9993	2.47e+01	2	0.9987	6.88e+01

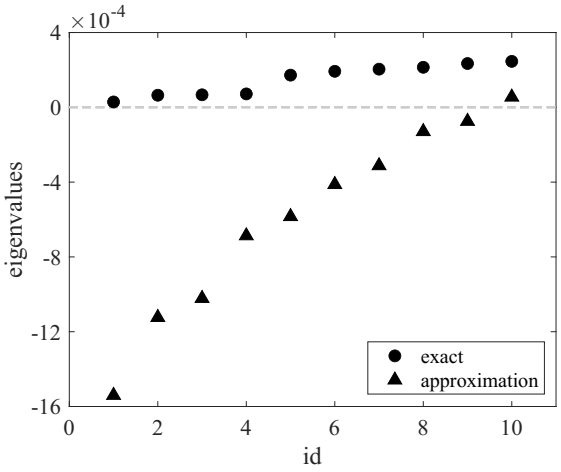

FIGURE 3.23: Case P_A: ten smallest eigenvalues of $\boldsymbol{S}$ and $\hat{\boldsymbol{S}}$ computed through Eq. (3.112) with $\tau = 5\times10^{-1}$.

(with τ equal to 5×10^{-1}) Schur complement for the case P_A are shown. While $\boldsymbol{S}$ is positive definite, the eigenvalues of $\hat{\boldsymbol{S}}$ are both positive and negative.

In the last test, the preconditioner is computed approximating both $\boldsymbol{S}_D$ and $\boldsymbol{S}_E$:

$$\hat{\boldsymbol{S}} = \hat{\boldsymbol{S}}_D - \hat{\boldsymbol{S}}_E \tag{3.114}$$

To this aim, a sparsified $\boldsymbol{F}$ is computed by filtering the smallest entries. Since $\boldsymbol{F}$ is block diagonal, it can be efficiently computed in a parallel computational environment exploiting a Cholesky factorization of the blocks of $\boldsymbol{A}$. A relative drop tolerance is used, removing the entries such that:

$$|F_{ij}| < \tau \left\|F_j\right\|_2 \tag{3.115}$$

The numerical results are reported in Table 3.15. The iterations count decreases significantly with respect to Table 3.12, with densities that are even smaller than those obtained keeping $\boldsymbol{S}_D$ only. However, in difficult problems, such as $\mathrm{P_C}$, quite a large fill-in is required and the performance can become very sensitive to the τ selection.

TABLE 3.15: Results computing $\hat{\boldsymbol{S}}$ with the approximation of $\boldsymbol{F}$ as in Eq. (3.115).

τ	case $\mathrm{P_A}$			case $\mathrm{P_B}$		
	iter	μ	$\kappa\left(\hat{S}_3^{-1}S_3\right)$	iter	μ	$\kappa\left(\hat{S}_3^{-1}S_3\right)$
10^{-1}	28	0.2697	3.75e+04	136	0.1226	1.88e+07
5×10^{-2}	19	0.8595	5.85e+04	57	0.2508	1.45e+07
10^{-2}	1	1.0000	1	17	0.6072	1.48e+06
	case $\mathrm{P_C}$			case $\mathrm{P_D}$		
5×10^{-2}	1483	0.5400	1.08e+11	445	0.3196	1.06e+09
2.5×10^{-2}	8	0.9952	1.64e+06	128	0.5663	8.89e+07
10^{-2}	4	0.9990	3.38e+04	41	0.8100	1.57e+07
10^{-3}	1	1.0000	1	5	0.9912	1.10e+05

Considering as a preconditioner an approximation $\hat{\boldsymbol{S}}$ obtained by filtering $\boldsymbol{S}$ or its entries can be efficient (as results in Table 3.15 demonstrate), but also quite fragile because of the possible indefiniteness of the approximation (see Table 3.13 and Table 3.14).

3.4.5 Discussion

A symmetric saddle-point matrix with a rank-deficient leading block arises from the combination of DFN models with an appropriate optimization formulation. Here, the focus is on the acceleration of the iterative solution of this linear system with a block preconditioning technique. First, an appropriate permutation of the matrix is performed and then a projection onto the flux space is computed obtaining a Schur complement. Since this proves to be the key factor for an effective preconditioner, different approaches for its approximation have been investigated. Both the diagonal and off-diagonal blocks of the Schur complement are fundamental for an efficient solution of the system. Independent filterings of such components reveal the fragility of the approximated Schur complement, that can easily become indefinite. When the filter step regards the matrix $\boldsymbol{F}$, before the computation of the Schur complement, results are more promising. This suggests to investigate new filtering approaches for $\boldsymbol{F}$, aiming at finding a more robust and less τ-dependent solution.

Comparing the investigated approaches, it can be noted that the iterations number does not vary according to the conditioning number, as one can expect. This can be related to the distribution of the eigenvalues, which means that the eigenspectrum is mainly clustered, but there are few outliers. In order to fix this problem, a deflation approach can be used to remove the eigenvectors related to the extreme eigenvalues. This technique requires an a-priori knowledge of these eigenvalues, that can be quite computationally expensive, but reasonable in an iterative framework.

Chapter 4

A methodological approach for DA in geomechanics

4.1 Introduction

Surface movements can be induced by many energy-related human activities, such as the production of natural gas, geothermal heat extraction, ground water exploitation or hydrocarbon storage [Zoback, 2007]. Here, the focus is on land subsidence induced by hydrocarbon extraction, which is one of the main anthropogenic causes of land subsidence [Gambolati et al., 2006]. Fluid withdrawal from the subsurface produces a decrease in the reservoir pressure, thus leading to the compaction of the reservoir rock which can propagate from the underground up to the land surface inducing land subsidence. The consequences of this phenomenon for the environment and for human activities may be non-negligible, see e.g. van Thienen Visser et al. [2015], Simeoni et al. [2017] and Dinar et al. [2021]. Consequently, a proper modeling of the deep reservoir geomechanics is of fundamental importance for both the energy companies and the control agencies. In this context, the use of all the available measurements takes on a central role in the monitoring and forecasting phases [Bernardi et al., 2021].

A traditional procedure to study land subsidence consists on the definition of a number of deterministic scenarios as input for a numerical model whose outcomes are combined to determine confidence intervals. One of the principal drawbacks of this deterministic approach is that it does not allow to properly account for the uncertainties that unavoidably affect the modeling of real-world phenomena. Indeed, the numerical model itself is by definition built on top of number of approximations, despite its

accuracy and reliability. Moreover, other sources of errors and uncertainties may arise, for example from the imposition of initial and boundary conditions, the definition of the external forces and the parameter characterization. Instead of deterministic analyses, which can induce an excessive confidence in the solution, stochastic approaches should be preferred since they allow to maintain a certain range of uncertainty on the outcomes. A second drawback of the traditional methodology is that it does not take full advantages from the increasing availability of monitoring data during the life span of the reservoir.

Given these issues, it becomes natural to consider Data Assimilation (DA) methods to improve the quality of the prediction. DA combines prior information from numerical model simulations with observed data to obtain the best possible description of a dynamical system and its uncertainty. The purpose of using DA is often to compute the best possible estimate of the model state or of the model parameters, so as to infer the best characterization of the model [Evensen et al., 2022]. DA was originally used in the field of weather prediction and operational oceanography, and later broaden to many other fields, such as geosciences, medicine, economy and physics. Over the last 30 years, several techniques have been developed, ranging from simple approaches to advanced methodologies. However, a common mathematical basis can be derived from Bayesian inference, control theory, and variational calculus. In the literature there are many books and review papers that derive e compare the main DA techniques; the reader can refer for example to Evensen [2009], Carrassi et al. [2018], Jung et al. [2018] and Evensen et al. [2022]. Ensemble-based methodologies are generally preferred by the Earth science community (e.g. in Zoccarato et al. [2016] and Jha et al. [2015]) since these techniques allow to consider a wide parameter space at reasonable computational cost [Emerick, 2016]. These approaches belong to the general class of so-called particle methods which use a Monte Carlo (MC) or ensemble representation for the Probability Density Function (PDF), an ensemble integration using stochastic models to simulate the time evolution of the PDFs, and different schemes for conditioning the predicted PDFs given the observations [Evensen, 2009]. Here, *ensemble* implies that multiple subsidence realizations are built based on the possible choices of processes and subsurface parameters.

A comprehensive methodological approach is presented herein with the aim at combining advanced numerical models with different measurements. It uses DA to integrate the available observations into the numerical model, so as to improve the subsidence prediction over deep reservoirs. This original methodology has been published in Gazzola et al. [2021]. In brief, after the identification of the sources of uncertainties and the creation of the forecast ensembles, the χ^2-test, the Red Flag (RF) and the Ensemble Smoother (ES) techniques are performed in time to progressively update the overall geomechanical reservoir model. The first two methods are used for a preliminary qualitative evaluation of the forecast ensembles, while ES provides an update of both the model states and parameters, as will be extensively discussed later on in this Chapter. These techniques have been already separately used for a number of underground applications, like hydrology and geomechanics engineering. The reader can refer to Fokker et al. [2016], Kang and Choe [2017] and Oliver and Alfonzo [2018], just to cite a few.

Several DA methods have been developed for the update of the model and the solution of the inverse problem. Among the others, Ensemble Kalman Filter (EnKF) and ES are the most used in the reservoir-engineering community. EnKF has been firstly proposed by Evensen [1994] based on the Kalman filter [Kalman, 1960]. Skjervheim et al. [2011] introduced ES as an alternative to EnKF for history-matching reservoir models. The main difference is that ES computes a global update in the space-time domain rather than using recursive updates in time as EnKF does. ES demonstrated to be the preferred choice in the petroleum community [Evensen and Eikrem, 2018]. The main disadvantages of EnKF are: (i) the computational time required for the sequential updates; (ii) the possible nonphysical update of the parameters in case of nonlinear relations, and (iii) the need to assume that the observations are independent in time.

ES has been also used in a few specific applications in the field of land subsidence prediction, e.g., Baù et al. [2015], Jha et al. [2015] and Zoccarato et al. [2020]. The workflow presented herein is not a mere application of DA techniques which were already available in the literature, rather the definition of a step-by-step procedure which can support the decision making process and the management of the field by training the reservoir model in time using all the available measurements.

Only recently, Candela et al. [2022] propose another integrated approach targeted to optimize the Dutch subsidence forecasting caused by gas production. Their framework combines ES and a 3D geological subsurface model of the Netherlands to discriminate which reservoir rock compaction model is activated at depth and to reduce uncertainty on subsidence prediction.

First, this Chapter provides a global overview of the workflow and its possible uses, then each of the steps included in the methodology are described in detail.

4.2 Overview of the methodological approach

A sketch of the methodological approach is graphically depicted in Fig. 4.1.

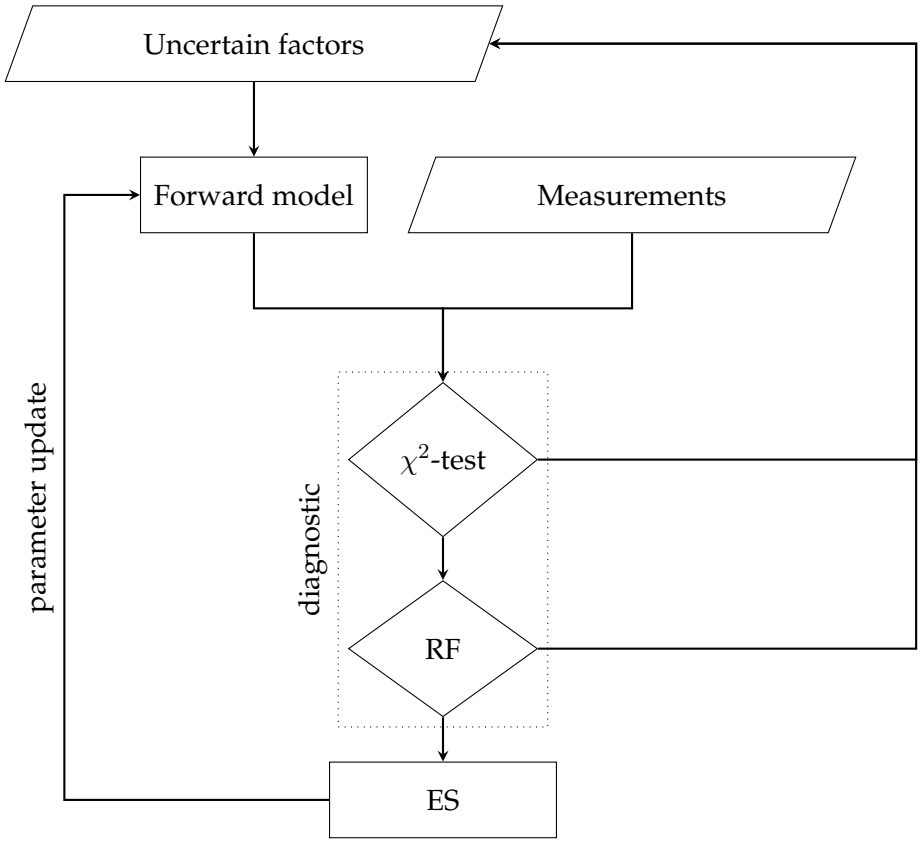

FIGURE 4.1: Flowchart of the methodological approach.

The first crucial step of the workflow is the identification of the *uncertain factors*. Several sources of uncertainty can affect the modelling process, especially at the beginning of a study when only few pieces of information are available. In a land subsidence analysis, uncertainties can be related for instance to the geometry and the lithology of

the porous medium, the variation and distribution of the pore pressure, the mechanical behavior of the deforming rock and the variability ranges of the main mechanical parameters. Among all the uncertainties, it is essential to recognize the most influential ones. Moreover, only the factors that can be explicitly included as input of the simulation model can be taken into account. An exaggerated number of uncertain factors or considering parameters with a weak impact on the model solution can in both cases limit the measurements constraint of the model. A preliminary sensitivity analysis can help in defining the main sources of uncertainty.

Once the uncertain factors are identified, a *forward model* is used to propagate the input uncertainties to the output, by the generation of a group of forecast ensembles by means of MC realizations. The outcomes of the model are generally called states and are the quantities that can be directly compared with the available measurements. Here, the geomechanical model described in Section 4.4 is used. However, the overall methodological approach investigated herein is independent of the specific forward model and can be easily adapted to others.

Once the ensembles are created, the *measurements* are integrated into the model and used to reduce the uncertainties thanks to DA. All the available measurements on the field can be used, avoiding a redundancy of information that can be detrimental for the DA update. In land subsidence applications, measurements of shallow and deep movements are generally available. The measurements are integrated periodically in time according to their availability, in order to dynamically improve the model prediction by a progressive reduction of the uncertainties and an increase of the model reliability.

First, the measurements are used for the *diagnostic* step, i.e. for a preliminary evaluation of the ensembles by means of the χ^2*-test* and the *RF*. These techniques are based on the mismatch between the measurements and the model (more details are provided in Section 4.6.1) and can help in identifying the suitability of the ensembles for the successive update of the model. According to the outcomes of the diagnostic steps, the forecast ensembles can proceed to the final update of the model, or can be discarded, meaning that the initial hypotheses on the uncertain factors are revised and new forecast ensembles are created and evaluated.

The final step consists in the *ES* application that provides a simultaneous update of both the states and the parameters ensembles. The update of the states represents the improved model prediction, that has been constrained with the available observations. The update of the parameters is used as input for the forward model to create the new ensembles when new measurements become available and the DA procedure can be repeated. Mathematical details on ES are provided in Section 4.6.2.

4.3 Identification of the sources of uncertainties

Several sources of uncertainties can affect the analyses of land subsidence over a hydrocarbon reservoir. Uncertainties are commonly linked to the knowledge of the constitutive rock behavior, the geometry of the depleted formations and the diffusion of the pressure perturbation. The identification of the most significant sources of uncertainty is tightly related to the specific field object of analysis. A major role is performed by the experience and expertise of the operators, who can establish the most critical factors. In geomechanical problems, the main uncertainties are generally related to the nature and value of the governing parameters for the constitutive behavior of the reservoir rock, i.e. to the definition of the operator $\hat{\mathbf{D}}$ of Eq. (2.13). As a matter of fact, the mechanics-to-flow coupling is usually weak in the context of real-world oil and gas reservoir engineering applications [Gambolati et al., 2000; Wang, 2000b; Pearse et al., 2014], since the gas compressibility is orders of magnitude higher than the rock compressibility. Considering also the large amount of pressure data generally available from in-situ wells, which usually allows a well-developed history-matching process, the uncertainties linked to the pressure field can be assumed to be negligible as compared with those related to the reservoir geomechanics.

The operator $\hat{\mathbf{D}}$, that is generally non-linear, is chosen according to the characteristics of the porous medium, but this selection is usually a source of uncertainty since it depends on the availability of tests, the geological nature of the basin, and previous experiences, that can be limited. Moreover, while the behavior of the overburden and underburden does not significantly affect the surface movements, the constitutive law chosen for the active layers, i.e., aquifer and reservoir, highly impacts on the model

outcome [Ferronato et al., 2010; Teatini et al., 2011]. In the following applications, two different non-linear constitutive laws have been considered: (i) the modified Cam Clay (MCC) [De Souza Neto et al., 2008] and (ii) the visco-elasto-plastic (VEP) model [Vermeer and Neher, 1999]. These laws have proven to be suitable for land subsidence analyses [Gemelli et al., 2020]. More details on their characteristics are given in Section 2.3.

Laboratory and field experiments can help defining the importance of the geomechanical parameters and their range of variability. A sensitivity analysis can be performed in order to establish the influence of the input parameters on the model outcomes, thus it can help in identifying which parameters should be treated as uncertain variables. Sobol' indices can be computed to carry out a global sensitivity analysis. In the following, the basic idea behind Sobol' indices is provided. For completeness, the reader is referred to the work of Sobol' [1990] or to the application developed in Zoccarato et al. [2019].

For the sake of simplicity, let us consider the model outcome ψ, i.e., the quantity of interest, as a one-dimensional variable function f of the n-variate random vector $\boldsymbol{Z} = (Z_1, Z_2, \dots, Z_n)$ of mutually independent components defined over an n - dimensional hypercube Σ^n. Assuming f to be a square-integrable function, the functional decomposition of $\psi = f(\boldsymbol{Z})$ reads

$$f = f_0 + \sum_{i=1}^{n} f_i + \sum_{i=1}^{n} \sum_{j>i}^{n} f_{i,j} + \cdots + f_{1,2,\dots,n} \tag{4.1}$$

where f_0 is a constant representing the mean value of f, and f_i, $f_{i,j}$, $\dots$, $f_{1,2,\dots,n}$ are the uncorrelated random effects associated to the factors in their indices, e.g., $f_i = f_i(Z_i)$ are the main effects due to the factors Z_i and $f_{i,j} = f_{i,j}(Z_i, Z_j)$ are the effects related to interactions between the factors Z_i and Z_j with $j > i$. It has been proved in Sobol' [1990] that a unique expansion of Eq. (4.1) exists for any function $f(\boldsymbol{Z})$ integrable in Σ^n under the hypothesis of zero mean of all expansion terms with respect to each variable. The expansion (4.1) for the quantity of interest ψ is used to derive the associated variance $V(\psi)$. In fact, squaring Eq. (4.1) and using the orthogonality condition holding

for the expansion terms [Sobol', 1990], it can be demonstrated that $V(\psi)$ reads:

$$V(\psi) = \sum_{i=1}^{n} V_i + \sum_{i=1}^{n}\sum_{j>i}^{n} V_{i,j} + \cdots + V_{1,2,\ldots,n} \tag{4.2}$$

where $V_i, V_j, \ldots, V_{1,2,\ldots,n}$ are the partial variances of $f_i, f_j, \ldots, f_{1,2,\ldots,n}$, respectively. Generally, the partial variance $V_{i_1,\ldots,i_s}$ in Eq. (4.2) reads:

$$V_{i_1,\ldots,i_s} = \int_{\Sigma^s} f^2_{i_1,\ldots,i_s}(Z_{i_1},\ldots,Z_{i_s}) d(Z_{i_1},\ldots,Z_{i_s}) \tag{4.3}$$

which can be written in terms of conditional expectations as:

$$\begin{aligned}
V_i &= V(\mathbb{E}(\psi|Z_i)) \\
V_{i,j} &= V(\mathbb{E}(\psi|Z_i,Z_j)) - V_i - V_j \\
V_{i,j,k} &= V(\mathbb{E}(\psi|Z_i,Z_j,Z_k)) - V_i - V_j - V_k - V_{i,j} - V_{i,k} - V_{j,k} \\
&\vdots \\
V_{1,\ldots,n} &= V(\psi) - \sum_{i=1}^{n} V_i - \sum_{i=1}^{n}\sum_{j>i}^{n} V_{i,j} - \ldots - \sum_{1\le i_1<\cdots<i_{n-1}\le n}^{n} V_{i_1,\ldots,i_{n-1}}
\end{aligned} \tag{4.4}$$

Eqs. (4.4) provide practical relationships for the computation of partial variances for any indices combination. The Sobol' first and higher-order indices are defined as:

$$S_i = \frac{V_i(\psi)}{V(\psi)} \tag{4.5}$$

$$S_{1,\ldots,s} = \frac{V_{1,\ldots,s}(\psi)}{V(\psi)} \tag{4.6}$$

where S_i measures the relative importance of a single factor Z_i on the total model variance and the higher-order indices $S_{1,\ldots,s}$ represent a measure of the combined model sensitivity to the group of factors $Z_1,\ldots,Z_s$. The total effects $S_{T,i}$ are also computed to quantify the contribution of the i-th factor to the total output variation as [Saltelli et al., 2007]:

$$S_{T,i} = 1 - \frac{V(\mathbb{E}(\psi|\boldsymbol{Z}_{\sim i}))}{V(\psi)} \tag{4.7}$$

where $V(\mathbb{E}(\psi|\boldsymbol{Z}_{\sim i}))/V(\psi)$ includes first and higher-order interactions of all factors except Z_i.

4.4 Forward model

The forward model is used to propagate the input uncertainties to the output and create a set of ensembles of MC realizations. Herein, for the simulation of land subsidence, a model based on a one-way coupled approach is considered. As discussed in Section 2.5, this means that the outcomes of a flow model in terms of pressure distribution in time and space are used as input for a geomechanical model at each time step. This approach is fully justified for the time and space scale of interest [Gambolati et al., 2000; Pearse et al., 2014] and has been widely used in the past to study land subsidence, e.g., Baú et al. [2001] and Teatini et al. [2006], without an appreciable detrimental effect for the model accuracy.

The overall workflow is independent from the forward model, the choice of the solution approach and the discretization methods. In the following, the specific models that will be used for the applications of Chapter 5 are presented.

4.4.1 Geomechanical FEM simulator

The geomechanical model solves the balance of linear momentum, i.e., Eq. (2.11), here recalled for the sake of clarity:

$$-\nabla \cdot \widehat{\boldsymbol{\sigma}} = \boldsymbol{F}_V \tag{4.8}$$

As common in reservoir problems, the following hypotheses are considered: (i) quasi-static conditions; (ii) infinitesimal strains and (iii) negligible variation of body forces. Thus, Eq. (4.8) becomes:

$$-\nabla \cdot \hat{\boldsymbol{\sigma}} = 0 \tag{4.9}$$

Considering Terzaghi's principle (2.1), Eq. (4.9) can be rewritten as:

$$-\nabla \cdot (\boldsymbol{\sigma} - \alpha_B p \boldsymbol{i}) = 0 \tag{4.10}$$

where the effective stress tensor $\boldsymbol{\sigma}$ can be written as function of the displacements $\boldsymbol{u}$, which are now the only unknown:

$$-\nabla \cdot \left(\hat{\mathbf{D}} : \nabla^s \boldsymbol{u}\right) - \alpha_B \nabla p = 0 \tag{4.11}$$

A classical way to address the solution of Eq. (4.11) uses the Virtual Work Principle [Zienkiewicz et al., 2000], which means equaling the internal δW_{int} and the external δW_{ext} virtual work:

$$\int_\Omega \delta\boldsymbol{\varepsilon}^T \left(\hat{\mathbf{D}} : \nabla^s \boldsymbol{u}\right) dV = -\alpha_B \int_\Omega \delta \boldsymbol{u}^T \nabla p dV + \int_{\partial\Omega} \delta \boldsymbol{u}^T \boldsymbol{F}_S dS \tag{4.12}$$

where Ω is the continuum domain and $\partial\Omega$ its boundary, $\boldsymbol{F}_S$ is the vector of the surface forces as defined in Eq. (2.12), and $\boldsymbol{\varepsilon}$ the strain tensor, which can be written according to the small strain hypothesis as in Eq. (2.14). Thus, Eq. (4.12) becomes:

$$\int_\Omega \delta\nabla^s \boldsymbol{u}^T \left(\hat{\mathbf{D}} : \nabla^s \boldsymbol{u}\right) dV = -\alpha_B \int_\Omega \delta \boldsymbol{u}^T \nabla p dV + \int_{\partial\Omega} \delta \boldsymbol{u}^T \boldsymbol{F}_S dS \tag{4.13}$$

Eq. (4.13) can be solved in the framework of the FEM [Zienkiewicz et al., 2000]. The displacement $\boldsymbol{u}$ is approximated by the function $\boldsymbol{u}^h$:

$$\boldsymbol{u}^h \in \mathcal{S}^h = span\{\boldsymbol{\xi}_1, \boldsymbol{\xi}_2, ...\boldsymbol{\xi}_n, \} \tag{4.14}$$

where $\mathcal{S}^h$ is the finite Hilbert function space generated by the piece-wise polynomials $\boldsymbol{\xi}_i$, $i = 1, ..., n_\Omega$, with n_Ω the number of FE nodes in Ω. The polynomials $\boldsymbol{\xi}_i$ can be written as:

$$\boldsymbol{\xi}_i = \xi_i \begin{vmatrix} 1 & 0 & 0 \\ 0 & 1 & 0 \\ 0 & 0 & 1 \end{vmatrix} \equiv \boldsymbol{N}_i \tag{4.15}$$

Thus, the approximate solution $\boldsymbol{u}^h$ is:

$$\boldsymbol{u}^h = \boldsymbol{N}\boldsymbol{u} \tag{4.16}$$

where $\boldsymbol{u}$ is the array of the displacement nodal values. Introducing the matrix $\boldsymbol{B} = \boldsymbol{L}\boldsymbol{N}$, where $\boldsymbol{L}$ is the differential operator in Voigt notation

$$\boldsymbol{L} = \begin{bmatrix} \frac{\partial}{\partial x} & 0 & 0 \\ 0 & \frac{\partial}{\partial y} & 0 \\ 0 & 0 & \frac{\partial}{\partial z} \\ \frac{\partial}{\partial y} & \frac{\partial}{\partial x} & 0 \\ 0 & \frac{\partial}{\partial z} & \frac{\partial}{\partial y} \\ \frac{\partial}{\partial z} & 0 & \frac{\partial}{\partial x} \end{bmatrix}$$

Eq. (4.13) can be written in a compact form as:

$$\int_{\Omega} \delta \boldsymbol{u}^T \boldsymbol{B}^T \left(\hat{\mathbf{D}} \boldsymbol{B} \boldsymbol{u} \right) dV = -\alpha_B \int_{\Omega} \delta \boldsymbol{u}^T \boldsymbol{N}^T \nabla p \, dV + \int_{\partial\Omega} \delta \boldsymbol{u}^T \boldsymbol{N}^T \boldsymbol{F}_S dS \tag{4.17}$$

which must hold for any virtual displacement compatible with the constraints. Thus, the final governing equation which is solved by the geomechanical simulator is:

$$\int_{\Omega} \boldsymbol{B}^T \left(\hat{\mathbf{D}} \boldsymbol{B} \boldsymbol{u} \right) dV = -\alpha_B \int_{\Omega} \boldsymbol{N}^T \nabla p \, dV + \int_{\partial\Omega} \boldsymbol{N}^T \boldsymbol{F}_S dS \tag{4.18}$$

The geomechanical simulator which solves the system (4.18) used in the applications described in Chapter 5 is the one implemented as in Janna et al. [2012a], Spiezia et al. [2017] and Isotton et al. [2019].

4.4.2 Surrogate model

When dealing with large-scale real-world problems, running a FEM code multiple times to create many MC ensembles can become unaffordable, both in terms of CPU and memory requirements. In this context, surrogate models can help.

Here, the Generalized Polynomial Chaos Expansion (gPCE) approach [Wiener, 1938; Ghanem and Spanos, 1991; Xiu and Karniadakis, 2002; Najm, 2009] is used to approximate the model presented in Section 4.4.1. The basic idea behind gPCE is the use of orthogonal polynomial approximations of the random input to project the stochastic model output. In the following, the general mathematical framework is reported,

however more details can be found in Xiu [2007].

The model outcome ψ can be written as a function $\psi = \psi\left(\boldsymbol{Z}, \mathcal{F}_Z(z_1, \ldots, z_n)\right)$ of the random vector of mutually independent components $\boldsymbol{Z} = (Z_1, Z_2, \ldots, Z_n)$ and distribution function $\mathcal{F}_Z(z_1, \ldots, z_n) = \mathcal{P}(Z_1 \leq z_1, \ldots, Z_n \leq z_n)$, where $\mathcal{F}_{Z_i}(z_i)$ is the marginal distribution function $\mathcal{F}_{Z_i}(z_i) = \mathcal{P}(Z_i \leq z_i)$. The independence assumption implies that $\mathcal{F}_Z(\boldsymbol{z}) = \prod_{i=1}^{n} F_{Z_i}(z_i)$. Any random variable may be represented as a series of polynomials in uncorrelated and independent Gaussian variables [Wiener, 1938] and, in its generalized extension, in non-Gaussian measures, gPCE basis functions of a univariate random variable Z_i are defined as the polynomials $\{\phi_k(Z_i)\}_{k=0}^{N}$ of Nth-degree satisfying the orthogonality conditions:

$$\mathbb{E}[\phi_s(Z_i)\phi_r(Z_i)] = \int_{\Sigma_i} \phi_s(z_i)\phi_r(z_i) dF_{Z_i}(z_i) = \zeta_s \delta_{s,r} \quad 0 \leq s, \quad r \leq N \tag{4.19}$$

where $\zeta_s = \mathbb{E}[\phi_s^2(Z_i)]$ is the normalization factors, $\delta_{s,r}$ the Kronecker delta function and Σ_i is the support of Z_i. In the multivariate case, the gPCE basis functions $\Phi_{\boldsymbol{\alpha}}(\boldsymbol{Z})$ of degree up to N are products of the univariate orthogonal polynomials:

$$\Phi_{\boldsymbol{\alpha}}(\boldsymbol{Z}) = \phi_{\alpha_1}(Z_1) \ldots \phi_{\alpha_n}(Z_n) \quad \text{with} \quad 0 \leq |\boldsymbol{\alpha}| \leq N \tag{4.20}$$

where $\boldsymbol{\alpha} = (\alpha_1, ..., \alpha_n) \in \mathbb{N}_0^n$ is a multi-index with $|\boldsymbol{\alpha}| = \alpha_1 + \cdots + \alpha_n$. The multivariate basis functions are orthogonal polynomials in the space $L^2_{dF_z}$ of all mean-square integrable functions of $\boldsymbol{Z}$ with respect to the inner product based on the measure dF_Z:

$$\mathbb{E}[\Phi_{\boldsymbol{\alpha}}(\boldsymbol{Z})\Phi_{\boldsymbol{\beta}}(\boldsymbol{Z})] = \int_{\Sigma} \Phi_{\boldsymbol{\alpha}}(\boldsymbol{z})\Phi_{\boldsymbol{\beta}}(\boldsymbol{z}) dF_Z(\boldsymbol{z}) = \gamma_{\boldsymbol{\alpha}} \delta_{\boldsymbol{\alpha}\boldsymbol{\beta}} \tag{4.21}$$

where Σ is defined by $\Sigma = \Sigma_1 \times \Sigma_2 \cdots \times \Sigma_n$. As a consequence, the class of orthogonal polynomials is selected according to the measure F_{Z_i}. The polynomials orthogonal for the standard normal distribution are the Hermite polynomials, which form an ideal basis for the output stochastic domain [Xiu, 2010].

Here, the aim is to find an approximation $\widetilde{\psi}_N(\boldsymbol{Z})$ of the random function $\psi(\boldsymbol{Z})$ in the N-th degree polynomial space generated by the basis functions $\Phi_{\boldsymbol{\alpha}}(\boldsymbol{Z})$:

$$\psi(\boldsymbol{Z}) \approx \widetilde{\psi}_N(\boldsymbol{Z}) = \sum_{|\boldsymbol{\alpha}|\leq N} \boldsymbol{c}_{\boldsymbol{\alpha}} \Phi_{\boldsymbol{\alpha}}(\boldsymbol{Z}) \tag{4.22}$$

where $\boldsymbol{c}_{\boldsymbol{\alpha}}$ are the coefficients of the expansion. For $\psi(\boldsymbol{Z})$, the coefficients $\boldsymbol{c}_{\boldsymbol{\alpha}}$ can be computed by defining $\widetilde{\psi}_N$ as the orthogonal projection of ψ onto the polynomial space $\mathcal{Z} = \text{span}\{\Phi_{\boldsymbol{\alpha}}\}$. By prescribing the orthogonality condition $\left(\psi - \widetilde{\psi}_N\right) \perp \text{span}\{\Phi_{\boldsymbol{\alpha}}\}$:

$$\int_{\Sigma} \left[\psi(\boldsymbol{Z}) - \widetilde{\psi}_N(\boldsymbol{Z})\right] \Phi_{\boldsymbol{\alpha}} dF_Z = \boldsymbol{0} \tag{4.23}$$

the coefficients $\boldsymbol{c}_{\boldsymbol{\alpha}}$ simply read

$$\boldsymbol{c}_{\boldsymbol{\alpha}} = \frac{1}{\gamma_{\boldsymbol{\alpha}}} \mathbb{E}[\psi(\boldsymbol{Z}) \Phi_{\boldsymbol{\alpha}}(\boldsymbol{Z})] = \frac{1}{\gamma_{\boldsymbol{\alpha}}} \int_{\Sigma} \psi(\boldsymbol{z}) \Phi_{\boldsymbol{\alpha}}(\boldsymbol{z}) dF_Z(\boldsymbol{z}) \quad |\boldsymbol{\alpha}| \leq N \tag{4.24}$$

i.e., they can be numerically computed as an integral of the product of $\Phi_{\boldsymbol{\alpha}}$ and ψ. The expansion term of Eq. (4.24) guarantees the optimal approximation of ψ in the sense of the norm defined in $L^2_{dF_Z}$.

The coefficients $\boldsymbol{c}_{\boldsymbol{\alpha}}$ are numerically computed by a non-intrusive approach, where the forward model providing $\psi(\boldsymbol{Z})$ is used in a black-box fashion. We use a pseudo-spectral projection, with the integral term approximated by a high-dimensional quadrature rule:

$$\boldsymbol{c}_{\boldsymbol{\alpha}} \approx \widetilde{\boldsymbol{c}}_{\boldsymbol{\alpha}} = \sum_{j=1}^{n_q} \psi(\boldsymbol{z}^j) \Phi_{\boldsymbol{\alpha}}(\boldsymbol{z}^j) w(\boldsymbol{z}^j) \tag{4.25}$$

where $\boldsymbol{z}^j$ and $w(\boldsymbol{z}^j)$ are the n_q integration nodes and weights, respectively. Since $\Phi_{\boldsymbol{\alpha}}$ is at most of degree N, the integrand function has at most degree $2N$. In the univariate case, this requires the use of $n_{q,1} = N + 1$ points for the Gaussian quadrature rule, while in the multivariate case with n random variables the number of points grows up to $n_q = (N+1)^n$. Using this approximation, the surrogate model needs the evaluation of ψ through the numerical solver of the forward model at the n_q integration points $\boldsymbol{z}^j$.

Another advantage of using the gPCE approximation regards the computation of

the Sobol' indices. Indeed, the Sobol' indices can be evaluated directly from the coefficients of the gPCE [Sudret, 2008; Crestaux et al., 2009; Formaggia et al., 2013]. The idea is to replace the functional decomposition of Eq. (4.1) with the Nth-degree polynomial expansion of Eq. (4.22) by defining [Crestaux et al., 2009]:

$$f_{i_1,\dots,i_s}(Z_{i_1},\dots,Z_{i_s}) \simeq \sum_{|\boldsymbol{\gamma}|\leq N} c_{\boldsymbol{\gamma}}\Phi_{\boldsymbol{\gamma}}(Z_{i_1},\dots,Z_{i_s}) \tag{4.26}$$

where the multi-index $\boldsymbol{\gamma} = (\gamma_1, ..., \gamma_s)$ satisfies $|\boldsymbol{\gamma}| = \gamma_1 + \cdots + \gamma_s$ and $\Phi_{\boldsymbol{\gamma}}(Z_{i_1},\dots,Z_{i_s})$ are the s-variate Nth-degree gPCE basis functions.

4.5 Measurements

Several kinds of measurements may be available over the field object of study, and the workflow presented herein can include all of them. However, in land subsidence analyses the most useful sources of information arise from surface and deep displacements. These data can be derived from Continuous Global Positioning System (CGPS) stations, bathymetric surveys or radioactive markers. CGPS stations provide continuous position information, i.e. they measure the displacements of a point (the station) on the land surface over time. Bathymetric surveys map the depths and shapes of underwater terrain, thus making it possible to obtain a representative image of the seabed motion with the identification, for example, of the shape and the extension of the subsidence bowl. Compaction measurements at the reservoir depth can be collected by radioactive markers. This technique consists of monitoring the relative position of a set of weakly radioactive bullets regularly shot in the formation along a vertical unproductive well prior to the casing operations [De Loos, 1973; Mobach and Gussinklo, 1994].

4.6 Data Assimilation techniques

Generally, the vector of the true state variables in both space and time $\boldsymbol{\psi^t} \in \mathbb{R}^{n_\psi}$ can be defined as a function of the vector of the true model parameters $\boldsymbol{\theta^t} \in \mathbb{R}^{n_\theta}$ through the forward operator $\mathcal{G}$:

$$\boldsymbol{\psi^t} = \mathcal{G}\left(\boldsymbol{\theta^t}\right)$$

with n_ψ and n_θ the number of states and parameters, respectively. Focusing on the land subsidence problem, the operator $\mathcal{G}$ is the geomechanical simulator that relates the true state variables, such as land settlements, to the true model parameters, for example the geomechanical parameters that control the rock behavior. The vector $\boldsymbol{\psi^t}$ is related to the vector of noisy empirical measurements $\mathbf{d} \in \mathbb{R}^{n_d}$, with n_d the number of measurements, through the generally non-linear relationship:

$$\mathbf{d} = \mathbf{d^t} + \boldsymbol{\varepsilon_d} = \mathbf{H}\left[\boldsymbol{\psi^t}\right] + \boldsymbol{\varepsilon_d} \tag{4.27}$$

where $\mathbf{H}$ is the measurement operator mapping from $\boldsymbol{\psi^t}$ to the true observable vector $\mathbf{d^t} \in \mathbb{R}^{n_d}$ and $\boldsymbol{\varepsilon_d} \sim \mathcal{N}(0, \mathbf{C_d}) \in \mathbb{R}^{n_d}$ is the measurement error, with $\mathbf{C_d} \in \mathbb{R}^{n_d \times n_d}$ the covariance matrix of measurement error. The matrix $\mathbf{C_d}$ depends on the kind and accuracy of the available measurements.

The vector of the model state $\boldsymbol{\psi} \in \mathbb{R}^{n_\psi}$ is related to $\boldsymbol{\psi^t}$ by the relation:

$$\boldsymbol{\psi} = \boldsymbol{\psi^t} + \boldsymbol{\varepsilon_\psi} \tag{4.28}$$

where $\boldsymbol{\varepsilon_\psi} \sim \mathcal{N}(0, \mathbf{C}_\psi) \in \mathbb{R}^{n_\psi}$ is the unknown error in the model states with $\mathbf{C}_\psi \in \mathbb{R}^{n_\psi \times n_\psi}$ the covariance matrix of the model state.

In the following, $\boldsymbol{\varphi} \in \mathbb{R}^{n_\varphi \times n_{MC}}$ denotes the matrix of augmented ensemble of states $\boldsymbol{\psi} \in \mathbb{R}^{n_\psi}$ and parameters $\boldsymbol{\theta} \in \mathbb{R}^{n_\theta}$ and $\mathbf{C_f} \in \mathbb{R}^{n_\varphi \times n_\varphi}$ the related covariance matrix, with n_φ the sum of n_ψ and n_θ, and n_{MC} the size of the Monte Carlo ensemble. The superscripts *for* and *upd* designate the forecast and update ensembles, respectively.

4.6.1 Diagnostic stage

The diagnostic step allows for a preliminary evaluation of the forecast ensembles, providing an indication as to their suitability for the successive update based upon the mismatch between the available measurements and the model outcomes. Herein, two methods have been considered: (i) χ^2-test and (ii) RF. These methods provide qualitative outcomes in an easy and computationally inexpensive fashion.

χ^2-test

The main objectives of the χ^2-test are to verify if the assumptions are violated, if the uncertainties are underestimated and if too much confidence is given to the *a priori* model [Tarantola, 2005]. This approach is based on the mismatch between model results and observations, that is:

$$\mathcal{J}(\boldsymbol{\theta}) = \frac{1}{2}\left(\boldsymbol{\theta} - \boldsymbol{\theta}^{for}\right)^T \mathbf{C}_\theta{}^{-1}\left(\boldsymbol{\theta} - \boldsymbol{\theta}^{for}\right) + \frac{1}{2}\left[\boldsymbol{\psi}(\boldsymbol{\theta}) - \mathbf{d}\right]^T \mathbf{C}_\mathbf{d}{}^{-1}\left[\boldsymbol{\psi}(\boldsymbol{\theta}) - \mathbf{d}\right] \tag{4.29}$$

For linear problems, the minimum of $\mathcal{J}(\boldsymbol{\theta})$ allows for a χ^2 distribution with degrees of freedom equal to the number of measurements n_d [Tarantola, 2005]. Consequently, it is well recognized that an ensemble ensures better results in DA applications when

$$\chi^2 = \frac{\mathcal{J}(\boldsymbol{\theta})}{n_d} \simeq 1 \tag{4.30}$$

This could be used as a general guideline to define a range for the acceptable size of $\mathcal{J}(\boldsymbol{\theta})$ in non-linear inverse problems [Chen and Oliver, 2013; Oliver and Alfonzo, 2018]. Generally, the data mismatch part of the cost function in Eq. (4.29) dominates the magnitude of the total function $\mathcal{J}(\boldsymbol{\theta})$ [Chen and Oliver, 2013], so the first contribution of Eq. (4.29) can be neglected [Oliver et al., 2008]. The χ^2-test has been already used for geomechanical applications, for example in Fokker et al. [2016] to validate the forecast ensemble before the update of the model and in Fokker et al. [2019] to estimate the assimilation results.

Red Flag

RF, as introduced in Nepveu et al. [2010], is a statistical technique that computes the probability of an event (a MC realizations in this case) by combining prior information with the likelihood of the measurements. Evaluating the probability distribution of the MC realizations allows for an inexpensive qualitative assessment of the ensemble, since the inverse problem is not solved. Moreover, a guess on the more suitable values of the combination of uncertain factors can be drawn.

The Bayesian probability $P(\boldsymbol{\psi}_k|\mathbf{d})$ of a particular realization k of the ensemble is:

$$P(\boldsymbol{\psi}_k|\mathbf{d}) = \frac{P(\boldsymbol{\psi}_k)\, P(\mathbf{d}|\boldsymbol{\psi}_k)}{\sum_{j=1}^{n_{MC}} P\left(\boldsymbol{\psi}_j\right) P\left(\mathbf{d}|\boldsymbol{\psi}_j\right)} \tag{4.31}$$

where $P(\boldsymbol{\psi}_k)$ is the prior probability of the realization, $P(\mathbf{d}|\boldsymbol{\psi}_k)$ is the associated likelihood of the measurements, and the denominator is a normalizing factor [Nepveu et al., 2010]. To define the likelihood, the measurements must be compared with the model outcome calculated at each time and space location for the realization k. Considering a Gaussian distribution for the likelihood and introducing a cost function I_k, the likelihood reads [Nepveu et al., 2010]:

$$P(\mathbf{d}|\boldsymbol{\psi}_k) = e^{(-I_k)} \tag{4.32}$$

with

$$I_k = \frac{1}{2}\mathbf{q}^T \mathbf{C}_\mathbf{d} \mathbf{q} \tag{4.33}$$

where $\mathbf{q}$ is the vector of the differences between measurements and model results in both space and time.

4.6.2 Model update

The workflow presented in Section 4.2 uses ES to update the model by solving the ensemble-based inverse problem. The use of ES with Multiple Data Assimilation (MDA) has been suggested in several works, e.g., Fokker et al. [2016] and Emerick [2018], to improve the performance of ES when the relation between model solution and parameters is non-linear. MDA has proven its efficiency in many history-matching problems, however there is a lack of its use for land subsidence applications. For these reasons, MDA is presented herein and applied in Chapter 5 to evaluate its advantages for the specific application of land subsidence.

Ensemble Smoother

ES is a non-sequential DA algorithm originally proposed by van Leeuwen and Evensen [1996]. It is a variance-minimizing estimator that combines prior information, measurements, and the solution of the forward model to update model states and parameters. With ES, the solution of the inverse problem can be written in a matrix form as:

$$\boldsymbol{\varphi^{upd}} = \boldsymbol{\varphi^{for}} + \mathbf{K}\left(\mathbf{D} - \mathbf{H}\left[\boldsymbol{\varphi^{for}}\right]\right) \tag{4.34}$$

where $\mathbf{D} \in \mathbb{R}^{n_d \times n_{MC}}$ is the matrix of measurements and $\mathbf{K} \in \mathbb{R}^{n_\varphi \times n_d}$ the Kalman gain, calculated as:

$$\mathbf{K} = \left(\mathbf{H}\left[\mathbf{C_f}\right]\right)^T \left(\mathbf{H}\left[\left(\mathbf{H}\left[\mathbf{C_f}\right]\right)^T\right] + \mathbf{C_d}\right)^{-1} \tag{4.35}$$

With a slight notation abuse, here $\mathbf{H}$ denotes the same mapping operator from model to the observational space as defined in Eq. (4.27), but extended to the vector of state variables augmented by the parameters.

The analyses that follow are carried out with the ES implementation according to the approach introduced in Evensen [2003]. Results are optimal when the probability distribution of uncertain parameters is Gaussian [van Leeuwen and Evensen, 1996]. The quality of the outcome of the ES application can be evaluated by comparing the prior and update ensemble through two performance indices, the Average absolute Error (AE) and the Average Ensemble Spread (AES) [Hendricks Franssen and Kinzelbach, 2008]:

$$AE = \frac{1}{n_{MC} n_d} \sum_{k=1}^{n_{MC}} \sum_{i=1}^{n_d} |\varphi_{i,k} - \varphi_i^{true}| \tag{4.36}$$

$$AES = \frac{1}{n_{MC} n_d} \sum_{k=1}^{n_{MC}} \sum_{i=1}^{n_d} |\varphi_{i,k} - \varphi_i^{mean}| \tag{4.37}$$

where $\varphi_{i,k}$ is either the prior or the posterior value of the k_{th} realization for the i_{th} observation, φ_i^{true} is the true reference value and φ_i^{mean} is the ensemble mean for the observations. These metrics were already used in other works as well, e.g., Baù et al. [2015] and Zoccarato et al. [2016]. The AE index is a measure of the algorithm capability to approach the truth, as it compares the model outcome with the true reference value for each observation. This index can be computed only in a synthetic case where

the true reference is known. In real applications, AE can be computed only for the state variables using the observations as true reference. The AES index accounts for the deviation of the model results from the ensemble mean. Hence, it provides an indication of the spread of the distribution, i.e., it is a measure of the confidence in the predicted value. Generally, results of the assimilation are satisfactory when AE and AES of the update ensemble decrease with respect to the corresponding indices of the forecast ensemble. For this reason, the relative variation J of these indices from forecast to update is also computed:

$$J = \frac{\zeta^{for} - \zeta^{upd}}{\zeta^{for}} \tag{4.38}$$

where ζ is either the AE or AES index.

Multiple Data Assimilation

MDA was originally introduced by Emerick and Reynolds [2012] to improve the results of history-matching problems using seismic data, and was later combined with ES approach [Emerick and Reynolds, 2013]. MDA is basically an iterative application of ES, which means that Eq. (4.34) is repetitively applied for a predefined number of *iterations* n_{MDA} using an inflated covariance matrix of the measurement error to avoid an overconfidence in the available measurements. The covariance matrix $\mathbf{C_d}$ is multiplied by an inflation coefficient $\alpha_k \geq 1$ for every iteration k, such that:

$$\sum_{k=1}^{n_{MDA}} \frac{1}{\alpha_k} = 1 \tag{4.39}$$

This condition makes MDA equivalent to ES for Gaussian-linear problems [Emerick, 2018]. The selection of α_k is still a matter of debate, with several different proposals currently advanced by some researches. Several works use the simplest option, i.e., constant α_k equal to the number of iterations n_{MDA}, e.g. Emerick and Reynolds [2012] and Emerick [2018]. However, some recent works show that using decreasing α_k can improve the final outcome, e.g., Le et al. [2016] and Rafiee and Reynolds [2017].

One issue with the standard implementation of MDA is that the number n_{MDA} must be selected in advance, but there are no rigorous proofs about its convergence [Evensen, 2018]. Thus, conceptually, if after n_{MDA} iterations the data matches are not

satisfactory, it is not possible to iterate more because condition (4.39) would be violated, instead the process should be started from the beginning considering a larger n_{MDA}. To avoid such problem, adaptive algorithms for the choice of α_k have been developed, e.g., Emerick [2016].

As for ES, the indices AE and AES and their improvement J can be computed to assess the performance of MDA, as defined in Eqs. (4.36), (4.37) and (4.38).

Chapter 5

Application to producing hydrocarbon reservoir

The capabilities and possible drawbacks of the methodological approach described in Chapter 4 have been first investigated in a synthetic test case. In order to mimic a realistic configuration, the test case is built on the basis of the structural and mechanical properties of a real-world hydrocarbon reservoir.

Then, the workflow has been applied on a real case with the aim to develop a comprehensive geomechanical reservoir model integrating all the available measurements in an automatic and dynamic manner. This allows to better identify the possible limitations, thus suggesting also remediation and improvements.

5.1 Synthetic test case

The test case is based on the typical geometries and properties of the off-shore hydrocarbon reservoirs buried in the Northern Adriatic sedimentary basin, Italy. A possible hydrocarbon production program is assumed along with realistic measurements over the field. The model characteristics are first presented, then different DA analyses are performed, in order to test the feasibility of the steps proposed for the workflow.

5.1.1 Model set-up

The reservoir is located in a central position within the domain of interest, at a depth interval between 1,038 m and 1,075 m.

The model domain covers an area of 50 km $\times$ 50 km and extends down to 5 km depth (Fig. 5.1). It is discretized into a 3D mesh, which consists of 71,734 nodes and 410,030 tetrahedrons. A part of the mesh showing the aquifer and reservoir is presented in the leftmost panel of Fig. 5.1.

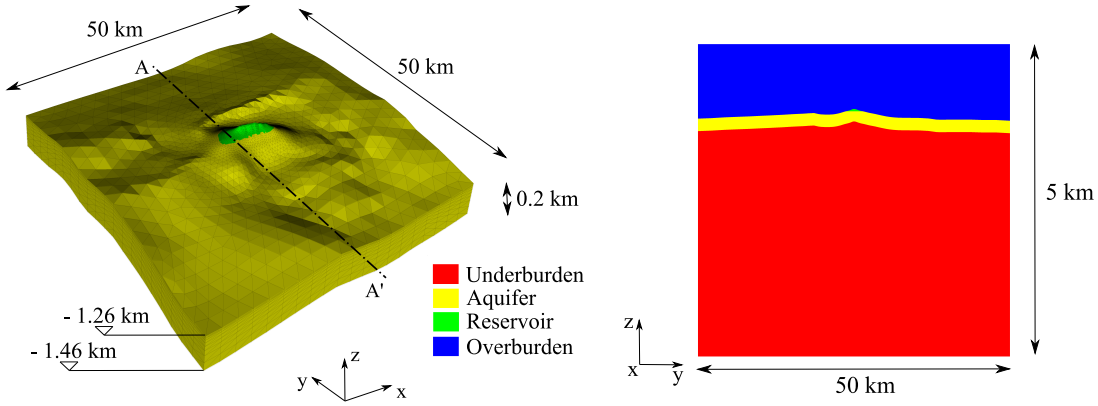

FIGURE 5.1: Views of the discretized domain with the distinction of different layers. 3D view of the partial mesh of the aquifer and reservoir where axis Z is scaled by a factor 30 (left) and vertical section A-A' with vertical coordinates multiplied by a factor 10 (right).

Poisson and Biot coefficients are assumed homogeneous and equal to 0.30 and 1.00, respectively. The vertical compressibility c_m is assumed to follow the hysteretic law vs the effective vertical stress σ_z developed by Baú et al. [2002] and Ferronato et al. [2013] for the Northern Adriatic basin, Italy:

$$c_m^{Icycle} = 1.0044 \cdot 10^{-2} \cdot \sigma_z^{-1.1347} \tag{5.1}$$

$$c_m^{IIcycle} = 2.9087 \cdot 10^{-4} \cdot \sigma_z^{-0.4315} \tag{5.2}$$

where c_m and σ_z are in [MPa^{-1}] and [MPa], respectively. Homogeneous null boundary conditions are prescribed for displacements, on the lateral and bottom boundaries, and for stress, on the top surface.

The pore pressure variation due to reservoir exploitation (Fig. 5.2) is prescribed in the active layers (aquifer and reservoir) to simulate a possible program of hydrocarbon production. In order to take into consideration a scenario as realistic and general as possible, two production phases (the first three years and from year 5 to year 7) are simulated with a halfway temporary stop of extraction. After the second production

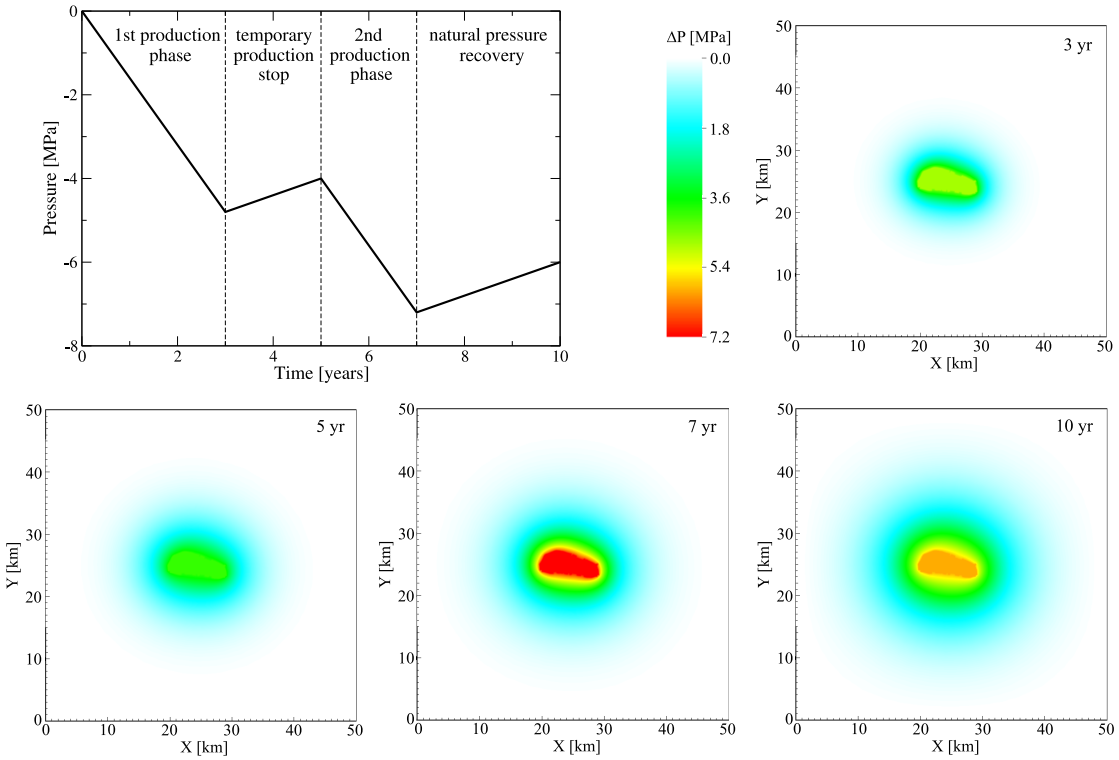

FIGURE 5.2: Prescribed pore pressure variation in time on reservoir elements (top left) and its propagation from reservoir to the hydraulically connected aquifer after three, five, seven and ten years.

phase, a natural pressure recovery is experienced. The pressure variation propagates from the reservoir to the hydraulically connected aquifer, as shown in Fig. 5.2 for some instants. As is common in reservoir simulations, the availability of a well-developed history-matched pressure behavior in time is assumed, so that the pressure-related uncertainties can be neglected (as already mentioned in Section 4.3).

Surface displacements and deep compaction values are supposed to be measured by a CGPS station and a radioactive marker borehole installed over the field.

5.1.2 Sources of uncertainty and generation of the ensembles

The most significant sources of uncertainty in a land subsidence analysis are often related to the characterization of the constitutive behavior of the reservoir rock (see Section 4.3), i.e., to the definition of the operator $\hat{\mathbf{D}}$ of Eq. (2.13).

In particular, here two different non-linear constitutive laws have been considered for the active layers: (i) MCC [De Souza Neto et al., 2008] and (ii) VEP [Vermeer and Neher, 1999]. In addition to the choice of the most suitable constitutive behavior, also

the ranges of the most influential parameters that govern these laws are uncertain. The material parameters required by both the MCC and VEP models are the modified compression index λ^* and the modified swelling index k^*, while the modified creep index μ^* and the geotechnical initial overconsolidation ratio $\mathrm{R} = {}^{p_{c,y,0}}/_{p_{c,0}}$ are needed only by the VEP model. Their physical meaning is here recalled:

- λ^* is the slope of the normal consolidation profile in the plot of volumetric strain vs axial stress in natural logarithmic scale, i.e., it is a parameter that mainly controls the rock behavior in I-cycle (virgin loading) conditions;
- k^* is the slope of the unloading profile in the same plot as λ^*, thus it mainly impacts on II-cycle (unloading-reloading) conditions;
- μ^* represents the slope of the volumetric strain profile vs time in natural logarithmic scale, so its value is a measure of the delay between the pressure variation and the related reservoir and land deformation;
- R is the ratio ${}^{p_{c,y,0}}/_{p_{c,0}}$, where $p_{c,y,0}$ is a function of the maximum volumetric stress ever experienced by the material before loading and $p_{c,0}$ depends on the volumetric stress state at initial conditions. Hence, R is related to the initial overconsolidation coefficient.

All material parameters listed above are dimensionless. For more details on the model properties and implementations, the reader is referred to Nguyen et al. [2016]; Spiezia et al. [2017] and Isotton et al. [2019]. The variability range for the first two parameters is chosen according to the confidence interval at the average depth of the producing reservoir of the vertical compressibility c_m, which is defined in Eq. (5.1) and Eq. (5.2), as described in Baú et al. [2002]. The variability of μ^* and R is chosen according to the typical values reported in the literature, e.g., Vermeer and Neher [1999] and Isotton et al. [2019]. The following statistical distributions arise:

$$ln(\lambda^*) \sim \mathcal{N}(-4.9363; 0.33295)$$

$$ln(k^*) \sim \mathcal{N}(-6.7271; 0.50975)$$

$$\mu^* \sim \mathcal{U}(0.0001; 0.0002)$$

$$\mathrm{R} \sim \mathcal{U}(1.4; 1.8)$$

i.e., λ^* and k^* are Gaussian parameters in a log-scale, while μ^* and R have a uniform distribution. These parameters are assumed to be constant over the portion of the domain where a pressure variation takes place. The reason for this assumption is twofold:

1. the variability in space of the geomechanical parameters is usually much lower than that of the hydraulic parameters. In particular, in sedimentary basins such a variability is expected to take place more along the vertical direction than in a horizontal plain. However, in this application the reservoir and aquifer thickness is relatively small to present a significant geomechanical heterogeneity in λ^*, k^* and μ^*. Nonetheless, the compressibility c_m is not constant and is varying with depth as a function of the vertical effective stress σ_z.

2. The available measurements over off-shore reservoirs usually reduce to displacement time series over a small (1 or 2) number of points, and this is not sufficient to effectively characterize the spatial heterogeneity of the uncertain parameters [Zoccarato et al., 2018].

5.1.3 Field monitoring program

Since a synthetic test case is taken into account, no real measurements are available. Thus, a run of the forward model with a predefined set of parameters values is used to build hypothetical measurements. This realization is not included in the forecast ensembles. The *true* parameter configuration is selected as follows:

$$\lambda^* = 0.004992, \qquad k^* = 0.000700, \qquad \mu^* = 0.00015, \qquad \mathrm{R} = 1.50$$

Fig. 5.3 shows the vertical displacements in time for the *true* configuration, where the maximum vertical motion is recorded. As it can be easily seen, the difference between the MCC and VEP behavior is not only related to the displacement values, but also to their evolution in time. The VEP model is typically characterized by a delay between

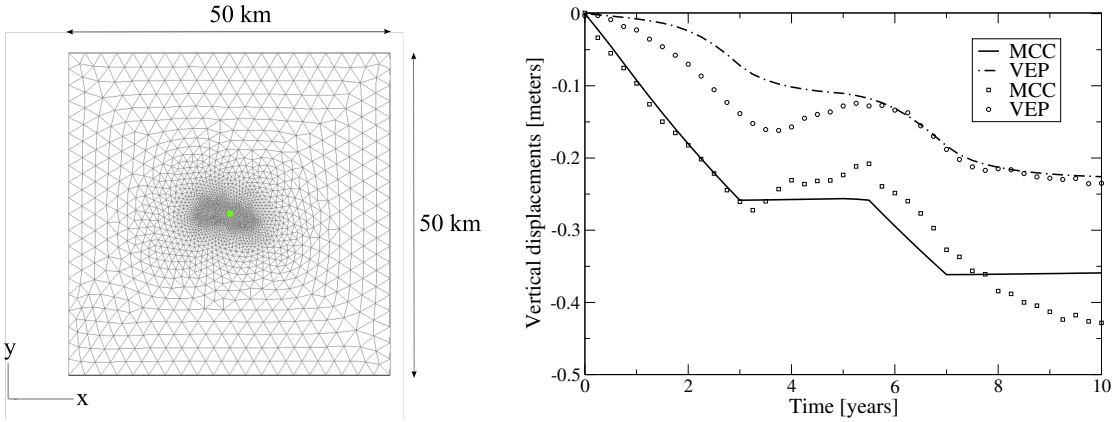

FIGURE 5.3: On the left, 2D view of the model top with the green point indicating the location where the CGPS station is supposed to be. On the right, maximum vertical displacements in time resulting from the geomechanical model run with the *true* parameter configuration. Squares and circles are an example of such outcomes perturbed to get the synthetic measurements, respectively for the MCC and the VEP model.

the variations of fluid production rates and the resulting land settlement, which is not accounted for with a traditional VEP law.

To mimic a real off-shore application, a CGPS station and a marker borehole are supposed to be located over the reservoir and to collect surface displacements and compaction measurements in time, respectively. Specifically, a single CGPS is supposed to be located at the reservoir center, collecting measurements of the vertical displacements in time. A marker borehole is supposed to be placed near the CGPS location, where the reservoir is approximately 30 m-thick. Since the initial space between two adjacent radioactive markers is approximately 10 m, three compaction measurements are available for the assimilation. Surface displacements are assimilated every three months, while compaction measurements every three years.

In order to simulate real recordings and avoid a trivial application, the outcome of the geomechanical model at the 'measurement' location is properly perturbed to get the synthetic assimilation data, that are for example the dots in Fig. 5.3.

According to NAM [2017], the covariance matrix of measurement error $\mathbf{C_d}$ can be defined considering that the uncertainties related to the observations can be computed as the sum of a measurement and an idealisation noise. The first contribution depends on the accuracy of the tool used for the measurements and the representativeness of the mathematical model for reproducing the observations, and affects only the diagonal

entries of $\mathbf{C_d}$. The idealisation noise affects both the diagonal and the extra-diagonal entries according to the spatial and temporal correlation among measurements. In subsidence modeling, any deformation caused by sources other than the deep compacting layers should be considered as noise. Therefore, all signal components in geodetic observations that are not related to the signal of interest are treated as a noise and included in the idealisation part of $\mathbf{C_d}$. Following the fractional Brownian motion approach [NAM, 2017], the idealisation noise terms are computed as:

$$(\mathbf{C_d})_{ii} = \varsigma^2 t_i^{p_h} \tag{5.3a}$$

$$(\mathbf{C_d})_{ij} = \frac{1}{2}\varsigma^2 \left(t_i^{p_h} + t_j^{p_h} - |t_i - t_j|^{p_h} \right) \tag{5.3b}$$

where t_i is the time of the measurement i, ς the standard deviation and p_h the Hurst index. In real-world studies, parameters ς and p_h derive from specific studies on the measurement quality. Here, for the vertical displacements recorded by the CGPS station, they have been computed through a fitting process of the variogram of the model outcome run with the *true* parameters (Fig. 5.3), as described in NAM [2017]. For the selected constitutive laws, such parameters read:

$$p_{MCC} = 1.672, \qquad \varsigma^2_{MCC} = 1.112 \cdot 10^{-3}\ m^2/yr^{p_h}$$

$$p_{VEP} = 1.895, \qquad \varsigma^2_{VEP} = 4.158 \cdot 10^{-4}\ m^2/yr^{p_h}$$

The measurement noise is defined from a normal distribution with zero mean and standard deviation equal to 1.5 mm [NAM, 2017]. On the contrary, motivated by their large time interval, compaction measurements are considered uncorrelated. To define $\mathbf{C_d}$, the measurement noise is computed from a normal distribution with zero mean and standard deviation equal to 1.0 cm.

5.1.4 Workflow validation

Initially, the FEM geomechanical simulator and its approximation through the gPCE surrogate are compared. Then, the role of each parameter is investigated by a sensitivity analysis performed through the Sobol' indices. The three DA steps are tested

for different combinations of the uncertain parameters. First, each parameter alone is considered uncertain and then some combinations are analyzed. Table 5.1 lists the analyzed configurations: a total number of 12 sets is considered, 3 referring to VEP and 9 to VEP. Initially, the model state ψ of Eq. (4.29) includes only the surface displacements from CGPS. Compaction measurements are added in the analysis later on, to evaluate separately their contribution.

TABLE 5.1: Analyzed configuration sets with their associated uncertain parameters and constitutive law, and χ^2 values.

Set	**Parameters**	**Law**	$\boldsymbol{\chi^2}$
1	λ^*	MCC	1.22
2	k^*	MCC	0.95
3	λ^* k^*	MCC	1.32
4	λ^*	VEP	1.47
5	k^*	VEP	1.41
6	μ^*	VEP	0.93
7	R	VEP	1.03
8	λ^* k^*	VEP	4.35
9	λ^* R	VEP	1.91
10	λ^* k^* μ^*	VEP	1.85
11	λ^* k^* R	VEP	1.79
12	λ^* k^* μ^* R	VEP	1.65

Surrogate model

The first objective of the analysis is to test the quality of gPCE as a surrogate of the outcome of the FEM simulator. The validation is performed under the most challenging configuration as to the number of uncertain parameters, i.e., considering the VEP behavior in scenario 12 of Table 5.1 (four uncertain parameters).

Different degrees of the gPCE polynomial truncation, $N = 1, 2, 3$, have been taken into account. A full tensor approach is used for $N = 1$ and $N = 2$, leading to a total number n_q of forward model runs equal to 16 and 81, respectively. Since with $N = 3$ there would be the need of $n_q = 256$ full model runs, a sparse grid approach based on Smolyak's coarse tensorization [Smolyak, 1963] is used, thus reducing n_q to 137. It should be noticed that the use of such sparse grid numerical integration might lead to

unacceptable errors in the expansion coefficients with higher order polynomials [Constantine et al., 2012]. This issue is not encountered in the present application, however alternative accurate approaches can be also employed if needed, such as those advanced in Constantine et al. [2012] and Conrad and Marzouk [2013].

A quantitative evaluation of the fitting quality of the gPCE surrogate is provided by employing the leave-one-out (LOO) cross-validation [Sudret, 2014], where an estimate of the mean-square error of the residuals between the full model and surrogate solution is given by the value SSE_{LOO} defined as:

$$\text{SSE}_{\text{LOO}} = \frac{1}{n_q} \sum_{i=1}^{n_q} (\boldsymbol{\psi}_i - \widehat{\boldsymbol{\psi}}_i^{\sim i})^2 \tag{5.4}$$

where $\boldsymbol{\psi}_i$ is the full model result at a certain time t and parameter combination i and $\widehat{\boldsymbol{\psi}}_i^{\sim i}$ is the surrogate solution at the same t and parameter combination i with the gPCE built without the point denoted by i. In practice, the n_q residuals can be obtained without building n_q different gPCE but using the original gPCE constructed with the whole set of collocation points. The coefficient Q^2, similar to the coefficient of determination R^2, can be defined as:

$$Q^2 = 1 - \frac{\text{SSE}_{\text{LOO}}}{\text{SST}}, \tag{5.5}$$

where SST is the sum of the squared deviations of $\boldsymbol{\psi}_i$ from their mean values μ_ψ at the instant t. Values of Q^2 close to 1.0 indicates a good match between the model outcome and the gPCE surrogate approximation. Table 5.2 reports the mean and variance of vertical displacements at the times t =1, 5, and 10 years, along with the Q^2 value. Q^2 progressively increases to the upper limit of 1 for increasing N, proving the convergence of both the polynomial expansion and the high-dimensional quadrature formula. This holds true for t > 5 years with a gPCE surrogate solution less accurate at the onset of the simulation.

Sensitivity analysis

The influence of the uncertain parameters on the model outputs can be evaluated through the estimation of the Sobol' indices. Here, the Sobol' indices are computed

TABLE 5.2: Mean μ_ψ, variance σ^2_ψ and coefficient Q^2 with the gPCE approximation up to degree $N = 1$, $N = 2$ and $N = 3$ (sparse grid).

$N = 1$ (n_q = 16)				$N = 2$ (n_q = 81)		
t [yr]	μ_ψ [m]	σ^2_ψ [m^2]	Q^2	μ_ψ [m]	σ^2_ψ [m^2]	Q^2
1	-2.1×10^{-3}	2.0×10^{-6}	0.820	-2.3×10^{-3}	3.1×10^{-6}	0.931
5	-1.7×10^{-1}	1.4×10^{-2}	0.860	-1.7×10^{-1}	1.5×10^{-2}	0.995
10	-3.6×10^{-1}	2.6×10^{-2}	0.904	-3.7×10^{-1}	2.8×10^{-2}	0.999

$N = 3$ (n_q = 137)			
t [yr]	μ_ψ [m]	σ^2_ψ [m^2]	Q^2
1	-2.3×10^{-3}	3.0×10^{-6}	0.823
5	-1.7×10^{-1}	1.5×10^{-2}	0.999
10	-3.7×10^{-1}	2.8×10^{-2}	1.000

considering the gPCE surrogate solution of the VEP model with four uncertain parameters (scenario 12 of Table 5.1). The results are presented in Fig. 5.4. First-order indices clearly show the higher impact on the total variance with a negligible influence of the factors interactions. In particular, parameters λ^* and R appear to have the major impact on the solution at several times, except for the first two years where k^* and μ^* have a non-negligible effect. However, the significance of the quantity of interest, that is, vertical displacements, is quite limited at the beginning of the production period, because both the pressure variation and the geomechanical answer of the system are still very small and possibly influenced by the measurement errors. Thus, the sensitivity analysis can be limited to the time interval between 3 and 10 years. In this temporal window, based on the total Sobol' indices $S_{T,i}$ (bottom panels of Fig. 5.4) if a threshold equal to 0.1 is set, it is possible to remove from the parameter space the parameters k^* and μ^*.

χ^2-test

To investigate the role of the χ^2-test, all the twelve combinations of uncertain parameters reported in Table 5.1 are considered, using the distributions described in Section 5.1.2. The resulting χ^2 values are shown in Table 5.1. The χ^2-test provides only a qualitative analysis of the ensemble and it is not possible to identify a clear trend. Most of the values are close to one. Nonetheless, when the number of uncertain parameters grows, the χ^2 value is higher, as in set #3 for MCC and in the last five sets of Table 5.1 for VEP. Higher values of χ^2 denote a probable increasing difficulty in constraining the model with ES. Vice versa, if χ^2 is smaller than one, the variance associated to the

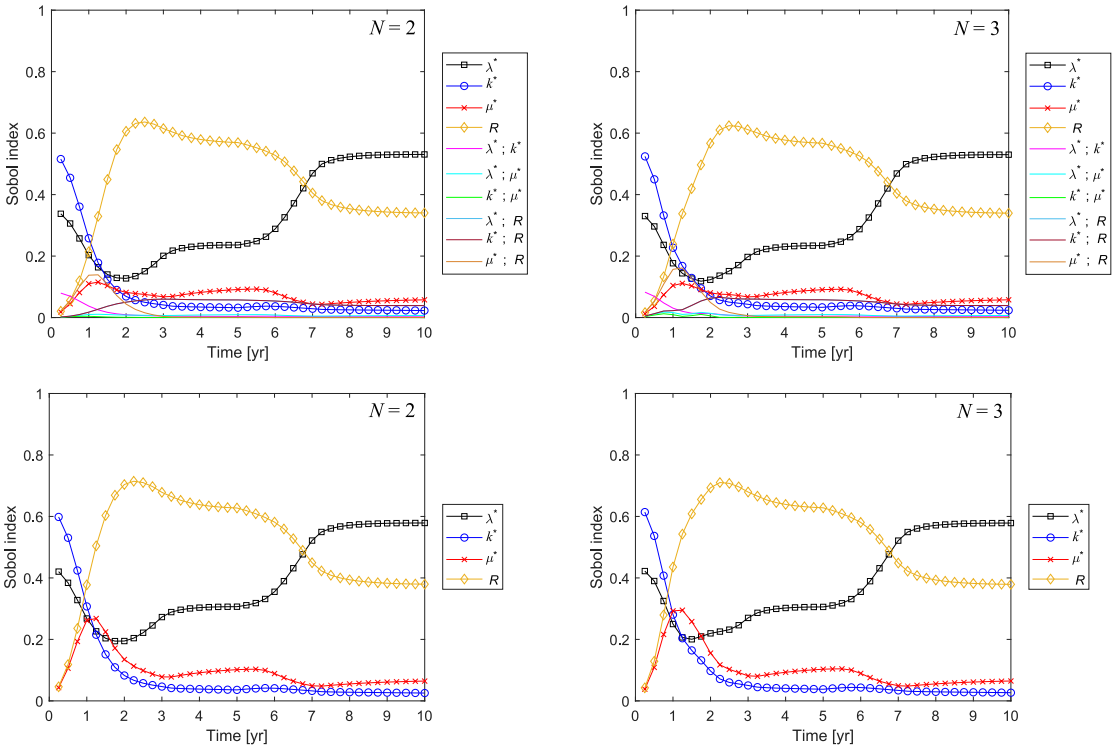

FIGURE 5.4: Sobol' indices versus simulated time. Profiles with markers are used for the single parameters, while continuous profiles are used for the combinations of parameters. On the left the gPCE is created up to degree $N = 2$, on the right the gPCE degree is $N = 3$ and a sparse grid is used. The bottom panels show the total effects.

ensemble is lower than the variance associated to the measurements, meaning that ES cannot provide improvements in the update of the ensemble and is therefore likely that DA processes are ineffective.

Generally, the constitutive law that describes the behavior of the porous medium is unknown a priori. However, a guess could be obtained from available information, e.g., laboratory tests, in-situ measurements or data provided by other reservoirs in the same basin. The χ^2-test can be also used as a preliminary tool to select the most appropriate constitutive law for the geomechanical model, as the relationship that appears to be more representative from the available measurements. As an example, we consider cases with the uncertain modified compression index λ^* and modified swelling index k^*, with the related forecast ensembles. Results are shown in Table 5.3. We compute the χ^2 value when the observations are obtained with the same constitutive law of the ensemble and when they are computed with a constitutive law different from the one used to generate the ensemble. The latter test allows to mimic the case where the

choice of the constitutive law in the modeling workflow is not consistent with the actual physical governing process. As expected, the χ^2 value associated to the ensemble created with the same constitutive law of the measurements is always closer to 1 than the inconsistent one. Consequently, χ^2-test can provide a useful and cheap preliminary screening of the generated forecast ensembles.

TABLE 5.3: Outcome of χ^2-test used for the choice of the most appropriate constitutive law for the forecast ensemble.

Estimate parameters	**Measurements constitutive law**	**Ensemble constitutive law**	$\boldsymbol{\chi^2}$
λ^*	MCC	MCC	1.22
λ^*	MCC	VEP	1.38
λ^*	VEP	VEP	1.47
λ^*	VEP	MCC	6.53
k^*	MCC	MCC	0.95
k^*	MCC	VEP	1.49
k^*	VEP	VEP	1.41
k^*	VEP	MCC	5.29
λ^* k^*	MCC	MCC	1.32
λ^* k^*	MCC	VEP	1.73
λ^* k^*	VEP	VEP	4.35
λ^* k^*	VEP	MCC	9.51

Red Flag

As for the χ^2-test, the RF approach is carried out for every configuration shown in Table 5.1. Every realization of the forecast ensembles is characterized by its own probability using Eq. (4.31), where $P(\boldsymbol{\psi}_k)$ is derived from the joint probability of the parameter set used to define the realization. Table 5.4 provides for each case listed in Table 5.1 the realization characterized by the largest probability of occurrence, along with the corresponding parameter values. The configuration with the largest probability is not always the one closest to the *true* parameter set. The reason can be that RF compares the state ensemble with the vertical displacements, which are the 'effect' through the geomechanical model of the parameter selection and not directly parameters themselves. In other words, the image of the parameters $\boldsymbol{\theta}_k$ for the k-realization through the forward model $\mathcal{G}$ is considered, and the RF approach computes a 'score' for each of such images. In some cases, more than one set provides displacements close to the

observations and consequently has a high probability. This could suggest a possible over-parameterization of the problem, i.e., different combinations of the parameters values can be able to reproduce similarly the available measurements. This is usually an unfortunate situation, where ES is expected to have a low effectiveness on the parameter characterization. Despite this, in most cases, there is an important difference between the largest and the smallest probability. Therefore, RF can help to preliminary reduce the uncertainties by neglecting the realizations characterized by the smallest probability of occurrence.

TABLE 5.4: RF approach: combination of parameters with maximum probability of occurrence.

Set	$max\left(P\left(\psi_k\|\mathbf{D}\right)\right)$ [%]	λ^*	k^*	μ^*	R
1	7.11	0.005591			
2	2.84		0.001189		
3	8.27	0.004990	0.000958		
4	20.33	0.005113			
5	5.95		0.000843		
6	2.58			0.000151	
7	3.90				1.5032
8	27.52	0.004990	0.000958		
9	22.65	0.005410			1.4655
10	13.82	0.005520	0.001004	0.000165	
11	41.83	0.005365	0.000930		1.5278
12	25.29	0.005437	0.001142	0.000150	1.5157

Ensemble Smoother

In this section, the effectiveness of ES has been evaluated for different purposes. The quality of the outcome is evaluated through the indices AE and AES computed as in Eq. (4.36) and Eq. (4.37), respectively, and their variation J, defined as in Eq. (4.38). A positive value of J indicates a restriction around the true configuration of the updated ensemble with respect to the prior. Note that in the computation of such indices, the matrix of updated state variables refers to the solution of the forward model by using the updated parameter vector.

Parameter constraints

For the test cases of Table 5.1, the outcome of the ES approach is provided in Table 5.5. The assimilation effectiveness strongly depends on the uncertain parameter set.

The choice of the set of uncertain parameters has a significant impact on the model in relation to the geometry of the domain, the constitutive law, the observed data, the boundary conditions and the imposed external load. For example, the uncertainty associated to the modified compression index λ^* and the modified swelling index k^* has a similar range of variability, as defined in paragraph 5.1.2. Nevertheless, the corresponding state ensembles for the MCC constitutive law (set # 1 and # 2) have very different forecast AES. A variation of k^* in the model does not provide significant changes in the resulting state in term of land vertical motion, u_z. As a matter of fact, k^* is a parameter mainly controlling the rock behavior in II-cycle conditions, so it appears to play a secondary role for the selected production program (Fig. 5.2). Consequently, in this case ES cannot help constrain k^* because variations related to the state ensemble are lower than the errors associated to measurements. By distinction, variations in λ^* produce a significant change in the forecast state ensemble that provide enough information to constrain the model outcome close to the observations, with a reduction of the a priori parameter uncertainties.

ES has been applied considering uncertainty related to each parameter individually and some of their combinations to evaluate ES capability of conditioning the model in different situations with the same available observations. The results of Table 5.5 point out that an over-parameterized problem can prevent from constraining the model to the measurements, as in the last four parameter sets. For the VEP model, this can be seen when the set of uncertain parameters includes both λ^* and the ratio R (set # 9). In this case measurements are not enough to constrain the model, while results of set # 4 and # 7, in which these parameters are separately considered into the ES approach, provide a satisfactory reduction of the ensembles spread around the true configuration.

TABLE 5.5: ES approach: AE and AES for the forecast ensembles and the relative variation J of AE and AES from the update ensembles. The larger J, the more effective is the assimilation approach on the parameter or state (vertical displacements, u_z) that is indicated in column 2.

Set	**Ensemble**	$\mathbf{AE_{forecast}}$	J [%]	$\mathbf{AES_{forecast}}$	J [%]
1	λ^*	$4.159 \cdot 10^{-1}$	51	$2.429 \cdot 10^{-1}$	16
	u_z	$1.432 \cdot 10^{-1}$	62	$9.260 \cdot 10^{-2}$	42
2	k^*	$6.488 \cdot 10^{-1}$	**-29**	$3.706 \cdot 10^{-1}$	**-125**
	u_z	$6.331 \cdot 10^{-3}$	**-37**	$3.348 \cdot 10^{-3}$	**-150**
3	λ^*	$3.996 \cdot 10^{-1}$	49	$2.563 \cdot 10^{-1}$	30
	k^*	$6.488 \cdot 10^{-1}$	**-20**	$3.706 \cdot 10^{-1}$	**-109**
	u_z	$1.454 \cdot 10^{-1}$	64	$1.000 \cdot 10^{-1}$	53
4	λ^*	$4.159 \cdot 10^{-1}$	71	$2.429 \cdot 10^{-1}$	51
	u_z	$3.530 \cdot 10^{-2}$	69	$2.001 \cdot 10^{-2}$	45
5	k^*	$6.488 \cdot 10^{-1}$	46	$3.706 \cdot 10^{-1}$	6
	u_z	$5.440 \cdot 10^{-2}$	65	$3.772 \cdot 10^{-2}$	49
6	μ^*	$2.503 \cdot 10^{-5}$	43	$2.485 \cdot 10^{-5}$	42
	u_z	$2.513 \cdot 10^{-2}$	42	$2.504 \cdot 10^{-2}$	42
7	R	$1.193 \cdot 10^{-1}$	47	$9.400 \cdot 10^{-2}$	34
	u_z	$4.026 \cdot 10^{-2}$	38	$3.092 \cdot 10^{-2}$	19
8	λ^*	$3.996 \cdot 10^{-1}$	54	$2.563 \cdot 10^{-1}$	31
	k^*	$6.488 \cdot 10^{-1}$	53	$3.706 \cdot 10^{-1}$	24
	u_z	$4.650 \cdot 10^{-2}$	44	$4.519 \cdot 10^{-2}$	42
9	λ^*	$3.900 \cdot 10^{-1}$	**-87**	$2.483 \cdot 10^{-1}$	**-190**
	R	$1.348 \cdot 10^{-1}$	21	$9.623 \cdot 10^{-2}$	**-10**
	u_z	$6.137 \cdot 10^{-2}$	15	$3.444 \cdot 10^{-2}$	**-57**
10	λ^*	$4.333 \cdot 10^{-1}$	38	$2.851 \cdot 10^{-1}$	7
	k^*	$6.089 \cdot 10^{-1}$	43	$3.501 \cdot 10^{-1}$	5
	μ^*	$1.325 \cdot 10^{-5}$	**-165**	$8.957 \cdot 10^{-6}$	**-292**
	u_z	$4.879 \cdot 10^{-2}$	8	$4.490 \cdot 10^{-2}$	**-2**
11	λ^*	$4.083 \cdot 10^{-1}$	**-34**	$2.351 \cdot 10^{-1}$	**-117**
	k^*	$6.351 \cdot 10^{-1}$	43	$3.380 \cdot 10^{-1}$	**-3**
	R	$1.276 \cdot 10^{-1}$	6	$9.295 \cdot 10^{-2}$	**-28**
	u_z	$5.208 \cdot 10^{-2}$	**-23**	$4.976 \cdot 10^{-2}$	**-32**
12	λ^*	$3.992 \cdot 10^{-1}$	**-87**	$2.308 \cdot 10^{-1}$	**-206**
	k^*	$6.144 \cdot 10^{-1}$	24	$3.927 \cdot 10^{-1}$	**-12**
	μ^*	$1.323 \cdot 10^{-5}$	**-9**	$9.152 \cdot 10^{-6}$	**-35**
	R	$5.423 \cdot 10^{-2}$	**-145**	$5.373 \cdot 10^{-2}$	**-145**
	u_z	$5.621 \cdot 10^{-2}$	**-90**	$4.716 \cdot 10^{-2}$	**-140**

Prediction of land subsidence

Table 5.5 suggests that the most satisfactory results can be obtained in the configurations with uncertain λ^*, sets # 1 and # 4 for MCC and VEP, respectively. For these cases, the ES capabilities are evaluated also in a predictive sense by assimilating 3, 5 and 7 years of displacement measurements only, with respect to the assimilation of observation data during the entire simulation period, i.e., 10 years. This is to investigate the use of ES during the productive life of the reservoir, introducing into the DA framework the up-to-date set of measurements. The resulting forecast and update state ensembles are shown in Fig. 5.5 together with the improvement index J.

As the number of assimilated measurements increases, the effectiveness of the ES algorithm grows. Using a MCC model, the assimilation of few observation data enables ES to reduce significantly the model uncertainties. In the case of VEP behavior, the assimilation of three years of measurements (top right panel of Fig. 5.5) is not enough for constraining the model. Since the spread of the VEP forecast state ensemble ($\mathrm{AES} = 0.020$) is already smaller than the one for MCC ($\mathrm{AES} = 0.092$), the model characterization is intrinsically more difficult. Nevertheless, seven years of measurements appear to be enough to reduce uncertainties and improve the model predictive capabilities. In other words, the continuous assimilation of new land displacement observations in time appears to be effective for automatically training the model, thus increasing its reliability in the prediction capability.

Influence of measurement covariance matrix

The results presented in Table 5.5 and Fig. 5.5 are obtained with the covariance matrix of the measurement error $\mathbf{C_d}$ described in section 5.1.3. Reduction in observation errors, i.e., increase in measurement reliability, usually implies a better performance of DA algorithms [Baù et al., 2015]. To evaluate the importance of the measurement errors, the standard deviation ς in the computation of $\mathbf{C_d}$ has been reduced, i.e. ς^2 equal to $1.112 \cdot 10^{-5}\ m^2/yr^{p_h}$ for MCC and to $4.158 \cdot 10^{-6}\ m^2/yr^{p_h}$ for VEP. Results provided in Fig. 5.6 show the outcome of ES for the estimate of the modified compression index λ^* by assimilating displacement measurements for the first five years of the simulation

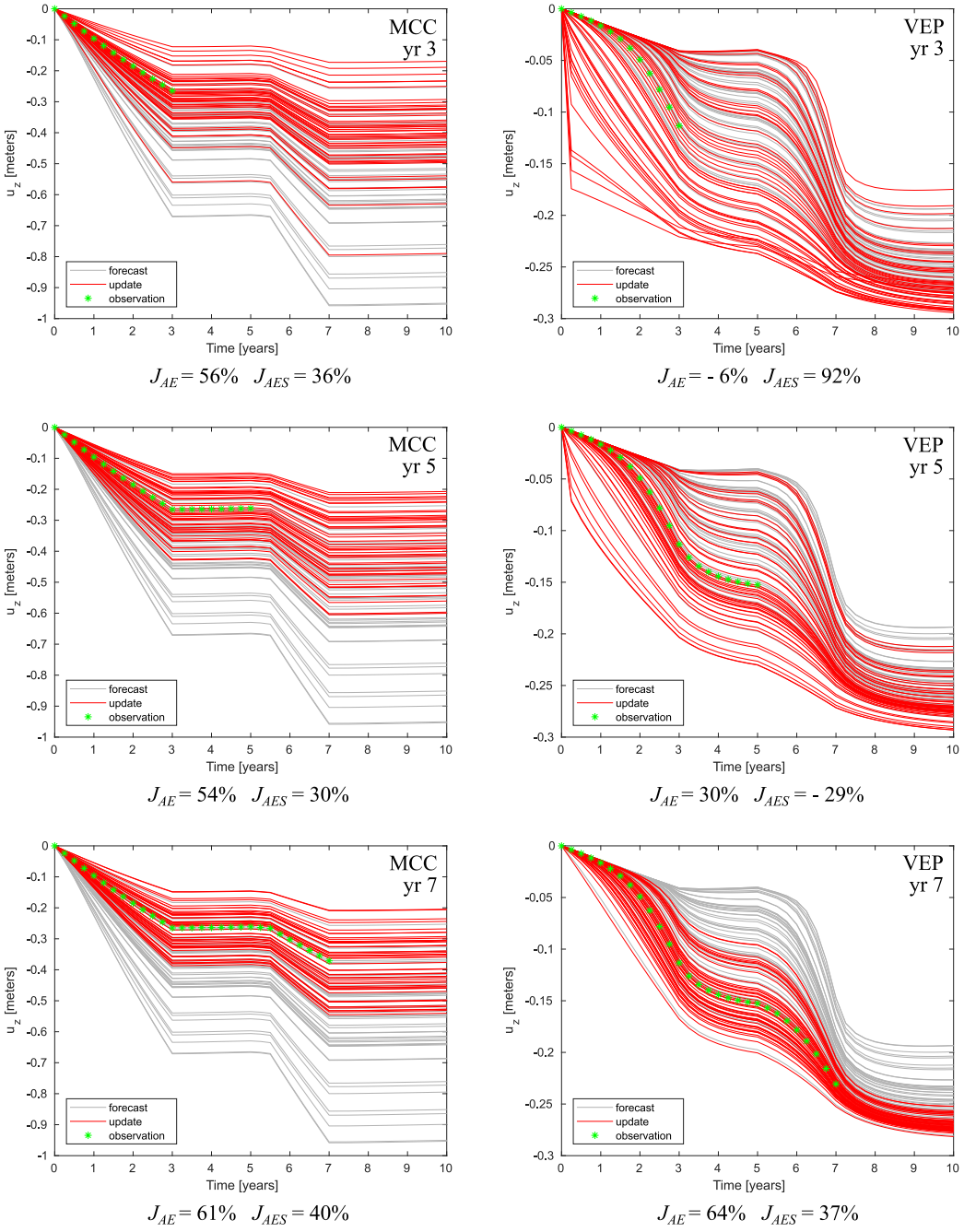

J_{AE} = 56% J_{AES} = 36% | J_{AE} = - 6% J_{AES} = 92%

J_{AE} = 54% J_{AES} = 30% | J_{AE} = 30% J_{AES} = - 29%

J_{AE} = 61% J_{AES} = 40% | J_{AE} = 64% J_{AES} = 37%

FIGURE 5.5: State ensembles resulting from ES application: maximum land subsidence in time for MCC (left) and VEP (right) by assimilating 3, 5, and 7 years of displacement measurements. The forecast and update ensembles are gray and red, respectively, while green stars denote the exact outcome of the geomechanical model used to get the perturbed observations that are shown in Fig. 5.3. Variations J of AE and AES with respect to the forecast state ensemble are reported.

process. These results, compared to those obtained with the original $\mathbf{C_d}$ (state ensembles in the central panels of Fig. 5.5 and parameter ensembles in the left panels of Fig. 5.6), point out a clear improvement in the solution of inverse problem with an increase of J by over 61%.

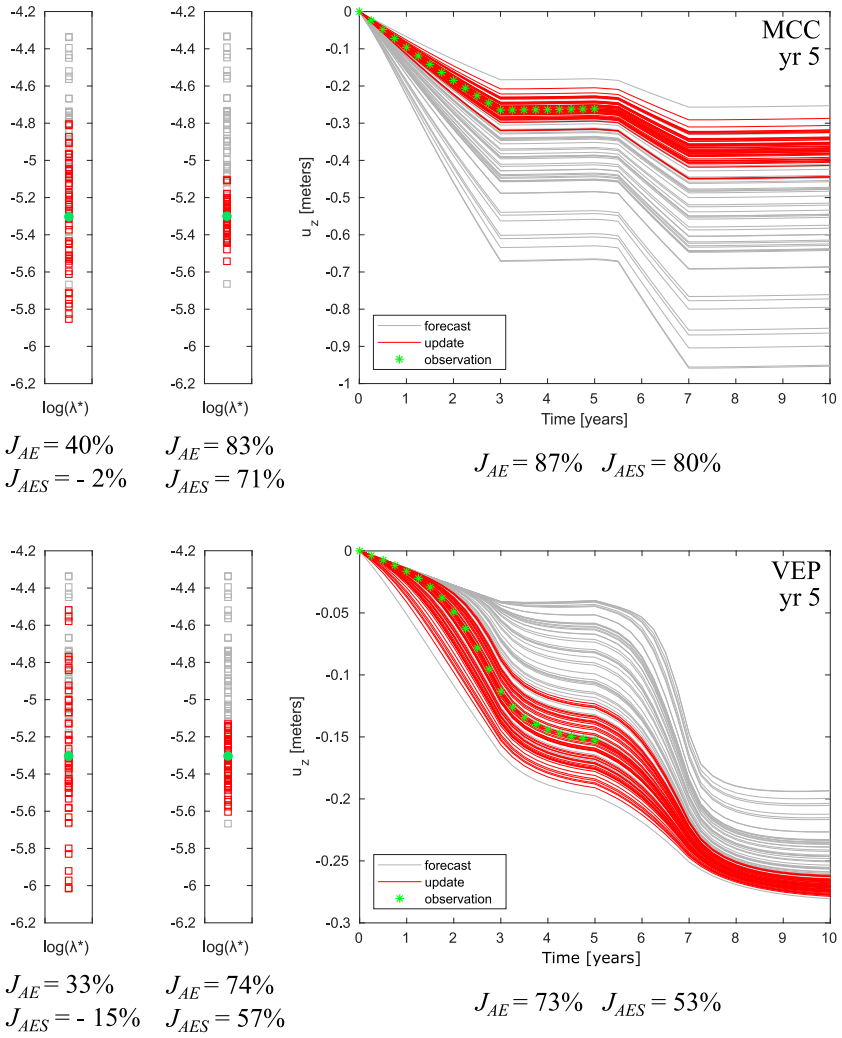

FIGURE 5.6: Ensembles resulting from ES application: parameter ensembles with the original covariance matrix $\mathbf{C_d}$ (left) and the reduced one (center) considering the MCC and the VEP model, respectively; state ensembles (right) with the reduced $\mathbf{C_d}$ for the MCC (top) and the VEP (bottom) model. Forecast and update ensembles are gray and red, respectively. The AE and AES improvements J with respect to the forecast ensembles are reported.

Assimilation of compaction measurements

In this section, synthetic measurements of the formation compaction have been added to the assimilation. To evaluate the influence of these additional measurements, four

significant configuration sets of uncertain parameters (set # 1, # 4, # 6 and # 12) have been considered. Fig. 5.7 shows the variation J of AE and AES indices from the forecast to the update ensemble when both displacement and compaction measurements are assimilated. Comparing Fig. 5.7 with the results in Table 5.5 allows to understand when adding more accurate measurements with a different nature could be useful.

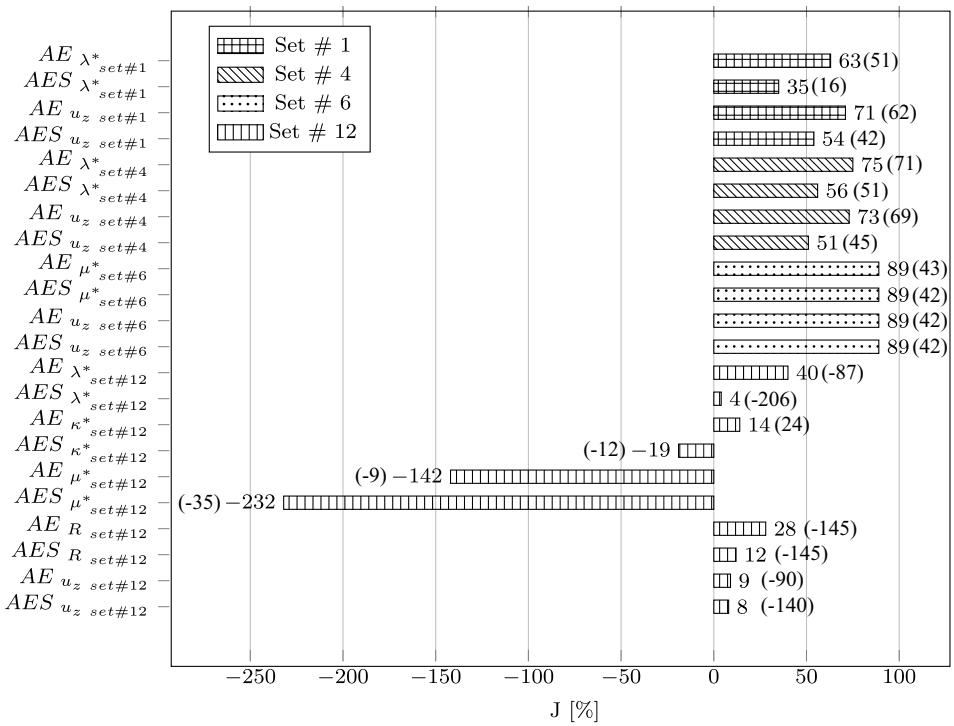

FIGURE 5.7: Variation J of AE and AES with respect to the forecast ensembles reported in Table 5.5 when both displacement and compaction measurements are assimilated for parameter sets # 1, # 4, # 6 and # 12. In brackets, values of J when only the displacement measurements are assimilated (the same as in Table 5.5) are recalled.

First, set # 1 and # 4 are considered, where λ^* is uncertain in the MCC and VEP model, respectively. In these cases, the assimilation of only CGPS measurements allows to constrain the model. Adding other observations does not provide a relevant improvement in the ES application. Then, set # 6 is considered, i.e., the modified creep index μ^* with the VEP model is kept uncertain. This parameter has a low range of variability. In this case, the assimilation of both displacement and compaction measurements with the covariance matrix as described in paragraph 5.1.3 proves a significant variation in the ES results, with an improvement of J of about 107% with respect to the assimilation of vertical displacements only. Finally, the case of a probable over-parameterized problem is evaluated, i.e., set # 12 of Table 5.1. Results obtained with the

assimilation of both CGPS and marker measurements cannot be considered thoroughly satisfactory, because of the small, or even negative, values of J. Nevertheless, they are better than results in Table 5.5 for the assimilation of surface vertical displacements only, at least for parameter λ^*, ratio R and displacement u_z.

Ensemble size

The influence of the ensemble size, i.e., the number of MC realizations, have been analyzed. Results in terms of index AE are reported in Fig. 5.8 and Fig. 5.9, where the VEP law is assumed and the parameters λ^* and R have been considered uncertain (set # 9). Two sets of parameters have been used to build the CGPS synthetic measurements: the one already defined in Section 5.1.3 and one with $\lambda^* = 0.011$ and R = 1.25. Even if these two configurations provide very different observation data, the convergence behavior is similar. Ensembles of size up to 20.000 realizations are analyzed. The parameter index AE (Fig. 5.8) generally decreases with n_{MC} for both cases and stabilizes after ~ 100 n_{MC}. Fig. 5.9 shows that ensemble size greater than 2.000 realizations do not provide any significant improvement in the update of the state variable.

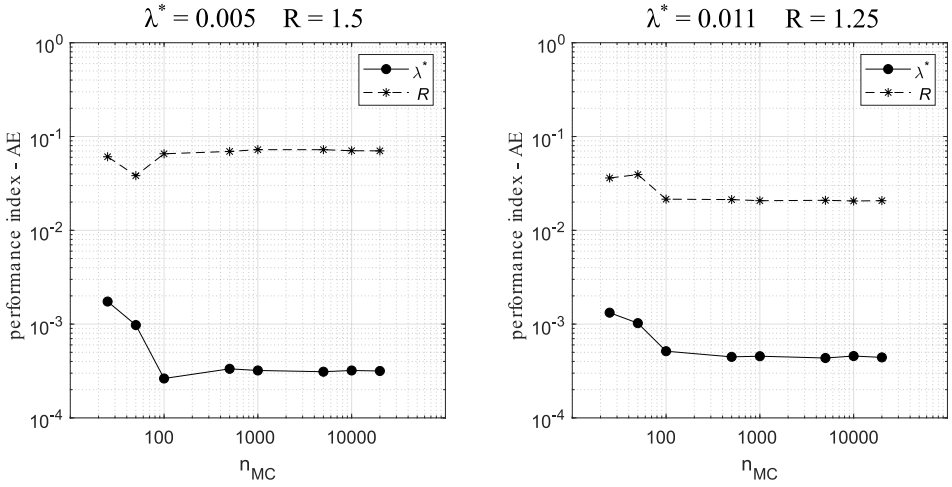

FIGURE 5.8: Convergence of ES for increasing ensemble size. On the top of the panels, the two sets of *true* parameters that have been used to compute the synthetic measurements are reported.

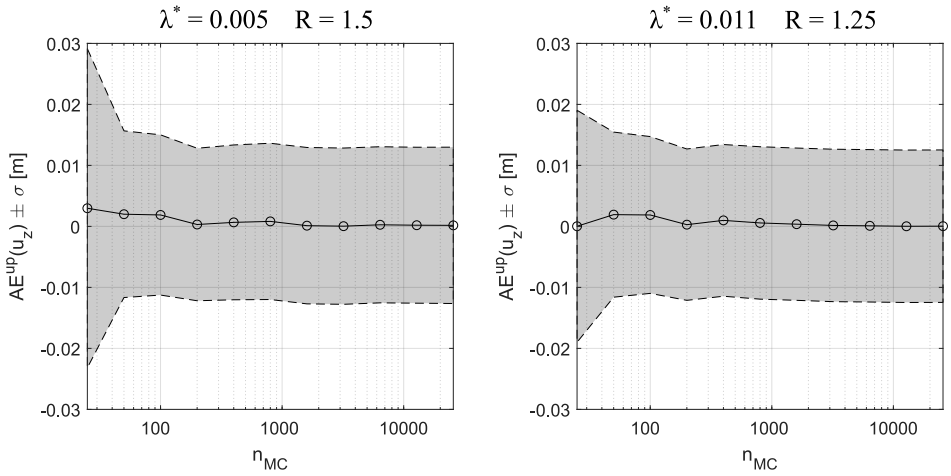

FIGURE 5.9: Mean and standard deviation for the updated displacements on the observation point varying the size of the ensembles. On the top of the panels, the two sets of *true* parameters that have been used to compute the synthetic measurements are reported.

Multiple Data Assimilation

MDA is recognized to improve the effectiveness of the ES when there is a strongly nonlinear relationship between the uncertain parameters and the state variables [Emerick and Reynolds, 2012]. The multiple applications of ES implies an increase in the computational cost, which makes the use of MDA unworkable for complex real cases. This is probably the reason why in the literature there is a lack of study regarding MDA in the context of land subsidence analyses.

Here, we compare the results of ES and MDA for some significant set of uncertain parameters. The influence of the measurement covariance matrix is also investigated.

Influence of measurement covariance matrix

Two groups of simulations are carried out to point out the influence of the measurement error in the MDA approach: (i) using the measurement covariance matrix is as described in Section 5.1.3, and (ii) considering a reduced one. To build the reduced $\mathbf{C_d}$, the entries of the measurement noise are sampled from a normal distribution with zero mean and standard deviation equal to 1 mm, while the terms of the idealisation noise have been calculated considering Eq. (5.3) with Hurst index $p_h = 1.67$ and variance $\varsigma^2 = 2 \cdot 10^{-5}\ m^2/yr^{p_h}$. For MDA three *iterations* have been considered.

Fig. 5.10 shows a comparison between ES and MDA for the estimation of parameter set # 1 considering both the measurement covariance matrices. The final update ensembles of ES and MDA appear quite similar when the original $\mathbf{C_d}$ is used, with the exception for a few outliers (top panels of Fig. 5.10). Conversely, considering the reduced covariance matrix (bottom panels of Fig. 5.10), progressive improvements at every successive assimilation are registered with MDA and the final ensemble is more clustered and centered around the true value than the one derived from a single ES assimilation.

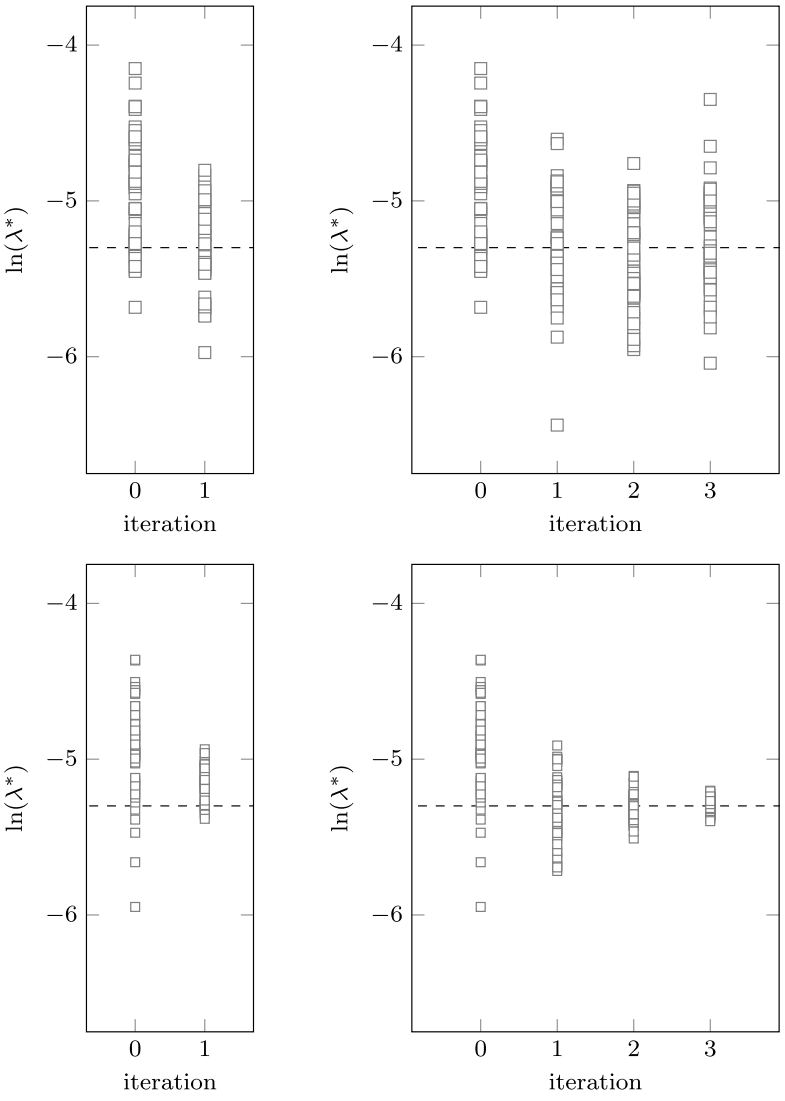

FIGURE 5.10: Parameter ensembles resulting from ES (left) and MDA (right) for set # 1, i.e., uncertain λ^* and MCC model. The top and bottom panels are the outcomes using the original and the reduced measurement covariance matrix, respectively. Dashed lines correspond to the true value of the parameter.

Comparison between ES and MDA for parameter constraint

In this section, the reduced measurement covariance matrix is used. ES and MDA are compared in constraining case # 9 (λ^* and R uncertain, Fig. 5.11) and set # 13 (λ^* and μ^* uncertain, Fig. 5.12).

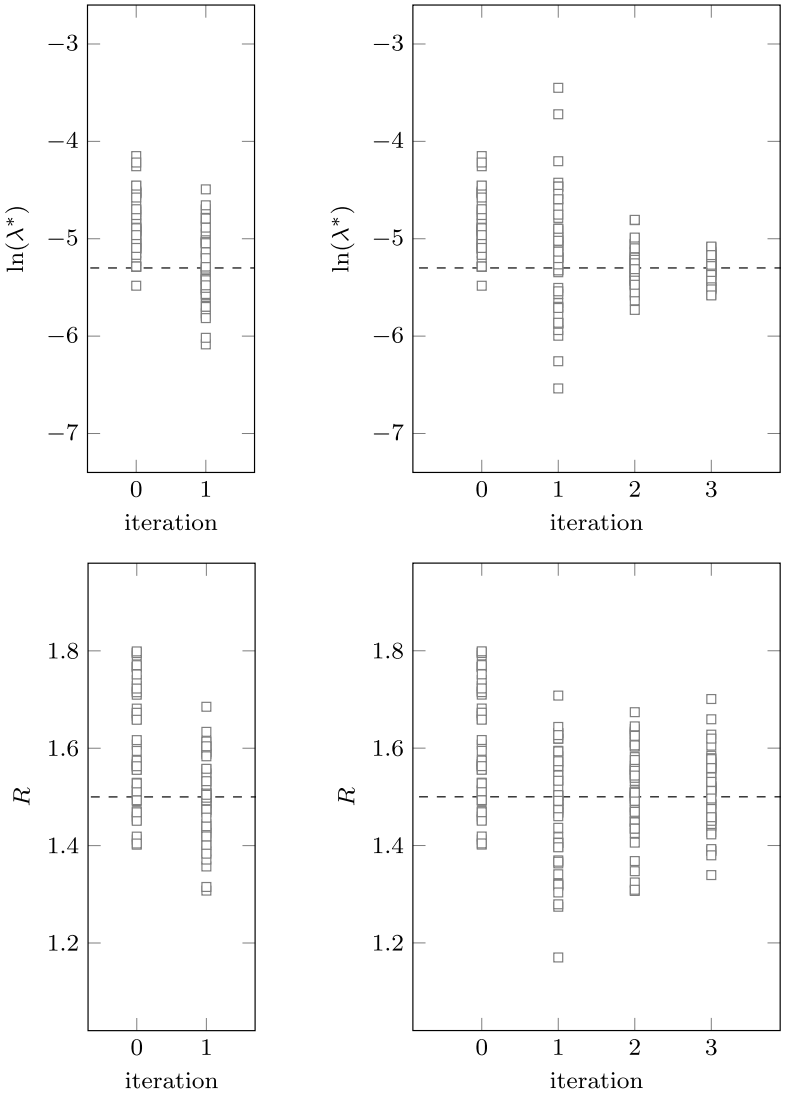

FIGURE 5.11: Parameter ensembles resulting from ES (left) and MDA (right) for set # 9, i.e. λ^* (top) and R (bottom) uncertain, with the reduced $\mathbf{C_d}$. Dashed lines correspond to the true value of the parameters.

Similarly to the outcomes shown in the bottom panels of Fig. 5.10, Fig. 5.11 shows that in the MDA process progressive improvements are achieved and the final result is better than the one of a single ES assimilation to constrain λ^*. By distinction, if the set of parameters is formed by λ^* and μ^* (Fig. 5.12), MDA does not provide any improvement with respect to ES. This can be motivated by the difficulty in the μ^* estimation using

vertical land displacements only, as already observed in Table 5.5.

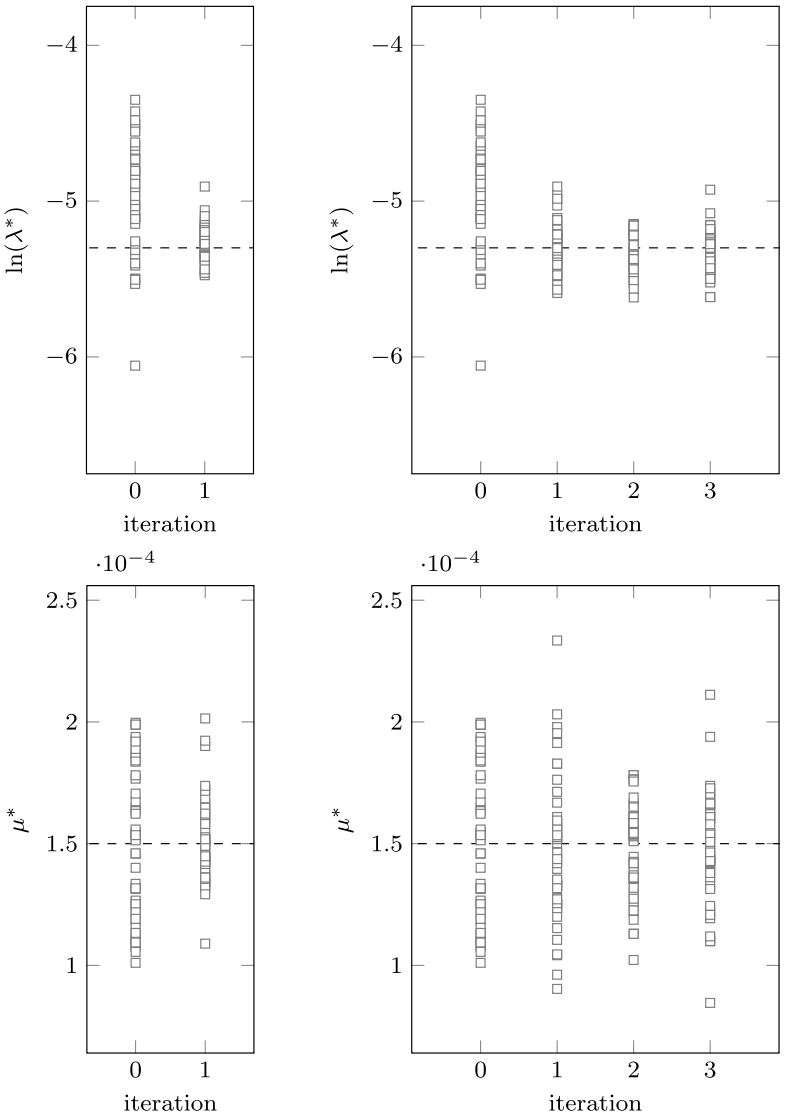

FIGURE 5.12: Parameter ensembles resulting from ES (left) and MDA (right) for set # 13, i.e. λ^* (top) and μ^* (bottom) uncertain, with the reduced $\mathbf{C_d}$. Dashed lines correspond to the true value of the parameters.

5.1.5 Discussion

In Section 5.1, the effectiveness of the integration of DA techniques into numerical models for land subsidence prediction above producing hydrocarbon reservoirs has been analyzed. The aim is to define a modern methodological approach able to take into consideration, quantify and reduce uncertainties in land subsidence prediction by a progressive 'training' of the forward numerical model through the assimilation of the

available pieces of information. The potential and drawbacks of the different DA approaches have been investigated in a synthetic test case, representative of a real-world hydrocarbon producing reservoir buried in a sedimentary basin. Selected mechanical behaviors and parameter ranges are typical of the Northern Adriatic basin, Italy. On the basis of the numerical experimentation carried out in the previous sections, the following main considerations are worth summarizing.

1. *Preliminaries.* Land subsidence models, as any other numerical model of real-world processes, are affected by a number of different sources of uncertainties. The first preliminary step consists of recognizing the most influential uncertain factors and, among these, the ones that can be explicitly included as stochastic variables in the construction of the model ensembles. For instance, uncertainties in the subsurface geometry or in the mathematical description of the governing processes cannot be easily quantified, while it is often convenient, and more supported by available information, to treat some material parameters as stochastic variables. Uncertainties in the geometry or the mathematical modeling can be implicitly accounted for by artificially inflating the errors associated to assimilated measurements. Then, the appropriate selection of the set of uncertain material parameters is a fundamental aspect for the application success. A necessary condition for an effective DA is that the uncertain material parameter has a significant impact on the monitored model outcome, i.e. ground motion in this case, while including parameters with a low relevance is often detrimental for the quality of the overall assimilation process. For this reason, a preliminary sensitivity analysis on the relative influence of each material parameter on the model outcome, along with the identification of feasible variation ranges, is of paramount importance. Here, it has been quantitatively performed by means of Sobol's indices, allowing to identify the most influential geomechanical parameters.

2. *Model diagnostic.* Once the most significant governing parameters are defined, a model diagnostic analysis is useful to preliminarily evaluate the quality of the forecast ensemble. This step is important especially to help identify the most

appropriate constitutive behavior of deep rocks and recognize the actual representativeness of the selected ranges for the uncertain parameter set. To this aim, here the χ^2-test and RF are used. The numerical experiments show that χ^2-test can be helpful for choosing the most appropriate constitutive law as the one better fitting the observation data. It should be recalled, however, that the χ^2-test has mainly a qualitative meaning. In case the outcome of the χ^2-test is not definitely clear, as it can often happen when the quantity and/or quality of the available measurements is limited, it is useful to keep more than one ensemble and select the most appropriate one as new pieces of information come in. In the RF outcomes, there is usually an important difference between the highest and the lowest probability, with a relatively small number of realizations with a relevant probability of occurrence. Some exceptions to this outcome has been found for the cases in which χ^2 is lower than one, i.e. when the ensemble should have been rejected a priori in the diagnostic stage. RF provides a preliminary idea of the most likely parameter combination and allows to exclude some realizations that can be considered too unrealistic. In this way, a refinement of the feasible ranges for the uncertain parameter set can be performed, with the possibility of building more representative model ensembles. Of course, the most likely parameter combination along with the expected ranges can change as new observations become available, hence such a refinement should be done with some caution, especially when the amount and quality of such data is limited.

3. *Assimilation.* The assimilation stage allows to incorporate the available measurements and progressively train the geomechanical model as the monitoring of the ongoing process proceeds. The outcome of this stage is a new updated ensemble with a progressively smaller uncertainty in the model prediction. To this aim, ES and MDA have been employed. ES proves to depend on three different aspects: (i) the set of uncertain parameters, (ii) the measurements, and (iii) the error associated to the observations, i.e., ultimately the definition of the measurement covariance matrix. First, the uncertain parameter set has to be actually relevant for the observed process without leading to over-parametrization, i.e., multiple combinations can provide similar results with respect to the measurements. Generally,

if the choice of the uncertain parameter set is consistent with the available observations, ES appears to be especially suitable for subsidence predictions, with a progressive model improvement as the quantity of assimilated measurements increases. The effectiveness of ES application improves with the decrease of the error associated to the observations. Hence, the definition of the covariance matrix of the measurement error, which might be also artificially inflated to account for other sources of uncertainty, plays a fundamental role in the application of the DA algorithm. In principle, MDA can be used to improve ES outcomes, especially in case of a strongly non-linear relationship between state variables and uncertain parameters. In our numerical experiments, it does not always provide better results than ES, despite the higher computational cost, and appears to be strongly influenced by the selection of the uncertain parameter set and the covariance matrix of the measurement error.

The validation of the single steps on a synthetic test case allows to delineate the methodology as it has been presented in Chapter 4.

5.2 real-world producing reservoir application

After the analysis carried out on the synthetic test case, the methodological approach is applied on a real producing hydrocarbon reservoir in Italy, namely the Arlua reservoir. The aim is to test its effectiveness in a complex case study with a real-world data set of deformation measurements in space, time and depth.

In this section, the model is first described along with its uncertainties and the available data on the field, then the outcomes of the DA steps are presented and discussed.

Due to confidentiality reasons, all the displacement and pressure data in the following paragraphs have been normalized with respect to a reference value that is positive and constant for the successive assimilations.

5.2.1 Model set-up

The reservoir structure of the Arlua field is made up by an anticline with two culminations (Fig. 5.13), surrounded by several minor hydrocarbon accumulations that

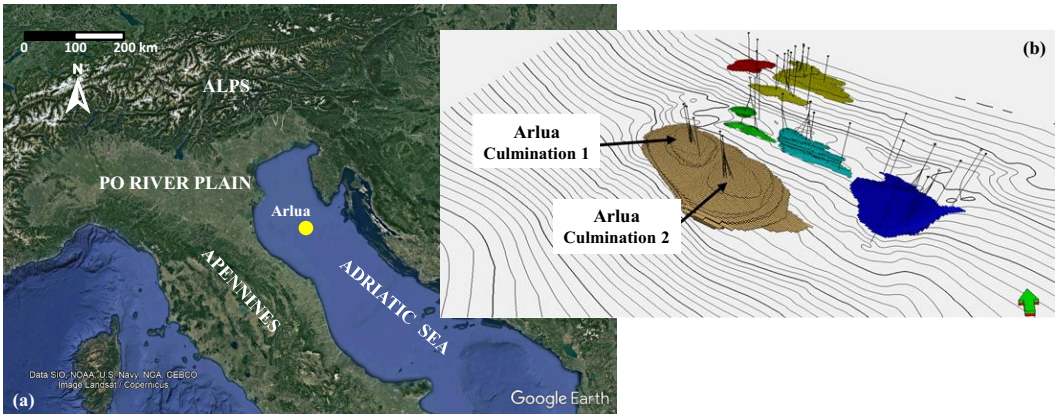

FIGURE 5.13: Location of the Arlua reservoir in the Northern Adriatic Sea (a) and perspective view of the Arlua field with paths of the wells targeting the two culminations (b). Neighboring hydrocarbon accumulations are also shown.

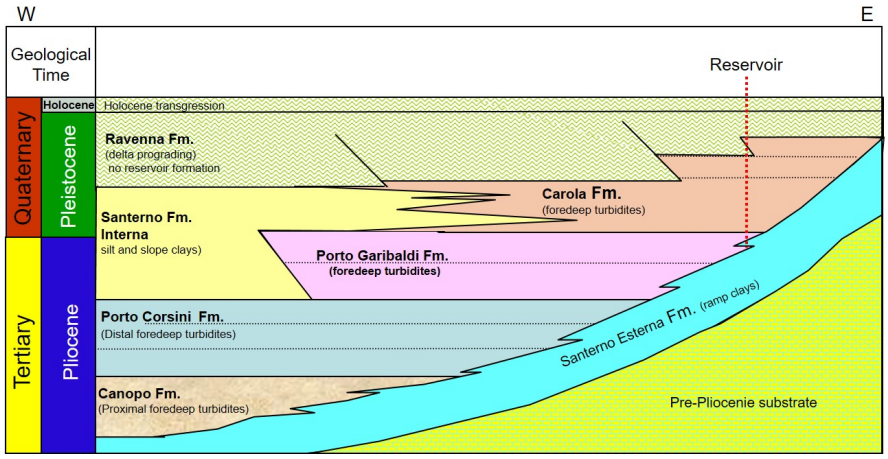

FIGURE 5.14: Stratigraphic profile with the identification of the reservoir location.

have also been included in the fluid-flow and geomechanical simulation models. The proximal turbiditic sand lobes of the Pleistocene Carola Formation represent the shallowest and most recent reservoir layers. The trap is a structural four-way dip closure resulting from the compaction processes related to the draping of the faulted carbonate basement on the structural highs. The deepest reservoir layers of the Pliocene Porto Garibaldi Formation are composed of distal turbidite sand lobes and fringes that have a different trap caused by the pinching out of the sandy layers on the Santerno Formation shales toward NE (Fig. 5.14). The origin of these turbiditic deposits is related to the Po river depositional environment. They come from the dismantling of the Alps chain and are widely distributed into the Periadriatic Foredeep Basin. The deeper deposits

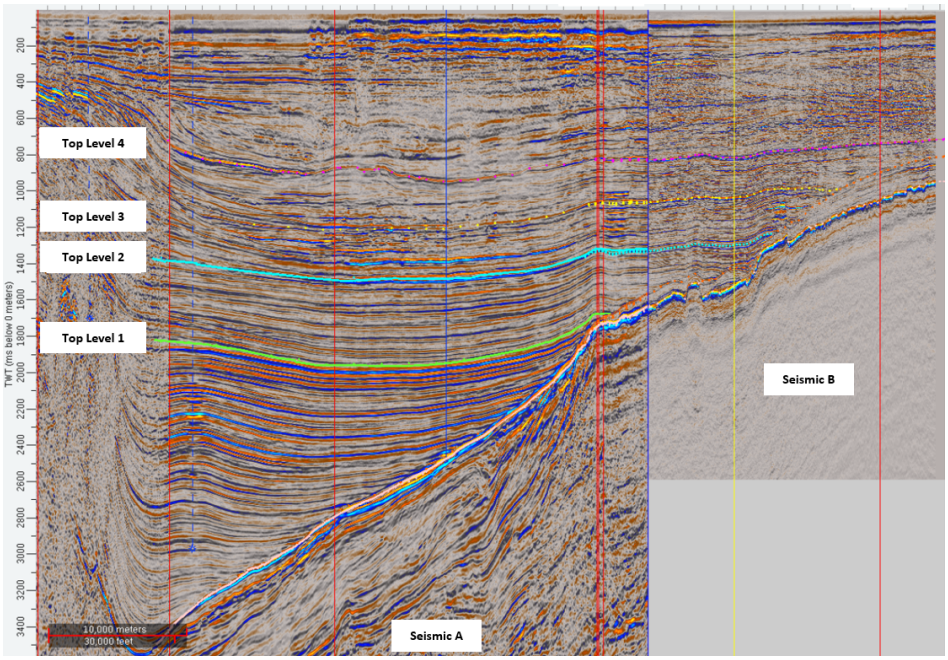

FIGURE 5.15: Seismic section through the Arlua field with interpreted horizons for the main reservoir layers.

of the Porto Garibaldi Formation are represented by distal turbidite sand lobes and fringes while the upper deposits of the Carola Formation are considered more proximal turbiditic sand lobes. In the very upper portion of the turbiditic series of the field, the sandy levels of the turbiditic deposits are interrupted by the presence of channel-like features, probably relevant to a turbiditic system with localized sediments entry points from the Balkan and superimposed on the regional sediments source coming from North. Nonetheless, this does not affect the lateral continuity of the turbiditic sandy levels that can be mapped for tens of kilometers from 3D seismic acquisitions (Fig. 5.15). This results in a multi-pay system in which every layer may have its own gas-water contact and a thickness variable from centimeters to meters. The portion we refer to consists of more than one hundred active layers lying from 900 m to 1800 m below mean sea level.

Gas is withdrawn by 28 producing wells, connected to two platforms, about 5 km apart. The two platforms are equipped with CGPS stations that have been acquiring data since the start-up of the production. The production program varies with the specific layer, according to the geometry, local pressure conditions and gas volume in place. Fig. 5.16 reports the pressure evolution in time for three representative points,

highlighting the high pressure variation between different layers. Fig. 5.16 also points out the complex reservoir layering, which can be appreciated in the section reported in the right panels.

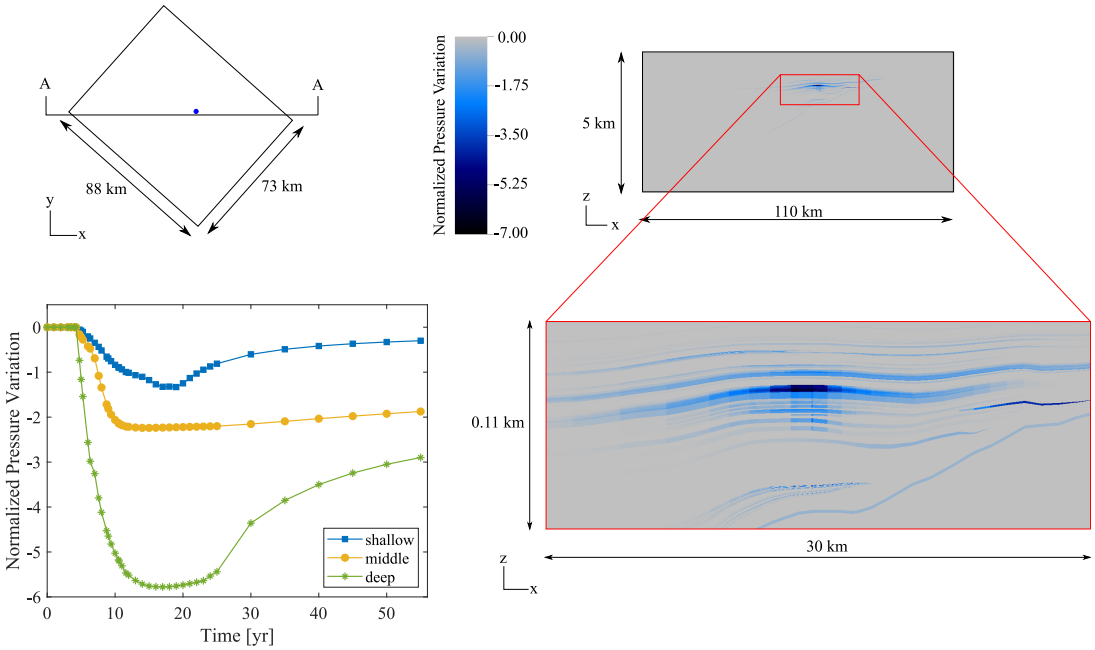

FIGURE 5.16: Pressure change evolution in the Arlua field. The bottom-left panel shows the maximum punctual values over time in a shallow, middle and deep layer of the reservoir. The markers indicate the time when the pressure data are available. The plain location of the point is shown in the sketch on the top left along with the indication of the trace of section A-A. The full view of section A-A and a zoom centered on the active layers are reported on the right, showing the normalized pressure at year 15. The vertical axis is exaggerated by a factor 10.

A dedicated well continuously acquires pressure data in six different layers, along with the measurements routinely acquired in the other producing wells. The large amount of available pressure data allowed for the development of an accurate history-matching process within a dynamic multi-phase flow model of the reservoir. For this reason, uncertainties related to the pressure field can be considered much smaller than those depending on other factors, hence the history-matched pressure behavior in time and space is used as input for the geomechanical model. This is also supported by the fact that the the mechanics-to-flow coupling is weak, since the gas compressibility is orders of magnitude higher than the rock compressibility and the space-time scale of interest is pretty large [Gambolati et al., 2000; Wang, 2000a; Pearse et al., 2014]. As a consequence, the update of the fluid-dynamic model with the updated geomechanics

parameters is needed only for specific detailed analyses.

The geomechanics of the multi-pay reservoir is investigated with the aid of a FEM simulator. The model domain covers an area of about 88 km $\times$ 73 km and extends down to 5 km depth (Fig. 5.17). It includes also the rocks surrounding the reservoir and the active aquifers, namely the overburden, underburden and sideburden. In the model, the behavior of the porous medium is described by appropriate constitutive laws, that are generally nonlinear. The choice of the most appropriate law represents a significant source of uncertainty, as described in the next section. The volume of interest has been discretized into a 3D FE mesh composed of 572,934 nodes and 550,800 hexahedrons (Fig. 5.17). This model has been used to train a gPCE surrogate that generates the ensemble realizations. The numerical simulations covers 55 years, according to the availability of the pressure data (bottom-left panel of Fig. 5.16).

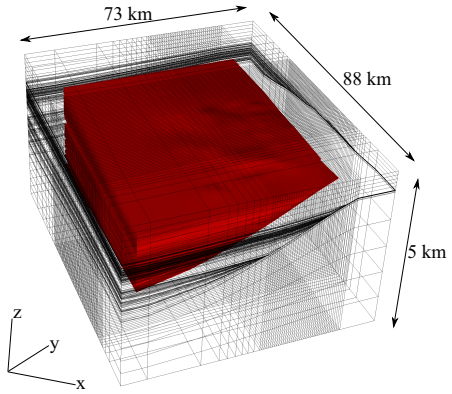

FIGURE 5.17: Discretized 3D domain with the active layers (reservoir and aquifer) in red. The vertical axis is exaggerated by a factor 10.

5.2.2 Sources of uncertainty and generation of the ensembles

The first step of the workflow consists in identifying the uncertain factors that have the main influence on the model outcomes and that can be explicitly treated as stochastic input variables in the simulations.

As already highlighted before, the main uncertainties are related to the nature and governing parameters for the constitutive behavior of the reservoir rock. Since the behavior of underburden and overburden does not significantly affect surface movements [Ferronato et al., 2010; Teatini et al., 2011], a deterministic linear elastic law may suffice, while different non-linear models can be selected for the active layers. The choice of

the most appropriate constitutive law depends on the availability of laboratory tests, the geological nature of the basin, and previous experiences. Uncertainties can be significant, especially at the beginning of the reservoir development, when the knowledge on the field behavior is generally quite limited. For this case, we select the constitutive laws already considered in the remainder of this thesis and generally used for real-world land subsidence analyses carried out in similar basins [Cassiani and Zoccatelli, 2000; Capasso and Mantica, 2006; Gemelli et al., 2020]: the MCC [Roscoe and Burland, 1968] and the VEP [Vermeer and Neher, 1999] model (see Section 2.3).

Among the governing parameters, the focus is on the ones that (i) are more uncertain and (ii) have a major impact on the outcomes. In particular, following the analyses reported in the previous section and in Zoccarato et al. [2020] and Gazzola et al. [2021], uncertainties have been associated to the modified compression index λ^* and the ratio R ($R \geq 1$), with the latter required only by the VEP model. A range of feasible values for those parameters can be identified thanks to the results of laboratory tests on samples cored from the reservoir. In particular, values of λ^* can be extrapolated from standard oedometer tests, while the values of R can be derived from the expression for the volumetric visco-plastic strain. The reader can refer to Musso et al. [2021] for additional details. According to the nature of the variables, a log-normal and a uniform distribution are assumed, as reported in Table 5.6. These values are assumed to be constant in space within the active layers. Indeed, as already stated before, the variability in space of the geomechanical parameters is much lower than that of the hydraulic parameters, and especially so along horizontal planes. Variations along the vertical direction are expected, but usually in a smooth way at the scale of the reservoir thickness. For this reason, we assume a geomechanically homogeneous rock formation in the reservoir layers, while in the overburden and underburden a simple linear elastic behavior is postulated with the geomechanical parameters varying with depth as a function of the vertical effective stress according to the law developed by Baú et al. [2002] for the Northern Adriatic basin, Italy. The Poisson coefficient is set homogeneous and equal to 0.30 everywhere, while the Biot coefficient is unitary. The modified swelling index k^* and the modified creep index μ^* are computed as $1/10\lambda^*$ and $1/60\lambda^*$, respectively.

Two forecast ensembles including 200 MC realizations each have been generated

[Zoccarato et al., 2020]. Their features are reported in Table 5.6. They are used to generate the initial guess of the expected field geomechanical behavior for the programmed development history.

TABLE 5.6: Characterization of the forecast ensembles. Constitutive law and prior distribution (with mean and variance) of the parameters.

Ensemble	**Law**	**Uncertain parameter distribution**
M01	MCC	$ln\,(\lambda^*) \sim \mathcal{N}\,(-2.58; 0.44)$
V01	VEP	$ln\,(\lambda^*) \sim \mathcal{N}\,(-2.58; 0.44)$ $\quad$ R $\sim \mathcal{U}\,(1.1; 1.5)$

5.2.3 Field monitoring program

The monitoring program on the field includes land surface movement and deep compaction measurements. The instrumentation has been installed at different dates, so that different pieces of information are available in different monitoring periods.

Measurements of sea bottom displacements over time are available since the early production phases by two CGPS permanent stations located on the two off-shore production platforms. The first station has been installed 4 years after the beginning of the modelling, while the second one started to operate 6 months later. Both stations have been recording data for about 8 years. Fig. 5.18 shows such data, normalized with respect to a constant positive value. Bathymetric and compaction measurements (Fig. 5.19 and Fig. 5.20, respectively) are normalized as well by the same value. We notice that the behavior over time of the measured displacements in Fig. 5.18 appears to be consistent with the pressure change in the reservoir (Fig. 5.16).

Two full coverage multibeam bathymetric surveys have been carried out before starting the production (at year 3) and after 7 years (at year 10). The difference between the two bathymetries allows for a spatially distributed measurement of the displacement of the seabed and the identification of the shape and the extension of the subsidence bowl (Fig. 5.19). The measurements along two orthogonal lines passing through the reservoir center have been considered for the assimilation.

Finally, compaction measurements at the reservoir depth are collected by radioactive markers. This technique consists of monitoring the relative position of a set of

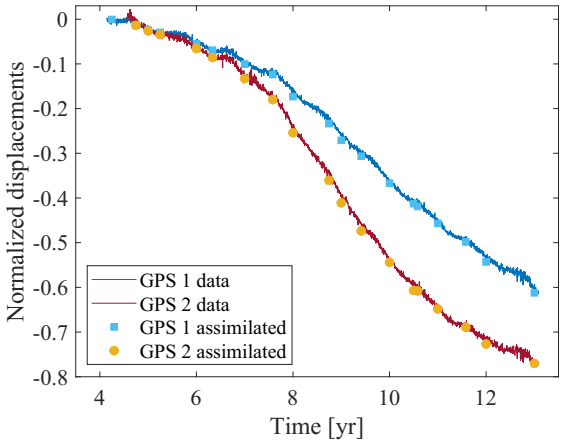

FIGURE 5.18: Surface displacements over time measured by the two CGPS stations. Continuous lines connect the recorded data, while dots are the assimilated values.

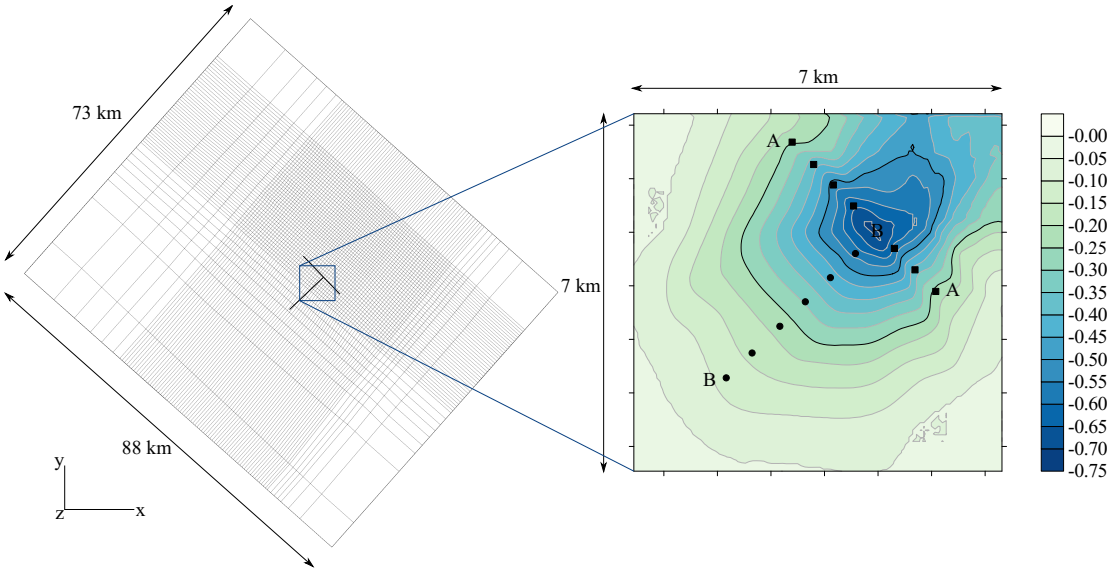

FIGURE 5.19: On the left, top of the discretized domain with the indication of the two bathymetric lines and the interpolation area. On the right, interpolated difference between the two bathymetric surveys performed 3 and 10 years after the model start, with the indication of the points used in the assimilation process.

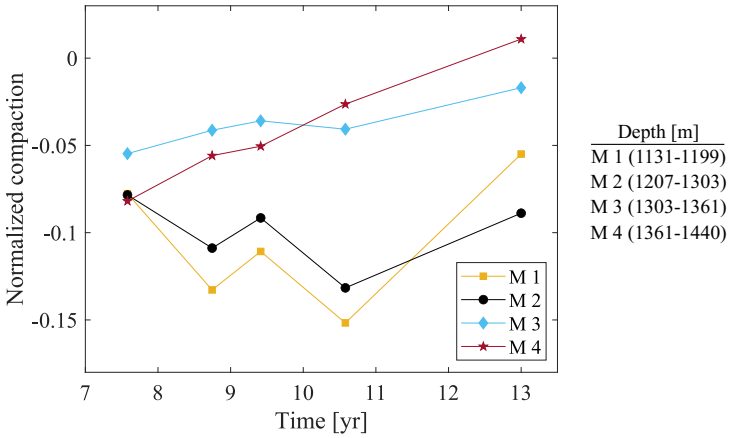

FIGURE 5.20: Values of compaction recorded by the radioactive marker techniques. The depth of the cumulative spacings is reported on the right. Notice that compaction generally decreases over time in agreement with the decrease of the yearly pressure depletion after year 8 (Fig. 5.16).

weakly radioactive bullets regularly shot in the formation along a vertical unproductive well prior to the casing operations [De Loos, 1973; Mobach and Gussinklo, 1994]. Four years after the beginning of the production (at year 7), 100 radioactive markers have been shot at a depth between 970 m and 1775 m, collecting data for about 6 years.

Fig. 5.21 summarizes the availability of different kinds of measurements with respect to the pressure information, i.e. to the output times of the production simulator.

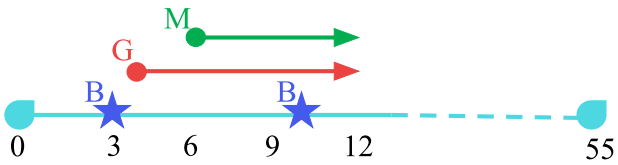

FIGURE 5.21: Timeline of pressure and measurement data. 55 years of pressure data are available from a reservoir simulator properly history-matched. Purple stars indicate the years of the bathymetric surveys (B), while the red and green arrows point out the availability of CGPS (G) and radioactive markers (M) measurements, respectively.

A number of significant observations have been used for the following DA process. In particular, the CGPS measurements at the times of the pressure known values (that are the markers in the bottom left panel of Fig. 5.16) have been selected, thus a total of 19 and 18 measurements for the first and second CGPS station, respectively (Fig. 5.18). To capture the spatial distribution of the subsidence bowl 13 points (dots and squares in Fig. 5.19) of the bathymetric surveys are used, corresponding to the original

points used to draw the subsidence map. Finally, since the recording of a single spacing (10.5 m) between two adjacent radioactive bullets can be often characterized by a high signal-to-noise ratio, compaction measurements have been cumulated in sets of adjacent spacings according to the geology of the active layers in order to reduce the errors. Thus, 4 cumulative compaction intervals for 5 time steps have been used (Fig. 5.20). Considering the number of measurements progressively available, the update of the overall field model through the DA steps is performed every 3 years starting from the beginning of the monitoring program. The total number of measurements used in each update step is reported in Table 5.7.

TABLE 5.7: Amount of available measurements for each assimilation date, respectively recorded from the CGPS stations (G), radioactive markers (M) and the bathymetry (B).

Year	Measurements			
	G	M	B	Tot
7	13	-	-	13
10	25	12	-	37
13	37	20	13	70

The error associated to each measurement accounts for both the accuracy of the measurement itself and the potential contribution of other simultaneous processes (e.g., tectonics, sediment deposition on the sea bottom), which are not modeled and could affect anyway the data. The error is drawn from a normal probability distribution with zero mean and standard deviation equal to 3 cm, 10 cm and 2 cm respectively for CGPS [van Leijen et al., 2016; Cenni et al., 2021], bathymetric surveys [Ernstsen et al., 2006] and radioactive markers [Macini and Mesini, 2002; Zoccatelli et al., 2010].

5.2.4 Results

The procedure presented in Chapter 4 is applied to develop an integrated geomechanical model for the reservoir management. As previously mentioned, an initial uncertain model is built prior to the reservoir development and then updated every 3 years from the beginning of the monitoring program. At every update, the correctness of the initial hypotheses is checked and the improvement of the prediction reliability is evaluated. If the update is not satisfactory, the initial hypotheses are re-discussed and the procedure

starts from the beginning. The amount of available measurements for each assimilation is reported in Table 5.7. As new observations are integrated in the process, uncertainties are expected to decrease both in the parameter and in the state ensembles.

Initial forecast

The environmental monitoring program of the field activities starts at year 4 (Fig. 5.21). At this point of the reservoir life, all the input uncertainties simply propagate to the output because no information is available to constrain the model. The resulting ensembles, denoted as initial forecast ensembles, are built considering the ranges of the parameters in Table 5.6. Fig. 5.22 shows the range of the predicted normalized displacements in time at the location of the two CGPS stations considering the MCC and the VEP constitutive behavior.

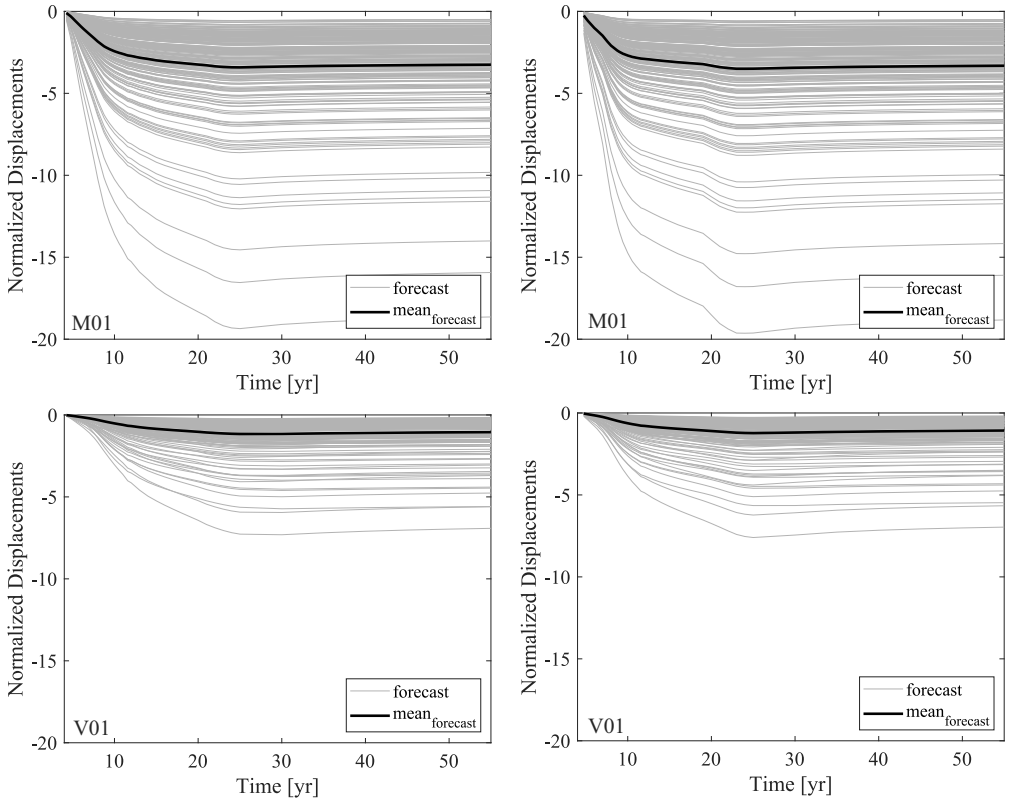

FIGURE 5.22: Forecast of the M01 (top) and V01 (bottom) ensembles modeling the displacements over time at the two CGPS locations. Left and right columns refer to CGPS 1 and CGPS 2, respectively.

Notice the large output uncertainty associated to the initial ranges of the governing parameters. The initial forecast ensembles predict a maximum displacement as large

as 20 times the minimum profile. Also, the two ensembles show quite a different uncertainty propagation, with the output range for M01 that is approximately twice V01. This is due to the different role played by the uncertain parameters in the constitutive models, as already observed in Section 5.1.4 and shown in Gazzola et al. [2021].

Since the prediction for the two CGPS locations is very similar, in the sequel only the first one is shown.

Update no. 1: year 7

The first model update is performed 3 years after the beginning of CGPS measurements, i.e. at year 7 of the simulation.

At this stage we can incorporate in the model 13 CGPS measurements (Table 5.7). The χ^2 values for the two forecast ensembles are reported in Table 5.8. This first result suggests the greater representativeness of the VEP compared to the MCC. The large difference between the values of the two ensembles can be explained considering (i) the greater spread of the ensembles M01 with respect to V01 and that (ii) the measurements are not even comprised within the forecast ensembles M01, as will be better highlighted later on.

TABLE 5.8: Update no.1, year 7: χ^2 values. The subscript points out the state, in this case $G1$ for CGPS 1, $G2$ for CGPS 2 and A for all the measurements.

Ensemble	χ^2_{G1}	χ^2_{G2}	χ^2_A
M01	1075.47	1395.90	1223.36
V01	12.30	19.53	15.63

The RF method assesses the probability of occurrence of each realization, as shown in Fig. 5.23. The probabilities of the realizations of the ensemble M01 are all close to zero, with the exception of a single realization close to probability 1 (left boxplot of Fig. 5.23). Conversely, the distribution of the probabilities for the ensemble V01 (right boxplot of Fig. 5.23) exhibits a larger spread. However, about half values are close to zero (third and fourth quartiles of the boxplot) and there are no realizations with probability larger than 3%. These results are in agreement with the outcomes of the χ^2-test, confirming that the ensemble V01 appears more appropriate to describe the

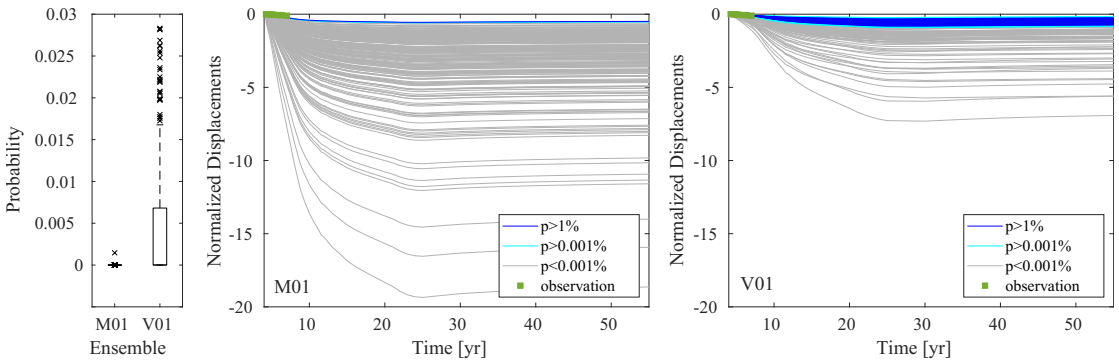

FIGURE 5.23: Update no. 1, year 7: RF analysis on the normalized displacements at CGPS 1 location for the M01 and the V01 ensembles. On the left the boxplots show the distribution of the probability for the two ensembles. The vertical axis has been truncated, so that one outlier close to 1 for the ensemble M01 is not visible.

measurements compared with the ensemble M01. However, due to the limited amount of data assimilated at this stage, we decided to cautiously update both the ensembles through the ES application. This allows also to verify a posteriori the reliability of the diagnostic tools in a challenging real application with few available measurements.

The outcomes of the assimilation step through the ES algorithm are shown in Fig. 5.24 and 5.25, and in Table 5.9. Fig. 5.24 shows the variation of the vertical displacements at the CGPS 1 location before (gray) and after (red) the ES application. Green squares denote the assimilated measurements. As noticed before, the forecast ensemble M01 (gray stack in the upper panels of Fig. 5.24) does not even include the observations (green squares), thus explaining the poor results obtained in the diagnostic stage (χ^2 and RF analysis). Therefore, we can conclude that the forecast ensemble V01 appears to be more suitable to describe the measurements.

TABLE 5.9: Update no. 1, year 7: AE and AES values for the forecast ensembles and improvement J.

Ensemble	**M01**				**V01**			
	AE	***J* [%]**	**AES**	***J* [%]**	**AE**	***J* [%]**	**AES**	***J* [%]**
GPS 1	6.36e-01	98.52	1.36e+00	98.39	5.61e-02	85.58	4.30e-01	68.46
GPS 2	7.61e-01	98.14	1.45e+00	98.54	6.75e-02	86.22	4.70e-01	71.04
$ln(\lambda^*)$	-	-	5.28e-01	60.27	-	-	5.28e-01	50.46
R	-	-	-	-	-	-	9.47e-02	16.40

Nevertheless, the conditioning of the model appears more effective in case M01, i.e.

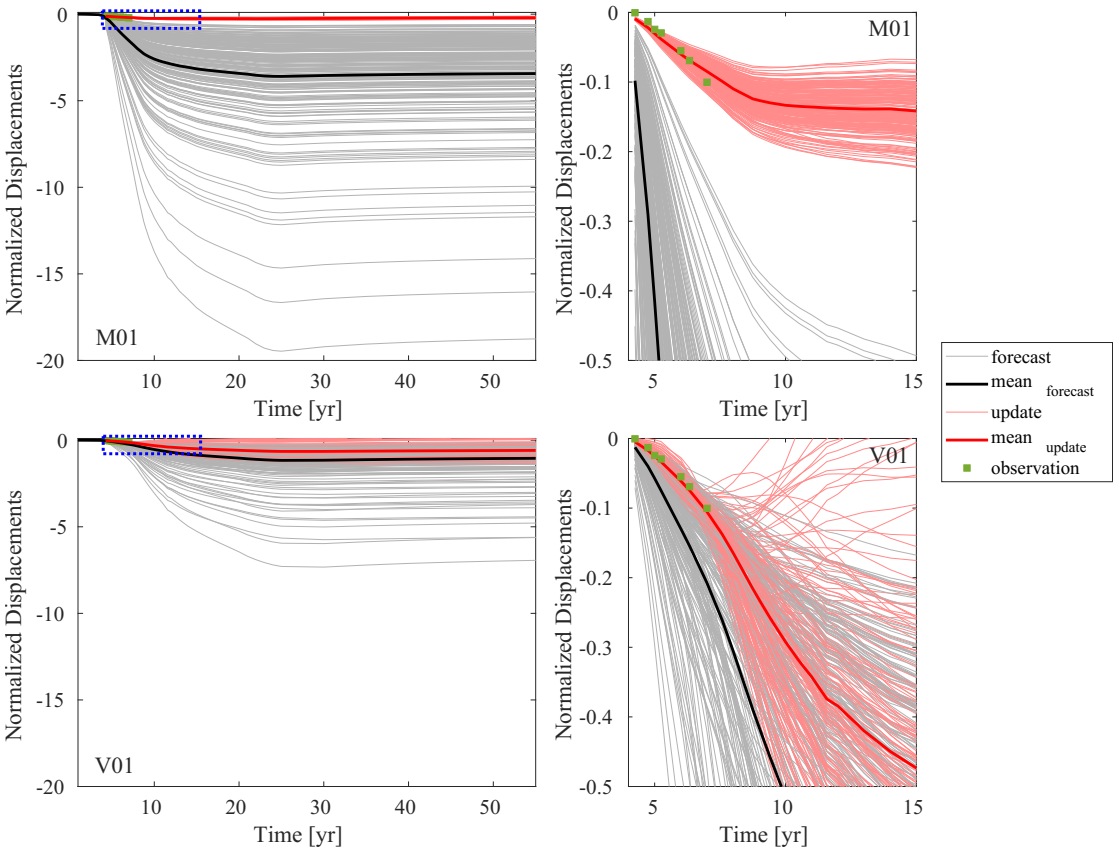

FIGURE 5.24: Update no. 1, year 7: displacements over time at CGPS 1 location for the ensemble M01 (top) and V01 (bottom). On the left, the total displacements from the beginning of the simulation are plotted. In the first 4 years, the mean of the forecast parameters is assumed to run the model, since no measurements are available. On the right, a zoom around the CGPS measurements (corresponding to the blue box on the left) is shown.

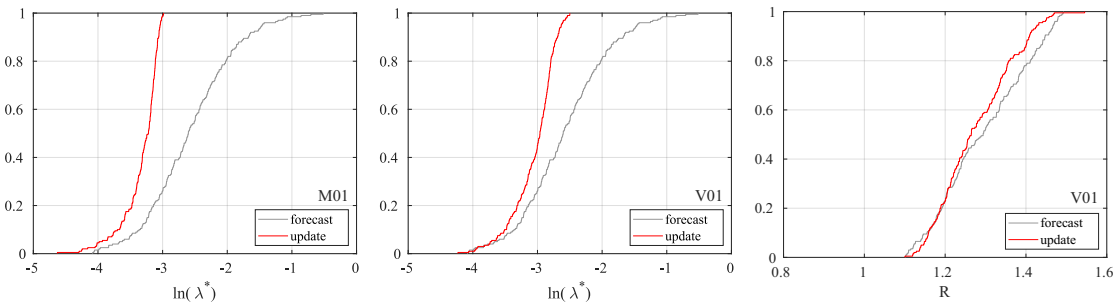

FIGURE 5.25: Update no. 1, year 7: CDF of $ln(\lambda^*)$ for M01 (left) and V01 (center), and CDF of the parameter R for V01 (right).

the update (red) ensemble of Fig. 5.24 is less spread than the update of V01, whose behavior appears sometimes unrealistic. Moreover, the J values provided in Table 5.9 are higher for M01, though the motivation is partially due to the higher values of the forecast indices (AE and AES) because the ensembles are farther from the measurements with respect to the case V01. It is worth mentioning that the update ensembles used for the red plots and to compute the improvements J are those resulting directly from the ES update of the state variables.

Also the improvement J for the parameter λ^* is slightly better in the case M01, that is the update parameter ensemble is slightly narrower than in the V01 update. This is shown graphically in Fig. 5.25, where the forecast and update distributions of the parameters for the ensemble M01 and V01 are plotted. By distinction, the distribution of the parameter R appears to be almost unaffected by the integration of the displacement observations.

The red profiles in Fig. 5.25 are converted into the Gaussian distributions in Table 5.10. These distributions are used to create the new forecast ensembles for the successive model update.

TABLE 5.10: Update no. 2, year 10: probability distributions for the uncertain parameters. The parameter R is now characterized by a Gaussian distribution (and not uniform as in the forecast, Table 5.6), due to the ES update.

Ensemble	**Law**	**Uncertain parameter**
M02	MCC	$ln\,(\lambda^*) \sim \mathcal{N}\,(-3.32; 0.08)$
V02	VEP	$ln\,(\lambda^*) \sim \mathcal{N}\,(-3.05; 0.11) \quad R \sim \mathcal{N}\,(1.28; 0.01)$

Update no. 2: year 10

The second update of the integrated model is carried out at year 10 using 37 observations. In this case, marker measurements are available in addition to CGPS (Table 5.7). The new forecast ensembles, M02 and V02, have been created with the distributions reported in Table 5.10.

The first evaluation of the ensembles is made by the χ^2-test, which results are in Table 5.11. Despite χ^2_{M02} is significantly smaller that χ^2_{M01}, it remains $\chi^2_{M02} \gg \chi^2_{V02}$. The difference between the two models is mainly due to the χ^2 values related to the

TABLE 5.11: Update no.2, year 13: χ^2 values. The subscript M stands for marker only.

Ensemble	χ^2_{G1}	χ^2_{G2}	χ^2_M	χ^2_A
M02	159.11	172.14	7.51	114.17
V02	7.89	19.64	11.06	12.73

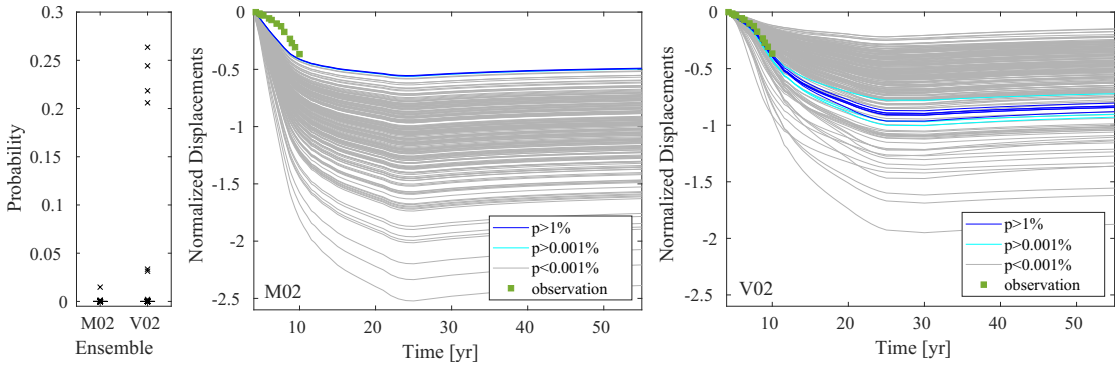

FIGURE 5.26: Update no. 2, year 13: the same as Fig. 5.23 for the M02 and the V02 ensembles. The vertical axis of the boxplot on the left has been truncated, thus it is not visible one outlier close to 1 for the ensemble M02.

CGPS observations. On the contrary, the value χ^2_M associated to the compaction measurements is quite similar for the two ensembles, with the M02 model slightly better than V02.

The outcomes of the RF algorithm are shown in Fig. 5.26. First, it can be noticed that the ensembles of the update no. 2 are considerably narrower (about 10 times for the MCC constitutive law) with respect to those of the previous assimilation. Moreover, they appear closer to the CGPS measurements, thus proving the effectiveness of the ES at year 7. The current RF results show higher probabilities of occurence for the realizations of both the constitutive laws with respect the previous assimilation (boxplots of Fig. 5.23). However, most of the realizations have an almost null probability of occurrence. Again, the VEP constitutive model appears more appropriate to describe the available measurements in the field. This is particularly clear in the right panels of Fig. 5.26 where the forecast ensembles related to CGPS 1 state, colored according to the RF probabilities, are plotted along with the observations. The MCC model is not able to capture the behavior in time of the measurements, i.e. the plot of the displacements has a totally different curvature than the observations with the latter falling out of the expected forecast.

Based on the diagnostic outcome, we elect to discard the MCC and focus only on the VEP constitutive law for the following updates.

The results of the application of the ES algorithm are reported in Fig. 5.27, 5.28 and 5.29, and in Table 5.12. Fig. 5.27 shows the evolution of the vertical displacements over time at the location of CGPS 1 station. The measurements are centered inside the ensemble and the update from ES (red stack) allows to reduce the uncertainty and match the available observations. By distinction, the compaction measurements are not always comprised within the model forecast (Fig. 5.28), especially for the shallowest spacing (M1). In general, more difficulties can be noticed in constraining the model with respect to the CGPS states.

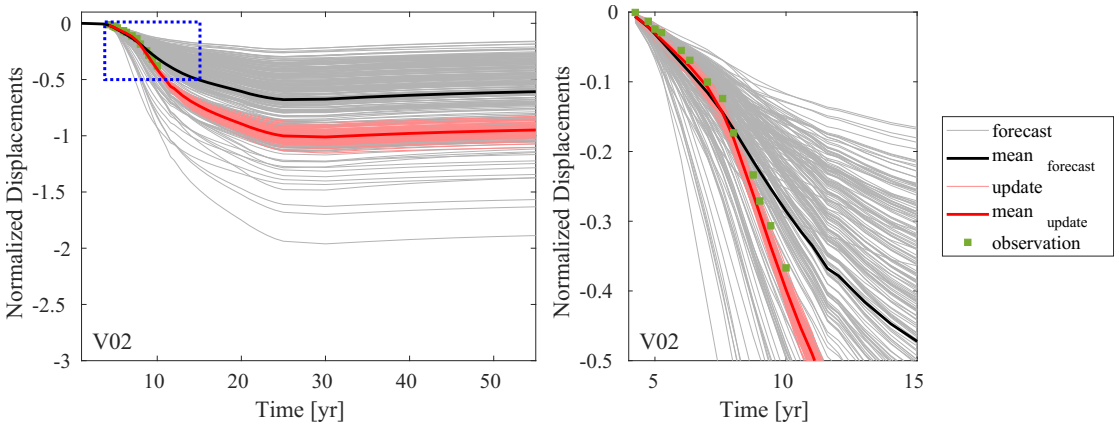

FIGURE 5.27: Update no. 2, year 10: displacements over time in correspondence of CGPS 1 station. Forecast (gray) and update (red) ensemble for the case V02. A zoom around the CGPS measurements (corresponding to the blue box on the left) is shown on the right.

TABLE 5.12: Update no. 2, year 10: AE and AES values for the forecast ensembles and improvement J.

Ensemble	**V02**			
	AE	***J* [%]**	**AES**	***J* [%]**
GPS 1	5.03e-02	69.86	1.37e-01	85.09
GPS 2	8.70e-02	82.56	1.44e-01	83.20
marker	5.87e-02	21.04	9.56e-03	71.06
$ln(\lambda^*)$	-	-	2.61e-01	31.43
R	-	-	7.20e-02	49.67

The improvements J in Table 5.12 are all positive, pointing to both a reduction of the prediction spread and a forecast closer to the observations. However, the update of the parameters is not fully satisfactory, because the probability distribution for the

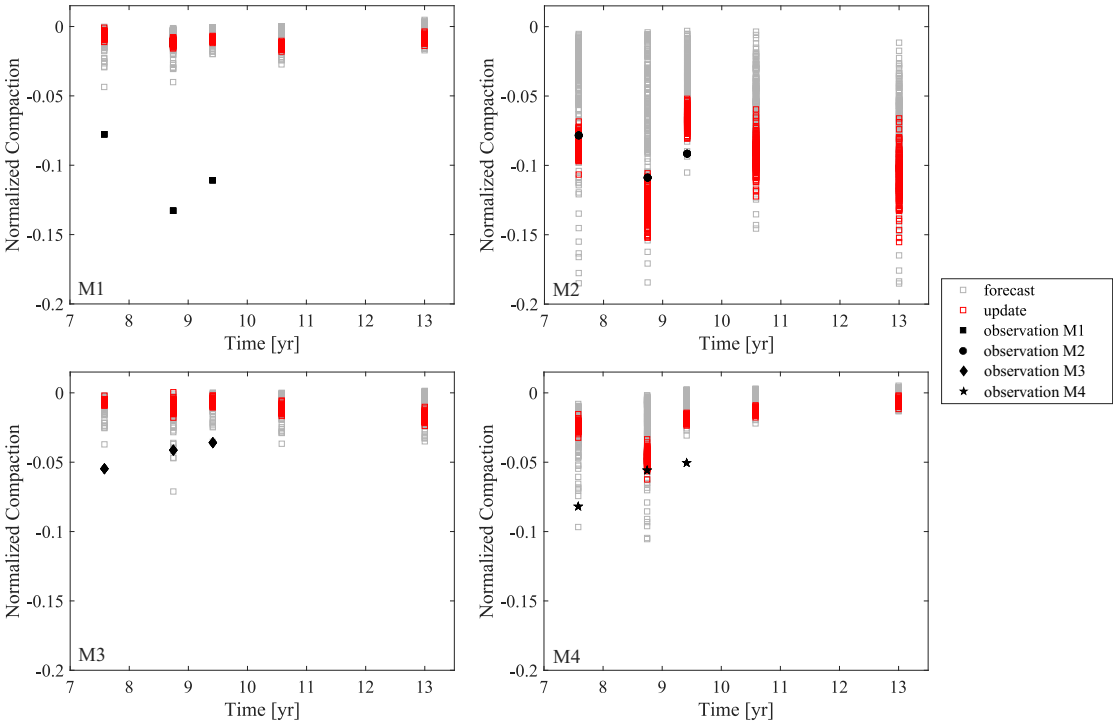

FIGURE 5.28: Update no. 2, year 10: compaction over time for the four spacings. Forecast (gray) and update (red) ensemble for the case V02.

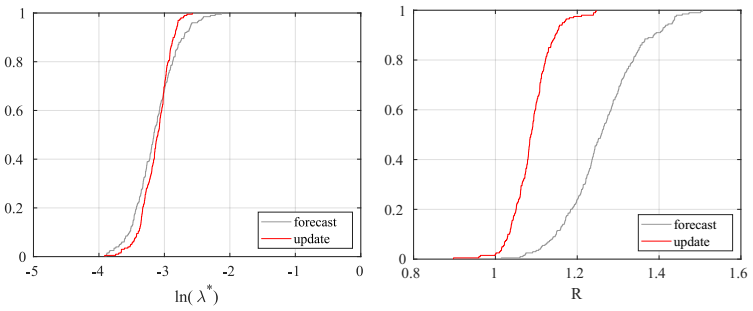

FIGURE 5.29: Update no. 2, year 10: CDF for $ln(\lambda^*)$ and R for the ensemble V02.

ratio R (right panel of Fig. 5.29) includes also non-physical values, i.e. values of R lower than 1. These outcomes probably reflect the difficulties in constraining the compaction states.

At this point, two scenarios have been taken into account to generate the new forecast ensembles for the next update:

1. The previous results could be a symptom of the inability of the ES algorithm to constrain both the uncertain parameters with the available measurements. A possible explanation is that the problem might be over-parameterized, in the sense that different pairs of values can provide similar outcomes. A possible choice for

building the VEP ensemble for the next update is to consider only λ^* uncertain, whose distribution is obtained from the updated probability distribution of Fig. 5.29:

$$ln\,(\lambda^*) \sim \mathcal{N}\,(-3.13; 0.05)$$

while the parameter R is kept constant and equal to the update mean, i.e. R = 1.08. Even if neglecting the remaining uncertainty on R is a strong assumption, it can be useful in the context of this paper to test the robustness of the proposed approach.

2. Since the non-physical values are the final tail of the R distribution, it is possible to remove only the few values of R that are lower than 1. Hence, both λ^* and R are kept uncertain for the next assimilation in the attempt that the increase in the assimilated measurements improves that condition. Table 5.13 reports the distributions that summarize the red curves in Fig. 5.29 and are used to create the new forecast ensemble in this case.

TABLE 5.13: Update no. 3, year 13: probability distribution of the uncertain parameters.

Ensemble	**Law**	**Uncertain parameter**
V03	VEP	$ln\,(\lambda^*) \sim \mathcal{N}\,(-3.13; 0.05)$ $R \sim \mathcal{N}\,(1.08; 0.002)$

Update no. 3: year 13

The third update of the integrated model is carried out at year 13 and includes also the bathymetric surveys. Details on the number of available measurements are in Table 5.7. In the following the results obtained assuming uncertain only λ^* or both λ^* and R are presented.

Uncertainty on λ^*

As before, a preliminary evaluation is made by the χ^2-test. The outcomes are:

$$\chi^2_{V03,G1} = 91.06 \qquad \chi^2_{V03,G2} = 64.58 \qquad \chi^2_{V03,M} = 7.33 \qquad \chi^2_{V03,B} = 5.47$$

$$\chi^2_{V03,A} = 44.43$$

where the subscript B refers to the bathymetric data. With respect to the previous assimilation (V02, Table 5.11), the average χ^2 value for the ensemble V03 is higher due to the increase in the χ^2 values of the CGPS states.

The results of the RF are shown in Fig. 5.30. Fixing the R value seems to worsen the forecast ensembles capability to reproduce the CGPS observations (top of Fig. 5.30), with the measurements that are not completely comprised within the stacks.

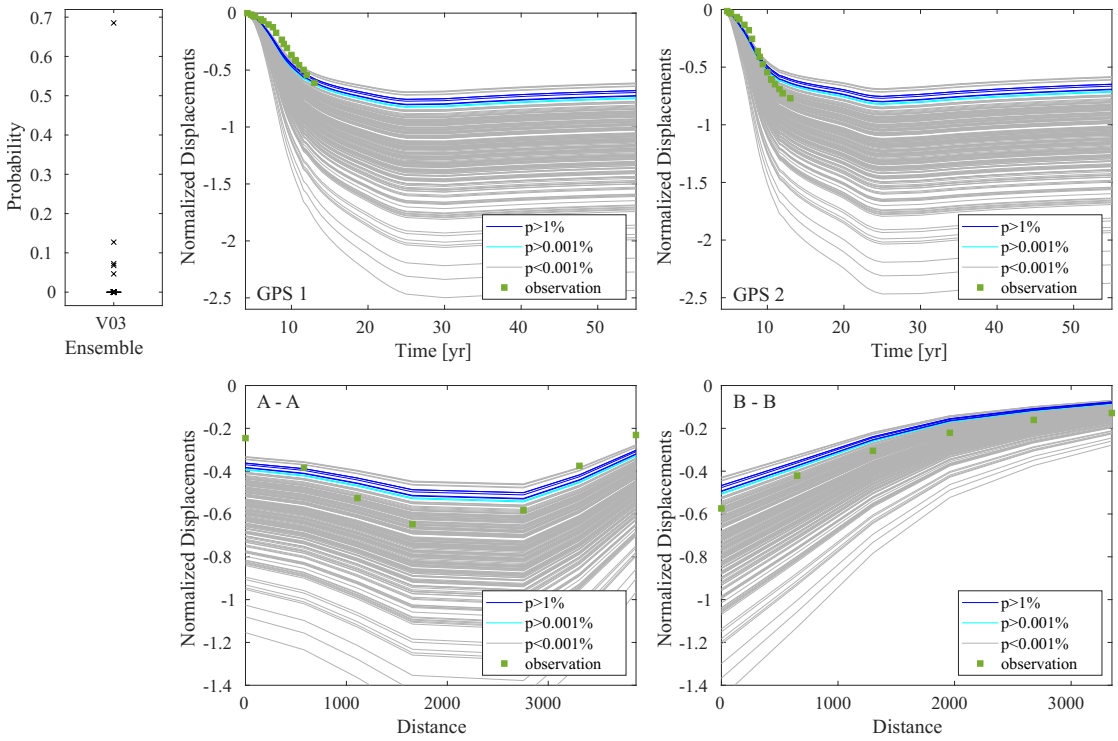

FIGURE 5.30: Update no. 3, year 13 (λ^* uncertain): RF outcomes for the V03 ensemble, using all the available measurements. The top panels provide the ensembles of the CGPS measurements, and the bottom panels the ensembles of the bathymetric observations along the two profiles A-A and B-B shown in Fig. 5.19. On the top left the boxplot representation.

The ES outcomes are shown in Fig. 5.31 for the CGPS states, in Fig. 5.32 for the

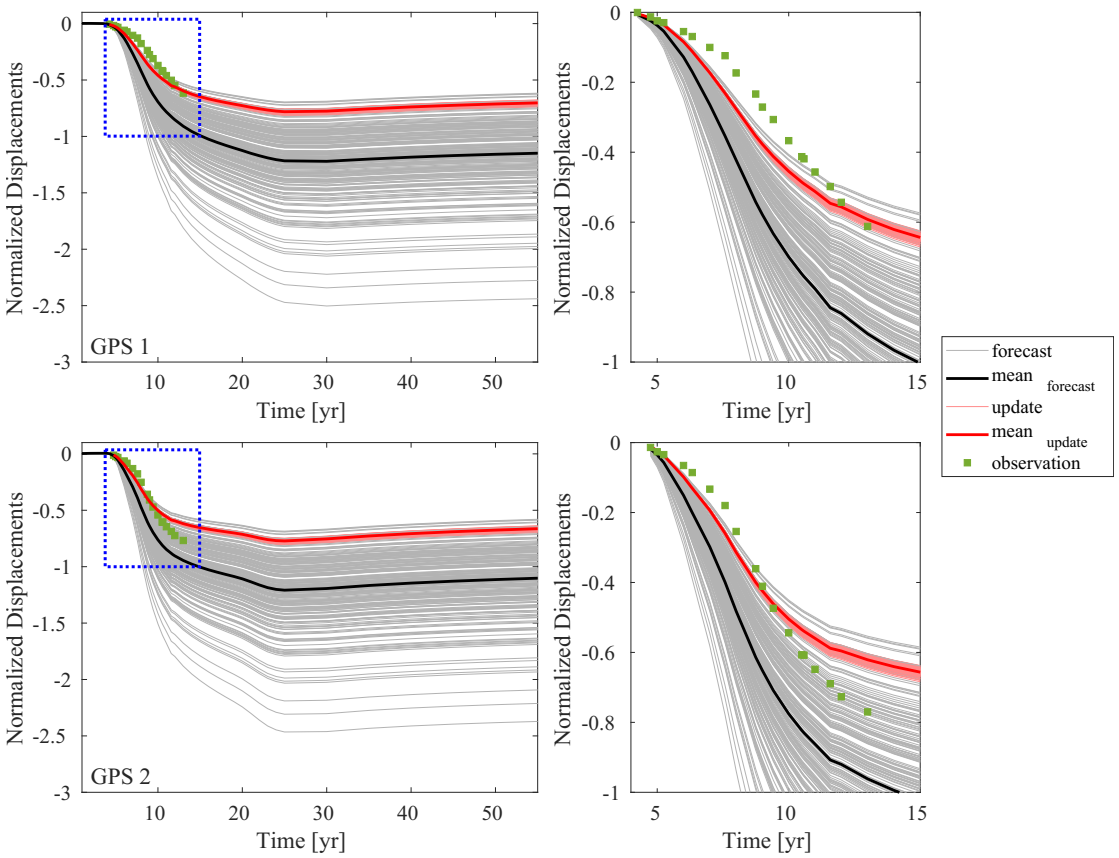

FIGURE 5.31: Update no. 3, year 13 (λ^* uncertain): displacements over time in correspondence of the two CGPS stations. Forecast (gray) and update (red) ensemble for the case V03. Zoom around the CGPS measurements (corresponding to the blue box on the left) are provided on the right.

marker measurements and in Fig. 5.33 for the bathymetric surveys, while Fig. 5.34 refers to the parameter λ^*, and Table 5.14 summarizes the indices AE and AES and their improvements. As noticed before, the CGPS measurements are now partially out of the ensembles and the behavior in time is not perfectly matched (Fig. 5.31). The compaction measurements still remain difficult to constrain (Fig. 5.32), while the bathymetric ensembles approximate quite accurately the data (Fig. 5.33). Looking at Table 5.14, it can be noted that the indices AE related to the CGPS forecast ensembles, i.e. the measure on average of the distance between the ensemble and the measurements, are higher than those of the previous update (Table 5.12). This means that the choice of the parameter distributions used to create the updated forecast ensemble and the addition of new observations penalize the match with the CGPS measurements. In any case, ES tends to effectively constrain the model to the available observations, with

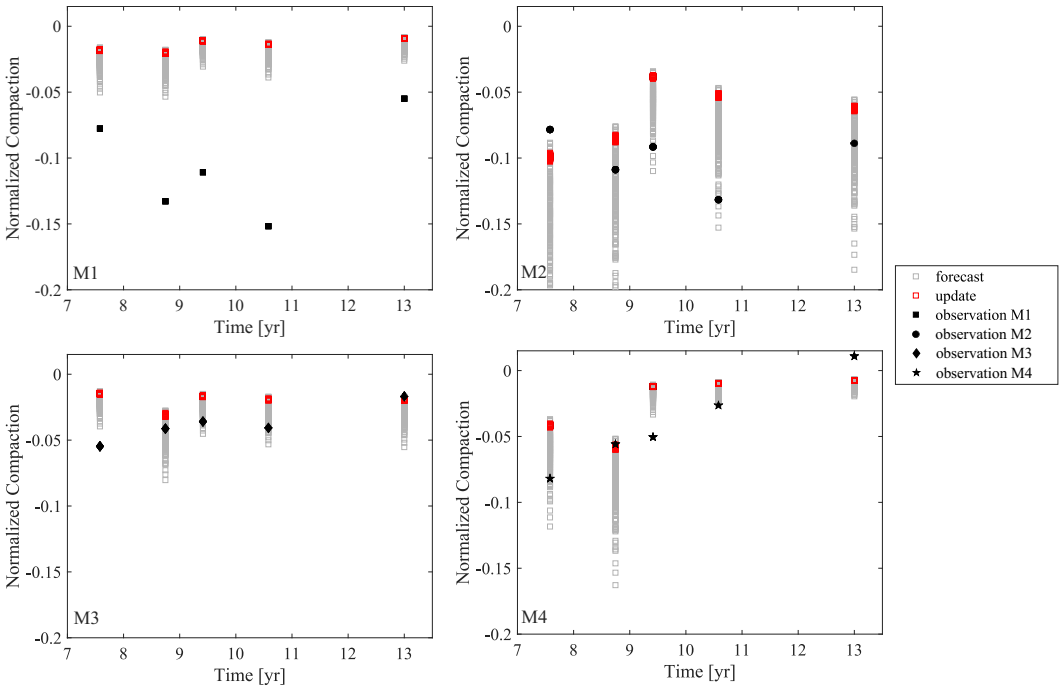

FIGURE 5.32: Update no. 3, year 13 (λ^* uncertain): compaction over time for the four spacings. Forecast (gray) and update (red) ensembles for the case V03. Due to visualization reason, few values between -0.20 and -0.28 have been left out for the spacing M2 at time 7.5 yr.

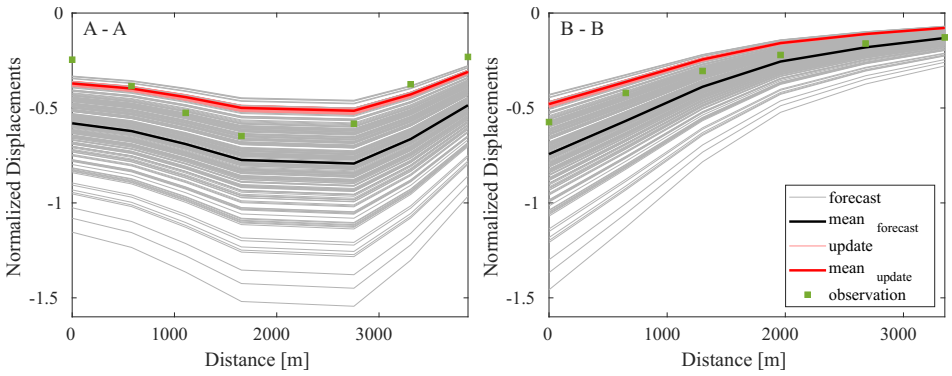

FIGURE 5.33: Update no. 3, year 13 (λ^* uncertain): model displacements and bathymetric measurements. Forecast (gray) and update (red) ensembles for the case V03.

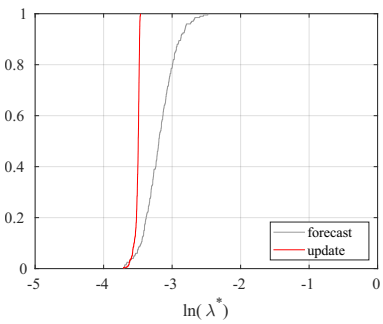

FIGURE 5.34: Update no. 3, year 13 (λ^* uncertain): CDF for $ln(\lambda^*)$ for the ensemble V03.

TABLE 5.14: Update no. 3, year 13 (λ^* uncertain): AE and AES values for the forecast ensembles and improvement J.

Ensemble	**V03**			
	AE	***J* [%]**	**AES**	***J* [%]**
GPS 1	2.17e-01	74.14	1.51e-01	96.58
GPS 2	1.77e-01	68.66	1.59e-01	96.57
marker	4.07e-02	-6.54	8.25e-03	96.31
bathymetry	1.72e-01	57.71	9.89e-02	96.53
$ln(\lambda^*)$	-	-	1.81e-01	85.57

the exception of the compaction measurements that present a negative J (Table 5.12). Observe, however, that the cumulative AE value for the compaction measurement is already much smaller than the AE values for the other observations. The final update of the parameter distribution is:

$$ln\left(\lambda^*\right) \sim \mathcal{N}\left(-3.51; 0.001\right)$$

This updated parameter distribution is used as input for the final geomechanical model used for the prediction of the future reservoir behavior. The resulting state ensembles in terms of variation of the vertical displacements over time at the two CGPS locations are shown in Fig. 5.35.

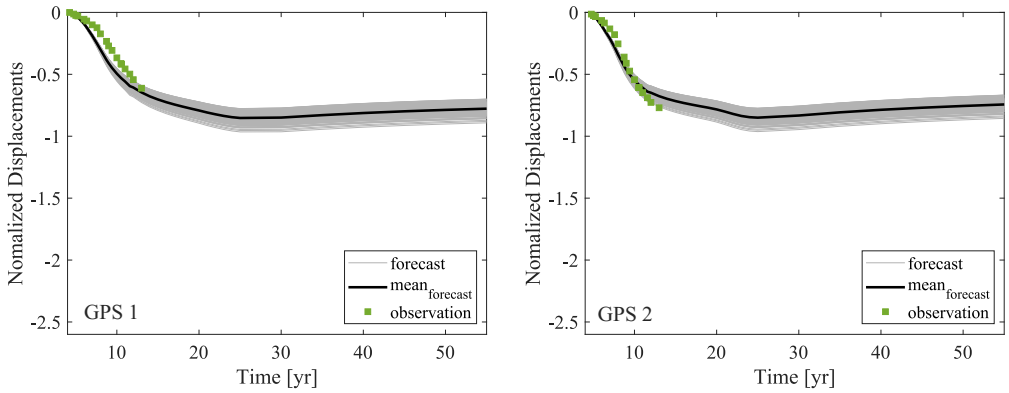

FIGURE 5.35: Update no. 3, year 13 (λ^* uncertain): ensembles of the CGPS states obtained running the geomechanical model with the final update of the parameters.

Uncertainty on λ^* and R

Finally, the forecast ensembles are created with the updated distribution of both λ^* and R from the previous assimilation (Table 5.13), neglecting the few values of R lower than 1. Thus, the distribution of R has been restricted to the condition $R \geq 1$ to consider only physical values.

The results of the χ^2-test are:

$$\chi^2_{V03,G1} = 110.33 \qquad \chi^2_{V03,G2} = 85.57 \qquad \chi^2_{V03,M} = 7.61 \qquad \chi^2_{V03,B} = 7.41$$

$$\chi^2_{V03,A} = 55.50$$

These values are higher than the ones of the V02 ensembles, especially for the CGPS states, just as those of V03 with only λ^* uncertain.

The results of the RF are shown in Fig. 5.36. The spread of the stacks is comparable with the previous scenario where only λ^* is kept uncertain (Fig. 5.30), but now the behavior in time is better reproduced and the measurements are completely comprised within the forecast ensembles.

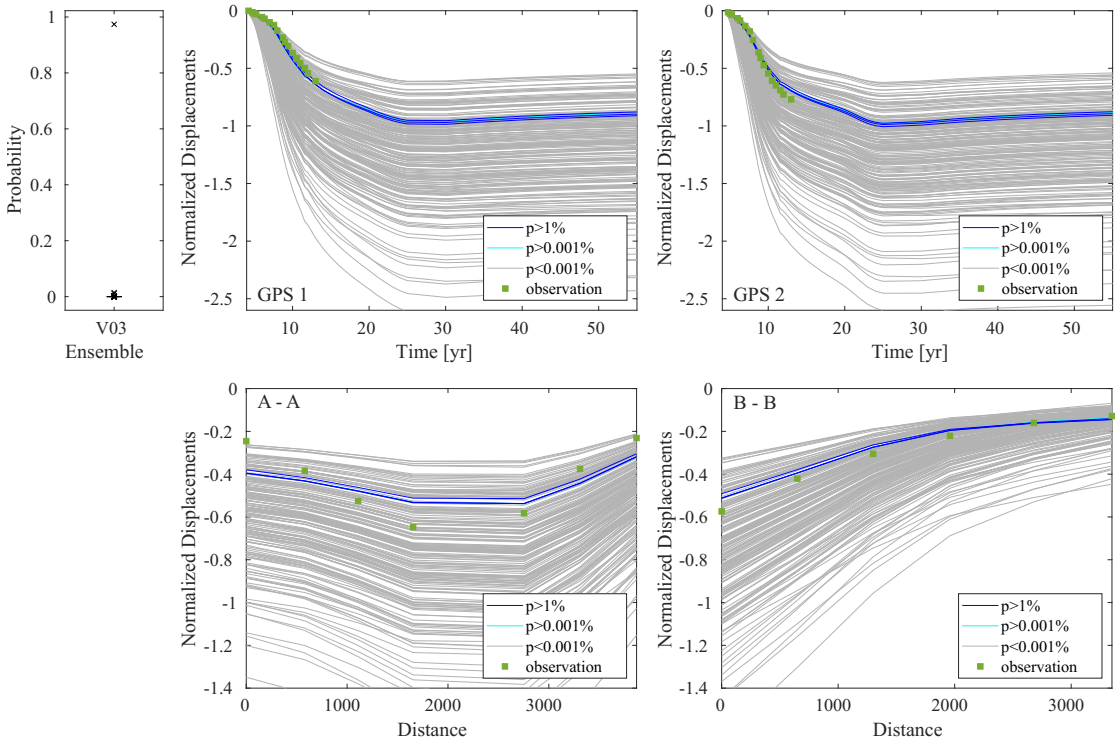

FIGURE 5.36: Update no. 3, year 13 (λ^* and R uncertain): RF outcomes as in Fig. 5.30

The outcomes of ES are shown in Fig. 5.37 for the CGPS states, in Fig. 5.38 for the radioactive marker measurements and in Fig. 5.39 for the bathymetric surveys. Fig. 5.40 refers to the parameter λ^* and R. Finally, Table 5.15 summarizes the indices AE and AES and their improvements. As before, the best results from ES regard the forecast of the vertical displacements in time. The CGPS measurements (Fig. 5.37) are quite accurately approximated as well as the bathymetric surveys (Fig. 5.39), while the compaction observations (Fig. 5.38) are still difficult to model.

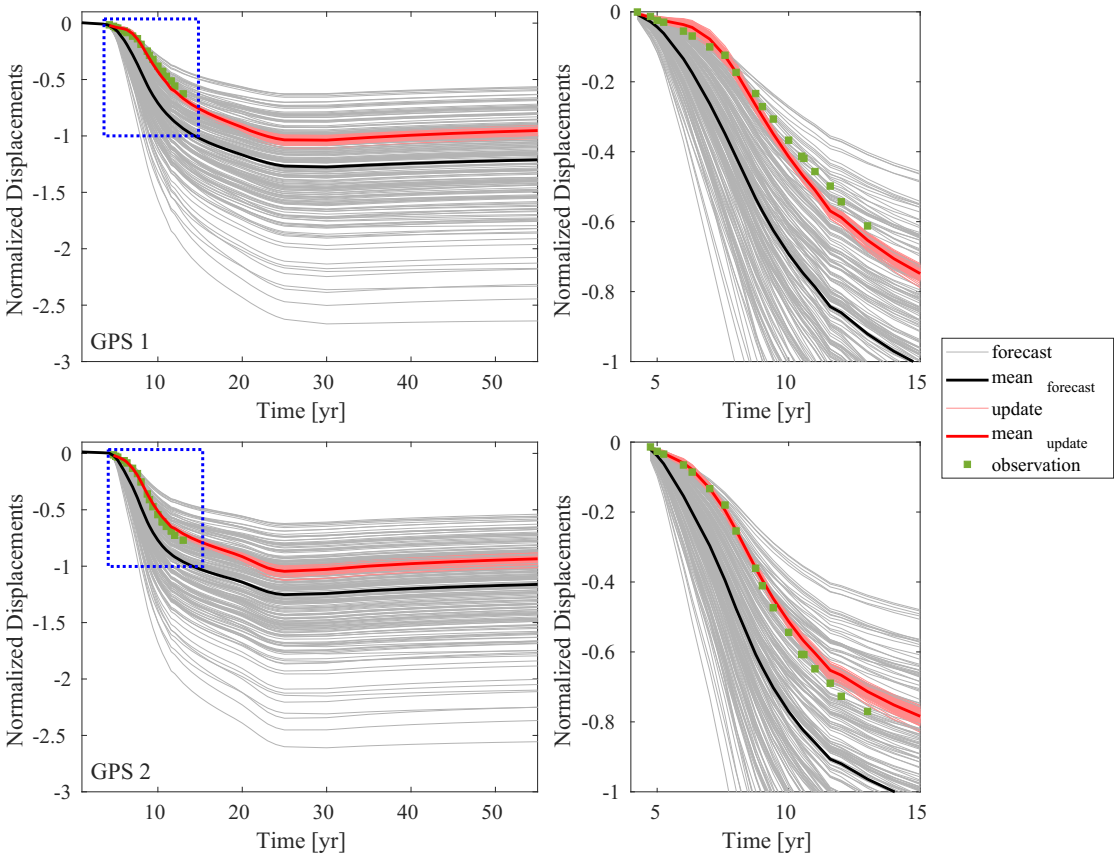

FIGURE 5.37: Update no. 3, year 13 (λ^* and R uncertain): displacements over time at the two CGPS locations. Forecast (gray) and update (red) ensemble for the case V03. Zoom around the CGPS measurements (corresponding to the blue box on the left) are provided on the right.

The red curves in Fig. 5.40 are converted in the final update of the parameter distribution, that is:

$$ln\left(\lambda^*\right) \sim \mathcal{N}\left(-2.82; 0.005\right)$$

$$\mathrm{R} \sim \mathcal{N}\left(1.21; 0.0002\right)$$

with the update of R returning inside physical values ($\mathrm{R} \geq 1$). This updated parameter

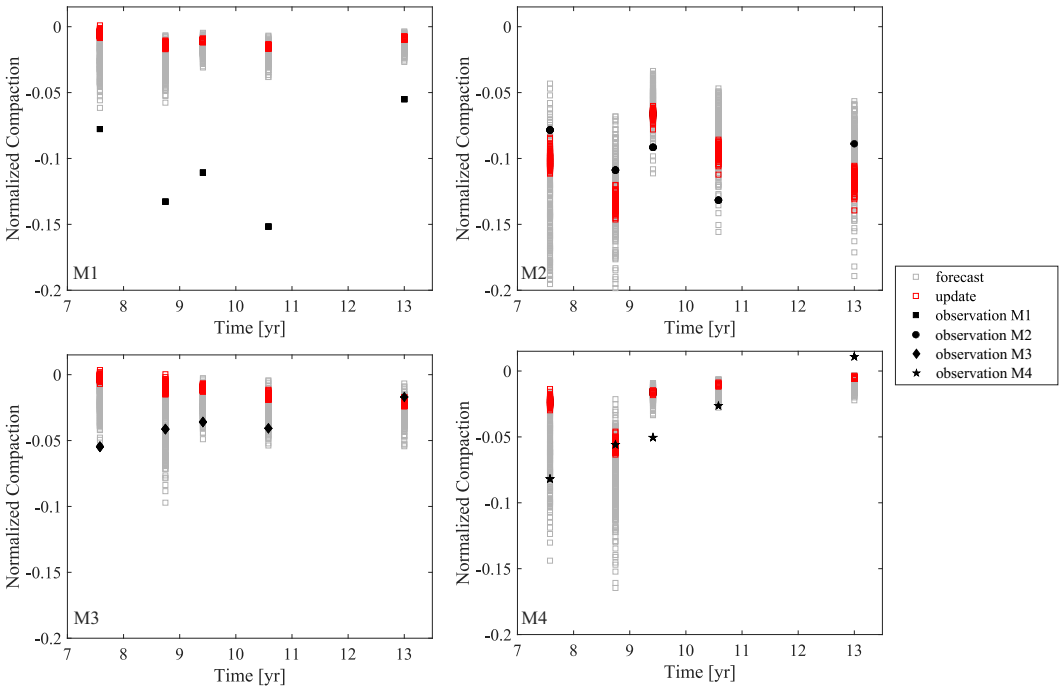

FIGURE 5.38: Update no. 3, year 13 (λ^* and R uncertain): compaction over time for the four spacings. Forecast (gray) and update (red) ensembles for the case V03. Due to visualization reason, few values between -0.20 and -0.28 have been left out for the spacing M2 at time 7.5 yr.

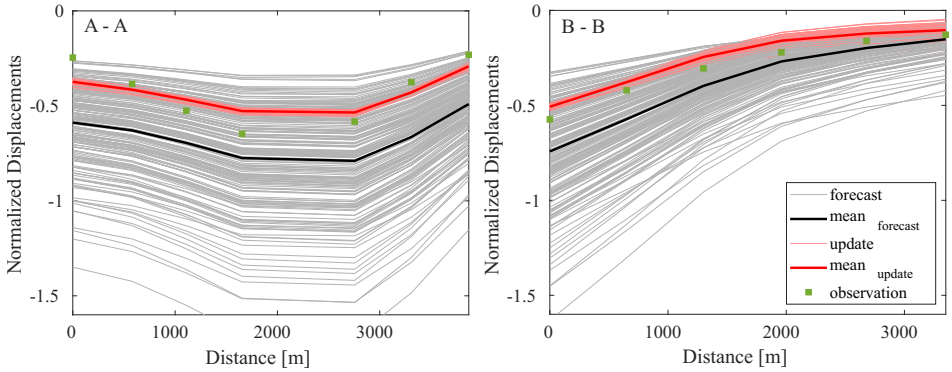

FIGURE 5.39: Update no. 3, year 13 (λ^* and R uncertain): model displacements and bathymetric measurements. Forecast (gray) and update (red) ensembles for the case V03.

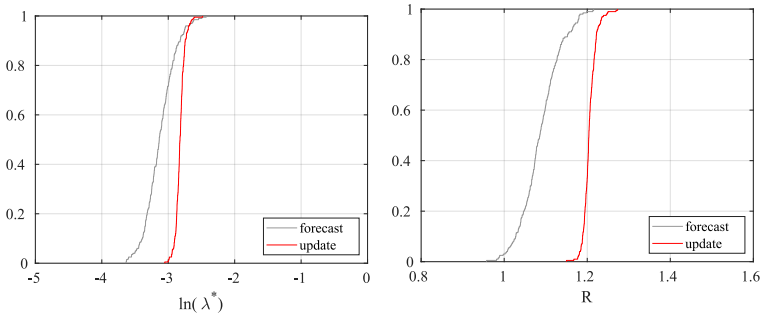

FIGURE 5.40: Update no. 3, year 13 (λ^* and R uncertain): CDF for $ln(\lambda^*)$ and R for the ensemble V03.

TABLE 5.15: Update no. 3, year 13 (λ^* and R uncertain): AE and AES values for the forecast ensembles and improvement J.

Ensemble	**V03**			
	AE	***J* [%]**	**AES**	***J* [%]**
GPS 1	2.20e-01	86.51	2.11e-01	95.17
GPS 2	1.94e-01	88.31	2.11e-01	94.89
marker	4.17e-02	-4.96	1.12e-02	87.25
bathymetry	1.95e-01	68.50	1.43e-01	93.68
$ln(\lambda^*)$	-	-	1.79e-01	70.84
R	-	-	3.78e-02	70.57

distribution is used as input for the geomechanical model. The resulting CGPS state ensembles are shown in Fig. 5.41, where an important reduction in the uncertainty with the model constrained around the measurements is evident. The overall observations are better reproduced by this update, with the final prediction more uncertain with respect to the previous ensemble (only λ^* uncertain). It can be expected, however, that the following model update will adjust the prediction and further reduce the uncertainty.

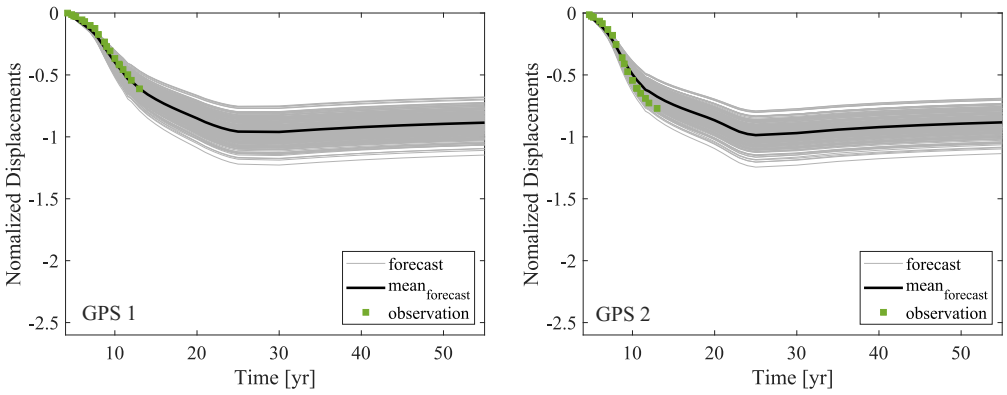

FIGURE 5.41: Update no. 3, year 13 (λ^* and R uncertain): ensembles of the CGPS states obtained running the geomechanical model with the final update of the parameters.

Importance of different measurements

Finally, the relative importance of different types of measurements on the assimilation results is investigated considering the ensemble with both λ^* and R uncertain. Each measurement type (CGPS, marker or bathymetry) is excluded from the ES assimilation

one at a time, in order to evaluate its influence on the overall update at year 13. Results are shown in Fig. 5.42 and Fig. 5.43.

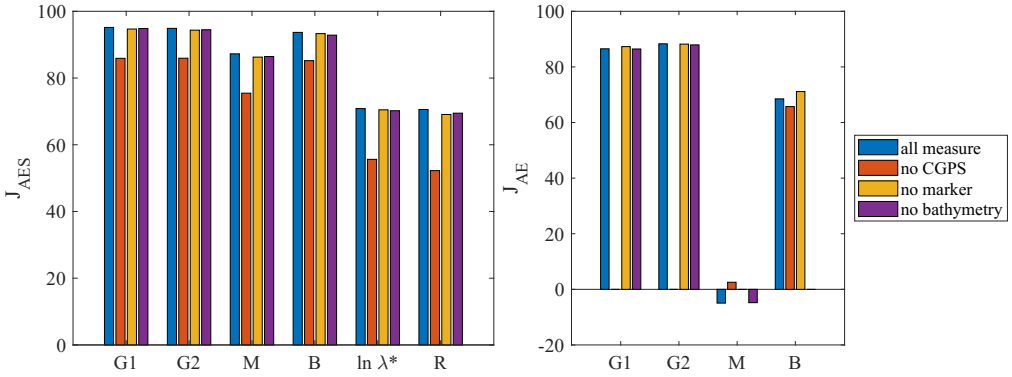

FIGURE 5.42: Update no. 3, year 13 (λ^* and R uncertain): improvement J of the indices AES (left) and AE (right) considering different kind of assimilated data. For comparison, the blue bars (all measure) report the results obtained in the previous paragraph. Since the AE value considers the available measurements, J_{AE} cannot be computed for the excluded measurement type.

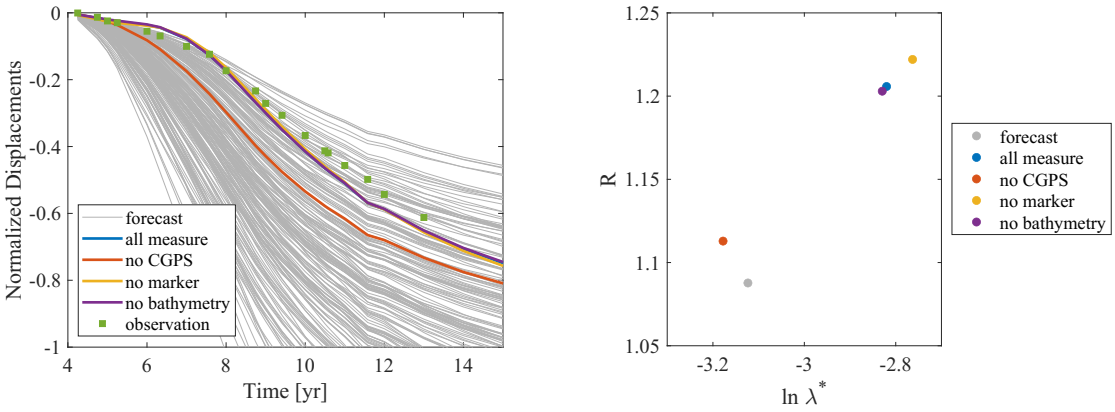

FIGURE 5.43: Update no. 3, year 13 (λ^* and R uncertain): updated states and parameters considering different types of assimilated data. On the left the displacements in time at CGPS 1 location are shown. The forecast ensemble is in grey, measurements are the green squares, while the colored solid lines are the updated mean. On the right the mean of the updated parameter ensembles is reported with the same colour coding.

Fig. 5.42 shows the improvement J for the indices AE and AES. The blue bars refer to the results presented in the previous paragraph, i.e., when all the measurements were used to update the model. The graphs clearly show that the absence of CGPS measurements from the assimilation process (orange bars in Fig. 5.42) worsens the prediction for both the states and the parameters.

In the leftmost panel of Fig. 5.43 a zoom around the CGPS measurements is reported, along with the forecast ensemble (grey stack) and the mean of the updates obtained with different combinations of the available measurements, i.e., excluding either CGPS (orange line), or markers (yellow line), or bathymetry (purple line). All mean update displacements are close to the measurements and in practice overlap, with the exception of the update that neglects the CGPS observations. The right panel of Fig. 5.43 shows the mean of the forecast and update parameters. Again, the exclusion of the marker or the bathymetry from the assimilation process does not significantly change the updated values. On the contrary, removing CGPS from the data-set leads to very different outcomes.

5.2.5 Discussion and conclusions

The main goal of Section 5.2 was to develop a comprehensive geomechanical reservoir model that automatically and dynamically integrates the available measurements in order to reduce uncertainties on land subsidence prediction in a real case study. The model learns from previous experience and evolves with the field, increasing its reliability as new pieces of information become available. The methodological approach described in Chapter 4 has been used on the Arlua reservoir, Italy. Uncertainties have been linked both to the constitutive law that describes the behavior of the active layers and the associated geomechanical parameters. Prior to the reservoir development and until few years after the beginning of the exploitation program, the information is usually poor and consequently the prediction uncertainty is large. However, the progressive integration of new observations allows to greatly reduce such uncertainties. Here, different kinds of data have been used, like CGPS measurements, bathymetric surveys, and compaction from radioactive markers.

Considering the available measurements, the modeling prediction has been updated every few years. Since the first update, uncertainties on the predictions are reduced and the most suitable constitutive law becomes clear. In particular, surface displacements monitored for a few years (3 or 4) at a very few (1 or 2) points, for instance collected by CGPS stations, allow to identify easily the most appropriate rock deformation behavior. The assimilation of new data can modify the previous prediction and

new concerns can arise, e.g., keeping parameters uncertain or fixing them. However, the approach has proven to generally improve the prediction and keep a consistent behavior in consecutive updates. Finally, the mechanical characterization of the model, i.e., the prediction of the geomechanical parameters, can be non unique, but the reliability of the state prediction always increases. This ensures a remarkable robustness of the proposed workflow, which proves able to reduce the prediction uncertainty even if the parameter characterization is not fully satisfactory.

The application on a real-world reservoir allows to shed light on the effectiveness of each step of the proposed workflow. Even if mainly qualitative, the preliminary diagnostic stage carried out at each model update, consisting of the χ^2 and RF tests, proves to be useful in assessing the suitability of the ensembles, hence of the initial modeling hypotheses. For the specific application considered herein, the χ^2 value is always lower for the VEP model, thus suggesting a better geomechanical representativeness than the MCC constitutive law. This is a significant result for recognizing the importance of accounting for viscous effects also in deep geomechanical applications, which confirms the recent results by Musso et al. [2021]. Similarly, the RF approach gives a preliminary low-cost best guess and helps identifying possible flaws in the forecast ensembles, hence in the initial modeling hypotheses.

The application of ES to the Arlua case with a significant dataset composed of CGPS, deep compaction and bathymetric measurements proves able to effectively reduce the uncertainties both in the parameters and in the state ensembles, also when few measurements only are available. For land subsidence prediction, different observations are not equally important. The most effective piece of information appears to be the CGPS measurements, while bathymetry and deep compaction do not appear to be as important for the increase of the prediction reliability. Particular care must be paid on the total number of acquired observations, which should be well-balanced among the different sources in order to avoid a fictitious over-confidence on some data.

Here, the methodological approach has been applied for a reservoir geomechanical model in order to improve the prediction of the maximum expected land subsidence. However, the same approach can be easily extended to satisfy different requests by changing the numerical model. For example, it can be used to improve the predictions

in the field of gas storage or aquifer exploitation, or it can integrate a coupled flow-deformation model for an overall management of the underground resources.

Chapter 6

Conclusions

In the context of the simulation of flow and deformation processes in energy resources engineering, this thesis focused on (i) improving the solution of the set of linear systems arising from the hydro-poromechanical coupled problem in fractured domain and (ii) defining a comprehensive methodological approach for a stochastic analysis of land subsidence. The main findings for these two lines of development are worth summarized in the following paragraphs.

Preconditioning framework for flow and deformation coupling in fractured porous media

The modeling of flow and deformation processes in fractured porous media is particularly demanding from a computational standpoint because of the high level of coupling and non-linearity of the systems to solve. In a typical simulation, most of the computational burden is required for the solution of the linear systems. Thus, efficient linear solvers are required, implying the design of appropriate preconditioners. The preconditioners already available in the literature cannot be straightforwardly applied to the aforementioned problems because of the block structure of the systems and their properties. Thus, the development of ad-hoc preconditioners is required tailored on the specific problem to solve.

In this thesis, three formulations for the flow-deformation coupling have been considered. The preconditioning framework that has been developed aims at exploiting the block structure of the problem and taking advantage from the knowledge of the nature and the structure of the various blocks. It can be generalized in the following three steps:

1. a symbolic permutation of the coefficient matrix blocks in order to avoid singular leading blocks, if any, and to project the Schur complement onto different spaces;

2. an LDU block-factorization of the coefficient matrix, which allows to isolate the subsystems from the original coupled problem;

3. an approximation of the single blocks, and in particular the arising Schur complement.

According to the reordering of the unknowns and the techniques used for the approximations, different preconditioners can originate.

The first model analyzed in this thesis simulates the mechanics in the 3D medium and the flow through the fracture network. The discretization is performed with a blended finite element / finite volume approach where the contact constraints are enforced with the aid of Lagrange multipliers. At the end, a 3×3 block system arises. Two preconditioners have been derived following the aforementioned framework: the first one with the traction-pressure-displacement (t-p-u) order of the unknowns and the second one considering the traction-displacement-pressure (t-u-p) order. Theoretical analyses show that the proposed approaches are expected to have a similar convergence rate, with a slight advantage for the t-p-u approach thanks to a more clustered eigenvalue distribution for the preconditioned matrix and a smaller application cost. Indeed, this is confirmed by the numerical experiments when nested direct solvers are used in the preconditioner application. However, the t-p-u approach may soon lose robustness when AMG methods are introduced, because of the possible indefiniteness of the arising Schur complement, which is avoided in the t-u-p approach.

The t-u-p approach proves to be algorithmically scalable with respect to the computational grid size and the relative size of the discrete fracture network to the full 3D domain. Also, the proposed preconditioner demonstrates computational efficiency in a realistic application, with a very stable behavior of the linear solver throughout the full simulation despite the challenging combination of variable stick/slip/open operating modes for the different fractures.

The second model addresses the flow and deformation coupling in fractured domain with a unified finite volume discretization, imposing the contact constraints with

a penalty approach. A set of 3×3 block linear systems arises from the application of the Newton-Krylov method. Considering the properties and the nature of the sub-blocks, two preconditioners have been proposed: the first one following the order pressure-gap-displacement of the unknowns and the second one considering the order gap-pressure-displacement. The numerical testing phase shows the effectiveness of the approaches, albeit some limits in the approximation of the sub-blocks arise. Thus, further investigations on the importance of the approximations of the modeled processes have been carried out. Specifically, two additional preconditioners have been developed considering a 2×2 structure of the problem, where the mechanics of the 3D domain and the fractures have been joined together. Numerical experiments show the significant influence of the mechanical block approximation on the solution. In future works, this behavior could be improved moving from the MATLAB prototype code that has been used to validate the formulation, to a more sophisticated code which allows to use more suitable techniques for the approximation of the mechanics-related blocks, such as AMG.

Finally, the preconditioning framework has been adapted to the system arising from the PDE-constrained optimization reformulation of the flow problem in fracture networks. In this case, the problem has been projected onto the flow space. The key factor to build an effective preconditioner proves to be the approximation of the Schur complement, thus different approaches have been investigated. The numerical tests demonstrate that both the diagonal and off-diagonal blocks of the Schur complement are fundamental to efficiently solve the system. Independent filterings of such components reveal the fragility of the approximated Schur complement, that can easily become indefinite. Instead, a preliminary filtering of one of the block matrices used to compute the Schur complement appears more promising. This suggests to further investigate and test this filtering approach, in order to ensure the robustness of the formulation.

A comprehensive methodological approach to improve land subsidence prediction

Any modeling activity of real-world phenomena is affected by a number of approximations and hypotheses. In order to reliably investigate possible effects of subsurface

resources exploitation, it is fundamental to take into account the uncertainties in the numerical modeling. This thesis focused at designing a comprehensive methodological approach for a stochastic study of land subsidence. The workflow arises from several analyses on a synthetic test case, aiming at dynamically improving land subsidence predictions using the available measurements to progressively train the numerical model through DA techniques.

Specifically, the workflow starts with the identification of the most influential parameters, and among them, the ones that can be explicitly included as input in the numerical model. Generally, the main uncertainties in land subsidence analyses regard the geomechanical characterization of the reservoir rock. Then, the forward model propagates the uncertainties from the input to the output, generating a set of forecast ensembles of MC realizations. Any numerical model can be used within the workflow, here both a FEM simulator and a gPCE surrogate approach have been applied and compared. The outcomes of the numerical model are compared with the available measurements, which can be shallow or deep displacements, e.g., from CGPS or radioactive markers. The integration of the observations and the outcomes from the numerical model is performed using DA techniques. Specifically, the suitability of the forecast ensembles is first evaluated in the diagnostic step, using the χ^2-test and RF. If the outcomes from the diagnostic stage are not fully satisfactory, the initial assumptions on the uncertain factors should be revised. Otherwise, the model is updated through ES. The states update represents the most reliable land subsidence forecast according to the available measurements. The parameters update can be used to create new forecast ensembles, which are used to repeat the DA framework when new measurements become available, in order to keep the model updated in time.

The workflow has been validated on a synthetic test case, and then tested considering a real off-shore reservoir in Italy. The following results are worth summarizing.

- The DA effectiveness is strongly dependent on the choice of the uncertain factors, which should have a significant impact on the monitored model outcomes. Thus, a preliminary sensitivity analysis through, e.g., Sobol's indices helps in identifying the most influential factors and their range of variability. In addition to the definition of the constitutive law for the reservoir rock, the analyses reported in

this thesis show that the most important geomechanical parameters are the modified compression index λ^* and initial geotechnical initial overconsolidation ratio R.

- The diagnostic step proves particularly useful for a preliminary qualitative evaluation of the forecast ensembles. Specifically, it can be used to compare two or more ensembles, thus helping the selection of the most appropriate constitutive behavior of deep rocks and recognizing the actual representativeness of the selected ranges for the uncertain parameter set.

- ES provides an update of both state and parameter ensembles. The outcomes mainly depend on three different aspects: (i) the set of uncertain parameters, (ii) the measurements, and (iii) the error associated to the observations, i.e., the definition of the measurement covariance matrix. First, the uncertain parameter set has to be actually relevant for the observed process without leading to overparametrization, i.e., multiple combinations can provide similar results with respect to the measurements. The effectiveness of ES improves with the decrease of the error associated to the observations. Hence, the definition of the covariance matrix of the measurement error, which might be also artificially inflated to account for other sources of uncertainty, plays a fundamental role in the application of the DA algorithm. Both in the synthetic and in the real application, ES appears able to quantify and reduce the uncertainties in land subsidence predictions.

- An iterative application of ES, MDA, has been tested in a synthetic application. In principle, it can be used to improve the ES outcome, especially in case of a strongly non-linear relationship between state variables and uncertain parameters. However, in the applications investigated herein, MDA does not always provide better results than ES, despite the higher computational cost, and appears to be strongly influenced by the selection of the uncertain parameter set and the covariance matrix of the measurement error.

- Overall, the workflow proves to be robust and effective, generally providing a progressive decrease in the model prediction uncertainty as the quantity of assimilated measurements increases. The methodological approach has proven able to

improve the prediction while keeping a consistent behavior in consecutive updates.

- Different sources of assimilated data have been considered, i.e., punctual measurements in time, areal measurements at some instant and deep compaction estimates. Analyses show that different types of data are not equally important. In fact, the most effective piece of information appears to be the CGPS measurements, while bathymetry and deep compaction do not appear to be as important for the increase of land subsidence prediction reliability.

- Finally, analyses on a real reservoir also allow to recognize the importance of accounting for viscous effects in deep geomechanical applications.

In this thesis, a methodological approach has been designed and tested with the aim of improving land subsidence prediction. However, it has to be noted that the same approach can be easily extended to satisfy different requests by changing, e.g., the numerical model or the sources of uncertainty.

Bibliography

Agélas, L., Di Pietro, D. A., Eymard, R., and Masson, R. An abstract analysis framework for nonconforming approximations of diffusion problems on general meshes. *International Journal on Finite Volumes*, 7(1):1–29, 2010. URL https://hal.archives-ouvertes.fr/hal-00318390.

Anderson, E. and Saad, Y. Solving sparse triangular linear systems on parallel computers. *International Journal of High Speed Computing*, 01(01):73–95, 1989. doi: 10.1142/S0129053389000056. URL https://doi.org/10.1142/S0129053389000056.

Antil, H., Kouri, D. P., Lacasse, M. D., and Ridzal, D. *Frontiers in PDE-Constrained Optimization*. The IMA Volumes in Mathematics and its Applications. Springer New York, NY, 2006. doi: https://doi.org/10.1007/978-1-4939-8636-1.

Awasthi, S., Varade, D., Bhattacharjee, S., Singh, H., Shahab, S., and Jain, K. Assessment of Land Deformation and the Associated Causes along a Rapidly Developing Himalayan Foothill Region Using Multi-Temporal Sentinel-1 SAR Datasets. *Land*, 11(11), 2022. ISSN 2073-445X. doi: 10.3390/land11112009. URL https://www.mdpi.com/2073-445X/11/11/2009.

Bagheri-Gavkosh, M., Mossa Hosseini, S., Ataie-Ashtiani, B., Sohani, Y., Ebrahimian, H., Morovat, F., and Ashrafi, S. Land subsidence: A global challenge. *Science of The Total Environment*, 778:146193, 2021. ISSN 0048-9697. doi: https://doi.org/10.1016/j.scitotenv.2021.146193. URL https://www.sciencedirect.com/science/article/pii/S0048969721012602.

Balay, S., Abhyankar, S., Adams, M. F., Brown, J., Brune, P., Buschelman, K., Dalcin, L., Dener, A., Eijkhout, V., Gropp, W. D., Karpeyev, D., Kaushik, D., Knepley, M. G., May, D. A., McInnes, L. C., Mills, R. T., Munson, T., Rupp, K., Sanan, P., Smith, B. F.,

Zampini, S., Zhang, H., and Zhang, H. PETSc users manual. Technical Report ANL-95/11 - Revision 3.13, Argonne National Laboratory, 2020. URL https://www.mcs.anl.gov/petsc.

Bathe, K. J. *Finite Element Procedures*. Prentice Hall, 2006. ISBN 9780979004902. URL https://books.google.it/books?id=rWvefGICfO8C.

Baú, D., Ferronato, M., Gambolati, G., and Teatini, P. Land Subsidence Spreading Factor of the Northern Adriatic Gas Fields, Italy. *International Journal of Geomechanics*, 1(4):459–475, 2001. doi: 10.1080/15323640108500166. URL https://www.tandfonline.com/doi/abs/10.1080/15323640108500166.

Baú, D., Ferronato, M., Gambolati, G., and Teatini, P. Basin-scale compressibility of the northern Adriatic by the radioactive marker technique. *Géotechnique*, 52(8):605–616, 2002. doi: 10.1680/geot.2002.52.8.605. URL https://doi.org/10.1680/geot.2002.52.8.605.

Baù, D., Ferronato, M., Gambolati, G., Teatini, P., and Alzraiee, A. Ensemble smoothing of land subsidence measurements for reservoir geomechanical characterization. *International Journal for Numerical and Analytical Methods in Geomechanics*, 39(2):207–228, 2015. doi: https://doi.org/10.1002/nag.2309. URL https://onlinelibrary.wiley.com/doi/abs/10.1002/nag.2309.

Belytschko, T., Liu, W. K., Moran, B., and Elkhodary, K. *Nonlinear Finite Elements for Continua and Structures*. Wiley, 2 edition, 2013. ISBN 978-1-118-70008-2.

Benzi, M. Preconditioning Techniques for Large Linear Systems: A Survey. *Journal of Computational Physics*, 182(2):418–477, 2002. ISSN 0021-9991. doi: https://doi.org/10.1006/jcph.2002.7176. URL https://www.sciencedirect.com/science/article/pii/S0021999102971767.

Benzi, M., Meyer, C. D., and Tůma, M. A Sparse Approximate Inverse Preconditioner for the Conjugate Gradient Method. *SIAM Journal on Scientific Computing*, 17(5):1135–1149, 1996. doi: 10.1137/S1064827594271421. URL https://doi.org/10.1137/S1064827594271421.

Benzi, M., Golub, G. H., and Liesen, J. Numerical solution of saddle point problems. *Acta Numerica*, 14:1–137, 2005. doi: 10.1017/S0962492904000212.

Bergamaschi, L., Ferronato, M., and Gambolati, G. Novel preconditioners for the iterative solution to FE-discretized coupled consolidation equations. *Computer Methods in Applied Mechanics and Engineering*, 196(25):2647–2656, 2007. ISSN 0045-7825. doi: https://doi.org/10.1016/j.cma.2007.01.013. URL https://www.sciencedirect.com/science/article/pii/S0045782507000266.

Bergamaschi, L., Ferronato, M., and Gambolati, G. Mixed Constraint Preconditioners for the iterative solution of FE coupled consolidation equations. *Journal of Computational Physics*, 227(23):9885–9897, 2008. ISSN 0021-9991. doi: https://doi.org/10.1016/j.jcp.2008.08.002. URL https://www.sciencedirect.com/science/article/pii/S002199910800421X.

Berge, R. L., Berre, I., Keilegavlen, E., Nordbotten, J. M., and Wohlmuth, B. Finite volume discretization for poroelastic media with fractures modeled by contact mechanics. *International Journal for Numerical Methods in Engineering*, 121(4):644–663, 2020. doi: https://doi.org/10.1002/nme.6238. URL https://onlinelibrary.wiley.com/doi/abs/10.1002/nme.6238.

Bernardi, M. S., Africa, P. C., de Falco, C., Formaggia, L., Menafoglio, A., and Vantini, S. On the Use of Interferometric Synthetic Aperture Radar Data for Monitoring and Forecasting Natural Hazards. *Mathematical Geosciences*, 53(8):1781–1812, 2021. doi: 10.1007/s11004-021-09948-8.

Berrone, S., Pieraccini, S., and Scialò, S. A PDE-Constrained Optimization Formulation for Discrete Fracture Network Flows. *SIAM Journal on Scientific Computing*, 35(2): B487–B510, 2013. doi: 10.1137/120865884. URL https://doi.org/10.1137/120865884.

Berrone, S., Pieraccini, S., and Scialò, S. An optimization approach for large scale simulations of discrete fracture network flows. *Journal of Computational Physics*, 256:838–853, 2014. ISSN 0021-9991. doi: https://doi.org/10.1016/j.jcp.2013.

09.028. URL https://www.sciencedirect.com/science/article/pii/S0021999113006426.

Berrone, S., Pieraccini, S., and Scialò, S. Towards effective flow simulations in realistic discrete fracture networks. *Journal of Computational Physics*, 310:181–201, 2016. ISSN 0021-9991. doi: https://doi.org/10.1016/j.jcp.2016.01.009. URL https://www.sciencedirect.com/science/article/pii/S0021999116000103.

Berrone, S., Pieraccini, S., and Scialò, S. Non-stationary transport phenomena in networks of fractures: Effective simulations and stochastic analysis. *Computer Methods in Applied Mechanics and Engineering*, 315:1098–1112, 2017. ISSN 0045-7825. doi: https://doi.org/10.1016/j.cma.2016.12.006. URL https://www.sciencedirect.com/science/article/pii/S0045782516305230.

Berrone, S., Scialò, S., and Vicini, F. Parallel Meshing, Discretization, and Computation of Flow in Massive Discrete Fracture Networks. *SIAM Journal on Scientific Computing*, 41(4):C317–C338, 2019. doi: 10.1137/18M1228736. URL https://doi.org/10.1137/18M1228736.

Biot, M. A. General Theory of Three-Dimensional Consolidation. *Journal of Applied Physics*, 12(2):155–164, 1941. doi: 10.1063/1.1712886. URL https://doi.org/10.1063/1.1712886.

Bishop, A. W. The principle of effective stress. *Teknisk Ukeblad*, 106 (39):859–863, 1959. Text of lecture to NGI 1955.

Bollhöfer, M. and Saad, Y. Multilevel Preconditioners Constructed From Inverse-Based ILUs. *SIAM Journal on Scientific Computing*, 27(5):1627–1650, 2006. doi: 10.1137/040608374. URL https://doi.org/10.1137/040608374.

Brandt, A. Multi-level adaptive solutions to boundary-value problems. *Mathematics of Computation*, 31(138):333–390, 1977. doi: 10.2307/2006422.

Brandt, A., Brannick, J., Kahl, K., and Livshits, I. Bootstrap Algebraic Multigrid: Status Report, Open Problems, and Outlook. *Numerical Mathematics: Theory, Methods and Applications*, 8(1):112–135, 2015. doi: 10.4208/nmtma.2015.w06si.

Brezina, M., Ketelsen, C., Manteuffel, T., McCormick, S., Park, M., and Ruge, J. Relaxation-corrected bootstrap algebraic multigrid (rbamg). *Numerical Linear Algebra with Applications*, 19(2):178–193, 2012. doi: https://doi.org/10.1002/nla.1821. URL https://onlinelibrary.wiley.com/doi/abs/10.1002/nla.1821.

Bui, Q. M., Wang, L., and Osei-Kuffuor, D. Algebraic multigrid preconditioners for two-phase flow in porous media with phase transitions. *Advances in Water Resources*, 114:19–28, 2018. ISSN 0309-1708. doi: https://doi.org/10.1016/j.advwatres.2018.01.027. URL https://www.sciencedirect.com/science/article/pii/S0309170817306875.

Bui, Q. M., Osei-Kuffuor, D., Castelletto, N., and White, J. A. A scalable multigrid reduction framework for multiphase poromechanics of heterogeneous media. *SIAM Journal on Scientific Computing*, 42(2):B379–B396, 2020. doi: 10.1137/19M1256117. URL https://doi.org/10.1137/19M1256117.

Camargo, M., Cleto, P. R., Maedo, M. A., Rodrigues, E. A., Bitencourt, L. A., and Manzoli, O. L. Modeling the hydrodynamic behavior of fractures and barriers in porous media using coupling finite elements. *Journal of Petroleum Science and Engineering*, 208:109700, 2022. ISSN 0920-4105. doi: https://doi.org/10.1016/j.petrol.2021.109700. URL https://www.sciencedirect.com/science/article/pii/S0920410521013280.

Camargo, T. J., White, J. A., Castelletto, N., and Borja, R. I. Preconditioners for multiphase poromechanics with strong capillarity. *International Journal for Numerical and Analytical Methods in Geomechanics*, 45(9):1141–1168, 2021. doi: https://doi.org/10.1002/nag.3192. URL https://onlinelibrary.wiley.com/doi/abs/10.1002/nag.3192.

Candela, T. and Koster, K. The many faces of anthropogenic subsidence. *Science*, 376(6600):1381–1382, 2022. doi: 10.1126/science.abn3676. URL https://www.science.org/doi/abs/10.1126/science.abn3676.

Candela, T., Fokker, P. A., and Hegen, D. Ensemble-based subsidence interpretation and prediction ESIP: Technical Reference Manual. Technical Report

R11278, TNO, The Netherlands, January 2017. https://nam-feitenencijfers.data-app.nl/download/rapport/630f8041-25d9-48cd-9329-1ef0d29fc708?open=true.

Candela, T., Chitu, A. G., Peters, E., Pluymaekers, M., Hegen, D., Koster, K., and Fokker, P. A. Subsidence Induced by Gas Extraction: A Data Assimilation Framework to Constrain the Driving Rock Compaction Process at Depth. *Frontiers in Earth Science*, 10, 2022. ISSN 2296-6463. doi: 10.3389/feart.2022.713273. URL https://www.frontiersin.org/article/10.3389/feart.2022.713273.

Capasso, G. and Mantica, S. Numerical simulation of compaction and subsidence using abaqus. In Publ., S., editor, *Proceedings of 2006 ABAQUS Users' Conference*, pages 125–144, 2006.

Carrassi, A., Bocquet, M., Bertino, L., and Evensen, G. Data assimilation in the geosciences: An overview of methods, issues, and perspectives. *WIREs Climate Change*, 9(5):e535, 2018. doi: https://doi.org/10.1002/wcc.535. URL https://wires.onlinelibrary.wiley.com/doi/abs/10.1002/wcc.535.

Cassiani, G. and Zoccatelli, C. Subsidence risk in Venice and nearby areas, Italy, owing to offshore gas fields; a stochastic analysis. *Environmental and Engineering Geoscience*, 6(2):115–128, 05 2000. ISSN 1078-7275. doi: 10.2113/gseegeosci.6.2.115. URL https://doi.org/10.2113/gseegeosci.6.2.115.

Castelletto, N., Gambolati, G., and Teatini, P. Geological CO_2 sequestration in multi-compartment reservoirs: Geomechanical challenges. *Journal of Geophysical Research: Solid Earth*, 118(5):2417–2428, 2013. doi: https://doi.org/10.1002/jgrb.50180. URL https://agupubs.onlinelibrary.wiley.com/doi/abs/10.1002/jgrb.50180.

Castelletto, N., White, J. A., and Ferronato, M. Scalable algorithms for three-field mixed finite element coupled poromechanics. *Journal of Computational Physics*, 327:894–918, 2016. ISSN 0021-9991. doi: https://doi.org/10.1016/j.jcp.2016.09.063. URL https://www.sciencedirect.com/science/article/pii/S0021999116304843.

Cenni, N., Fiaschi, S., and Fabris, M. Monitoring of Land Subsidence in the Po River Delta (Northern Italy) Using Geodetic Networks. *Remote Sensing*, 13(8), 2021. ISSN

2072-4292. doi: 10.3390/rs13081488. URL https://www.mdpi.com/2072-4292/13/8/1488.

Chen, Y. and Oliver, D. S. Levenberg–Marquardt forms of the iterative ensemble smoother for efficient history matching and uncertainty quantification. *Computational Geosciences*, 17(4):689–703, 2013. doi: 10.1007/s10596-013-9351-5. URL https://doi.org/10.1007/s10596-013-9351-5.

Chen, Z., Huan, G., and Ma, Y. *Computational Methods for Multiphase Flows in Porous Media*. Society for Industrial and Applied Mathematics, 2006. doi: 10.1137/1.9780898718942. URL https://epubs.siam.org/doi/abs/10.1137/1.9780898718942.

Conrad, P. R. and Marzouk, Y. M. Adaptive Smolyak Pseudospectral Approximations. *SIAM Journal on Scientific Computing*, 35(6):A2643–A2670, 2013. doi: 10.1137/120890715. URL https://doi.org/10.1137/120890715.

Constantine, P. G., Eldred, M. S., and Phipps, E. T. Sparse pseudospectral approximation method. *Computer Methods in Applied Mechanics and Engineering*, 229-232: 1–12, 2012. ISSN 0045-7825. doi: 10.1016/j.cma.2012.03.019. URL https://www.sciencedirect.com/science/article/pii/S0045782512000953.

Crestaux, T., Le Maître, O., and Martinez, J. M. Polynomial chaos expansion for sensitivity analysis. *Reliability Engineering & System Safety*, 94(7):1161–1172, 2009. ISSN 0951-8320. doi: https://doi.org/10.1016/j.ress.2008.10.008. URL https://www.sciencedirect.com/science/article/pii/S0951832008002561. Special Issue on Sensitivity Analysis.

Cusini, M., Fryer, B., van Kruijsdijk, C., and Hajibeygi, H. Algebraic dynamic multilevel method for compositional flow in heterogeneous porous media. *Journal of Computational Physics*, 354:593–612, 2018. ISSN 0021-9991. doi: https://doi.org/10.1016/j.jcp.2017.10.052. URL https://www.sciencedirect.com/science/article/pii/S0021999117308197.

Davis, T. A. *Direct Methods for Sparse Linear Systems*. Society for Industrial and Applied Mathematics, 2006. doi: 10.1137/1.9780898718881. URL https://epubs.siam.org/doi/abs/10.1137/1.9780898718881.

de Hoop, S., Voskov, D. V., Bertotti, G., and Barnhoorn, A. An advanced discrete fracture methodology for fast, robust, and accurate simulation of energy production from complex fracture networks. *Water Resources Research*, 58(5):e2021WR030743, 2022. doi: https://doi.org/10.1029/2021WR030743. URL https://agupubs.onlinelibrary.wiley.com/doi/abs/10.1029/2021WR030743. e2021WR030743 2021WR030743.

De Loos, J. M. *In-situ compaction measurements in Groningen observation wells.*, volume 28. Verhandenlingen Kon. Ned. Geol. Mijnbouwk Gen., 1973.

De Souza Neto, E., Peric, D., and Owen, D. *Computational methods for plasticity, theory and application*. Wiley, UK, 2008.

Dinar, A., Esteban, E., Calvo, E., Herrera, G., Teatini, P., Tomás, R., Li, Y., Ezquerro, P., and Albiac, J. We lose ground: Global assessment of land subsidence impact extent. *Science of The Total Environment*, 786:147415, 2021. doi: 10.1016/j.scitotenv.2021.147415.

Dolean, V., Jolivet, P., and Nataf, F. *An Introduction to Domain Decomposition Methods*. Society for Industrial and Applied Mathematics, Philadelphia, PA, 2015. doi: 10.1137/1.9781611974065. URL https://epubs.siam.org/doi/abs/10.1137/1.9781611974065.

Droniou, J. Finite volume schemes for diffusion equations: Introduction to and review of modern methods. *Mathematical Models and Methods in Applied Sciences*, 24(08):1575–1619, 2014. doi: 10.1142/S0218202514400041. URL https://doi.org/10.1142/S0218202514400041.

D'Ambra, P., Filippone, S., and Vassilevski, P. S. BootCMatch: A Software Package for Bootstrap AMG Based on Graph Weighted Matching. *ACM Trans. Math. Softw.*, 44 (4), jun 2018. ISSN 0098-3500. doi: 10.1145/3190647. URL https://doi.org/10.1145/3190647.

Eid, C., Benetatos, C., and Rocca, V. Fluid Production Dataset for the Assessment of the Anthropogenic Subsidence in the Po Plain Area (Northern Italy). *Resources*, 11 (6), 2022. ISSN 2079-9276. doi: 10.3390/resources11060053. URL https://www.mdpi.com/2079-9276/11/6/53.

Elman, H. C., Silvester, D. J., and Wathen, A. J. *Finite Elements and Fast Iterative Solvers: with Applications in Incompressible Fluid Dynamics*. Oxford University Press, 2005. ISBN 978-0198528685.

Emerick, A. A. Analysis of the performance of ensemble-based assimilation of production and seismic data. *Journal of Petroleum Science and Engineering*, 139:219–239, 2016. ISSN 0920-4105. doi: 10.1016/j.petrol.2016.01.029. URL https://www.sciencedirect.com/science/article/pii/S0920410516300250.

Emerick, A. A. Deterministic ensemble smoother with multiple data assimilation as an alternative for history-matching seismic data. *Computational Geosciences*, 22:1175–1186, 2018. doi: 10.1007/s10596-018-9745-5. URL https://doi.org/10.1007/s10596-018-9745-5.

Emerick, A. A. and Reynolds, A. C. History matching time-lapse seismic data using the ensemble Kalman filter with multiple data assimilations. *Computational Geosciences*, 16:639–659, 2012. doi: 10.1007/s10596-012-9275-5. URL https://www.sciencedirect.com/science/article/pii/S0920410516300250.

Emerick, A. A. and Reynolds, A. C. Ensemble smoother with multiple data assimilation. *Computers & Geosciences*, 55:3–15, 2013. ISSN 0098-3004. doi: 10.1016/j.cageo.2012.03.011. URL https://www.sciencedirect.com/science/article/pii/S0098300412000994. Ensemble Kalman filter for data assimilation.

Ernstsen, V. B., Noormets, R., Hebbeln, D., Bartholomä, A., and Flemming, B. W. Precision of high-resolution multibeam echo sounding coupled with high-accuracy positioning in a shallow water coastal environment. *Geo-Marine Letters*, 26:141–149, 2006. doi: 10.1007/s00367-006-0025-3.

Estrin, R. and Greif, C. On nonsingular saddle-point systems with a maximally rank deficient leading block. *SIAM Journal on Matrix Analysis and Applications*, 36(2):367–384, 2015. doi: 10.1137/140989996. URL https://doi.org/10.1137/140989996.

Evans, K. F., Moriya, H., Niitsuma, H., Jones, R. H., Phillips, W. S., Genter, A., Sausse, J., Jung, R., and Baria, R. Microseismicity and permeability enhancement of hydrogeologic structures during massive fluid injections into granite at 3 km depth at the Soultz HDR site. *Geophysical Journal International*, 160(1):388–412, 01 2005. ISSN 0956-540X. doi: 10.1111/j.1365-246X.2004.02474.x. URL https://doi.org/10.1111/j.1365-246X.2004.02474.x.

Evensen, G. Sequential data assimilation with a nonlinear quasi-geostrophic model using Monte Carlo methods to forecast error statistics. *Journal of Geophysical Research: Oceans*, 99(C5):10143–10162, 1994. doi: https://doi.org/10.1029/94JC00572. URL https://agupubs.onlinelibrary.wiley.com/doi/abs/10.1029/94JC00572.

Evensen, G. The Ensemble Kalman Filer:theoretical formulation and pratical implementation. *Ocean Dynamics*, 53:343–367, 2003. doi: 10.1007/s10236-003-0036-9.

Evensen, G. *Data Assimilation. The Ensemble Kalman Filter*. Springer Berlin, Heidelberg, 2009. ISBN 978-3-642-03710-8. doi: 10.1007/978-3-642-03711-5.

Evensen, G. Analysis of iterative ensemble smoothers for solving inverse problems. *Computational Geosciences*, 22(3):885–908, 2018. doi: 10.1007/s10596-018-9731-y. URL https://doi.org/10.1007/s10596-018-9731-y.

Evensen, G. and Eikrem, K. S. Conditioning reservoir models on rate data using ensemble smoothers. *Computational Geosciences*, 22(5):1251–1270, 2018. doi: 10.1007/s10596-018-9750-8.

Evensen, G., Vossepoel, F. C., and van Leeuwen. P. J. *Data Assimilation Fundamentals*. Springer Textbooks in Earth Sciences, Geography and Environment (STEGE). Springer Cham, 2022. ISBN 978-3-030-96708-6. doi: 10.1007/978-3-030-96709-3.

Eymard, R., Gallouët, T., and Herbin, R. *Finite volume methods*, volume 7 of *Handbook of Numerical Analysis*, pages 713–1018. Elsevier, 2000. doi: https://doi.org/10.1016/S1570-8659(00)07005-8. URL https://www.sciencedirect.com/science/article/pii/S1570865900070058.

Eymard, R., Gallouët, T., and Herbin, R. A new finite volume scheme for anisotropic diffusion problems on general grids: convergence analysis. *Comptes Rendus Mathematique*, 344(6):403–406, 2007. ISSN 1631-073X. doi: https://doi.org/10.1016/j.crma.2007.01.024. URL https://www.sciencedirect.com/science/article/pii/S1631073X07000465.

Fan, C., Elsworth, D., Li, S., Zhou, L., Yang, Z., and Song, Y. Thermo-hydro-mechanical-chemical couplings controlling CH_4 production and CO_2 sequestration in enhanced coalbed methane recovery. *Energy*, 173:1054–1077, 2019. ISSN 0360-5442. doi: https://doi.org/10.1016/j.energy.2019.02.126. URL https://www.sciencedirect.com/science/article/pii/S0360544219303251.

Farah, P., Popp, A., and Wall, W. A. Segment-based vs. element-based integration for mortar methods in computational contact mechanics. *Computational Mechanics*, 55:209–228, 2015. doi: 10.1007/s00466-014-1093-2. URL https://doi.org/10.1007/s00466-014-1093-2.

Ferronato, M., Gambolati, G., and Teatini, P. Ill-conditioning of finite element poroelasticity equations. *International Journal of Solids and Structures*, 38(34):5995–6014, 2001. ISSN 0020-7683. doi: https://doi.org/10.1016/S0020-7683(00)00352-8. URL https://www.sciencedirect.com/science/article/pii/S0020768300003528.

Ferronato, M., Pini, G., and Gambolati, G. The role of preconditioning in the solution to FE coupled consolidation equations by Krylov subspace methods. *International Journal for Numerical and Analytical Methods in Geomechanics*, 33(3):405–423, 2009. doi: https://doi.org/10.1002/nag.729. URL https://onlinelibrary.wiley.com/doi/abs/10.1002/nag.729.

Ferronato, M., Gambolati, G., Janna, C., and Teatini, P. Geomechanical issues of anthropogenic CO_2 sequestration in exploited gas fields. *Energy Conversion and Management*, 51(10):1918–1928, 2010. doi: 10.1016/j.enconman.2010.02.024.

Ferronato, M., Janna, C., and Pini, G. Parallel solution to ill-conditioned FE geomechanical problems. *International Journal for Numerical and Analytical Methods in Geomechanics*, 36(4):422–437, 2012. doi: https://doi.org/10.1002/nag.1012. URL https://onlinelibrary.wiley.com/doi/abs/10.1002/nag.1012.

Ferronato, M., Castelletto, N., Gambolati, G., Janna, C., and Teatini, P. II cycle compressibility from satellite measurements. *Géotechnique*, 63(6):479–486, 2013. doi: 10.1680/geot.11.P.149. URL https://doi.org/10.1680/geot.11.P.149.

Ferronato, M., Franceschini, A., Janna, C., Castelletto, N., and Tchelepi, H. A. A general preconditioning framework for coupled multiphysics problems with application to contact- and poro-mechanics. *Journal of Computational Physics*, 398:108887, 2019. ISSN 0021-9991. doi: https://doi.org/10.1016/j.jcp.2019.108887. URL https://www.sciencedirect.com/science/article/pii/S0021999119305856.

Firme, P. A., Roehl, D., and Romanel, C. Salt caverns history and geomechanics towards future natural gas strategic storage in Brazil. *Journal of Natural Gas Science and Engineering*, 72:103006, 2019. ISSN 1875-5100. doi: https://doi.org/10.1016/j.jngse.2019.103006. URL https://www.sciencedirect.com/science/article/pii/S1875510019302586.

Fokker, P. A., Wassing, B. B. T., van Leijen, F. J., Hanssen, R. F., and Nieuwland, D. A. Application of an ensemble smoother with multiple data assimilation to the Bergermeer gas field, using PS-InSAR. *Geomechanics for Energy and the Environment*, 5:16–28, 2016. ISSN 2352-3808. doi: https://doi.org/10.1016/j.gete.2015.11.003. URL https://www.sciencedirect.com/science/article/pii/S2352380815000532.

Fokker, P. A., Gunnink, J. L., Koster, K., and de Lange, G. Disentangling and Parameterizing Shallow Sources of Subsidence: Application to a Reclaimed Coastal Area,

Flevoland, the Netherlands. *Journal of Geophysical Research: Earth Surface*, 124(5):1099–1117, 2019. doi: https://doi.org/10.1029/2018JF004975. URL https://agupubs.onlinelibrary.wiley.com/doi/abs/10.1029/2018JF004975.

Formaggia, L., Guadagnini, A., Imperiali, I., Lever, V., Porta, G., Riva, M., Scotti, A., and Tamellini, L. Global sensitivity analysis through polynomial chaos expansion of a basin-scale geochemical compaction model. *Computational Geosciences*, 17:25–42, 2013. doi: 10.1007/s10596-012-9311-5. URL https://doi.org/10.1007/s10596-012-9311-5.

Franceschini, A., Ferronato, M., Janna, C., and Teatini, P. A novel lagrangian approach for the stable numerical simulation of fault and fracture mechanics. *Journal of Computational Physics*, 314:503–521, 2016. ISSN 0021-9991. doi: https://doi.org/10.1016/j.jcp.2016.03.032. URL https://www.sciencedirect.com/science/article/pii/S0021999116001844.

Franceschini, A., Castelletto, N., and Ferronato, M. Block preconditioning for fault/fracture mechanics saddle-point problems. *Computer Methods in Applied Mechanics and Engineering*, 344:376–401, 2019a. ISSN 0045-7825. doi: https://doi.org/10.1016/j.cma.2018.09.039. URL https://www.sciencedirect.com/science/article/pii/S0045782518304924.

Franceschini, A., Paludetto Magri, V. A., Mazzucco, G., Spiezia, N., and Janna, C. A robust adaptive algebraic multigrid linear solver for structural mechanics. *Computer Methods in Applied Mechanics and Engineering*, 352:389–416, 2019b. ISSN 0045-7825. doi: https://doi.org/10.1016/j.cma.2019.04.034. URL https://www.sciencedirect.com/science/article/pii/S0045782519302373.

Franceschini, A., Castelletto, N., White, J. A., and Tchelepi, H. A. Algebraically stabilized Lagrange multiplier method for frictional contact mechanics with hydraulically active fractures. *Computer Methods in Applied Mechanics and Engineering*, 368:113161, 2020. ISSN 0045-7825. doi: 10.1016/j.cma.2020.113161. URL https://www.sciencedirect.com/science/article/pii/S0045782520303467.

Franceschini, A., Gazzola, L., and Ferronato, M. A scalable preconditioning framework for stabilized contact mechanics with hydraulically active fractures. *Journal of Computational Physics*, 463:111276, 2022. ISSN 0021-9991. doi: 10.1016/j.jcp.2022.111276. URL https://www.sciencedirect.com/science/article/pii/S0021999122003382.

Frederickson, P. O. Fast approximate inversion of large sparse linear systems. *Math. Report*, 7, 1975.

Galloway, D. L. and Burbey, T. J. Review: Regional land subsidence accompanying groundwater extraction. *Hydrogeology Journal*, 19:1459–1486, 2011. doi: 10.1007/s10040-011-0775-5. URL https://doi.org/10.1007/s10040-011-0775-5.

Gallyamov, E., Garipov, T., Voskov, D., and Van den Hoek, P. Discrete fracture model for simulating waterflooding processes under fracturing conditions. *International Journal for Numerical and Analytical Methods in Geomechanics*, 42(13):1445–1470, 2018. doi: https://doi.org/10.1002/nag.2797. URL https://onlinelibrary.wiley.com/doi/abs/10.1002/nag.2797.

Gambolati, G., Teatini, P., Baú, D., and Ferronato, M. Importance of poroelastic coupling in dynamically active aquifers of the Po river basin, Italy. *Water Resources Research*, 36(9):2443–2459, 2000.

Gambolati, G., Teatini, P., and Ferronato, M. *Anthropogenic Land Subsidence*, chapter 158. American Cancer Society, 2006. ISBN 9780470848944. doi: 10.1002/0470848944.hsa164b.

Garipov, T. T., Karimi-Fard, M., and Tchelepi, H. A. Discrete fracture model for coupled flow and geomechanics. *Computational Geosciences*, 20:149–160, 2016. doi: 10.1007/s10596-015-9554-z.

Gaspar, F. J., Lisbona, F. J., and Vabishchevich, P. N. A finite difference analysis of biot's consolidation model. *Applied Numerical Mathematics*, 44(4):487–506, 2003. ISSN 0168-9274. doi: https://doi.org/10.1016/S0168-9274(02)00190-3. URL https://www.sciencedirect.com/science/article/pii/S0168927402001903.

Gaspar, F., Lisbona, F., and Vabishchevich, P. Staggered grid discretizations for the quasi-static biot's consolidation problem. *Applied Numerical Mathematics*, 56 (6):888–898, 2006. ISSN 0168-9274. doi: https://doi.org/10.1016/j.apnum.2005.07.002. URL https://www.sciencedirect.com/science/article/pii/S0168927405001522.

Gazzola, L., Ferronato, M., Frigo, M., Janna, C., Teatini, P., Zoccarato, C., Antonelli, M., Corradi, A., Dacome, M. C., and Mantica, S. A novel methodological approach for land subsidence prediction through data assimilation techniques. *Computational Geosciences*, 25(5):1731–1750, 2021. doi: 10.1007/s10596-021-10062-1. URL https://doi.org/10.1007/s10596-021-10062-1.

Gemelli, F., Corradi, A., Volonté, G., Mantica, S., and De Simoni, M. Elasto-viscoplastic modeling of subsidence above gas fields in the Adriatic Sea. *Proceedings of the International Association of Hydrological Sciences*, 382:463–467, 2020. doi: 10.5194/piahs-382-463-2020. URL https://piahs.copernicus.org/articles/382/463/2020/.

Ghanem, R. G. and Spanos, P. D. *Stochastic Finite Elements: A Spectral Approach*. Springer New York, NY, 1991. ISBN 978-1-4612-7795-8. doi: 10.1007/978-1-4612-3094-6.

González, P. J., Tiampo, K. F., Palano, M., Cannavó, F., and Fernández, J. The 2011 Lorca earthquake slip distribution controlled by groundwater crustal unloading. *Nature Geoscience*, 5(11):821–825, 2012. doi: 10.1038/ngeo1610. URL https://doi.org/10.1038/ngeo1610.

Grote, M. J. and Huckle, T. Parallel Preconditioning with Sparse Approximate Inverses. *SIAM Journal on Scientific Computing*, 18(3):838–853, 1997. doi: 10.1137/S1064827594276552. URL https://doi.org/10.1137/S1064827594276552.

Gupta, A. Enhancing Performance and Robustness of ILU Preconditioners by Blocking and Selective Transposition. *SIAM Journal on Scientific Computing*, 39(1):A303–A332, 2017. doi: 10.1137/15M1053256. URL https://doi.org/10.1137/15M1053256.

Hadjesfandiari, A. R. and Dargush, G. F. Couple stress theory for solids. *International Journal of Solids and Structures*, 48(18):2496–2510, 2011. ISSN 0020-7683. doi: 10.1016/j.ijsolstr.2011.05.002. URL https://www.sciencedirect.com/science/article/pii/S0020768311001727.

Hansbo, A. and Hansbo, P. An unfitted finite element method, based on Nitsche's method, for elliptic interface problems. *Computer Methods in Applied Mechanics and Engineering*, 191(47):5537–5552, 2002. ISSN 0045-7825. doi: https://doi.org/10.1016/S0045-7825(02)00524-8. URL https://www.sciencedirect.com/science/article/pii/S0045782502005248.

Hansbo, P. Nitsche's method for interface problems in computational mechanics. *GAMM-Mitteilungen*, 28, 2005.

Hendricks Franssen, H. J. and Kinzelbach, W. Real-time groundwater flow modeling with the Ensemble Kalman Filter: Joint estimation of states and parameters and the filter inbreeding problem. *Water Resources Research*, 44(9), 2008. doi: https://doi.org/10.1029/2007WR006505. URL https://agupubs.onlinelibrary.wiley.com/doi/abs/10.1029/2007WR006505.

Herrera-García, G., Ezquerro, P., Tomás, R., Béjar-Pizarro, M., López-Vinielles, J., Rossi, M., Mateos, R. M., Carreón-Freyre, D., Lambert, J., Teatini, P., Cabral-Cano, E., Erkens, G., Galloway, D., Hung, W.-C., Kakar, N., Sneed, M., Tosi, L., Wang, H., and Ye, S. Mapping the global threat of land subsidence. *Science*, 371(6524):34–36, 2021. doi: 10.1126/science.abb8549.

Hild, P. and Renard, Y. A stabilized Lagrange multiplier method for the finite element approximation of contact problems in elastostatics. *Numerische Mathematik*, 115:101–129, 2010. doi: 10.1007/s00211-009-0273-z.

Hughes, T. J. R. *The Finite Element Method: Linear Static and Dynamic Finite Element Analysis*. Dover Civil and Mechanical Engineering. Dover Publications, 2012. ISBN 9780486135021. URL https://books.google.it/books?id=cHH2n_qBK0IC.

Hysom, D. and Pothen, A. Efficient Parallel Computation of ILU(k) Preconditioners. In *Proceedings of the 1999 ACM/IEEE Conference on Supercomputing*, SC '99, page

29–es, New York, NY, USA, 1999. Association for Computing Machinery. ISBN 1581130910. doi: 10.1145/331532.331561. URL https://doi.org/10.1145/331532.331561.

Improta, L., Valoroso, L., Piccinini, D., and Chiarabba, C. A detailed analysis of wastewater-induced seismicity in the Val d'Agri oil field (Italy). *Geophysical Research Letters*, 42(8):2682–2690, 2015. doi: https://doi.org/10.1002/2015GL063369. URL https://agupubs.onlinelibrary.wiley.com/doi/abs/10.1002/2015GL063369.

Isotton, G., Teatini, P., Ferronato, M., Janna, C., Spiezia, N., Mantica, S., and Volonte, G. Robust numerical implementation of a 3D rate-dependent model for reservoir geomechanical simulations. *International Journal for Numerical and Analytical Methods in Geomechanics*, 43(18):2752–2771, 2019. doi: 10.1002/nag.3000.

Janna, C. and Ferronato, M. Adaptive Pattern Research for Block FSAI Preconditioning. *SIAM J. Sci. Comput.*, 33:3357–3380, 2011.

Janna, C., Castelletto, N., Ferronato, M., Gambolati, G., and Teatini, P. A geomechanical transversely isotropic model of the Po River basin using PSInSAR derived horizontal displacement. *International Journal of Rock Mechanics and Mining Sciences*, 51:105–118, 2012a. ISSN 1365-1609. doi: 10.1016/j.ijrmms.2012.01.015.

Janna, C., Ferronato, M., and Gambolati, G. Parallel inexact constraint preconditioning for ill-conditioned consolidation problems. *Computational Geosciences*, 16:661–675, 2012b. doi: 10.1007/s10596-012-9276-4.

Janna, C., Ferronato, M., and Gambolati, G. Enhanced Block FSAI Preconditioning Using Domain Decomposition Techniques. *SIAM Journal on Scientific Computing*, 35 (5):S229–S249, 2013. doi: 10.1137/120880860. URL https://doi.org/10.1137/120880860.

Jha, B. and Juanes, R. Coupled multiphase flow and poromechanics: A computational model of pore pressure effects on fault slip and earthquake triggering. *Water Resources Research*, 50(5):3776–3808, 2014. doi: https://doi.org/10.1002/

2013WR015175. URL https://agupubs.onlinelibrary.wiley.com/doi/abs/10.1002/2013WR015175.

Jha, B., Bottazzi, F., Wojcik, R., Coccia, M., Bechor, N., McLaughlin, D., Herring, T., Hager, B. H., Mantica, S., and Juanes, R. Reservoir characterization in an underground gas storage field using joint inversion of flow and geodetic data. *International Journal for Numerical and Analytical Methods in Geomechanics*, 39(14):1619–1638, 2015. doi: 10.1002/nag.2427. URL https://onlinelibrary.wiley.com/doi/abs/10.1002/nag.2427.

Jung, S., Lee, K., Park, C., and Choe, J. Ensemble-Based Data Assimilation in Reservoir Characterization: A Review. *Energies*, 11(2), 2018. ISSN 1996-1073. doi: 10.3390/en11020445. URL https://www.mdpi.com/1996-1073/11/2/445.

Kala, K. and Voskov, D. Element balance formulation in reactive compositional flow and transport with parameterization technique. *Computational Geosciences*, 24:609–624, 2019. doi: 10.1007/s10596-019-9828-y.

Kalman, R. E. A New Approach to Linear Filtering and Prediction Problems. *Journal of Basic Engineering*, 82(1):35–45, 03 1960. ISSN 0021-9223. doi: 10.1115/1.3662552. URL https://doi.org/10.1115/1.3662552.

Kang, B. C. and Choe, J. Initial model selection for efficient history matching of channel reservoirs using Ensemble Smoother. *Journal of Petroleum Science and Engineering*, 152:294–308, 2017. ISSN 0920-4105. doi: https://doi.org/10.1016/j.petrol.2017.03.020. URL https://www.sciencedirect.com/science/article/pii/S0920410516306908.

Karev, V. I. Geomechanical approach to improving the efficiency of the operation of underground gas storages. In Karev, V. I., Klimov, D., and Pokazeev, K., editors, *Physical and Mathematical Modeling of Earth and Environment Processes (2018)*, pages 150–158, Cham, 2019. Springer International Publishing. ISBN 978-3-030-11533-3.

Karush, W. Minima of functions of several variables with inequalities as side conditions. Master's thesis, University of Chicago, Department of Mathematics, 1939. URL http://pi.lib.uchicago.edu/1001/cat/bib/4111654.

Keranen, K. M. and Weingarten, M. Induced seismicity. *Annual Review of Earth and Planetary Sciences*, 46(1):149–174, 2018. doi: 10.1146/annurev-earth-082517-010054. URL https://doi.org/10.1146/annurev-earth-082517-010054.

Keranen, K. M., Weingarten, M., Abers, G. A., Bekins, B. A., and Ge, S. Sharp increase in central Oklahoma seismicity since 2008 induced by massive wastewater injection. *Science*, 345(6195):448–451, 2014. doi: 10.1126/science.1255802. URL https://www.science.org/doi/abs/10.1126/science.1255802.

Khait, M. and Voskov, D. Adaptive Parameterization for Solving of Thermal/Compositional Nonlinear Flow and Transport With Buoyancy. *SPE Journal*, 23 (02):522–534, 01 2018a. ISSN 1086-055X. doi: 10.2118/182685-PA. URL https://doi.org/10.2118/182685-PA.

Khait, M. and Voskov, D. Operator-based linearization for efficient modeling of geothermal processes. *Geothermics*, 74:7–18, 2018b. ISSN 0375-6505. doi: https://doi.org/10.1016/j.geothermics.2018.01.012. URL https://www.sciencedirect.com/science/article/pii/S0375650518300312.

Khakim, M. Y. N., Tsuji, T., and Matsuoka, T. Geomechanical modeling for InSAR-derived surface deformation at steam-injection oil sand fields. *Journal of Petroleum Science and Engineering*, 96-97:152–161, 2012. ISSN 0920-4105. doi: https://doi.org/10.1016/j.petrol.2012.08.003. URL https://www.sciencedirect.com/science/article/pii/S092041051200191X.

Kikuchi, N. and Oden, J. T. *Contact Problems in Elasticity*. Studies in Applied and Numerical Mathematics. Society for Industrial and Applied Mathematics, 1988. doi: 10.1137/1.9781611970845. URL https://epubs.siam.org/doi/abs/10.1137/1.9781611970845.

Kolotilina, L. Y. and Yeremin, A. Y. Factorized sparse approximate inverse preconditionings i. theory. *SIAM Journal on Matrix Analysis and Applications*, 14(1):45–58, 1993. doi: 10.1137/0614004. URL https://doi.org/10.1137/0614004.

Kuhn, H. W. and Tucker, A. W. Nonlinear programming. In *Proceedings of the Second Berkeley Symposium on Mathematical Statistics and Probability, 1950*, pages 481–492. University of California Press, Berkeley-Los Angeles, Calif., 1951.

Köppel, M., Martin, V., and Roberts, J. E. A stabilized lagrange multiplier finite-element method for flow in porous media with fractures. *GEM - International Journal on Geomathematics*, 10(7), 2019. doi: 10.1007/s13137-019-0117-7. URL https://doi.org/10.1007/s13137-019-0117-7.

Laursen, T. A. *Computational Contact and Impact Mechanics*. Springer Berlin, Heidelberg, 1 edition, 2003. doi: 10.1007/978-3-662-04864-1.

Le, D. H., Emerick, A. A., and Reynolds, A. C. An Adaptive Ensemble Smoother With Multiple Data Assimilation for Assisted History Matching. *SPE Journal*, 21(06):2195–2207, 12 2016. ISSN 1086-055X. doi: 10.2118/173214-PA. URL https://doi.org/10.2118/173214-PA.

Lin, C.-J. and Moré, J. J. Incomplete Cholesky Factorizations with Limited Memory. *SIAM Journal on Scientific Computing*, 21(1):24–45, 1999. doi: 10.1137/S1064827597327334. URL https://doi.org/10.1137/S1064827597327334.

Liu, P., Zhang, T., and Sun, S. A tutorial review of reactive transport modeling and risk assessment for geologic CO_2 sequestration. *Computers & Geosciences*, 127:1–11, 2019. ISSN 0098-3004. doi: https://doi.org/10.1016/j.cageo.2019.02.007. URL https://www.sciencedirect.com/science/article/pii/S0098300418311932.

Lyu, X., Khait, M., and Voskov, D. Operator-Based Linearization Approach for Modeling of Multiphase Flow with Buoyancy and Capillarity. *SPE Journal*, 26(04):1858–1875, 08 2021a. ISSN 1086-055X. doi: 10.2118/205378-PA. URL https://doi.org/10.2118/205378-PA.

Lyu, X., Voskov, D., and William, R. R. Numerical investigations of foam-assisted CO2 storage in saline aquifers. *International Journal of Greenhouse Gas Control*, 108:103314, 2021b. ISSN 1750-5836. doi: https://doi.org/10.1016/j.ijggc.2021.103314. URL https://www.sciencedirect.com/science/article/pii/S1750583621000669.

Macini, P. and Mesini, E. Measuring Reservoir Compaction Through Radioactive Marker Technique . *Journal of Energy Resources Technology*, 124(4):269–275, 11 2002. ISSN 0195-0738. doi: 10.1115/1.1506700. URL https://doi.org/10.1115/1.1506700.

MATLAB. *version 9.11.0.1837725 (R2021b)*. The MathWorks Inc., Natick, Massachusetts, 2021b.

May, D. A., Sanan, P., Rupp, K., Knepley, M. G., and Smith, B. F. Extreme-Scale Multigrid Components within PETSc. In *Proceedings of the Platform for Advanced Scientific Computing Conference*, number 5 in PASC '16, New York, NY, USA, 2016. Association for Computing Machinery. ISBN 9781450341264. doi: 10.1145/2929908.2929913. URL https://doi.org/10.1145/2929908.2929913.

McCormick, S. F. and Ruge, J. W. Multigrid Methods for Variational Problems. *SIAM Journal on Numerical Analysis*, 19(5):924–929, 1982. doi: 10.1137/0719067. URL https://doi.org/10.1137/0719067.

Mergheim, J., Kuhl, E., and Steinmann, P. A hybrid discontinuous Galerkin/interface method for the computational modelling of failure. *Communications in Numerical Methods in Engineering*, 20(7):511–519, 2004. doi: https://doi.org/10.1002/cnm.689. URL https://onlinelibrary.wiley.com/doi/abs/10.1002/cnm.689.

Mobach, E. and Gussinklo, H. J. In-situ reservoir compaction monitoring in the Groningen field. In *Rock Mechanics in Petroleum Engineering*. OnePetro, 1994.

Muskat, M. and Meres, M. W. The Flow of Heterogeneous Fluids Through Porous Media. *Physics*, 7(9):346–363, 1936. doi: 10.1063/1.1745403. URL https://doi.org/10.1063/1.1745403.

Musso, G., Volonté, G., Gemelli, F., Corradi, A., Nguyen, S. K., Lancellotta, R., Brignoli, M., and Mantica, S. Evaluating the subsidence above gas reservoirs with an elasto-viscoplastic constitutive law. Laboratory evidences and case histories. *Geomechanics for Energy and the Environment*, 28:100246, 2021. doi: 10.1016/j.gete.2021.100246.

Nabben, R. Comparisons between multiplicative and additive Schwarz iterations in domain decomposition methods. *Numerische Mathematik*, 95:145–162, 2003. doi: 10.1007/s00211-002-0444-7. URL https://doi.org/10.1007/s00211-002-0444-7.

Nagel, N. Compaction and subsidence issues within the petroleum industry: From Wilmington to Ekofisk and beyond. *Physics and Chemistry of the Earth, Part A: Solid Earth and Geodesy*, 26(1):3–14, 2001. ISSN 1464-1895. doi: https://doi.org/10.1016/S1464-1895(01)00015-1. URL https://www.sciencedirect.com/science/article/pii/S1464189501000151.

Najm, H. N. Uncertainty Quantification and Polynomial Chaos Techniques in Computational Fluid Dynamics. *Annual Review of Fluid Mechanics*, 41(1):35–52, 2009. doi: 10.1146/annurev.fluid.010908.165248.

NAM. Enseble based subsidence application to the Ameland gas field - long term subsidence study part two (LTS II). Technical report, Overview Report EP201701217189, 2017. URL https://nam-feitenencijfers.data-app.nl/download/rapport/2a2da56c-faee-4453-a8a7-c64c43b418a6?open=true.

Nepveu, M., Kroon, I. C., and Fokker, P. A. Hoisting a Red Flag: an early warning system for exceeding subsidence limits. *Mathematical Geosciences*, 42:187–198, 2010. doi: 10.1007/s11004-009-9252-2.

Nguyen, S. K., Volontè, G., Musso, G., Brignoli, M., Gemelli, F., and Mantica, S. Implementation of an elasto-viscoplastic constitutive law in Abaqus/Standard for an improved characterization of rock materials. *Proceedings of the 51st U.S. Rock Mechanics/Geomechanics Symposium*, 2016. doi: papern.ARMA--2017--1043.

Nocedal, J. and Wright, S. J. *Numerical Optimization*. Springer Series in Operations Research and Financial Engineering. Springer New York, NY, 2 edition, 2006. doi: https://doi.org/10.1007/978-0-387-40065-5.

Novikov, A., Voskov, D., Khait, M., Hajibeygi, H., and Jansen, J. D. A scalable collocated finite volume scheme for simulation of induced fault slip. *Journal of*

Computational Physics, 469:111598, 2022. ISSN 0021-9991. doi: https://doi.org/10.1016/j.jcp.2022.111598. URL https://www.sciencedirect.com/science/article/pii/S002199912200660X.

Oliver, D. S. and Alfonzo, M. Calibration of imperfect models to biased observations. *Computational Geosciences*, 22(1):145–161, 2018. doi: 10.1007/s10596-017-9678-4. URL https://doi.org/10.1007/s10596-017-9678-4.

Oliver, D. S., Reynolds, A. C., and Liu, N. *Inverse Theory for Petroleum Reservoir Characterization and History Matching*. Cambridge University Press, 2008. doi: 10.1017/CBO9780511535642.

Paludetto Magri, V. A., Franceschini, A., and Janna, C. A novel algebraic multigrid approach based on adaptive smoothing and prolongation for ill-conditioned systems. *SIAM Journal on Scientific Computing*, 41(1):A190–A219, 2019. doi: 10.1137/17M1161178. URL https://doi.org/10.1137/17M1161178.

Pan, S.-Y., Gao, M., Shah, K. J., Zheng, J., Pei, S.-L., and Chiang, P.-C. Establishment of enhanced geothermal energy utilization plans: Barriers and strategies. *Renewable Energy*, 132:19–32, 2019. ISSN 0960-1481. doi: https://doi.org/10.1016/j.renene.2018.07.126. URL https://www.sciencedirect.com/science/article/pii/S0960148118309248.

Pearse, J., Singhroy, V., Samsonov, S., and Li, J. Anomalous surface heave induced by enhanced oil recovery in northern Alberta: InSAR observations and numerical modeling. *Journal of Geophysical Research: Solid Earth*, 119(8):6630–6649, 2014. doi: 10.1002/2013JB010885. URL https://agupubs.onlinelibrary.wiley.com/doi/abs/10.1002/2013JB010885.

Peiró, J. and Sherwin, S. *Finite Difference, Finite Element and Finite Volume Methods for Partial Differential Equations*, pages 2415–2446. Springer Netherlands, Dordrecht, 2005. ISBN 978-1-4020-3286-8. doi: 10.1007/978-1-4020-3286-8_127. URL https://doi.org/10.1007/978-1-4020-3286-8_127.

Rafiee, J. and Reynolds, A. C. Theoretical and efficient practical procedures for the generation of inflation factors for ES-MDA. *Inverse Problems*, 33(11):115003, oct 2017. doi:

10.1088/1361-6420/aa8cb2. URL https://dx.doi.org/10.1088/1361-6420/aa8cb2.

Roscoe, K. and Burland, J. On the generalized stress-strain behaviour of the wet clay. *Engineering Plasticity*, pages 535–609, 1968.

Rutqvist, J. and Stephansson, O. The role of hydromechanical coupling in fractured rock engineering. *Hydrogeology Journal*, 11:7–40, 2003. doi: 10.1007/s10040-002-0241-5. URL https://doi.org/10.1007/s10040-002-0241-5.

Rutqvist, J., Rinaldi, A. P., Cappa, F., Jeanne, P., Mazzoldi, A., Urpi, L., Guglielmi, Y., and Vilarrasa, V. Fault activation and induced seismicity in geological carbon storage – Lessons learned from recent modeling studies. *Journal of Rock Mechanics and Geotechnical Engineering*, 8(6):789–804, 2016. ISSN 1674-7755. doi: https://doi.org/10.1016/j.jrmge.2016.09.001. URL https://www.sciencedirect.com/science/article/pii/S167477551630049X.

Saad, Y. ILUT: A dual threshold incomplete LU factorization. *Numerical Linear Algebra with Applications*, 1(4):387–402, 1994. doi: https://doi.org/10.1002/nla.1680010405. URL https://onlinelibrary.wiley.com/doi/abs/10.1002/nla.1680010405.

Saad, Y. *Iterative Methods for Sparse Linear Systems*. Society for Industrial and Applied Mathematics, second edition, 2003. doi: 10.1137/1.9780898718003. URL https://epubs.siam.org/doi/abs/10.1137/1.9780898718003.

Saad, Y. and Schultz, M. H. GMRES: A Generalized Minimal Residual Algorithm for Solving Nonsymmetric Linear Systems. *SIAM Journal on Scientific and Statistical Computing*, 7(3):856–869, 1986. doi: 10.1137/0907058. URL https://doi.org/10.1137/0907058.

Saad, Y. and Suchomel, B. ARMS: an algebraic recursive multilevel solver for general sparse linear systems. *Numerical Linear Algebra with Applications*, 9(5):359–378, 2002. doi: https://doi.org/10.1002/nla.279. URL https://onlinelibrary.wiley.com/doi/abs/10.1002/nla.279.

Salimzadeh, S., Paluszny, A., Nick, H. M., and Zimmerman, R. W. A three-dimensional coupled thermo-hydro-mechanical model for deformable fractured geothermal systems. *Geothermics*, 71:212–224, 2018. ISSN 0375-6505. doi: https://doi.org/10.1016/j.geothermics.2017.09.012. URL https://www.sciencedirect.com/science/article/pii/S0375650517301013.

Saltelli, A., Ratto, M., Andres, T., Campolongo, F., Cariboni, J., Gatelli, D., Saisana, M., and Tarantola, S. *Global Sensitivity Analysis. The Primer*. John Wiley & Sons, Ltd, 2007. ISBN 9780470725184. doi: 10.1002/9780470725184. URL https://https://onlinelibrary.wiley.com/doi/book/10.1002/9780470725184.

Segura, J. M., Fisher, Q. J., Crook, A. J. L., Dutko, M., Yu, J. G., Skachkov, S., Angus, D. A., Verdon, J. P., and Kendall, J.-M. Reservoir stress path characterization and its implications for fluid-flow production simulations. *Petroleum Geoscience*, 17(4):335–344, 2011. doi: 10.1144/1354-079310-034. URL https://www.lyellcollection.org/doi/abs/10.1144/1354-079310-034.

Seitz, A., Farah, P., Kremheller, J., Wohlmuth, B. I., Wall, W. A., and Popp, A. Isogeometric dual mortar methods for computational contact mechanics. *Computer Methods in Applied Mechanics and Engineering*, 301:259–280, 2016. ISSN 0045-7825. doi: https://doi.org/10.1016/j.cma.2015.12.018. URL https://www.sciencedirect.com/science/article/pii/S0045782515004247.

Settari, A., Walters, D. A., Stright, D. H. J., and Aziz, K. Numerical Techniques Used for Predicting Subsidence Due to Gas Extraction in the North Adriatic Sea. *Petroleum Science and Technology*, 26(10-11):1205–1223, 2008. doi: 10.1080/10916460701833889. URL https://doi.org/10.1080/10916460701833889.

Settgast, R. R., Fu, P., Walsh, S. D. C., White, J. A., Annavarapu, C., and Ryerson, F. J. A fully coupled method for massively parallel simulation of hydraulically driven fractures in 3-dimensions. *International Journal for Numerical and Analytical Methods in Geomechanics*, 41(5):627–653, 2017. doi: https://doi.org/10.1002/nag.2557. URL https://onlinelibrary.wiley.com/doi/abs/10.1002/nag.2557.

Shovkun, I. and Tchelepi, H. A. A Cut-Cell Polyhedral Finite Element Model for Coupled Fluid Flow and Mechanics in Fractured Reservoirs. *SPE Journal*, 27(02): 1221–1243, 04 2022. ISSN 1086-055X. doi: 10.2118/203958-PA. URL https://doi.org/10.2118/203958-PA.

Simeoni, U., Tessari, U., Corbau, C., Tosatto, O., Polo, P., and Teatini, P. Impact of land subsidence due to residual gas production on surficial infrastructures: The Dosso degli Angeli field study (Ravenna, Northern Italy). *Engineering Geology*, 229:1–12, 2017. ISSN 0013-7952. doi: https://doi.org/10.1016/j.enggeo.2017.09.008. URL https://www.sciencedirect.com/science/article/pii/S0013795217302934.

Simo, J. C. and Hughes, T. J. R. *Computational Inelasticity*. Interdisciplinary Applied Mathematics. Springer New York, 2006. ISBN 9780387227634. URL https://books.google.it/books?id=EILbBwAAQBAJ.

Simo, J. and Laursen, T. An augmented lagrangian treatment of contact problems involving friction. *Computers & Structures*, 42(1):97–116, 1992. ISSN 0045-7949. doi: https://doi.org/10.1016/0045-7949(92)90540-G. URL https://www.sciencedirect.com/science/article/pii/004579499290540G.

Skjervheim, J. A., Evensen, G., Hove, J., and Vabø, J. G. An Ensemble Smoother for assisted History Matching. In *All Days*, number SPE-141929-MS in SPE Reservoir Simulation Conference, The Woodlands, Texas, USA, 02 2011. doi: 10.2118/141929-MS. URL https://doi.org/10.2118/141929-MS.

Smolyak, S. A. Quadrature and Interpolation Formulas for Tensor Products of Certain Classes of Functions. *Doklady Akademii Nauk SSSR*, 148:1042–1043, 1963. English Russian Translation: Soviet Mathematics Doklady, Vol. 4, 1963, pp. 240-243.

Sobol', I. M. Sensitivity estimates for nonlinear mathematical models. *Matematicheskoe Modelirovanie*, 2:112–118, 1990. 1990 in Russian, translated in English in Sobol' (1993).

Spiezia, N., Ferronato, M., Janna, C., and Teatini, P. A two-invariant pseudoelastic model for reservoir compaction. *International Journal for Numerical and Analytical Methods in Geomechanics*, 41(18):1870–1893, 2017. doi: 10.1002/nag.2704.

Stein, E. *History of the Finite Element Method - Mathematics Meets Mechanics - Part I: Engineering Developments*, pages 399–442. Springer Berlin Heidelberg, Berlin, Heidelberg, 2014. ISBN 978-3-642-39905-3. doi: 10.1007/978-3-642-39905-3_22. URL https://doi.org/10.1007/978-3-642-39905-3_22.

Stüben, K. A review of algebraic multigrid. In Brezinski, C. and Wuytack, L., editors, *Numerical Analysis: Historical Developments in the 20th Century*, pages 331–359. Elsevier, Amsterdam, 2001. ISBN 978-0-444-50617-7. doi: https://doi.org/10.1016/B978-0-444-50617-7.50015-X. URL https://www.sciencedirect.com/science/article/pii/B978044450617750015X.

Sudret, B. Global sensitivity analysis using polynomial chaos expansions. *Reliability Engineering & System Safety*, 93(7):964–979, 2008. ISSN 0951-8320. doi: https://doi.org/10.1016/j.ress.2007.04.002. URL https://www.sciencedirect.com/science/article/pii/S0951832007001329. Bayesian Networks in Dependability.

Sudret, B. *Polynomial chaos expansions and stochastic finite element methods*, chapter 6, pages 265–300. Taylor & Francis, Boca Raton, 2014. ISBN 1-322-62941-2. doi: 10.1201/b17970. URL https://www.taylorfrancis.com/chapters/edit/10.1201/b17970-13/polynomial-chaos-expansions-stochastic-nite-element-methods-bruno-sudret?context=ubx&refId=9893883b-caf5-4209-99f1-5d039b6c48dc.

Tan, H., Xu, J., and Wong-Parodi, G. The politics of Asian fracking: Public risk perceptions towards shale gas development in China. *Energy Research & Social Science*, 54:46–55, 2019. ISSN 2214-6296. doi: https://doi.org/10.1016/j.erss.2019.03.007. URL https://www.sciencedirect.com/science/article/pii/S2214629618311381.

Tang, W.-P. Toward an Effective Sparse Approximate Inverse Preconditioner. *SIAM Journal on Matrix Analysis and Applications*, 20(4):970–986, 1999. doi: 10.1137/S0895479897320071. URL https://doi.org/10.1137/S0895479897320071.

Tarantola, A. *Inverse Problem Theory and Methods for Model Parameter Estimation*. Society for Industrial and Applied Mathematics, 2005. doi: 10.1137/1.9780898717921. URL https://epubs.siam.org/doi/abs/10.1137/1.9780898717921.

Teatini, P., Ferronato, M., Gambolati, G., and Gonella, M. Groundwater pumping and land subsidence in the Emilia-Romagna coastland, Italy: Modeling the past occurrence and the future trend. *Water Resources Research*, 42(1), 2006. doi: https://doi.org/10.1029/2005WR004242. URL https://agupubs.onlinelibrary.wiley.com/doi/abs/10.1029/2005WR004242.

Teatini, P., Castelletto, N., Ferronato, M., Gambolati, G., Janna, C., Cairo, E., Marzorati, D., Colombo, D., Ferretti, A., Bagliani, A., and Bottazzi, F. Geomechanical response to seasonal gas storage in depleted reservoirs: a case study in the Po river basin, Italy. *Journal of Geophysical Research: Earth Surface*, 116(F2), 2011. doi: 10.1029/2010JF001793.

Terekhov, K. M. Cell-centered finite-volume method for heterogeneous anisotropic poromechanics problem. *Journal of Computational and Applied Mathematics*, 365: 112357, 2020. ISSN 0377-0427. doi: https://doi.org/10.1016/j.cam.2019.112357. URL https://www.sciencedirect.com/science/article/pii/S0377042719303607.

Terzaghi, K. *Erdbaumechanik auf Bodenphysikalischer Grundlage.* F. Duticke, Vienna, 1925.

Toselli, A. and Widlund, O. B. *Domain Decomposition Methods - Algorithms and Theory*. Number 1 in Springer Series in Computational Mathematics. Springer Berlin, Heidelberg, 1 edition, 2005. ISBN 978-3-540-20696-5. doi: 10.1007/b137868.

Ucar, E., Keilegavlen, E., Berre, I., and Nordbotten, J. M. A finite-volume discretization for deformation of fractured media. *Computational Geosciences*, 22:993–1007, 08 2018. doi: 10.1007/s10596-018-9734-8. URL https://doi.org/10.1007/s10596-018-9734-8.

van der Vorst, H. A. Bi-CGSTAB: A Fast and Smoothly Converging Variant of Bi-CG for the Solution of Nonsymmetric Linear Systems. *SIAM Journal on Scientific and*

Statistical Computing, 13(2):631–644, 1992. doi: 10.1137/0913035. URL https://doi.org/10.1137/0913035.

van Leeuwen, P. J. and Evensen, G. Data Assimilation and Inverse Methods in Terms of a Probabilistic Formulation. *Monthly Weather Review*, 124 (12):2898–2913, 1996. doi: 10.1175/1520-0493(1996)124<2898:DAAIMI>2.0.CO;2. URL https://journals.ametsoc.org/view/journals/mwre/124/12/1520-0493_1996_124_2898_daaimi_2_0_co_2.xml.

van Leijen, F. J., van der Marel, H., and Hanssen, R. F. Integration of levelling, GNSS, and multi-platform Persistent Scatterer Interferometry data based on time series. In *European Space Agency Living Planet Symposium*, Prague, Czech Republic, 2016.

van Thienen Visser, K., Breunese, J. N., and Muntendam-Bos, A. G. Subsidence due to Gas Production in the Wadden Sea: how to Ensure no Harm will be done to Nature. In U.S. Rock Mechanics/Geomechanics Association ARMA, editor, *All Days*, San Francisco, California, 06 2015. ARMA-2015-098.

Vasco, D. W., Rucci, A., Ferretti, A., Novali, F., Bissell, R. C., Ringrose, P. S., Mathieson, A. S., and Wright, I. W. Satellite-based measurements of surface deformation reveal fluid flow associated with the geological storage of carbon dioxide. *Geophysical Research Letters*, 37(3), 2010. doi: https://doi.org/10.1029/2009GL041544. URL https://agupubs.onlinelibrary.wiley.com/doi/abs/10.1029/2009GL041544.

Vermeer, P. and Neher, H. A soft soil model that accounts for creep. *Proceedings of the International Symposium "Beyond 2000 in Computational Geotechnics"*, pages 249–261, 1999.

Verruijt, A. *Theory and problems of Poroelasticity*. Delft University of Technology, The Netherlands, 2013. URL https://geo.verruijt.net/software/PoroElasticity2016b.pdf.

Voigt, W. Theoretische Studien über die Elasticitätsverhältnisse der Krystalle. I. *Abhandlungen der Königlichen Gesellschaft der Wissenschaften in Göttingen*, 34:3–52, 1887. URL http://eudml.org/doc/135896.

Wang, H. F. *Theory of Linear Poroelasticity with Applications to Geomechanics and Hydrogeology*. Princeton University Press, 2000a. URL http://www.jstor.org/stable/j.ctt1jktrr4.

Wang, H. F. *Theory of Linear Poroelasticity with Applications to Geomechanics and Hydrogeology*. Princeton University Press, 2000b. URL http://www.jstor.org/stable/j.ctt1jktrr4.

Wang, Y., Voskov, D., Khait, M., and Bruhn, D. An efficient numerical simulator for geothermal simulation: A benchmark study. *Applied Energy*, 264:114693, 2020. ISSN 0306-2619. doi: https://doi.org/10.1016/j.apenergy.2020.114693. URL https://www.sciencedirect.com/science/article/pii/S0306261920302051.

Wathen, A. J. Preconditioning. *Acta Numerica*, 24:329–376, 2015. doi: 10.1017/S0962492915000021.

Wei, X., Feng, Z.-J., and Zhao, Y.-S. Numerical simulation of thermo-hydro-mechanical coupling effect in mining fault-mode hot dry rock geothermal energy. *Renewable Energy*, 139:120–135, 2019. ISSN 0960-1481. doi: https://doi.org/10.1016/j.renene.2019.02.070. URL https://www.sciencedirect.com/science/article/pii/S0960148119302241.

White, J. A., Castelletto, N., and Tchelepi, H. A. Block-partitioned solvers for coupled poromechanics: A unified framework. *Computer Methods in Applied Mechanics and Engineering*, 303:55–74, 2016. ISSN 0045-7825. doi: https://doi.org/10.1016/j.cma.2016.01.008. URL https://www.sciencedirect.com/science/article/pii/S0045782516000104.

Wiener, N. The homogeneous chaos. *American Journal of Mathematics*, 60(4):897–936, 1938. doi: 10.2307/2371268.

Williams, L. and Sovacool, B. K. The discursive politics of 'fracking': Frames, storylines, and the anticipatory contestation of shale gas development in the United Kingdom. *Global Environmental Change*, 58:101935, 2019. ISSN 0959-3780. doi: https://doi.org/10.1016/j.gloenvcha.2019.101935. URL https://www.sciencedirect.com/science/article/pii/S0959378019300123.

Witherspoon, P. A., Wang, J. S. Y., Iwai, K., and Gale, J. E. Validity of cubic law for fluid flow in a deformable rock fracture. *Water Resources Research*, 16 (6):1016–1024, 1980. doi: 10.1029/WR016i006p01016. URL https://agupubs.onlinelibrary.wiley.com/doi/abs/10.1029/WR016i006p01016.

Wohlmuth, B. Variationally consistent discretization schemes and numerical algorithms for contact problems. *Acta Numerica*, 20:569—-734, 2011. doi: 10.1017/S0962492911000079.

Wood, D. M. *Soil Behaviour and Critical State Soil Mechanics*. Cambridge University Press, 1991. doi: 10.1017/CBO9781139878272.

Wriggers, P. *Computational Contact Mechanics*. Springer Berlin, Heidelberg, 2 edition, 2006. ISBN 978-3-540-32608-3. doi: 10.1007/978-3-540-32609-0.

Wriggers, P. and Zavarise, G. *Computational Contact Mechanics*, chapter 6, pages 195–226. John Wiley & Sons, Ltd, 2004. ISBN 9780470091357. doi: https://doi.org/10.1002/0470091355.ecm033. URL https://onlinelibrary.wiley.com/doi/abs/10.1002/0470091355.ecm033.

Xiu, D. Efficient collocational approach for parametric uncertainty analysis. *Communications in Computational Physics*, 2(2):293–309, 2007. URL https://www.scopus.com/inward/record.uri?eid=2-s2.0-34447270699&partnerID=40&md5=12c12cbdbf72400219305eb597c0782c.

Xiu, D. *Numerical Methods for Stochastic Computations: A Spectral Method Approach*. Princeton University Press, 2010. ISBN 9780691142128. URL http://www.jstor.org/stable/j.ctv7h0skv.1.

Xiu, D. and Karniadakis, G. E. The Wiener-Askey Polynomial Chaos for Stochastic Differential Equations. *SIAM Journal on Scientific Computing*, 24(2):619–644, 2002. doi: 10.1137/S1064827501387826.

Xu, J. and Zikatanov, L. Algebraic multigrid methods. *Acta Numerica*, 26:591—-721, 2017. doi: 10.1017/S0962492917000083.

Ye, S., Franceschini, A., Zhang, Y., Janna, C., Gong, X., Yu, J., and Teatini, P. A Novel Approach to Model Earth Fissure Caused by Extensive Aquifer Exploitation and its Application to the Wuxi Case, China. *Water Resources Research*, 54(3):2249–2269, 2018. doi: https://doi.org/10.1002/2017WR021872. URL https://agupubs.onlinelibrary.wiley.com/doi/abs/10.1002/2017WR021872.

Zhang, J., Kamenov, A., Zhu, D., and Hill, A. D. Laboratory Measurement of Hydraulic Fracture Conductivities in the Barnett Shale. In *SPE Hydraulic Fracturing Technology Conference and Exhibition*, volume Day 2 Tue, February 05, 2013, 02 2013. doi: 10.2118/163839-MS. URL https://doi.org/10.2118/163839-MS. D021S005R006.

Zhu, L., Gong, H., Li, X., Wang, R., Chen, B., Dai, Z., and Teatini, P. Land subsidence due to groundwater withdrawal in the northern Beijing plain, China. *Engineering Geology*, 193:243–255, 2015. ISSN 0013-7952. doi: https://doi.org/10.1016/j.enggeo.2015.04.020. URL https://www.sciencedirect.com/science/article/pii/S0013795215001362.

Zienkiewicz, O., Taylor, R., and Taylor, R. *The Finite Element Method: Solid mechanics*. Fluid Dynamics. Butterworth-Heinemann, 2000. ISBN 9780750650557. URL https://books.google.it/books?id=MhgBfMWFVHUC.

Zoback, M. D. *Reservoir Geomechanics*. Cambridge University Press, 2007. doi: 10.1017/CBO9780511586477.

Zoccarato, C., Baù, D., Ferronato, M., Gambolati, G., Alzraiee, A., and Teatini, P. Data assimilation of surface displacements to improve geomechanical parameters of gas storage reservoirs. *Journal of Geophysical Research: Solid Earth*, 121(3):1441–1461, 2016. doi: https://doi.org/10.1002/2015JB012090. URL https://agupubs.onlinelibrary.wiley.com/doi/abs/10.1002/2015JB012090.

Zoccarato, C., Ferronato, M., and Teatini, P. Formation compaction vs land subsidence to constrain rock compressibility of hydrocarbon reservoirs. *Geomechanics for Energy and the Environment*, 13:14–24, 2018. ISSN 2352-3808. doi: https://doi.org/10.1016/j.gete.2017.12.002. URL https://www.sciencedirect.com/science/article/pii/S2352380817300205.

Zoccarato, C., Ferronato, M., Franceschini, A., Janna, C., and Teatini, P. Modeling fault activation due to fluid production: Bayesian update by seismic data. *Computational Geosciences*, 23:705–722, 2019. ISSN 1573-1499. doi: 10.1007/s10596-019-9815-3. URL https://doi.org/10.1007/s10596-019-9815-3.

Zoccarato, C., Gazzola, L., Ferronato, M., and Teatini, P. Generalized Polynomial Chaos Expansion for Fast and Accurate Uncertainty Quantification in Geomechanical Modelling. *Algorithms*, 13(7), 2020. ISSN 1999-4893. doi: 10.3390/a13070156. URL https://www.mdpi.com/1999-4893/13/7/156.

Zoccatelli, C., Verdecchia, F., Cassiani, G., Deiana, R., and Praticelli, N. In situ compaction measurements via radioactive markers: an analysis of data precision. In Eisols 2010 (Eighth International Symposium on Land Subsidence), Land Subsidence, editor, *Associated Hazards and the Role of Natural Resources Development*, volume 339, pages 364—367. IAHS Publication, 2010.